8-2015

Investigations into the Tectonics of Uranian and Saturnian Icy Satellites

Chloe Brett Beddingfield
University of Tennessee - Knoxville, cbeddin1@vols.utk.edu

To the Graduate Council:

I am submitting herewith a dissertation written by Chloe Brett Beddingfield entitled "Investigations into the Tectonics of Uranian and Saturnian Icy Satellites." I have examined the final electronic copy of this dissertation for form and content and recommend that it be accepted in partial fulfillment of the requirements for the degree of Doctor of Philosophy, with a major in Geology.

Devon M. Burr, Major Professor

We have read this dissertation and recommend its acceptance:

William M. Dunne, Joshua P. Emery, Liem T. Tran

Accepted for the Council:

Carolyn R. Hodges

Vice Provost and Dean of the Graduate School

(Original signatures are on file with official student records.)

Investigations into the Tectonics of Uranian and Saturnian Icy Satellites

A Dissertation Presented for the
Doctor of Philosophy
Degree
The University of Tennessee, Knoxville

Chloe Brett Beddingfield
August 2015

Dedication

To my parents and brother

Acknowledgements

I'd like to express my deepest gratitude to my Ph.D. advisor, Dr. Devon Burr for being an outstanding role model, for teaching me how to be a logical, scientific thinker, and for providing me with the perfect environment for research. I am grateful to my committee members Dr. William Dunne, Dr. Joshua Emery, and Dr. Liem Tran. Thank you Bill for helping me to develop a background in structural geology. Thank you Josh for helping me to develop a better understanding of the outer solar system icy satellites and geodynamics. Thank you Liem for expanding my knowledge of statistics. I am also thankful to Dr. Annie Howington-Kraus and Dr. Raad Saleh for teaching me how to use SOCET SET to create the digital elevation models used in my research. I am grateful for additional support from Dr. Jeffrey Moersch, Dr. Harry McSween, and Dr. Lawrence Taylor.

I want to thank my friends at the University of Tennessee in Knoxville, Dr. Arya Udry, Dr. Nicole Lunning, Nina Wong, Nate Wigton, Robert Jacobson, Michael Lucas, Dr. Sean Lindsay, Ashley Dameron, Samantha Peel, Keenan Golder, Emily Nield, Eric Maclennan, Dr. Latisha Brengman, Cameron Hughes, and Dr. Noemí Pinilla-Alonso. I am also thankful to my friends from Texas Tech University, Kevin and Amanda Wertz, Christopher Treat, and Maeghan Brundrett. Thank you all for many wonderful conversations about science, research, classes, teaching, and other things. I am so grateful to my undergraduate advisor, Dr. Aaron Yoshinobu, who helped inspire me to pursue a doctorate degree after college.

I'm grateful to my parents, Craig and Christina Beddingfield, and my brother and sister-in-law, John and Ashley Beddingfield who greatly encouraged and supported my dream of pursuing science throughout college and graduate school. I am additionally thankful for the support of other family members, including my grandparents Gary and Heidi Barner, and Willie Mack and Norma Jean Beddingfield. I am especially grateful to Richard Cartwright for tremendous support, for sharing my most memorable and exciting moments throughout graduate school, and for many extensive discussions about science, research, coursework, life, and everything in between.

Abstract

This dissertation reports a range of analyses of tectonic structures on various icy satellites and the implications of these analyses for each satellite's geologic history. On Miranda, I tested the hypothesis that faults of the Arden Corona boundary and the 340º [degree] Chasma are listric in geometry. A listric fault geometry implies the presence of a subsurface detachment, which likely marked Miranda's brittle-ductile transition (BDT) at the time of faulting. Results support the hypothesis for the Arden Corona boundary, although not for the 340˚ [degree] Chasma. Using the Arden Corona fault system geometry, the BDT depth, thermal gradient, and heat flux were estimated. Those estimates are consistent with a previously hypothesized heating event associated with an ancient tidal resonance of Miranda with Umbriel and/or Ariel.

On the Saturnian satellites Tethys, Rhea, and Dione, I analyzed normal fault slope geometries to test the hypothesis that faults on icy bodies reflect dip values derived from laboratory deformation experiments in cryogenic H_2O [water] ice. The results show that faults within Ithaca Chasma on Tethys, Avaiki Chasmata on Rhea, and one scarp within Dione's Wispy Terrain exhibits scarp slopes that are shallower than these values. Analyses of these fault systems indicate that viscous relaxation is the most viable explanation for these shallow slopes. I modeled the potential role of viscous relaxation in creating these shallow fault slopes. The modeling results support the formation of these faults with steep dips, consistent with deformation experiments, followed by their relaxation due to lithospheric heating events.

Finally, I tested for the presence of subtle and/or non-visible fractures within Dione's Non-Wispy Terrain. A set of statistical analyses of crater rim azimuth data was used to test for polygonal impact craters (PICs) at randomly distributed study locations. The results indicate that PICs are widespread throughout the Non-Wispy Terrain, supporting the hypothesis that fractures are widespread throughout this terrain, despite the lack of visible fractures. These results demonstrate that analysis of crater geometries is a useful tool for identifying and mapping fractures with dimensions below the resolution of available images.

Table of Contents

List of Tables

List of Figures

INTRODUCTION

The presence and patterns of tectonic structures on the surfaces of icy satellites may provide clues to the internal structure, lithospheric material properties, viscous relaxation, thermal history, and/or tectonic history of the satellite. Evidence for tectonism is exhibited on the surfaces of many icy satellites in the outer Solar System. Global and/or local stress fields may generate surface deformation on icy satellites (Collins et al., 2009). Global stress mechanisms include diurnal tides, nonsynchronous rotation, polar wander, despinning, orbital recession, and satellite volume change. Local stress mechanisms include convection, lateral pressure gradients, flexure, and impact cratering (Collins et al., 2010, and references therein).

Icy satellite tectonism is commonly extensional, and normal faulting is commonly involved with crustal deformation within tectonically extensional regions. A series of normal faults may create a set of sub-parallel ridges and troughs, which align perpendicular to the direction of extension on a planetary surface (Pappalardo and Greely, 1995). A sequence of normal faults may make up horst and graben terrain or tilted block terrain geometries, with many natural regions of extension possessing aspects of both terrain types (Stewart, 1980). On Earth, the sizes of these blocks vary, from less than 100 meters to kilometers across (Stewart, 1980).

Evidence for tectonism in the Uranian system includes large troughs and canyons on Miranda, Titania, Ariel, Oberon and Umbriel. These features have been interpreted to be extensional in nature, in the form of graben (Smith, 1986; Plescia, 1987; Croft, 1989; Croft and Soderblom, 1991). These graben may have formed due to stresses associated with expansion in the satellites' interiors as freezing occurred (Smith et al., 1986). On Miranda, ridges within the boundary of Arden Corona have been interpreted as normal fault blocks, and may have formed due to uplift of the surface associated with mantle convection (McKinnon, 1988; Pappalardo et al., 1997). In Chapter I, I analyze normal faults within the Arden Corona boundary and the 340º Chasma on Miranda by testing for a listric geometry. A listric fault geometry implies the presence of a brittle-ductile transition at the time of faulting, and the depth to that transition can be estimated, along with the thermal gradient and heat flux.

Several inferred extensional features are also present in the Saturnian system, including those that make up the Wispy Terrain on Dione (Moore, 1984; Wagner et al., 2006), Ithaca Chasma on Tethys (Moore and Ahern, 1983), and Avaiki Chasmata on Rhea (Thomas, 1988). The extensional features on these satellites may have formed from stresses associated with expansion due to freezing of the satellite's interiors (Smith et al., 1982), tidal stresses (Hussmann et al., 2010), and/or impact cratering (Moore and Ahern, 1983). In Chapter II, I investigate normal fault geometries on Tethys, Rhea, and Dione and test the hypothesis that fault slopes on icy bodies reflect dip values derived from laboratory deformation experiments. In Chapter III, I investigated the presence of subtle and/or nonvisible fractures in Dione's Non-Wispy Terrain by testing for polygonal impact craters, which reflect these fractures.

References

Collins G. C., W. B. McKinnon, J. M. Moore, F. Nimmo, R. T. Pappalardo, L. M. Prockter, P. M. Schenk (2009), Tectonics of the outer planet satellites. In Schultz RA, Watters TR (eds) Planetary tectonics, 264–350, Cambridge University Press, Leiden.

Croft, S.K., (1989), New geologic maps of the uranian satellites Titania, Oberon, Umbriel and Miranda, Lunar Planet. Sci. 20, 205.

Croft, S., and L. Soderblom (1991), Geology of the Uranian satellites, Uranus, 561-628, University of Arizona Press, Tucson.

Hussmann, H., G. Choblet, V. Lainey, D. L. Matson, C. Sotin, G. Tobie, T. Van Hoolst (2010), Implications of rotation, orbital states, energy sources, and heat transport for internal processes in icy satellites, *Space science reviews*, *153*(1-4), 317-348.

McKinnon, W. B. (1988), Odd tectonics of a rebuilt moon, *Nature 333*, 701–702, doi: 10.1038/333701a0.

Moore, J. M. (1984), The tectonic and volcanic history of Dione, *Icarus 59*(2), 205-220, doi:10.1016/0019-1035(84)90024-1.

Moore, J. M., and J. L. Ahern (1983), The geology of Tethys, *J. Geophys. Res. Solid Earth, 88(S02),* A577-A584.

Pappalardo, R. T., and R. Greeley, R. (1995), A review of the origins of subparallel ridges and troughs: Generalized morphological predictions from terrestrial models, *J. Geophys. Res. Planets*, *100*(E9), 18985-19007, doi:10.1029/94JE02638.

Pappalardo, R. T., S. J. Reynolds, and R. Greeley (1997), Extensional tilt blocks on Miranda: Evidence for an upwelling origin of Arden Corona, *J. Geophys. Res. Planets, 102*(E6), 13369-13379, doi:10.1029/97JE00802.

Smith, B. A., L. Soderblom, R. Batson, P. Bridges, J. Inge, H. Masursky, E. Shoemaker, R. Beebe, J. Boyce and G. Briggs (1982), A new look at the Saturn system: The Voyager 2 images, *Science 215(4532)*, 504-537, doi:10.1126/science.215.4532.504.

Smith, B. A., L. A. Soderblom, R. F. Beebe, K. Bollinger, J. M. Boyce, A. Brahic, G. A. Briggs, R. H. Brown, C. Chyba, S. A. Collins, A. F. Cook, S. K. Croft, D. Cruikshank, J. N. Cuzzi, G. E. Danielson, M. E. Davies, T. E. Dowling, D. Godfrey, C. J. Hansen, C. Harris, C. P. Helfenstein, G. E. Hunt, A. P. Ingersoll, T. V. Johnson, R. J. Krauss, H. Masursky, D. Morrison, T. Owen, J. B. Plescia, J. B. Pollack, C. C. Porco, K. Rages, C. Sagan, J. Schwartz, E. M. Shoemaker, L. A. Sromovsky, C. Stoker, R. G. Strom, V. E. Suomi, S. P. Synott, R. J. Terrile, P. Thomas, W. R. Thompson, J. Veverka (1986), Voyager 2 in the Uranian system: imaging science results, *Science 233(4759)*, 43–64, doi:10.1126/science.233.4759.43.

Stewart, J. H. (1980). Regional tilt patterns of late Cenozoic basin-range fault blocks, western United States. *Geological Society of America Bulletin*, *91*(8), 460-464.

Thomas, P. G. (1988), The tectonic and volcanic history of Rhea as inferred from studies of scarps, ridges, troughs, and other lineaments, *Icarus 74(3)*, 554-567, doi:10.1016/0019-1035(88)90121-2.

Wagner, R., G. Neukum, B. Giese, T. Roatsch, U. Wolf, T. Denk, and C. I. Team (2006), Geology, Ages and Topography of Saturn's Satellite Dione Observed by the Cassini ISS Camera, paper presented at Lunar Planet. Sci., 37, 1805, The Woodlands.

CHAPTER I
Fault Geometries on Uranus' Satellite Miranda: Implications for Internal Structure and Heat Flow

This chapter is a reformatted version of a paper by the same name published in Icarus in 2015 by Chloe Beddingfield, Devon Burr, and Joshua Emery. All data collection and analyses were performed by Chloe Beddingfield.

Beddingfield, C. B., Burr, D. M., and Emery, J. P. (2015). Fault geometries on Uranus' satellite Miranda: Implications for internal structure and heat flow. *Icarus, 247*, 35-52, doi:10.1016/j.icarus.2014.09.048.

Abstract

Miranda, a ~470-km-diameter Uranian icy satellite, has a surface that exhibits evidence of a complex tectonic history. Tectonic structures are mostly localized in three regions termed coronae, but also form a rift system inferred to be global in extent. Ridges within the boundary of Arden Corona, and those that make up the 340° Chasma, part of the global rift system, have been interpreted as normal fault blocks. Using Voyager data, we test the hypothesis that these Arden Corona faults, as well as those at the northern edge of the 340º Chasma, are listric in geometry. For this testing, we use four geometric criteria for listric faults: (1) progressive down-dip decrease in fault scarp dip, (2) progressive down-dip increase in back-tilted face slope, (3) concavity of the exposed scarp surface, and (4) presence of a rollover structure. Results of this analysis support the hypothesis that the faults within the Arden Corona boundary are listric in geometry, but do not strongly support the hypothesis for the faults within the 340˚ Chasma. By analogy with terrestrial structures, the listric character of faults within the Arden Corona boundary suggests the presence of a subsurface detachment. This detachment likely occurred at Miranda's brittle-ductile transition zone at the time of faulting. Measurements of the Arden Corona fault system geometry are used to estimate depths to the proposed brittle-ductile transition zone at the time of faulting, resulting in values of 6.7 – 9.0 km. Those depths in turn are used to estimate a thermal gradient of 6 – 25 K km^{-1} and a surface heat flux of 31 – 112 mW m^{-2}. The weaker evidence of a listric geometry for the faults of the 340˚ Chasma suggests that those faults did not interact with a brittle-ductile transition at the time of their formation. Our estimated thermal gradient of the Arden Corona region is consistent with a previous heating event on Miranda that was as significant as Europa's current resonance-induced tidal heating. This heating event may be associated with a hypothesized previous tidal resonance of Miranda with Umbriel and/or Ariel.

Introduction

Miranda, a small (~470-km-mean-diameter) icy satellite, is the innermost of the five major Uranian satellites. Like the other major icy satellites of Uranus, Miranda displays lineaments inferred to have resulted from regional or global rifting. Unlike any

other satellite in the Uranian system, Miranda exhibits enigmatic features known as coronae (Figure I-1). Coronae are characterized by ovoid or trapezoidal shapes in plan view, and are separated from the surrounding cratered terrain by a series of subparallel linear features that make up the coronae boundaries. These linear features are diverse in albedo and have been interpreted as ridges and troughs (Smith et al., 1986). Coronae interiors consist of smoother terrains and/or additional topographic linear features. Within Arden and Inverness Coronae, albedo contrasts highlight individual ridges and troughs, where the darker linear features correspond to outward facing ridge walls that exist within the coronae and the higher albedo linear features correspond to ridges (Smith et al., 1986; Pappalardo et al., 1997). In contrast, the ridges and troughs of Elsinore Corona appear to have a more uniform albedo (Figures I-1 and I-2).

Previous work indicates that Miranda's coronae are at least partially tectonic in origin (Thomas, 1988a; Greenberg et al., 1991; Schenk, 1991; Pappalardo, 1994; Pappalardo et al., 1997). Specifically, sloping surfaces have been inferred to be normal fault scarps based on multiple lines of evidence, including the presence of slope lineations that trend perpendicular to the ridges (Pappalardo et al., 1997). Although some of these lineations may be associated with mass wasting (see Pappalardo et al. (1997) for a summary of evidence for mass wasting on Miranda), most are instead inferred to be corrugations caused by the relative downward movement of the hanging walls along the scarps. Evidence supporting this interpretation includes consistent widths from the top to bottom of the slopes and the observation that lineations are only present on slopes that face away from the interior of Arden.

The parallel ridges and troughs within the Arden Corona boundary are interpreted as tilted normal fault blocks that may have been partially modified by mass wasting activity (Thomas, 1988a; Greenberg et al., 1991; Schenk, 1991; Pappalardo, 1994; Pappalardo et al., 1997). Three fault scarp dip measurements taken on separate faults by Pappalardo et al. (1997) along the limb of Miranda indicated a decrease in dip away from the interior of Arden Corona. On this basis, these authors suggested that this fault system might be listric in geometry.

As summarized in previous work (e.g., Croft and Soderblom, 1991), several fresh and mantled fault scarps make up a system of rifts. The section of the rift system that trends roughly 340° is termed the 340° Chasma (Croft and Soderblom, 1991) (Figures I-1 and I-2). The 340° Chasma transects the southern hemisphere of Miranda, between Inverness and Arden Coronae, and trends subparallel to the Arden-facing boundary of Inverness Corona (Figures I-1 and I-2). The faults forming the northern boundary of the 340˚ Chasma have been interpreted as a graben system, based on the sets of inward-facing slopes that make up the chasma (Croft and Soderblom, 1991).

Here, we investigate the hypothesis derived from previous work (Pappalardo et al., 1997) that the normal faults within the boundary of Arden Corona are listric in geometry. Given the availability of stereo images over the 340˚ Chasma, we investigate the additional hypothesis that the normal fault scarps within the 340˚ Chasma are also listric in geometry. Our alternative hypotheses are that the Arden Corona boundary fault system and the 340˚ Chasma fault system are planar in geometry.

For listric faults on Earth, measurements of fault geometry may be used to estimate the depth to a detachment (Gibbs, 1983; Williams and Vann, 1987; Poblet and Bulnes, 2005). A detachment may develop along a brittle-ductile transition zone at depth (Shelton, 1984; Ord and Hobbs, 1989; Regenauer-Lieb et al., 2004), which has been commonly inferred for icy bodies (e.g., Ruiz, 2005). If the faults on Miranda are listric and the detachment of the faults correlate with a brittle-ductile transition zone, the fault geometry measurements can be used to estimate the depth to this zone. An estimate of this depth provides information on Miranda's thermal gradient and heat flux around the coronae perimeters during faulting.

Background

Miranda's Coronae and Global Rift System

Only the southern hemisphere of Miranda, which was facing the Sun at the time of the Voyager 2 flyby, has been imaged. The hemispherical extent of the rift system mentioned above and its truncation by the limb led to the inference that the system is global in extent (Greenberg et al., 1991).

The inferred global rift system includes canyons that exhibit asymmetrical, inward-facing normal fault scarps, where in some locations a large single fault scarp defines one side and several small fault scarps define the other side. The canyons are up to 8 km deep. From the 340˚ Chasma, additional faults that make up the global rift system continue northward, paralleling the eastern edge of Inverness Corona, to Verona Rupes at the limb (Croft and Soderblom, 1991).

As shown in Figure I-1, Arden Corona is located in the equatorial region of Miranda on the leading (western) hemisphere. Elsinore Corona is located on Miranda's equator on the trailing (eastern) hemisphere. Inverness Corona is located near Miranda's south pole, and is the only corona that has been completely imaged. The coronae are surrounded by either the elements of the global rift system, including the 340˚ Chasma (Croft and Soderblom, 1991; Greenberg et al., 1991), or by cratered terrain. In some locations, scarps within the 340° Chasma are continuous with the scarps bounding Arden Corona, indicating that they may have formed at similar times (Croft and Soderblom, 1991).

Different estimates for the relative ages based on impact crater counts of the coronae exist in the literature due to the differences in techniques of identifying craters (McKinnon et al., 1991). Our consideration of the chronology of events on Miranda relies on the results from Zahnle et al. (2003), which in turn uses crater counts from Plescia (1998). As summarized in Zahnle et al. (2003), Arden and Inverness Coronae are estimated to be 1 Gyr in age with the assumption that the cratering rates in the Uranian system are similar to those inferred in the Jovian system. In this case, Elsinore Corona and the cratered terrain are estimated to be older than 3.5 Gyr. Alternatively, if the cratering rates are similar to an impactor flux consistent with the large number of small

craters on Triton, then Arden and Inverness Coronae may only be 100 Myr in age and Elsinore Corona and the cratered terrain may be as young as 2 Gyr.

Multiple formation mechanisms for Miranda's coronae and global rift system have been proposed. The coronae may have formed from downwelling mantle convection within the satellite, possibly caused by a large impact that resulted in a re-accretion event, after which greater density silicate material sank through the ice on Miranda's surface (Johnson et al., 1987; Janes and Melosh, 1988). This so-called "sinker" model requires the tectonic structures that bound each of Miranda's coronae to be contractional in nature, i.e. thrust faults and/or folds. This model is not supported, at least for Arden, by later work that identified extensional features within the Arden Corona boundary (Pappalardo et al., 1997).

Another proposed corona formation mechanism invokes impact and associated extrusive cryovolcanism along pre-existing fracture zones (Smith et al., 1986; Croft, 1987; Jankowski and Squyres, 1988; Schenk, 1991). In this scenario, a large impact formed the depression in which Arden Corona sits, as well as a deep fracture zone in this area through which cryolavas were emplaced (Croft, 1987; Croft and Soderblom, 1991). However, there is no evidence for cryovolcanic features associated with Arden Corona (Pappalardo et al., 1997). Elsinore Corona would have formed due to the generation of a fracture zone at the antipode of the Arden impact that later experienced cryovolcanic activity. The Inverness depression would have formed as part of the global rift system, and subsequent cryovolcanism formed the corona. Although cryovolcanism may have taken place along fractures and faults within Inverness and Elsinore Coronae (Croft and Soderblom, 1991; Greenberg et al., 1991; Schenk, 1991), the initiation of the corona depressions by impact is unlikely due to the lack of evidence for impact-crater-related features (as discussed in McKinnon et al., 1991).

An alternative hypothesis for corona formation is that upwelling occurred within Miranda's interior as low density diapirs ascended to the surface. The marginal uplift implied by this model requires the tectonic structures bounding each corona to be normal faults, resulting in a series of horst and graben structures and/or tilted-fault blocks (McKinnon, 1988; Pappalardo et al., 1997). This model is based on the interpretation by these authors of a normal fault boundary for Arden Corona, but lacks evidence of cryovolcanism to support it.

The global rift system may have formed due to the expansion of Miranda's surface, resulting from a tidally generated or radiogenic temperature increase that caused Miranda to expand volumetrically (Croft, 1987). As summarized in Greenberg et al. (1991), this extension may have occurred due to refreezing of water in Miranda's interior. An alternative explanation is that the canyons are related to volcanic events, although there is no evidence that cryovolcanic flows eminated from the rifts. The global rift system has also been interpreted as resulting from extension related to contractional wrinkle ridges within Inverness Corona (Janes and Melosh, 1988). Additionally, the formation of the rift system has been attributed to cooling of a pluton that formed Inverness Corona (Croft and Soderblom, 1991).

Extensional Tectonism on Other Icy Satellites

Besides Miranda's coronae and global rift system, evidence for tectonism in the Uranian system includes large canyons on Titania, Ariel, Oberon, and Umbriel (Croft, 1989). These features may be extensional in nature, formed as a result of stresses associated with expansion in the satellites' interiors as freezing occurred (Smith et al., 1986).

Satellites in other outer planet systems also show ridges and troughs attributed to crustal extension. In the Jovian system, Europa displays near-ubiquitous ridges and troughs that may have resulted from tensional stresses associated with nonsynchronous rotation and/or diurnal tides (Nimmo and Manga, 2002; Ruiz and Tejero, 2003; Tobie et al., 2003; Showman and Han, 2004; Ruiz, 2005), diapirism (Croft, 1987), and/or dike intrusions (White et al., 2013). Ganymede exhibits regions of ridged and grooved terrain that have been interpreted to be extensional in nature and in some cases show evidence for strike-slip motion (Lucchita, 1980; Murchie and Head, 1988; Pappalardo et al., 2004; Pappalardo and Collins, 2005) and transtension (Collins et al., 1998; Pappalardo et al., 1998; Deremer and Pappalardo, 2003). These structures may have been generated during an expansion of Ganymede's interior (Squyres, 1980; Mueller and McKinnon, 1988), or due to the heat generated during differentiation of the interior (Collins, 2006; Bland et al., 2010).

In the Saturnian system, Enceladus has four prominent sub-linear south polar features, termed "tiger stripes" that have been interpreted to be extensional in nature (Porco et al., 2006). The tiger stripes sit within a ridged and grooved terrain termed the "south polar terrain". The south polar terrain is surrounded by a topographically prominent set of ridges and troughs that make up the south polar terrain boundary. The south polar terrain boundary has been interpreted to be contractional in nature (Porco et al., 2006; Collins and Goodman, 2007; Grott et al., 2007; Helfenstein, 2010; Schultz et al., 2010; Patthoff and Kattenhorn, 2011). Other authors have suggested that an extensional boundary would better correlate with the global elevation dichotomy observed in the south polar region of Enceladus (Walker et al., 2012). Resurfaced terrains in the equatorial regions of Enceladus' leading and trailing hemispheres also exhibit ridges and grooves that may be extensional structures (Helfenstein, 2010).

Several other features interpreted to be extensional in nature are present in the Saturnian system, including those that make up the Wispy Terrain on Dione (Moore, 1984; Wagner et al., 2006), Ithaca Chasma on Tethys (Moore and Ahern, 1983), and Avaiki Chasmata on Rhea (Thomas, 1988b). The extensional features on these satellites may have formed from stresses associated with freeze expansion of the satellite's interiors (Smith et al., 1982), tidal stresses (Hussmann et al., 2010), and/or impact cratering (Moore and Ahern, 1983). Neptune's moon Triton exhibits ridges and grooves (Lewis, 1990) that may have formed from tidal stresses that occurred during a previous eccentric phase of Triton's orbit (Prockter et al., 2005).

Normal Listric Fault Geometries

On the basis of terrestrial examples, normal faults may be classified as either planar or listric, both of which are common in terrestrial settings (Shelton, 1984). Listric faults are characterized as curved, concave up faults that decrease in dip with increased depth and eventually transition into a sub-horizontal detachment (Figure I-3a) (Suess, 1909; Bally, 1983; Shelton, 1984). In contrast, planar faults do not change dip with increased depth (Figure I-3b). Knowledge of fault geometry, whether planar or listric, may provide clues to the subsurface rheology, because listric faults are likely indicative of a change in rheology with depth (Jackson and McKenzie, 1983; Shelton, 1984; Brune and Ellis, 1997) that is not indicated by planar faults.

A variety of characteristics may be used to identify the presence of a listric normal fault system (Figure I-3a). If multiple listric faults are present in a normal fault system, the fault blocks should be differentially tilted due to different amounts of rotation during differential transport down the curved fault planes. In the absence of post-transport modification of the fault scarps, the dips of each fault scarp should progressively decrease in the down-dip direction (Wernicke and Burchfiel, 1982). This systematic dip decrease of the fault scarps at the surface reflects the subsurface change in dips along individual faults as they curve into the detachment at depth.

Because the fault blocks are tilted, each block will exhibit a back-tilted face that was initially the sub-horizontal external surface of the fault block. In a listric fault system, the slopes of these back-tilted faces progressively increase in the down-dip direction (Wernicke and Burchfiel, 1982), due to increasing block rotation with increased displacement.

Viscous relaxation can shallow topographic slopes over geologic timescales. This process reduces the stresses associated with topographic relief by reducing topography over time (e.g., Cathles, 1975; Parmentier and Head, 1981), resulting in long-term ductile deformation of the material (e.g., Cathles, 1975; Dombard and McKinnon, 2006). Although relaxation may change initial fault scarp dips, we still expect a listric fault system to exhibit a progressive decrease in fault dip and increase in back-tilted face slope in the down-dip direction.

Because the dips of a single fault scarp progressively decrease with depth, well-exposed scarps may be noticeably concave up in geometry. However, this characteristic may not be observable in cases of insufficient exposure or where the displacement along an individual normal fault has been too small to substantially reveal the scarp surface. As a result, the presence of concave up fault scarps is indicative of a listric fault system, but non-detection of this geometry does not require that the fault system is planar.

Rollover structures, also called rollover anticlines, are commonly present at the margins of listric fault systems in the down-dip region of the system (e.g., Hamblin, 1965; Xiao and Suppe, 1992). These structures form in listric fault systems as the hanging wall collapses into the space created by the displacement along a curved fault plane (Figure I-4). Rollover structures consist of a wall that slopes in the opposite direction of the faults within the fault system and may contain one or multiple minor antithetic normal faults (Gibbs, 1983; Ellis and McClay, 1988). Rollover structures may consist of a lower section or sections of a fault scarp with possible observable

corrugations, and an upper section or sections without a scarp and without any observable corrugations on the fault-system-facing wall. Alternatively, an antithetic normal fault within the rollover structure may be absent.

In summary, evidence of a normal fault system being listric in nature includes: 1) a progressive decrease in fault dip of individual scarps in the down-dip direction of a fault system, 2) a progressive increase in slopes of individual back-tilted faces in the down-dip direction, 3) concave up geometries of the fault scarps, and 4) the existence of a rollover structure down-dip of the fault system. We use these criteria to test for a presence of listric normal fault systems within the Arden Corona boundary and within the 340º Chasma of Miranda through analysis of data from the Voyager 2 mission.

Possible Detachment Formation Mechanisms on Icy Satellites

Multiple formation mechanisms are possible for detachments on Earth. Detachments may form due to the presence of a mechanically weak layer (e.g., with a different composition than the host brittle material) that exhibits ductile behavior during faulting, i.e. shales or evaporites (Rettger, 1935; Woodbury et al., 1973; Bally et al., 1981; Ewing, 1983). This formation mechanism is unlikely for Miranda because no mechanisms for forming discrete sedimentary layers beneath a brittle crust have been inferred for icy satellites.

In terrestrial settings, a detachment in the crust may result from a higher fluid pressure at depth, also commonly within a shale or evaporate layer. This increase in fluid pressure causes refraction of the principle stress axes, resulting in a progressive decrease in fault dips with depth (Hafner, 1951; Bruce, 1973; Price, 1977; Crans et al., 1980; Jackson and McKenzie, 1983; Bradshaw and Zoback, 1988). However, neither liquid H_2O nor brines near Miranda's surface nor sedimentary layers at depth are likely.

Another formation mechanism for detachments is fault-zone related deformation processes achieving strain-softening behavior at depth (Bazant et al., 1984; Buck et al., 2005). In this case, strain-softening reduces the material's internal angle of friction with increasing strain, thereby weakening the layer in a shear zone and resulting in a decrease in fault dip at depth (Huismans et al., 2002). Results of laboratory experiments have indicated that strain-softening, particularly with added impurities such as HF (Jones, 1967; Jones and Glen, 1969b) and HCl (Nakamura and Jones, 1970), can occur in H_2O ice. In some cases, this softening has been attributed to the development of preferred orientations favoring basil slip (Steinemann, 1954; Kamb, 1972; Duval, 1979, 1981). Strain-softening has also been found to occur during laboratory strength experiments of cryogenic ice, and was attributed to dislocation multiplication and velocity-limited dislocation glide (Weertman, 1983; Durham, 1983, 1992).

Although strain-softening has been observed during the deformation of cryogenic ice, this behavior is not ubiquitous. For example, strain softening was observed in a laboratory study where ice samples were deformed at temperatures less than 250 K and stresses less than 10 MPa (Durham et al., 2001), while other studies conducted with the same temperature range, but with stresses greater than 10 MPa, did not show evidence for strain-softening (Durham et al., 1997). Strain-softening behavior tends to be present in

the initial stages of deformation, but ceases when the ice reaches a steady state (Stern et al., 1997). In a case involving quartz sand impurities in ice, a period of strain-hardening was observed to follow a period of strain softening (Durham et al., 1992). Because strain-softening behavior only occurs in specific situations and tends to be short-lived in cryogenic ice, we find that strain-softening as a formation mechanism for a detachment is possible, but unlikely on Miranda. The presence of a brittle-ductile transition at depth is considered a more reasonable explanation for a subsurface detachment.

Detachments may form at the brittle-ductile transition zone of a single type of material (Ord and Hobbs, 1989; Regenauer-Lieb et al., 2004). Above the brittle-ductile transition zone, deformation is dominantly brittle in nature, while below this zone deformation is mostly ductile (Brune and Ellis, 1997; Ruiz, 2003). In the simplest case, where the crust has a homogeneous composition, we infer that the detachment surface most likely represents the brittle-ductile transition, since a brittle-ductile transition should exist at some depth. If this simplest scenario is correct for Miranda, the depth of the detachment inferred from listric fault geometry provides an estimate of the depth to the brittle-ductile transition zone at the time of faulting.

Data and Methods

Images

All images used in this study were acquired by the Imaging Science Subsystem (Smith et al., 1986) onboard the Voyager 2 spacecraft. Ninety ISS images were taken of Miranda. We examined these images and found that resolutions less than 330 m px^{-1} do not allow confident analysis of individual tectonic structures within the coronae, and so were not used for our study. Eight images of Miranda have a spatial resolution of at least 330 m px^{-1}, with each image covering at least a portion of one corona (Table I-1). Of these eight images, only four of the images give a view of the normal faults at sufficient resolution to resolve fault geometry. The processing steps for these four images, using the Integrated Software for Imagers and Spectrometers (ISIS) (Anderson et al., 2004), are explained in Appendix I-A. The subsequent analyses utilize the qview application in ISIS, ImageJ, and the Environmental Systems Research Institute's (ESRI's) ArcMap software.

Digital Elevation Models

We use the Ames Stereo Pipeline (ASP) software (Broxton and Edwards, 2008; Moratto et al., 2010) to derive digital elevation models (DEMs) from overlapping images. Prior to DEM creation with ASP, some processing of images with ISIS is necessary. Appendix I-B explains the steps used in DEM creation.

Not all DEMs are useful for this study because of two important limitations. Holes occur in the DEMs as a result of removing the reseau points, and large error is present around these holes due to the lack of complete information. As a result, the

DEMs made with images having reseau points over the features of interest are unusable for our study. An additional issue with DEM usability is resolution. Although a DEM may cover features of interest, the DEM resolution might be too low to render those features with a sufficient number of pixels to enable reliable measurements.

Of the eight individual Voyager 2 images in Table I-1, six comprise image pairs appropriate for creating DEMs. Of these six DEMs, only one of them is of adequate quality and resolution to use for data collection in this study (Figure I-5). The image pair numbers, DEM resolutions, DEM triangulation error, and the coronae that are covered are listed in Table I-2, and the DEM coverage of Miranda's surface is shown in Figure I-1. We use the one adequate DEM, generated from image pair c2684611 and c2684626, to take topographic measurements (Figure I-6a,b). All future reference in this paper to the DEM refers to this particular DEM.

Criteria for a Listric Fault System

Based on the four characteristics for a listric fault system, we test for a listric normal fault system of the Arden Corona boundary and the 340º Chasma in four ways (Figure I-7). The first two tests involve assessing dips and slopes. Criterion 1 is a test for a progressive decrease in fault dip in the down-dip direction of the fault system, for each of the two fault scarp systems: Scarps 1 through 4, located within the Arden Corona boundary, and Scarps 5 and 6 of the 340˚ Chasma (Figure I-1 and I-2). Criterion 2 is a test for a progressive increase in back-tilted face slopes, in the down-dip direction of the fault system, for each fault scarp system. If the normal faults are listric in geometry, then the dips of Scarps 1 through 4 should progressively decrease in the down-dip direction, their slopes should progressively increase away from the interior of Arden, and the four sets of measurements for both Criteria 1 and 2 should be statistically different from each other. Likewise, the dip measurements of Scarp 5 should be greater than the measurements of Scarp 6, and the slope measurements of Scarp 5 should be less than those of Scarp 6. We would also expect the two sets of dip measurements to be statistically different from each other and the two sets of slope measurements to be statistically different from each other.

Voyager 2 image c2684626 shows the highest resolution view (247 m px^{-1}) of Scarps 1 through 4 on Miranda's limb (Figure I-8). Although additional fault scarps are present within the Arden Corona boundary, only these four scarps are sufficiently exposed to enable dip and slope measurements with the available image resolution. There is no evidence of foreground or background topographic features significant enough to obscure the apparent geometries of the fault scarps in limb view. Image c2684608 also displays the Arden Corona boundary along Miranda's limb, but at a lower resolution (330 m px^{-1}). The geometries of Scarps 1 through 4 are less prominent in this image. The resolutions of these two images are not sufficient to test for scarp concavity.

We use two separate methods for measuring both dip and slope values for these two tests. For our first method, which is used for Scarps 1 through 4, the Voyager 2 limb view image (c2684626) is analyzed. We estimate a horizontal surface along the limb of Miranda by plotting a curve with Miranda's diameter (~470 km) and then visually

placing the curve along Miranda's limb in image c2684626. To measure the apparent dips for Criterion 1, slopes are traced along each of the four scarps, and the apparent dip angles between these slopes and the curved surface is measured for each scarp (Figure I-8b). To measure apparent slopes of back-tilted faces for Criterion 2, slopes are traced along each back-tilted face, and the angles between these apparent slopes and the curved surface are measured (Figure I-8c). Ten repeat measurements are taken of each fault-scarp apparent dip and of each back-tilted face apparent slope. The averages of these ten values are taken to be the estimated apparent dip and apparent slope values of that particular fault block. Measurement error is calculated as the standard error for each set of measurements.

These measured apparent dip and slope values are then converted to true dip and slope values. These true dip and slope values, δ_{true}, are given by

$$\delta_{true} = \arctan\left(\frac{\tan\alpha}{\sin\beta}\right), \tag{I-1}$$

where α is the apparent dip or apparent slope that is measured, and β is the angle between the fault strike and apparent dip direction. β is measured by estimating the angle between the strike of the Arden Corona boundary and the trend of Miranda's limb in image c2684626. Ten repeat measurements of β are taken. The average measured value is taken to be the estimated value for β, and the standard error of these ten measurements is taken as the error.

For our second method, which is used to apply Criteria 1 and 2 to Scarps 5 and 6 of the 340˚ Chasma, we analyze the DEM (horizontal resolution ~842 meters, vertical accuracy ~95 m) by generating 15 profile lines across Scarp 5, and 15 profile lines across Scarp 6 (Figure I-6a). After plotting the topographic information for each of the 30 profile lines, we visually estimate the top and bottom point of each fault scarp for each profile line, using the greatest change in slope above and below each sub-planar surface (interpreted fault scarp) as a guide. All dip measurements are taken between those two points (Figure I-6c). For the rest of this paper, a 'scarp profile' refers to the section of a profile line that crosses a fault scarp. We also define the top and bottom of each back-tilted face in each profile line in the same way (Figure I-6d). The section of a profile line that crosses a back-tilted face is termed a 'back-tilted face profile'.

We calculate 30 dips of Scarps 5 and 6 along each scarp profile for Criterion 1 and 30 back-tilted face slopes for Criterion 2, by taking measurements between every pair of adjacent points of data, spaced at the horizontal resolution of the DEM, along the entire length of each scarp/back-tilted face profile. The average value measured along a particular scarp/back-tilted face profile is taken to be the estimated dip/slope of the scarp/back-tilted face for that particular location along strike. The measurement error for each average dip or slope is determined by calculating the standard error of each set of measurements.

We perform statistical tests on these data to determine if our results show a significant variation in value, consistent with a listric fault system, with the average values progressively decreasing with distance from the interior of Arden Corona. We apply the Shapiro-Wilk test to determine whether or not each set of data is normally

distributed (Table I-C2). A parametric t-test is used when statistically comparing two sets of normally distributed data. The nonparametric Mann-Whitney U test is used when comparing two sets of data where at least one set of data is not normally distributed.

We use these criteria to determine if the dip and slope measurements for Scarps 1 through 4 are statistically different from each other and to determine if the dip and slope measurements taken along Scarps 5 and 6 are statistically different. We use the average values to determine any trends in value with distance.

Criterion 3 assesses fault scarp concavity over Scarps 5 and 6. Using the 30 DEM-derived scarp profiles, we calculate the local curvature of all sets of three adjacent points on each scarp profile. The slopes between points 1 and 2 are termed "m12" and between points 1 and 3 are termed "m13" (Figure I-9). If the difference between m12 and m13 is negative, then the surface is concave up. An average m12 – m13 difference for each of the 15 scarp profiles for each of the two scarps is calculated. If the mean of all 15 calculations for a scarp is negative, then the scarp is mostly concave up. If the mean is positive, then the fault scarp is mostly convex up. The resulting classification of concave or convex is considered statistically significant if the mean of the 15 averages is more than two standard errors ($p = 0.05$) away from zero. In other words, the hypothesis of a listric fault system would be supported if the mean value is negative and is more than two standard errors away from zero.

We inspected the limb view image of Arden Corona (image c2684626) to determine if concavity might be estimated from those four scarps and also inspected the image of Inverness Corona (image c2684617) that provides a limb view of Verona Rupes. However, the resolution of both images is too low to allow collection of accurate measurements for this criterion.

Criterion 4 assesses the presence of rollover structures. We use three methods for this criterion. For the first method, we analyze the area around the positive topographic feature on the outer margin of Arden Corona in Voyager 2 limb view images c2684608 and c2684626. The following criteria would support the interpretation of this feature as a rollover structure (Figure I-4): 1) in both images, the feature slopes in the opposite direction of the fault system, inward toward Arden and the normal fault system; 2) one or more inward-dipping planar surfaces are present, consistent with antithetic normal faults; 3) corrugations, indicative of an exposed fault scarp, are visible, but do not cover the entire slope, indicative of an antithetic fault; and/or 4) at least part of the slope does not exhibit corrugations, which have been previously identified on the normal fault scarps. Regarding Criterion 3, the lack of an antithetic fault does not refute the interpretation of this feature as a rollover structure, given that not all rollover structures develop antithetic faults.

The second method of testing for a rollover structure involves analyzing the DEM that covers Scarps 5 and 6 of the 340˚ Chasma (Figures I-5 and I-6a). We analyze the terrain down-dip of Scarp 6 to determine if 1) it exhibits a feature that slopes inward, toward Scarps 5 and 6, and 2) if there is an angular topographic feature that tilted toward Scarps 5 and 6, which would be indicative of an antithetic normal fault.

The third method of testing for a rollover structure involves assessing the presence of an antithetic normal fault. One indicator of an antithetical normal fault would

be down-slope lineations, consistent with fault corrugations, on Scarp 6. The absence of visible lineations/corrugations would not necessarily refute the interpretation of this feature as a rollover structure, since not all rollover structures develop antithetic faults.

Results

Scarps 1 through 4 of the Arden Corona boundary show a progressive decrease in fault scarp dip in the down-dip direction (i.e., with distance from the center of Arden Corona). The average dip values change from 43˚ to 27˚ (Table I-C1 and Figure I-10). At the 99% confidence level, the t-test results show that, although the dip measurements recorded for Scarp 1 are not statistically different than those recorded for Scarp 2, the other sets of dip measurements are statistically different from each other (Table I-C3).

Scarps 5 and 6 of the 340º Chasma likewise show a decrease in fault dip in the down-dip direction (Table I-C1 and Figure I-11a), from 31˚ to 14˚. At the 99% confidence level, the t-test results show a statistically significant difference between the two sets of dip measurements taken along Scarps 5 and 6 (Table I-C3).

Scarps 1 through 4 show a progressive increase in slope in the down-dip direction from 14˚ to 30˚ (Table I-C1 and Figure I-10). At the 99% confidence level, the results of a set of t-tests show: 1) the slope measurements recorded for Scarp 2 are not statistically different than those recorded for Scarp 3, and 2) all other sets of dip measurements are statistically different from each other (Table I-C3).

Scarps 5 and 6 of the 340º Chasma show an increase in back-tilted face slope in the down-dip direction from 3˚ to 7˚ (Figure I-11). At the 99% confidence level, the Mann-Whitney U test results show a statistically significant difference between the two sets of slope measurements taken along Scarps 5 and 6 (Table I-C3).

Calculation results of the difference between m12 and m13 across the 30 scarp profiles of Scarps 5 and 6, do not show a concave up geometry of either scarp (Table I-C4 and Figure I-11c). The average m12-m13 is slightly positive (convex) for Scarp 5 and slightly negative (concave) for Scarp 6, though in neither case is the difference from zero statistically significant.

The results of Criterion 4, which assesses the possible presence of rollover structures in the down-dip regions of Scarps 1 through 4 and Scarps 5 & 6, are summarized in Table I-3. Both limb view images (c2684608 and c2684626) of the Arden Corona boundary exhibit a feature that slopes inward toward the interior of Arden. The feature in image c2684626 exhibits an angular, inward tilting face that may be an antithetic normal fault block, although this angular face is not apparent in image c2684608. No evidence of corrugations along the inward sloping feature is present in image c2684608. Some corrugations appear to exist in the region of the inward sloping feature in image c2684626, which would be consistent with the presence of an antithetic normal fault block. These corrugations are not evident near Miranda's limb, which may be due to the poorer resolution of those limb images. The inward-dipping feature in both images exhibits topographically smooth sections that show no evidence of corrugations.

Because the absence of visible lineations/corrugations would not necessarily refute the hypothesis, we find the results of this criterion inconclusive.

The DEM topography shows that a section of Miranda's surface down-dip of Scarps 5 and 6 of the 340˚ Chasma slopes inward, towards the two scarps. The sloping surface may be related to Inverness Corona, which consists of a series of normal fault scarps. Evidence in support of an antithetic normal fault, such as inward dipping angular fault blocks in the vicinity of Scarp 6, is not detectable in the DEM.

Multiple lineations, interpreted as sets of corrugations, are evident on the sloping surface down-dip of Scarps 5 and 6 in all three ISS images that cover that surface (c2684611, c2684617, and c2684626). It is ambiguous whether these normal faults formed from the generation of a rollover structure associated with the 340˚ Chasma, or if they are related to the set of fault scarps within Inverness Corona. Sections of the sloping surface are smooth and do not show evidence of corrugations.

The results of our criteria are summarized in Table I-4. Scarps 1 through 4 pass all three criteria that are possible with the data over the Arden Corona boundary. Scarps 5 and 6 pass two of the four criteria that are possible with the available data over the 340˚ Chasma. Based on these results, we conclude that the hypothesis that the faults within the Arden Coronae boundary (Scarps 1 through 4) are listric in geometry is supported. The hypothesis that the scarps that bound the 340˚ Chasma are listric in geometry is not well supported.

Analysis

Depth to Detachment during Faulting

Several techniques exist to estimate the depth to the sub-horizontal detachment surface of a listric normal fault system; all of these techniques use analysis of the rollover anticlines associated with the fault system (see summary in Poblet and Bulnes, 2005). On this basis, five characteristics of the faults provide information about the depth to detachment.

As shown in Figure I-12 and Table I-5, the depth to detachment of a listric fault system can be estimated if the following parameters are determined: 1) the area dropped below the regional surface (*A*) and the width of the listric fault system (*W*) (Gibbs, 1983), 2) *A* and the displacement of the rollover anticline assuming no shearing (*D*) (Gibbs, 1983), 3) *A* and the heave of the rollover anticline (*H*) (Williams and Vann, 1987), and 4) *A*, *H*, *D* and the folded bed length of the rollover anticline (*F*) (Williams and Vann, 1987).

We directly measure the values of each parameter for the Arden Corona boundary in the limb view image c2684626 (Figure I-8). The values listed in Table I-5 for *A, W, H, F,* and *D* represent averages of ten measurements each (Figure I-12 illustrates the measurements).

The uncertainties for each measurement arise from two sources: 1) the standard error of the ten measurements and 2) the image resolution, *res*. For the linear measurements (*W, H, F,* and *D*), we take the uncertainty from the image resolution to be equal to twice the image resolution for each measured segment. For the area, we assume the uncertainty is the same as it would be if the dropped area were rectangular. This rectangle is defined by the average length, *l*, and width, *w*, of the down-dropped polygon. In this case, the contribution to the uncertainty for *A* from the image resolution, ΔA_{res}, can be estimated as a 1-pixel margin that encompasses the boundary of the rectangle ($\Delta A_{res} = 2 \cdot res[l + w]$). The contribution to uncertainty from image resolution is added in quadrature with the standard error of the ten measurements to compute the final uncertainty values for each parameter listed in Table I-12.

Depth to detachment is calculated in four different ways from these measurements as outlined above and in Table I-5. We calculate the error for the result of each depth-to-detachment calculation using standard rules of error propagation (Taylor and Thompson, 1998). The maximum value for the depth to the detachment surface from these calculations is 9.0 km ± 632 m, and the minimum value is 6.7 km ± 476 m.

Thermal Gradient at the Time of Faulting

The calculations in the following section are based on the inference that the depth to detachment of Arden Corona's listric fault system represents the depth to the brittle-ductile transition. As described in section 2.4, this transition is the most likely explanation for detachments on icy moons. We take the scheme for calculating the thermal gradient and heat flow at the time of faulting from Ruiz and Tejero (2000) and Ruiz (2005). The temperature at the brittle-ductile transition depth can be found by equating the brittle strength of a material at the brittle-ductile transition depth with the ductile strength, and solving for temperature.

The brittle strength of a material, *S*, is given by

$$S = 2(\mu\sigma_3 + C)B, \tag{I-2}$$

where μ is the friction coefficient, σ_3 is the minimum compressive stress, *C* is the material's cohesion, and $B = (\mu^2 + 1)^{1/2} + \mu$. For this equality, the planes of fractures are randomly oriented, and there is no pore fluid pressure (Jaeger and Cook, 1979). When the material is in horizontal tension,

$$\sigma_3 = \rho g z - S. \tag{I-3}$$

Substituting Equation I-3 into Equation I-2 yields the brittle strength in an icy crust under tensional stress as

$$S_{ten} = \frac{2(\mu\rho g z + C)B}{2\mu B + 1}, \tag{I-4}$$

where ρ is the ice density, and g is the gravity. For μ, we use the range of estimated values for cryogenic H_2O ice of $\mu = 0$ (Durham et al., 1983) and $\mu = 0.55$ (Beeman et al., 1988). We use $C = 1$ MPa (Beeman et al., 1988), $\rho = 930$ kg m^{-3}, and $g = 0.079$ m s^{-2}. We use the four values calculated for the depth to the detachment surface for z.

As discussed in Ruiz (2005), ductile strength of water ice is given by

$$S_d = \left(\frac{\dot{\epsilon} d^p}{A}\right)^{\frac{1}{n}} \exp\left(\frac{Q}{nRT}\right), \quad \text{(I-5)}$$

where $\dot{\varepsilon}$ is the strain rate, A, p, and n are empirical constants, d is the grain size, Q is the activation energy of creep, $R = 8.3145$ J mol^{-1} K^{-1} is the gas constant, and T is the absolute temperature. The value of Q depends on the style of creep that is relevant for the given conditions. In the case of superplastic flow, $Q = 49$ kJ mol^{-1}, $A = 3.9 \times 10^{-3}$ MPa^{-n} m^p s^{-1}, $p = 1.4$, and $n = 1.8$ (Goldsby and Kohlstedt, 2001). In the case of dislocation creep $Q = 61$ kJ mol^{-1}, $A = 1.26 \times 10^5$ MPa^{-n} s^{-1}, $p = 0$ and $n = 4$ (Durham and Stern, 2001).

Because the grain size within Miranda's crust is unknown, we use a range of grain sizes in our calculations, beginning with the smallest estimated grain size of Europa's crust (Geissler et al., 1998; Ruiz, 2005). In our calculations, grain sizes range from d = 0.1 to 10 mm. For grain sizes of $d = 0.1$ and 1 mm, superplastic flow is the dominant creep mechanism, whereas dislocation creep is dominant when $d > 1$ mm (McKinnon, 1999; Durham et al., 2001). In our calculations, strain rates range from $\dot{\varepsilon} = 10^{-15}$ s^{-1}, which is an approximate strain rate of faults on Earth, and $\dot{\varepsilon} = 10^{-10}$ s^{-1}, which is the approximate estimated mean value for tidally induced strain rates on Europa ($\dot{\varepsilon} = 2 \times 10^{-10}$ s^{-1}) (Ojakangas and Stevenson, 1989). We have incorporated this Europan strain rate into our calculations because Miranda may have experienced greater strain rates in the past than associated with terrestrial conditions due to a previous tidal resonance with Umbriel and/or Ariel (Tittemore and Wisdom, 1990).

The thermal gradient is given by

$$\Delta T = (T_z - T_s)/z, \quad \text{(I-6)}$$

where T_z is temperature at depth z and T_s is surface temperature. We use T_s values of 70 K, which is the radiative equilibrium temperature of the surface of Miranda (Janes and Melosh, 1988), and 86 K, which is the maximum subsolar brightness temperature of Miranda's surface (Hanel et al., 1986). We calculate the temperature at the brittle-ductile transition and the thermal gradient of the Arden Corona boundary for all four of the calculated brittle-ductile transition depths (Table I-C5). We find that the temperature at the brittle-ductile transition was between 141 K and 264 K, and the thermal gradient of the Arden Corona boundary was between 6 K km^{-1} and 25 K km^{-1} (Figure I-13) at the time that faulting occurred.

Heat Flux at the Time of Faulting

The thermal conductivity of water ice is temperature dependent, following the form $k = k_0/T$. With this thermal conductivity, the heat flux is given by

$$F = \frac{k_0}{z}\ln(\frac{T_z}{T_s}) , \quad \text{(I-7)}$$

where k_0 = 567 W m^{-1} (Klinger, 1980).

Heat flux is calculated at the Arden Corona boundary for all four of the estimated brittle-ductile transition depths, with the range of estimated values for T_S (Table I-C6 and Figure I-14). We estimate that the heat flux of the Arden Corona boundary was between 31 mW m^{-2} and 112 mW m^{-2} during faulting.

Discussion and Implications

Our results for Scarps 1 through 4 better support the hypothesis that the Arden Corona boundary is a listric fault system over the hypothesis that it is a planar fault system. Our results for Scarps 5 and 6 only weakly support the hypothesis that the 340º Chasma is a listric fault system. Thus, the 340º Chasma is more likely to be planar in geometry.

Comparison of Thermal Results to those of other Icy Satellites

Our estimated thermal gradient for Miranda is greater than estimates for Rhea, Iapetus, and Ithaca Chasma on Tethys, and is less than estimates for the equatorial region of the trailing hemisphere of Enceladus. Our estimated thermal gradient is comparable to that estimated for Europa and the Janiculum Dorsa on Dione (see Table I-6 for references). Our thermal gradient calculations are consistent with results from Pappalardo et al. (1997), who derived a range of 8 to 20 K km^{-1} for Miranda, assuming a lithospheric thickness of 5 to 10 km. This comparatively high thermal gradient for Miranda is consistent with a hypothesized heating event that produced as large a heat flux as does Europa's current orbital resonance. A possible early orbital resonance that Miranda had with Umbriel and/or Ariel (Tittemore and Wisdom, 1990) would have increased the eccentricity of Miranda's orbit, which in turn may have been the cause of this heating event. The heat flux we derive for the Arden Corona boundary at the time of fault formation (between 31 and 112 mW m^{-2}) is consistent with that for other small icy satellites. For comparison, heat flux estimates for other ice satellites range from ≤ 2 to 270 mW m^{-2} (Table I-6).

Miranda's Surface Evolution

The difference in fault geometries of the Arden Corona boundary and the 340° Chasma can be explained either by a spatial or temporal variation in Miranda's brittle-ductile transition depth. If the Arden Corona boundary formed simultaneously with the 340˚ Chasma, the brittle-ductile transition depth may have varied spatially (e.g., due to localized heating), such that it was too deep in the region of the 340º Chasma to cause these faults to form a listric geometry. This scenario would imply that the coronae were regions of enhanced heat flow. On the other hand, if the Arden Corona and the 340˚ Chasma are different in age, then the apparent difference in fault system geometry could indicate temporal variability in the heat flow, leading to temporal variability in the transition depth. In this case, the transition depth would have been shallow enough to have affected the geometry of the Arden Corona faults during their formation, but too deep to have affected the geometry of the 340˚ Chasma faults during their formation.

We incorporate our findings with results from crater density analyses of surface terrain and cross-cutting relationships of surface features to infer a possible timeline of Miranda's surface evolution. Relative crater densities indicate that the cratered terrain is the oldest terrain imaged on Miranda (Plescia, 1988; Zahnle et al., 2003). Elsinore Corona is the most heavily cratered corona, and is interpreted to be older than both Arden and Inverness Coronae (Zahnle et al., 2003). Arden and Inverness Coronae have similar crater densities (Zahnle et al., 2003), although a slightly lower crater density on Inverness Corona may indicate a slightly younger age (Plescia, 1988).

Cross-cutting and stratigraphic relationships give additional evidence of this slight age difference. Croft and Soderblom (1991) observed that deposits related to Arden Corona are present in the region between Arden and Inverness Coronae. They interpret the 340° Chasma to cut the Arden deposits, but be overlain by Inverness deposits. These cross-cutting relationships show the 340° Chasma must be younger than Arden Corona, and Inverness Corona must be younger than the 340° Chasma. Because the 340° Chasma makes up a section of the global rift system, its age may represent the age of the entire global rift system, but evidence to support this suggestion is lacking.

The inferred difference in age between Arden Corona and the 340° Chasma, as well as our findings about their different fault geometries, lead us to the conclusion that a temporal variation of the brittle-ductile transition is a more likely scenario than the spatial variation hypothesis, for the difference in fault geometry. Although Arden and Inverness Coronae are broadly similar in age relative to the other major terrains on Miranda, inferred cross-cutting relationships as discussed above would make Arden older than Inverness. Based on this age difference, we propose that Miranda's brittle-ductile transition was shallow enough to interact with the Arden Corona faults during their earlier formation, but became too deep to interact with the 340° Chasma faults during their later formation.

This hypothesis is based on inferred relative ages of Arden Corona, the 340° Chasma, and Inverness Corona. Observations using high resolution images from a future spacecraft mission to the Uranian system (Squyres, 2011) can be used to reassess this relative age information. Our conclusion predicts the following: 1) fault scarps within Arden Corona should be more degraded than those of the 340° Chasma. Similarly, fault

scarps of the 340° Chasma should be more degraded than those of Inverness Corona. 2) The fault scarps within Arden Corona should have more impact craters per unit length of faults than those of the 340° Chasma, while those of Inverness Corona should have less. 3) Fault scarps within Arden Corona should have undergone more topographic relaxation than those of the 340° Chasma, while those within Inverness Corona should have undergone less relaxation.

Summary

We find sufficient evidence to interpret the Arden Corona boundary as a listric normal fault system. We do not find sufficient evidence to interpret the 340˚ Chasma as a listric normal fault system, and it may instead be planar in geometry. We estimate the brittle-ductile transition depth in the region of the Arden Corona boundary during faulting was between 6.7 and 9.0 km with an associated thermal gradient between 6 K km^{-1} and 25 K km^{-1}, and a heat flux between 31 mW m^{-2} and 112 mW m^{-2}. We conclude that Miranda's brittle-ductile transition was shallower at the time Arden Corona formed than at the time the global rift system formed. Future spacecraft to the Uranian system, such as prioritized by the 2012 Decadal Survey (Squyres, 2011), could provide images of Miranda's northern hemisphere and higher resolution images of the southern hemisphere. These data would enable both clearer discernment of the cross-cutting relationships of the coronae and the global rift system on the southern hemisphere and also indicate whether similar geospatial and stratigraphic relationships are present on the northern hemisphere, thereby enabling testing of our results.

References

Agarwal, S., Mierle, K., 2012. Ceres solver: Tutorial & reference, vol. 2. Google Inc.

Anderson, J.A., Sides, S.C., Soltesz, D.L., Sucharski, T.L., Becker, K.J., 2004. Modernization of the integrated software for imagers and spectrometers. Lunar Planet. Sci. 35, 2039.

Bally, A.W., 1983. Seismic expression of structural styles. Stud. Geol. 15 (3).

Bally, A., Bernoulli, D., Davis, G., Montadert, L., 1981. Listric normal faults. Oceanol. Acta 4 (1), 87–101.

Bazant, Z.P., Belytschko, T.B., Chang, T.P., 1984. Continuum theory for strain softening. J. Eng. Mech. 110 (12), 1666–1692.

Beeman, M., Durham, W., Kirby, S., 1988. Friction of ice. J. Geophys. Res.: Solid Earth (1978–2012) 93 (B7), 7625–7633.

Bland, M.T., Beyer, R.A., Showman, A.P., 2007. Unstable extension of Enceladus' lithosphere. Icarus 192 (1), 92–105.

Bland, M.T., McKinnon, W.B., Showman, A.P., 2010. The effects of strain localization on the formation of Ganymede's grooved terrain. Icarus 210 (1), 396–410.

Bland, M.T., Singer, K.N., McKinnon, W.B., Schenk, P.M., 2012. Enceladus' extreme heat flux as revealed by its relaxed craters. Geophys. Res. Lett. 39 (17), L17204. http://dx.doi.org/10.1029/2012GL052736.

Bradshaw, G., Zoback, M.D., 1988. Listric normal faulting, stress refraction, and the state of stress in the Gulf Coast basin. Geology 16 (3), 271–274.

Broxton, M.J., Edwards, L.J., 2008. The Ames Stereo Pipeline: Automated 3D surface reconstruction from orbital imagery. Lunar Planet. Sci. 39, 2419.

Bruce, C.H., 1973. Pressured shale and related sediment deformation; mechanism for development of regional contemporaneous faults. AAPG Bull. 57 (5), 878–886.

Brune, J.N., Ellis, M.A., 1997. Structural features in a brittle–ductile wax model of continental extension. Nature 387, 67–70.

Buck, W.R., Lavier, L.L., Poliakov, A.N., 2005. Modes of faulting at mid-ocean ridges. Nature 434 (7034), 719–723.

Cathles, L.M., 1975. The Viscosity of the Earth's Mantle, vol. 386. Princeton University Press, Princeton, NJ.

Chen, E.M.A., Nimmo, F., 2008. Implications from Ithaca Chasma for the thermal and orbital history of Tethys. Geophys. Res. Lett. 35 (19), L19203. http://dx.doi.org/10.1029/2008GL035402.

Collins, G., 2006. Global expansion of Ganymede derived from strain measurements in grooved terrain. Lunar Planet. Sci. 37, 2077.

Collins, G.C., Goodman, J.C., 2007. Enceladus' south polar sea. Icarus 189 (1), 72–82.

Collins, G.C., Head, J.W., Pappalardo, R.T., 1998. Formation of Ganymede grooved terrain by sequential extensional episodes: Implications of Galileo observations for regional stratigraphy. Icarus 135 (1), 345–359.

Crans, W., Mandl, G., Haremboure, J., 1980. On the theory of faulting: A geomechanical delta model based on gravity sliding. J. Pet. Geol. 2 (3), 265–307.

Croft, S., 1987. Miranda geology and tectonics: A non-catastrophic interpretation. Lunar Planet. Sci. 18, 207.
Croft, S.K., 1989. New geologic maps of the uranian satellites Titania, Oberon, Umbriel and Miranda. Lunar Planet. Sci. 20, 205.
Croft, S., Soderblom, L., 1991. Geology of the uranian satellites. Uranus 1, 561–628.
Deremer, L.C., Pappalardo, R.T., 2003. Manifestations of strike-slip faulting on Ganymede. Lunar Planet. Sci. 34, 2033.
Dombard, A.J., McKinnon, W.B., 2006. Folding of Europa's icy lithosphere: An analysis of viscous-plastic buckling and subsequent topographic relaxation. J. Struct. Geol. 28 (12), 2259–2269.
Durham, W., Stern, L., 2001. Rheological properties of water ice-applications to satellites of the outer planets 1. Annu. Rev. Earth Planet. Sci. 29 (1), 295–330.
Durham, W., Heard, H., Kirby, S., 1983. Experimental deformation of polycrystalline H2O ice at high pressure and low temperature: Preliminary results. J. Geophys. Res.: Solid Earth (1978–2012) 88 (S01), B377–B392.
Durham, W.B., Kirby, S.H., Stern, L.A., 1992. Effects of dispersed particulates on the rheology of water ice at planetary conditions. J. Geophys. Res.: Planets (1991-2012) 97 (E12), 20883–20897.
Durham, W.B., Kirby, S.H., Stern, L.A., 1997. Creep of water ices at planetary conditions: A compilation. J. Geophys. Res.: Planets 102 (E7), 16293–16302.
Durham, W.B., Stern, L.A., Kirby, S.H., 2001. Rheology of ice I at low stress and elevated confining pressure. J. Geophys. Res.: Solid Earth (1978–2012) 106 (B6), 11031–11042.
Duval, P., 1979. Creep and recrystallization of polycrystalline ice. Bull. Minér. 102 (2–3), 80–85.
Duval, P., 1981. Creep and fabrics of polycrystalline ice under shear and compression. J. Glaciol. 27, 129–140.
Ellis, P.G., McClay, K.R., 1988. Listric extensional fault systems – Results of analogue model experiments. Basin Res. 1 (1), 55–70.
Ewing, T.E., 1983. Growth Faults and Salt Tectonics in Houston Diapir Province: Relative Timing and Exploration Significance. Gulf Coast Association of Geologists Society Transactions, vol. 33, pp. 83–90.
Geissler, P., Greenberg, R., Hoppa, G., McEwen, A., Tufts, R., Phillips, C., Clark, B., Ockert-Bell, M., Helfenstein, P., Burns, J., 1998. Evolution of lineaments on Europa: Clues from Galileo multispectral imaging observations. Icarus 135 (1), 107–126.
Gibbs, A.D., 1983. Balanced cross-section construction from seismic sections in areas of extensional tectonics. J. Struct. Geol. 5 (2), 153–160.
Giese, B., Wagner, R., Neukum, G., Helfenstein, P., Thomas, P.C., 2007. Tethys: Lithospheric thickness and heat flux from flexurally supported topography at Ithaca Chasma. Geophys. Res. Lett. 34 (21), L21203.
Giese, B. et al., 2008. Enceladus: An estimate of heat flux and lithospheric thickness from flexurally supported topography. Geophys. Res. Lett. 35 (24), L24204. http://dx.doi.org/10.1029/2008GL036149.

Goldsby, D., Kohlstedt, D., 2001. Superplastic deformation of ice: Experimental observations. J. Geophys. Res.: Solid Earth (1978–2012) 106 (B6), 11017–11030.
Greenberg, R. et al., 1991. Miranda. Uranus 1, 693–735.
Grott, M., Sohl, F., Hussmann, H., 2007. Degree-one convection and the origin of Enceladus' dichotomy. Icarus 191 (1), 203–210.
Hafner, W., 1951. Stress distributions and faulting. Geol. Soc. Am. Bull. 62 (4), 373–398.
Hamblin, W.K., 1965. Origin of ''Reverse Drag'' on the downthrown side of normal faults. Geol. Soc. Am. Bull. 76 (10), 1145–1164.
Hammond, N., Phillips, C., Nimmo, F., Kattenhorn, S., 2013. Flexure on Dione: Investigating subsurface structure and thermal history. Icarus 223 (1), 418–422.
Hanel, R. et al., 1986. Infrared observations of the uranian system. Science 233 (4759), 70–74.
Helfenstein, P., 2010. Planetary science: Tectonic overturn on Enceladus. Nat. Geosci. 3 (2), 75–76.
Huismans, R.S., Beaumont, C., 2002. Asymmetric lithospheric extension: The role of frictional plastic strain softening inferred from numerical experiments. Geology 30 (3), 211–214.
Hussmann, H., Spohn, T., Wieczerkowski, K., 2002. Thermal equilibrium states of Europa's ice shell: Implications for internal ocean thickness and surface heat flow. Icarus 156 (1), 143–151.
Hussmann, H., Choblet, G., Lainey, V., Matson, D. L., Sotin, C., Tobie, G., Van Hoolst, T., 2010. Implications of rotation, orbital states, energy sources, and heat transport for internal processes in icy satellites. *Space science reviews*, *153*(1-4), 317-348.
Jackson, J., McKenzie, D., 1983. The geometrical evolution of normal fault systems. J. Struct. Geol. 5 (5), 471–482.
Jaeger, J., Cook, N., 1979. Fundamentals of Rock Mechanics. Chapman & Hall, p. 379.
Janes, D.M., Melosh, H.J., 1988. Sinker tectonics: An approach to the surface of Miranda. J. Geophys. Res.: Solid Earth 93 (B4), 3127–3143.
Jankowski, D.G., Squyres, S.W., 1988. Solid-state ice volcanism on the satellites of Uranus. Science 241 (4871), 1322–1325.
Johnson, T.V., Brown, R.H., Soderblom, L.A., 1987. The moons of Uranus. Sci. Am. 256, 48–60.
Jones, S., 1967. Softening of ice crystals by dissolved fluoride ions. Phys. Lett. A 25 (5), 366–367.
Jones, S., Glen, J., 1969. The mechanical properties of single crystals of pure ice. J. Glaciol. 8, 463–473.
Kamb, B., 1972. Experimental recrystallization of ice under stress. Am. Geophys. Union 16, 211–241.
Klinger, J., 1980. Influence of a phase transition of ice on the heat and mass balance of comets. Science 209, 271.
Lewis, S.R., 1990. The Voyager encounter with Neptune. Weather 45 (1), 14–19.
Lucchita, B.K., 1980. Grooved terrain on Ganymede. Icarus 44 (2), 481–501.

McKinnon, W.B., 1988. Odd tectonics of a rebuilt moon. Nature 333, 701–702, doi: 10.1038/333701a0.
McKinnon, W.B., 1999. Convective instability in Europa's floating ice shell. Geophys. Res. Lett. 26 (7), 951–954.
McKinnon, W.B., Chapman, C.R., Housen, K.R., 1991. Cratering of the uranian satellites. Uranus 1, 629–692.
Moore, J.M., 1984. The tectonic and volcanic history of Dione. Icarus 59 (2), 205–220.
Moore, J.M., Ahern, J.L., 1983. The geology of Tethys. J. Geophys. Res.: Solid Earth (1978–2012) 88 (S02), A577–A584.
Moratto, Z.M., Broxton, M.J., Beyer, R.A., Lundy, M., Husmann, K., 2010. Ames Stereo Pipeline, NASA's open source automated Stereogrammetry software. Lunar Planet. Sci. 41, 2364.
Mueller, S., McKinnon, W.B., 1988. Three-layered models of Ganymede and Callisto: Compositions, structures, and aspects of evolution. Icarus 76 (3), 437–464.
Murchie, S.L., Head, J.W., 1988. Possible breakup of dark terrain on Ganymede by large-scale shear faulting. J. Geophys. Res.: Solid Earth (1978–2012) 93 (B8), 8795–8824.
Nakamura, T., Jones, S., 1970. Softening effect of dissolved hydrogen chloride in ice crystals. Scr. Metall. 4 (2), 123–126.
Nimmo, F., Manga, M., 2002. Causes, characteristics and consequences of convective diapirism on Europa. Geophys. Res. Lett. 29 (23), 2109. http://dx.doi.org/10.1029/2002GL015754.
Nimmo, F., Bills, B., Thomas, P., Asmar, S., 2010. Geophysical implications of the long-wavelength topography of Rhea. J. Geophys. Res. 115 (E10), E10008.
Ojakangas, G.W., Stevenson, D.J., 1989. Thermal state of an ice shell on Europa. Icarus 81 (2), 220–241.
Ord, A., Hobbs, B.E., 1989. The strength of the continental crust, detachment zones and the development of plastic instabilities. Tectonophysics 158 (1–4), 269–289.
Pappalardo, R.T., 1994. The Origin and Evolution of Ridge and Trough Terrain and the Geological History of Miranda. Unpublished Ph.D. Thesis, Arizona State University, Tempe, AZ.
Pappalardo, R.T., Collins, G.C., 2005. Strained craters on Ganymede. J. Struct. Geol. 27 (5), 827–838.
Pappalardo, R.T., Reynolds, S.J., Greeley, R., 1997. Extensional tilt blocks on Miranda: Evidence for an upwelling origin of Arden Corona. J. Geophys. Res.: Planets 102 (E6), 13369–13379.
Pappalardo, R.T., Head, J.W., Collins, G.C., Kirk, R.L., Neukum, G., Oberst, J., Giese, B., Greeley, R., Chapman, C.R., Helfenstein, P., 1998. Grooved terrain on Ganymede: First results from Galileo high-resolution imaging. Icarus 135 (1), 276–302.
Pappalardo, R.T., Collins, G.C., Head III J.W., Helfenstein, P., McCord, T.B., Moore, J.M., Prockter, L.M., Schenk, P.M., Spencer, J.R., 2004. Geology of Ganymede. Jupiter: The Planet, Satellites and Magnetosphere, pp. 363–396.

Parmentier, E.M., Head, J.W., 1981. Viscous relaxation of impact craters on icy planetary surfaces: Determination of viscosity variation with depth. Icarus 47 (1), 100–111.
Patthoff, D.A., Kattenhorn, S.A., 2011. A fracture history on Enceladus provides evidence for a global ocean. Geophys. Res. Lett. 38 (18), L18201. http://dx.doi.org/10.1029/2011GL048387.
Plescia, J.B., 1988. Cratering history of Miranda: Implications for geologic processes. Icarus 73 (3), 442–461.
Poblet, J., Bulnes, M., 2005. Fault-slip, bed-length and area variations in experimental rollover anticlines over listric normal faults: Influence in extension and depth to detachment estimations. Tectonophysics 396 (1), 97–117.
Porco, C. et al., 2006. Cassini observes the active south pole of Enceladus. Science 311 (5766), 1393–1401.
Price, N., 1977. Aspects of gravity tectonics and the development of listric faults. J. Geol. Soc. 133 (4), 311–327.
Prockter, L.M., Nimmo, F., Pappalardo, R.T., 2005. A shear heating origin for ridges on Triton. Geophys. Res. Lett. 32 (14), L14202.
Regenauer-Lieb, K., Hobbs, B., Ord, A., 2004. On the thermodynamics of listric faults. Earth, Planets Space 56 (12), 1111–1120.
Rettger, R.E., 1935. Experiments on soft-rock deformation. AAPG Bull. 19 (2), 271–292.
Ruiz, J., 2003. Heat flow and depth to a possible internal ocean on Triton. Icarus 166 (2), 436–439.
Ruiz, J., 2005. The heat flow of Europa. Icarus 177 (2), 438–446.
Ruiz, J., Tejero, R., 2000. Heat flows through the ice lithosphere of Europa. J. Geophys. Res.: Planets (1991–2012) 105 (E12), 29283–29289.
Ruiz, J., Tejero, R., 2003. Heat flow, lenticulae spacing, and possibility of convection in the ice shell of Europa. Icarus 162 (2), 362–373.
Schenk, P.M., 1991. Fluid volcanism on Miranda and Ariel: Flow morphology and composition. J. Geophys. Res.: Solid Earth 96 (B2), 1887–1906.
Schultz, R.A., Hauber, E., Kattenhorn, S.A., Okubo, C.H., Watters, T.R., 2010. Interpretation and analysis of planetary structures. J. Struct. Geol. 32 (6), 855–875.
Shelton, J.W., 1984. Listric normal faults; an illustrated summary. AAPG Bull. 68 (7), 801–815.
Showman, A.P., Han, L., 2004. Numerical simulations of convection in Europa's ice shell: Implications for surface features. J. Geophys. Res.: Planets (1991–2012) 109 (E1).
Smith, B.A. et al., 1982. A new look at the Saturn system: The Voyager 2 images. Science 215 (4532), 504–537.
Smith, B.A. et al., 1986. Voyager 2 in the uranian system: Imaging science results. Science 233 (4759), 43–64.
Squyres, S.W., 1980. Volume changes in Ganymede and Callisto and the origin of grooved terrain. Geophys. Res. Lett. 7 (8), 593–596.

Squyres, S., 2011. Vision and Voyages for planetary science in the decade 2013–2022. Committee on the Planetary Science Decadal Survey; National Research Council. The National Academies Press, Washington, DC, ISBN: 0-309-20955-2.
Steinemann, S., 1954. Results of preliminary experiments on the plasticity of ice crystals. J. Glaciol. 2 (16), 404–412.
Stern, L.A., Durham, W.B., Kirby, S.H., 1997. Grain-size-induced weakening of H2O ices I and II and associated anisotropic recrystallization. J. Geophys. Res.: Solid Earth 102 (B3), 5313–5325.
Suess, E., 1909. The Face of the Earth. Clarendon Press. Taylor, John R., Thompson, W., 1998. An introduction to error analysis: The study of uncertainties in physical measurements. Meas. Sci. Technol. 9.6, 1015.
Thomas, P.C., 1988a. Radii, shapes, and topography of the satellites of Uranus from limb coordinates. Icarus 73 (3), 427–441.
Thomas, P.G., 1988b. The tectonic and volcanic history of Rhea as inferred from studies of scarps, ridges, troughs, and other lineaments. Icarus 74 (3), 554–567.
Tittemore, W.C., Wisdom, J., 1990. Tidal evolution of the uranian satellites: III. Evolution through the Miranda-Umbriel 3: 1, Miranda-Ariel 5: 3, and Ariel Umbriel 2:1 mean-motion commensurabilities. Icarus 85 (2), 394–443.
Tobie, G., Choblet, G., Sotin, C., 2003. Tidally heated convection: Constraints on Europa's ice shell thickness. J. Geophys. Res.: Planets 108 (E11), 5124. http://dx.doi.org/10.1029/2003JE002099.
Wagner, R., Neukum, G., Giese, B., Roatsch, T., Wolf, U., Denk, T., 2006. The Cassini ISS Team (2006) geology, ages and topography of Saturn's satellite Dione observed by the Cassini ISS camera. Lunar Planet. Sci. 37, 1805. Walker, C., Bassis, J., Liemohn, M., 2012. On the application of simple rift basin models to the south polar region of Enceladus. J. Geophys. Res.: Planets (1991–2012) 117 (E7), E07003. http://dx.doi.org/10.1029/2012JE004084.
Weertman, J., 1983. Creep deformation of ice. Annu. Rev. Earth Planet. Sci. 11, 215–240.
Wernicke, B., Burchfiel, B., 1982. Modes of extensional tectonics. J. Struct. Geol. 4 (2), 105–115.
White, O.L., Schenk, P.M., Dombard, A.J., 2013. Impact basin relaxation on Rhea and Iapetus and relation to past heat flow. Icarus 223 (2), 699–709.
Williams, G., Vann, I., 1987. The geometry of listric normal faults and deformation in their hanging walls. J. Struct. Geol. 9 (7), 789–795.
Woodbury, H., Murray Jr., I., Pickford, P., Akers, W., 1973. Pliocene and Pleistocene depocenters, outer continental shelf, Louisiana and Texas. AAPG Bull. 57 (12), 2428–2439.
Xiao, H., Suppe, J., 1992. Origin of rollover. AAPG Bull. 76 (4), 509–529.
Zahnle, K., Schenk, P., Levison, H., Dones, L., 2003. Cratering rates in the outer Solar System. Icarus 163 (2), 263–289.

Appendix I

Table I-1. Image information including resolution, area of Miranda covered, and whether or not the image was used in this work.

Image Number	Mean Ground Resolution	Coronae Covered & View of Coronae	Used for this Work?
c2684608	330 m px^{-1}	Arden: Limb & Plan	Yes (Figure I-2a)
c2684611	314 m px^{-1}	Arden: Limb & Plan Inverness: Plan	Yes (Figure I-2b)
c2684614	298 m px^{-1}	Arden: Plan Inverness: Plan Elsinore: Limb & Plan	No
c2684617	284 m px^{-1}	Inverness: Limb & Plan	Yes (Figure I-2c)
c2684620	270 m px^{-1}	Elsinore: Limb & Plan	No
c2684623	258 m px^{-1}	Elsinore: Plan	No
c2684626	247 m px^{-1}	Arden: Limb & Plan Inverness: Plan	Yes (Figure I-2d)
c2684629	237 m px^{-1}	Arden: Plan Inverness: Plan	No

Table I-2. DEM information including image pairs used, the region of Miranda covered, resolutions, DEM triangulation errors, and whether or not the DEM was used in this work.

Image Pair	Coronae Covered	DEM Horizontal Resolution	DEM Vertical Accuracy	Used for this Work?
c2684611 c2684617	Inverness	897 m px^{-1}	86 m	No
c2684611 c2684626	Inverness, Arden	842 m px^{-1}	95 m	Yes (Figures I-5 and I-6a)
c2684614 c2684620	Elsinore	852 m px^{-1}	147 m	No
c2684614 c2684626	Inverness	818 m px^{-1}	141 m	No
c2684620 c2684629	Elsinore	761 m px^{-1}	80 m	No
c2684623 c2684629	Elsinore	743 m px^{-1}	Unknown (camera pointing information not available)	No

Table I-3. The results of the assessment of criteria for a rollover structure.

Image # or DEM	Scarp Group	North Sloping Feature?	Angular North Tilted Topography?	Corrugations?	Smooth Sections?
c2684626	1 – 4	Yes	Yes	No	Yes
c2684608	1 – 4	Yes	No	No	Yes
DEM	5 & 6	Yes	No	-	-
c2684611	5 & 6	-	-	Yes	Yes
c2684617	5 & 6	-	-	Yes	Yes
c2684626	5 & 6	-	-	Yes	Yes

Table I-4. The results of all four criteria and whether those results support the hypotheses for listric fault systems.

Criterion #	Description	Images / DEM used	Supports Hypothesis?
Scarps 1 – 4 (Arden Corona boundary)			
1	Progressive decrease in fault dip with distance from Arden center	Images c2684626 & c2684608	Yes
2	Progressive increase in back-tilted face slope with distance from Arden center	Images c2684626 & c2684608	Yes
4	Existence of a rollover structure	Images c2684626 & c2684608	Yes
Scarps 5 & 6 (340˚ Chasma)			
1	Progressive decrease in fault dip with distance from Arden center	DEM	Yes
2	Progressive increase in back-tilted face slope with distance from Arden center	DEM	Yes
3	Fault scarps are concave up in geometry	DEM	No
4	Existence of a rollover structure	DEM & images c2684611, c2684617 & c2684626	No

Table I-5. The results of estimates of the depth to the detachment of the Arden Corona boundary.

Equation & Reference	Data Needed & Average Measured Values	Estimated Depth to Detachment (*z*)
$z = A/W$ Gibbs (1983)	*A*: area dropped below regional surface (2.2×10^5 km ± 1.5×10^4 km^2) *W*: width of the listric fault system (3.2 km ± 510 m)	6.7 km ± 476 m
$z = A/H$ Gibbs (1983)	*A* *H*: heave of the rollover anticline (2.4 km ± 1.7 km)	9.0 km ± 632 m
$z = A/D$ Williams and Vann (1987)	*A* *D*: displacement of the rollover anticline assuming no shearing (27 km ± 1.5 km)	7.9 km ± 713 m
$z=A/[(D + W - F)/2]$ Williams and Vann (1987)	*A*, *D*, *W* *F*: Folded bed length (7.4 km ± 564 m)	8.3 km ± 638 m

Table I-6. Estimated values of heat flux are given for icy satellites in order of increasing satellite diameter.

Satellite	Region	Heat Flux	Data Used	References
Miranda	Arden Corona Boundary	31 – 112 mW m^{-2}	Listric fault geometry	This work
Enceladus	Sarandib and Diyar Planitiae	110 – 270 mW m^{-2}	Ridge and trough wavelengths	Bland et al. (2007), Giese et al. (2008), Bland et al. (2012)
Tethys	Ithaca Chasma	18 – 30 mW m^{-2}	Topographic modeling as an elastic plate	Giese et al. (2007), Chen and Nimmo (2008)
Dione	Janiculum Dorsa	24 – 90 mW m^{-2}	Topographic modeling as an elastic plate	Hammond et al. (2013)
Iapetus	Global	$\leq$ 2 mW m^{-2}	Relaxation of impact basins	White et al. (2013)
Rhea	Global	15 – 30 mW m^{-2}	Ridge and trough wavelengths and relaxation of impact basins	Nimmo et al. (2010), White et al. (2013)
Europa	Global	20 – 210 mW m^{-2}	Estimates of elastic thickness and brittle-ductile transition depths	Hussmann et al. (2002), Nimmo and Manga (2002), Ruiz and Tejero (2003), Tobie et al. (2003), Showman and Han (2004), Ruiz (2005)

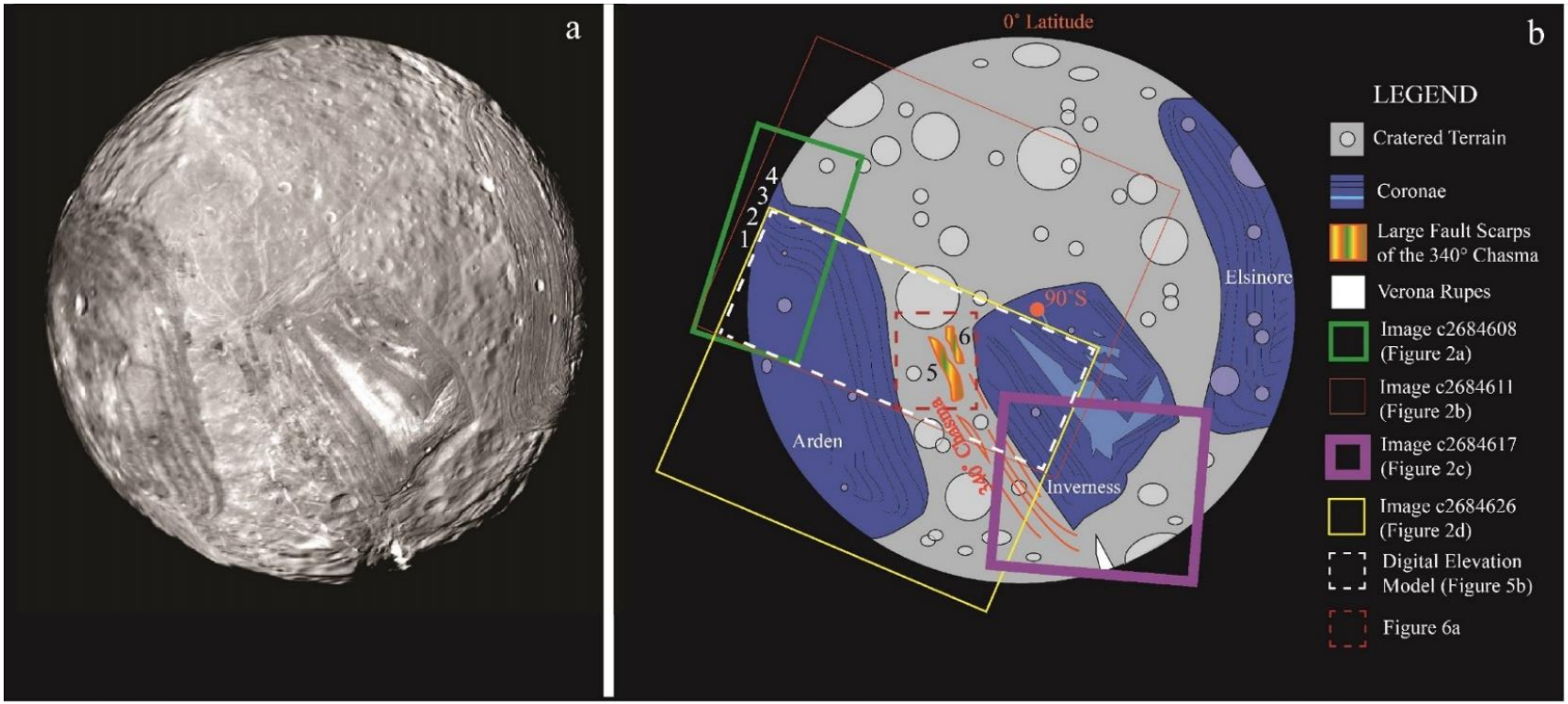

Figure I-1. a) A global mosaic of Miranda produced by the U.S. geological survey b) A map of Figure I-1a that shows the coronae, the locations of the ISS images, the DEM used in this study, and the locations of Faults 1-6.

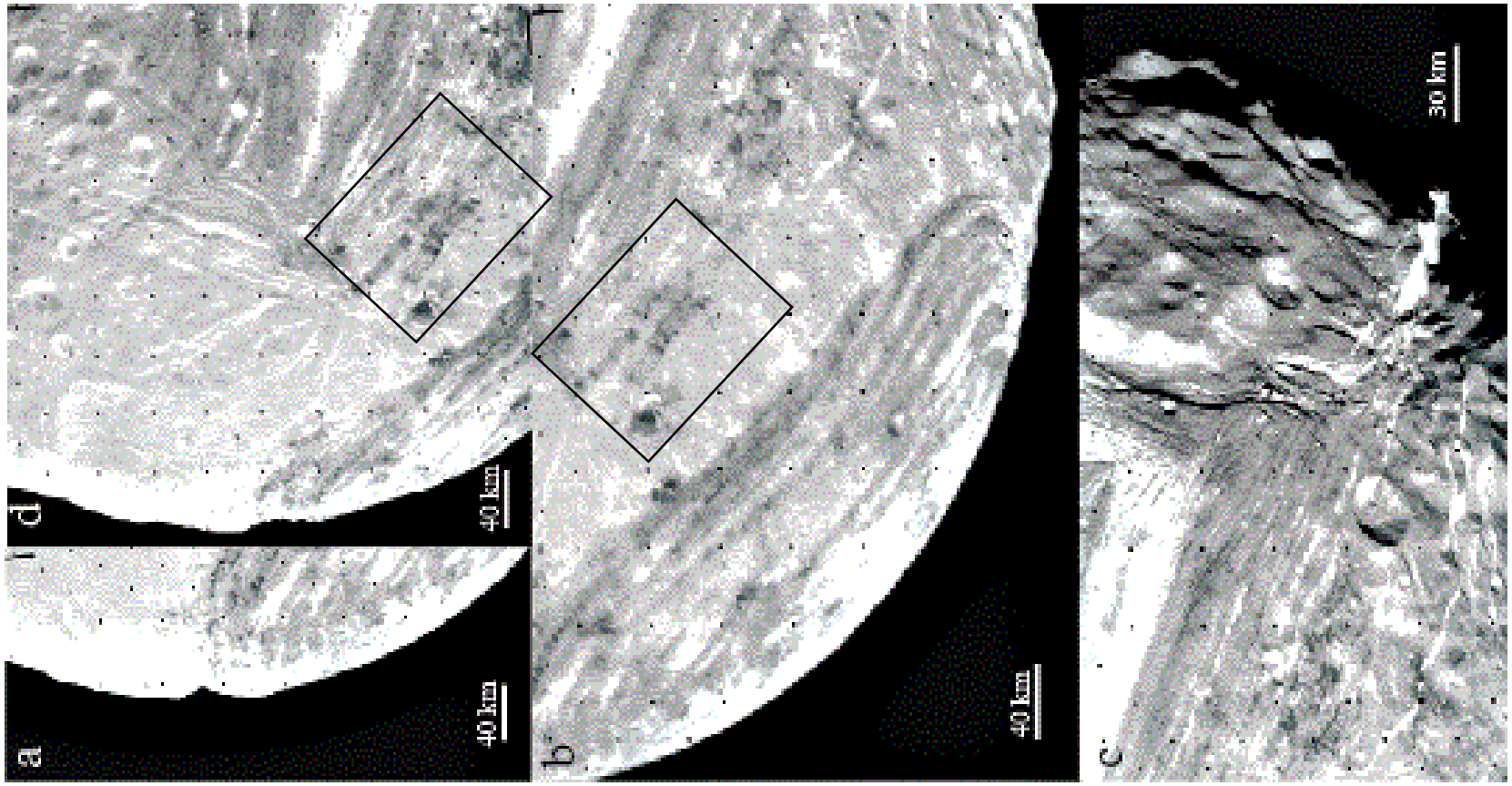

Figure I-2. Voyager 2 ISS images showing portions of the coronae. The black boxes show the coverage of the DEM used in this study. a) Image c2684608 of Arden in limb view, b) image c2684611 of Arden (bottom left), Inverness (top right), and the 340° Chasma (between Arden and Inverness), c) image c2684617 of Inverness and the 340° Chasma including Verona Rupes (bottom right) along Miranda's limb, d) image c2684626 of Arden (left) and Inverness (right), and between them, the 340° Chasma (bottom center).

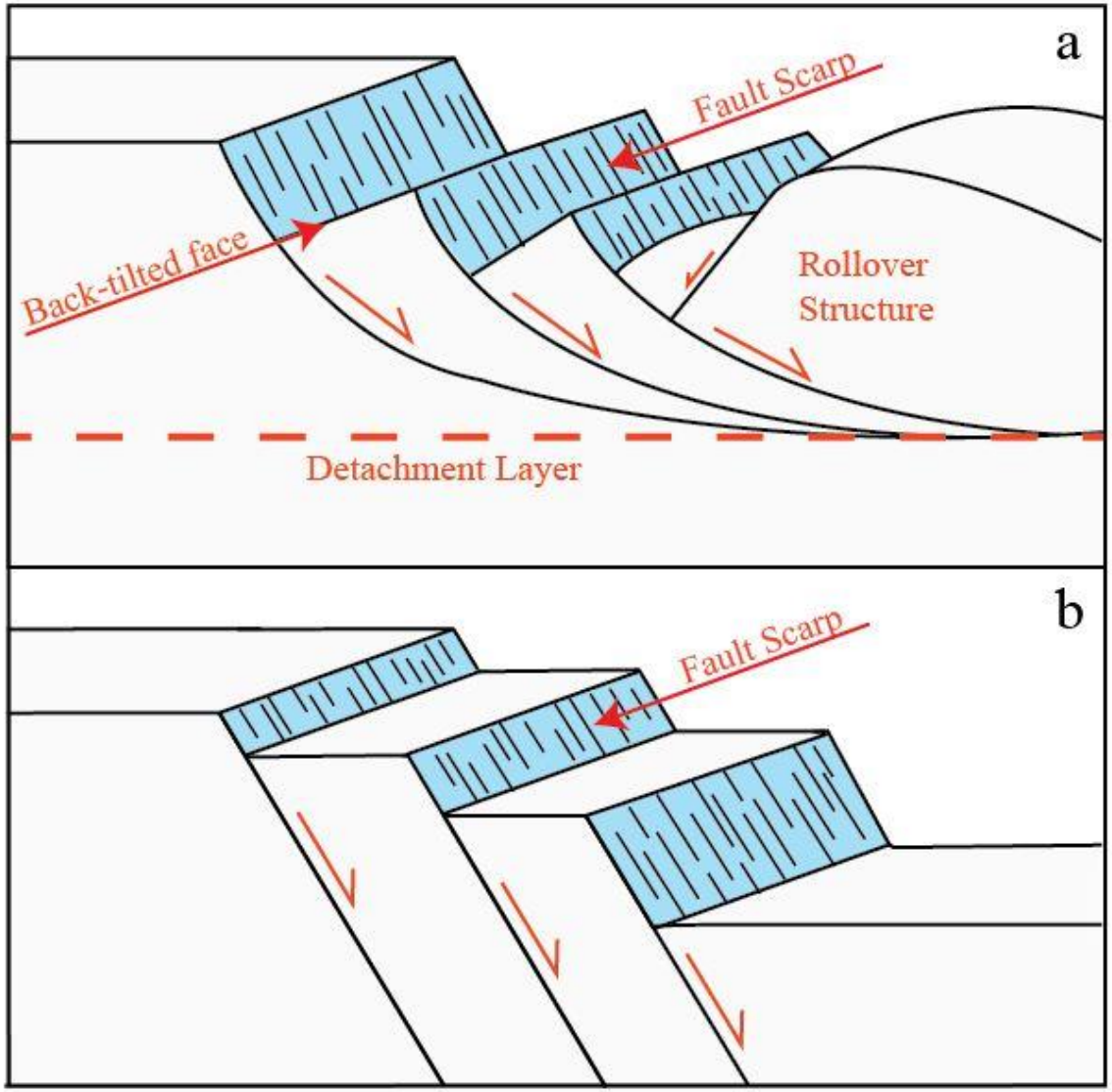

Figure I-3. Illustrations of listric (a) and planar (b) fault systems.

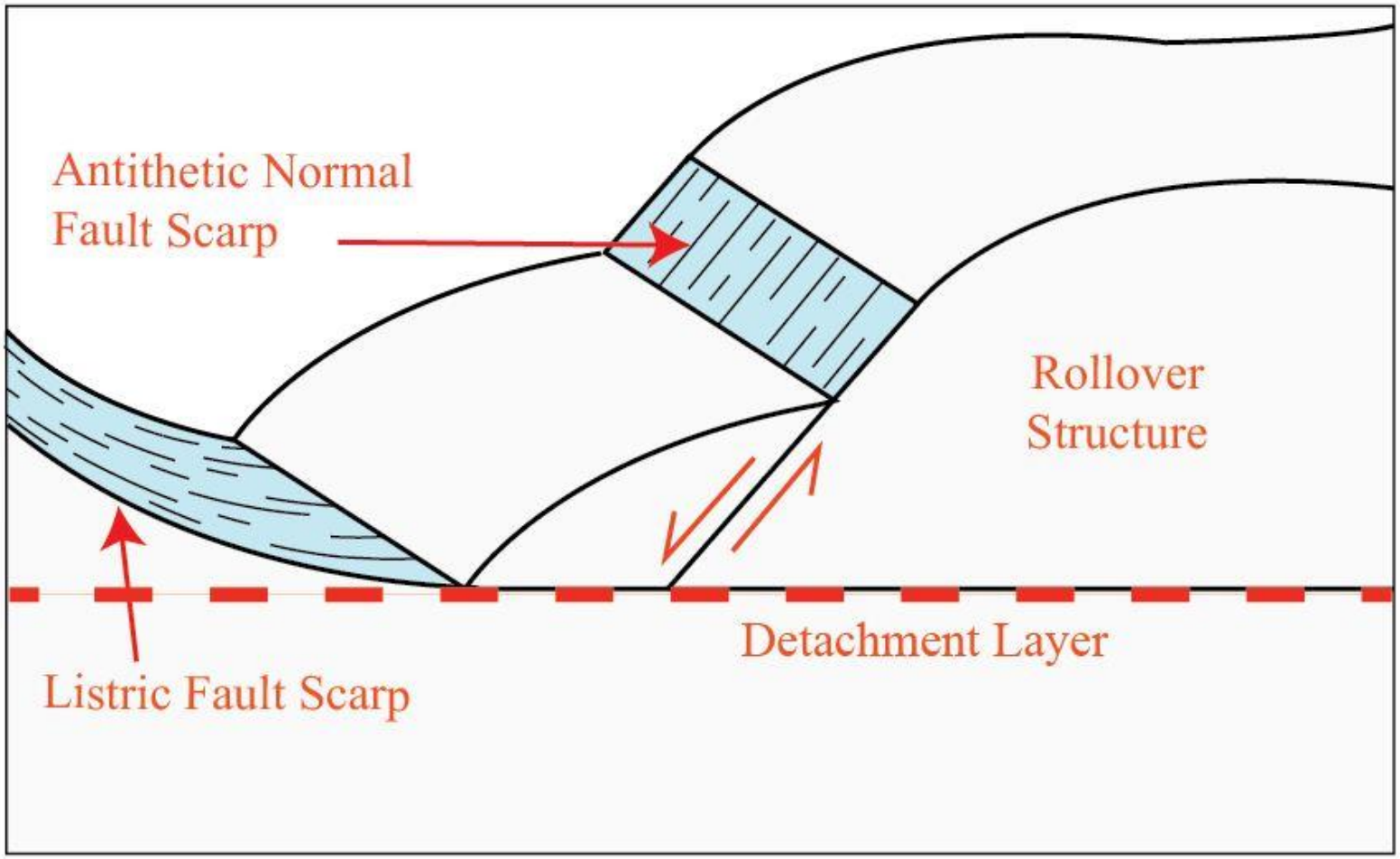

Figure I-4. An illustration of a rollover structure of a listric fault system.

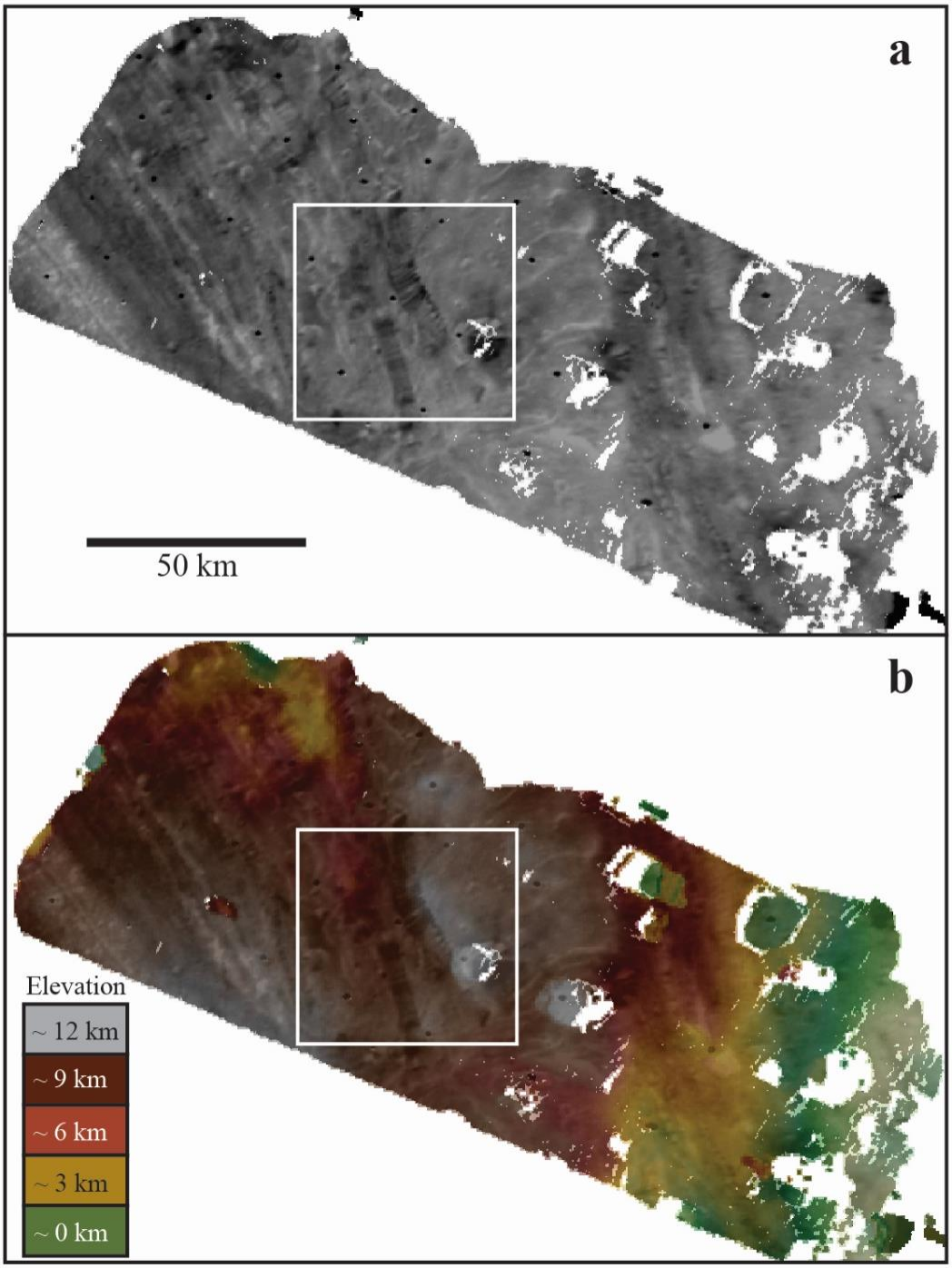

Figure I-5. a) The DEM of the region between Arden and Inverness that cover Scarps 5 and 6. The DEM colors represent relative surface elevations with green representing the lowest elevation and gray representing the highest elevation. North is up, Arden Corona is to the right and Inverness is to the left. The white box is the location of Figure I-6a and b. b) The orthorectified image covered by the DEM.

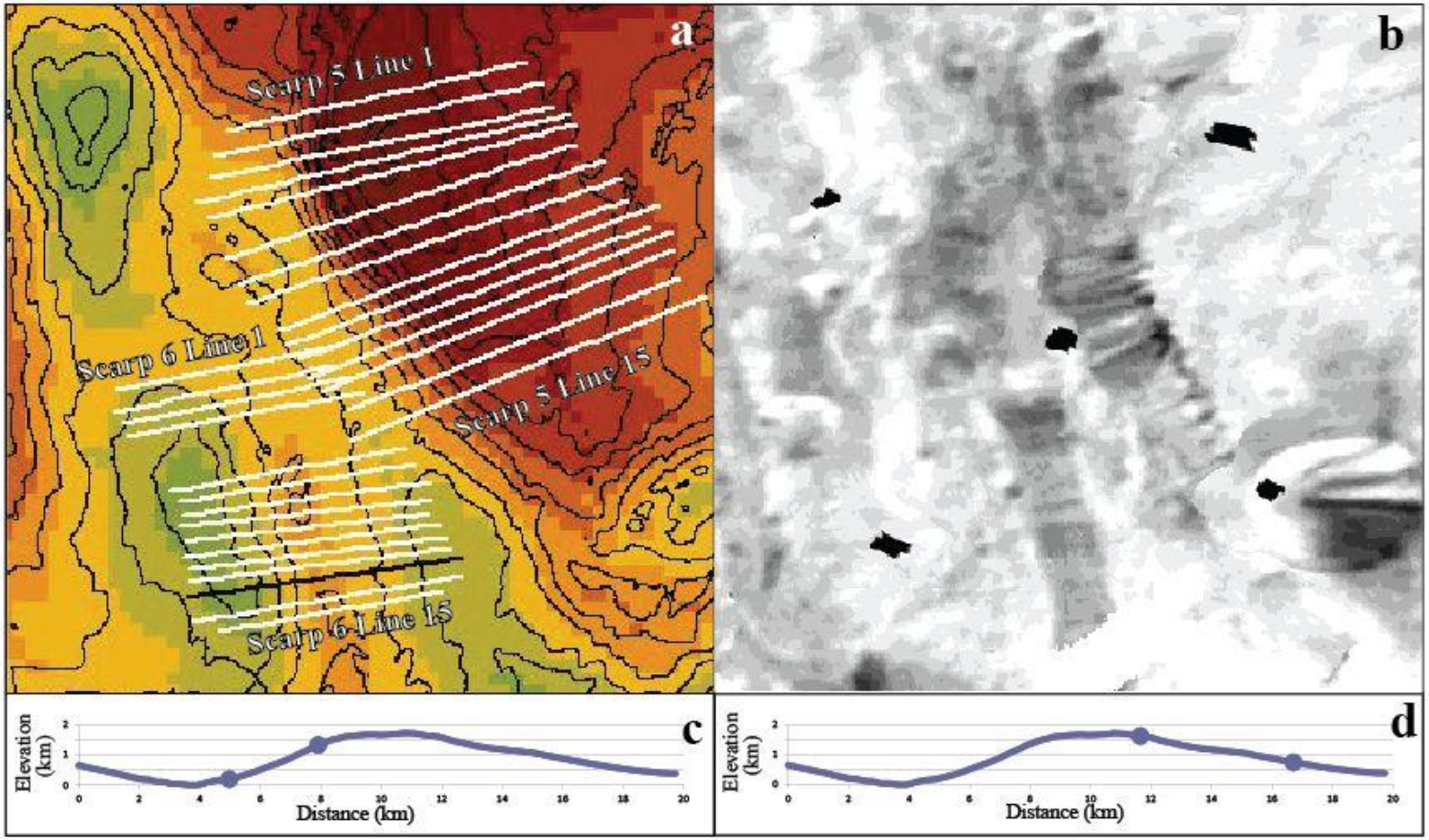

Figure I-6. a) The DEM of the region between Arden and Inverness that cover Scarps 5 and 6 with the locations of the 30 profile lines. The DEM colors represent relative surface elevations with green representing the lowest elevation and red representing the highest elevation. The contour interval is 500 meters. North is up, Arden Corona is to the right and Inverness is to the left. The black line in plan view is the profile line shown in 5c and 5d. b) The portion of the Voyager 2 ISS image covered by the DEM. c) The top and bottom of a scarp line is marked on the black profile line. d) The top and bottom of a slope line is marked on the black profile line.

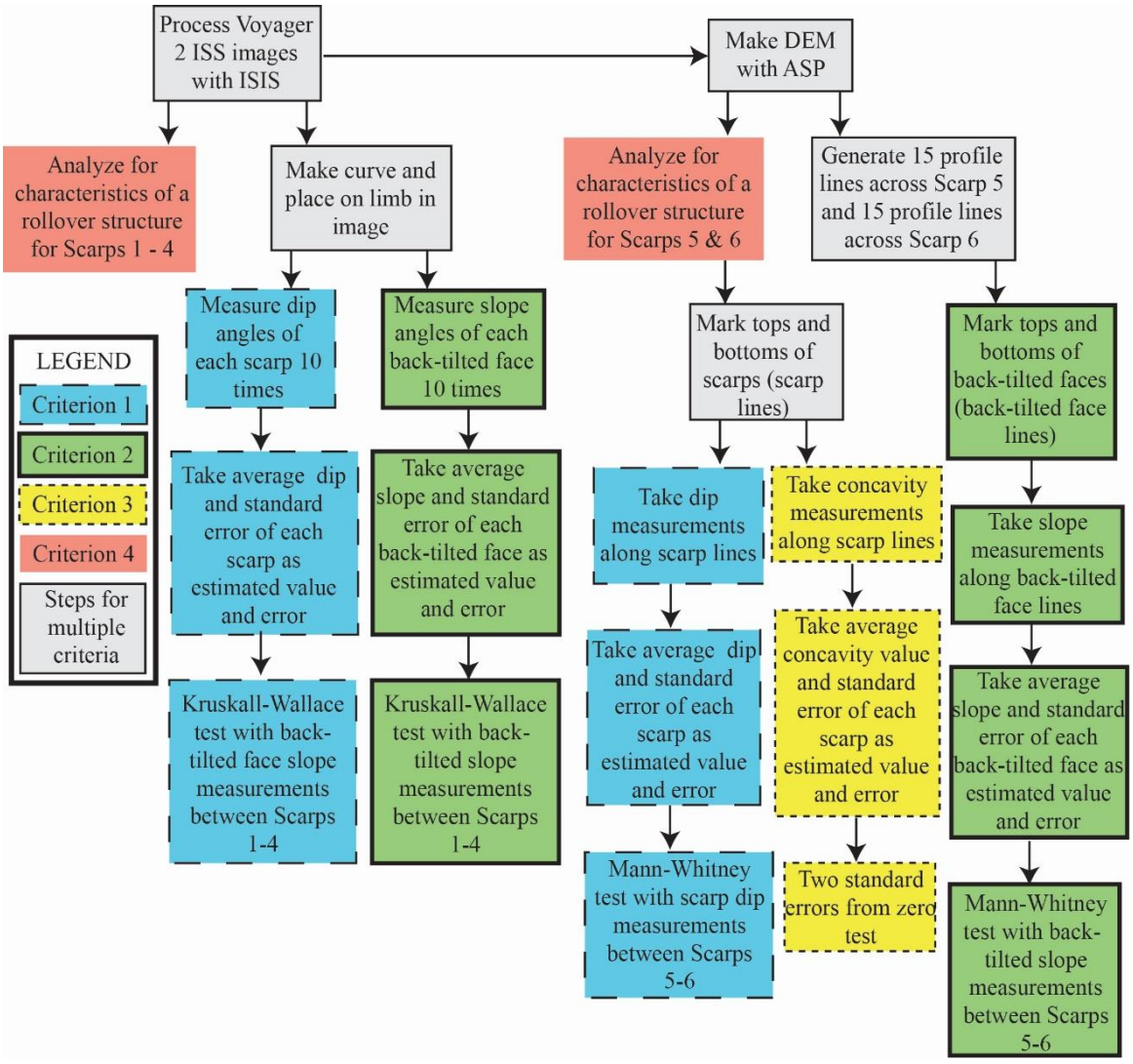

Figure I-7. Flow chart showing the methods for testing for a listric fault system.

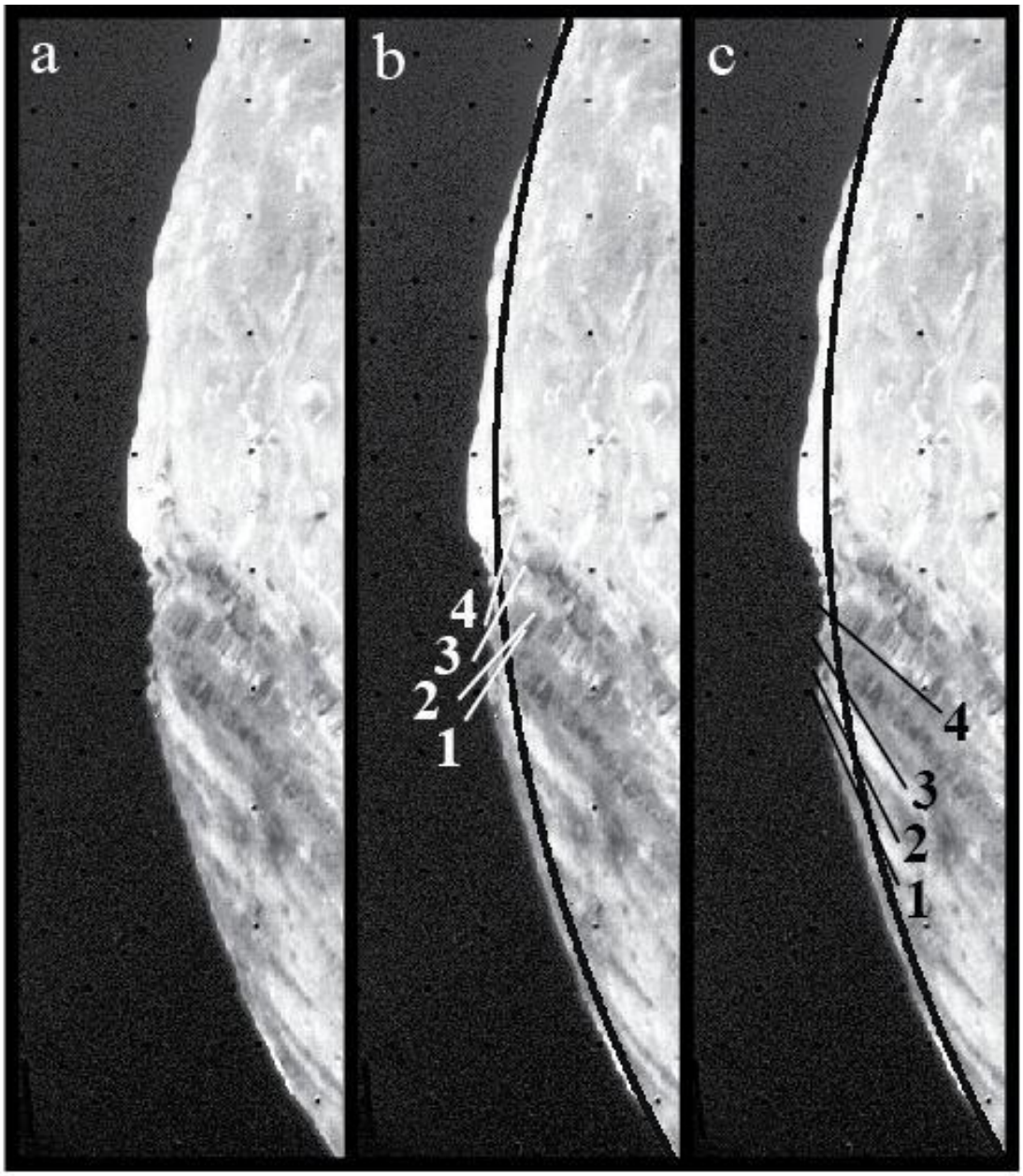

Figure I-8. a) The portion of image c2684626 (Figure I-2d) that shows the boundary of Arden on Miranda's limb. b) An example of how the fault scarp dip angles of Scarps 1 through 4 (labeled) were measured relative to the surface. c) An example of how the back-tilted face slopes of Scarps 1 through 4 (labeled) were measured relative to the surface.

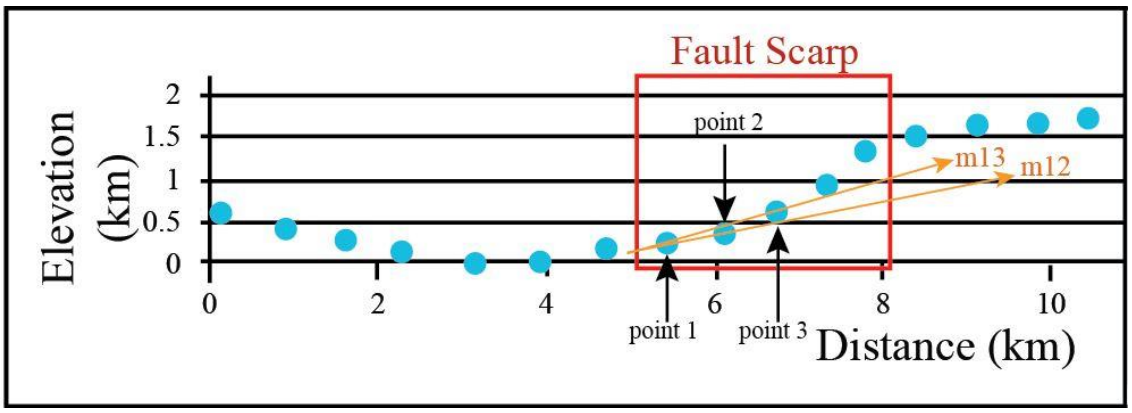

Figure I-9. An illustration of the methods of Criterion 3 (determining if fault scarps are concave up in geometry). The three points that were next to each other in a scarp profile were analyzed individually and were termed points 1 – 3, with point 1 being the furthest down-dip. The slope between points 1 and 2 was termed m12 and the slope between points 2 and 3 was termed m13. If the m12 - m13 is negative, then that section of the scarp is concave up.

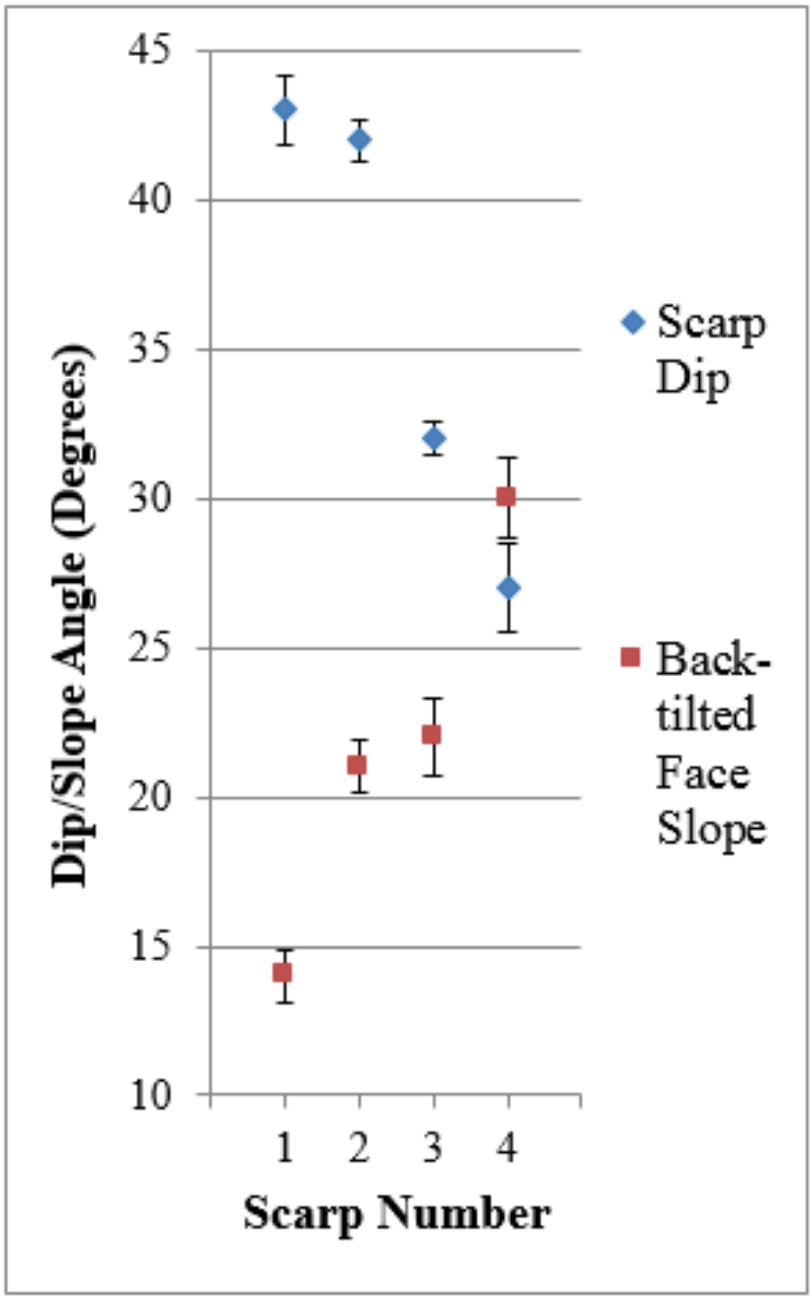

Figure I-10. The results of Criterion 1 (decrease in dip with distance from Arden's interior) and Criterion 2 (increase in back-tilted face slope with distance from Arden's interior), with Scarp 1 being the closest scarp to Arden's interior.

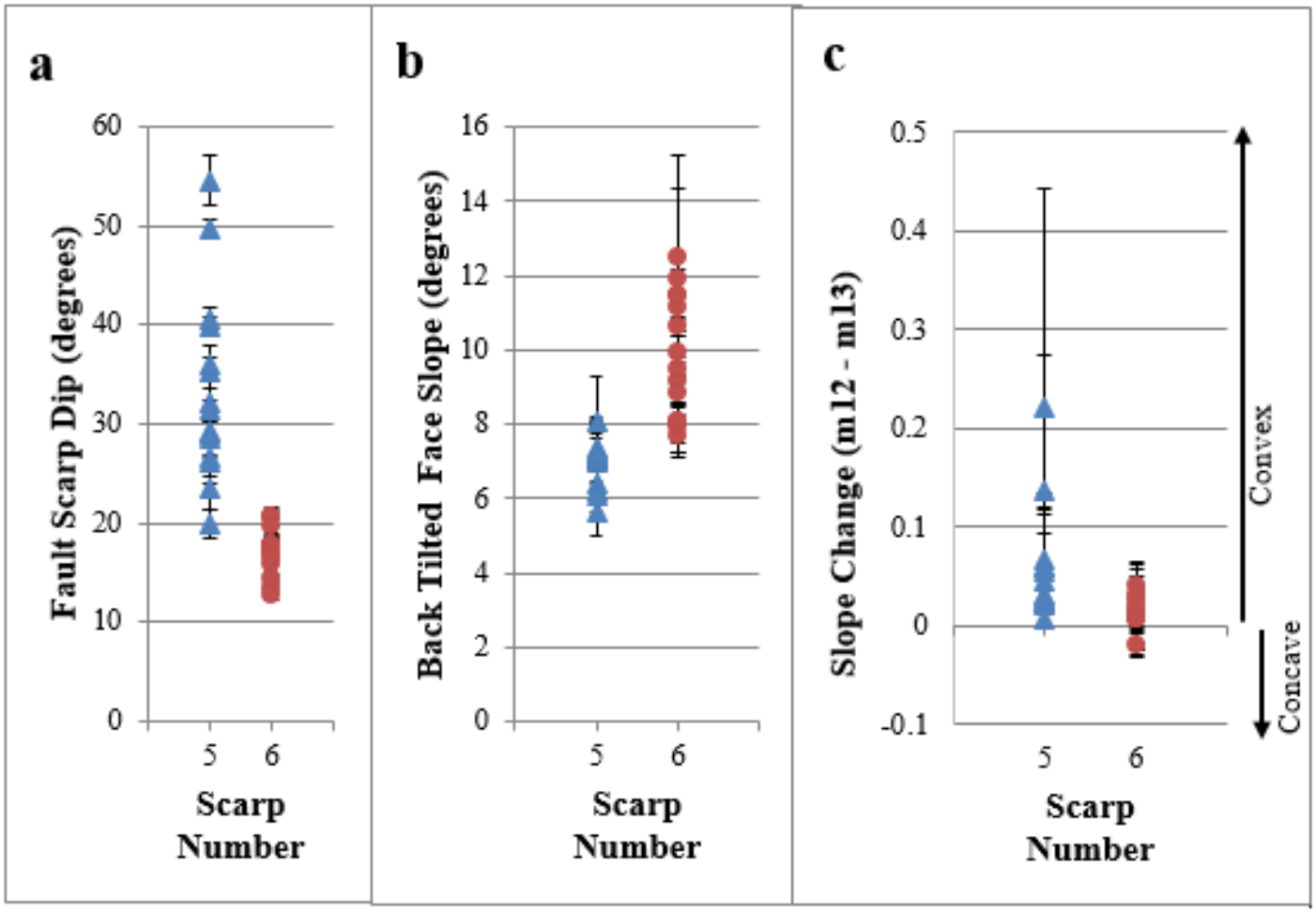

Figure I-11. a) The results of Criterion 1 (decrease in dip with distance from Arden) on Scarps 5 and 6, with Scarp 5 being the closest to Arden. b) The results of Criterion 2 (increase in back-tilted face slope with distance from Arden). c) The results of Criterion 3 (a concave up geometry of the fault scarps).

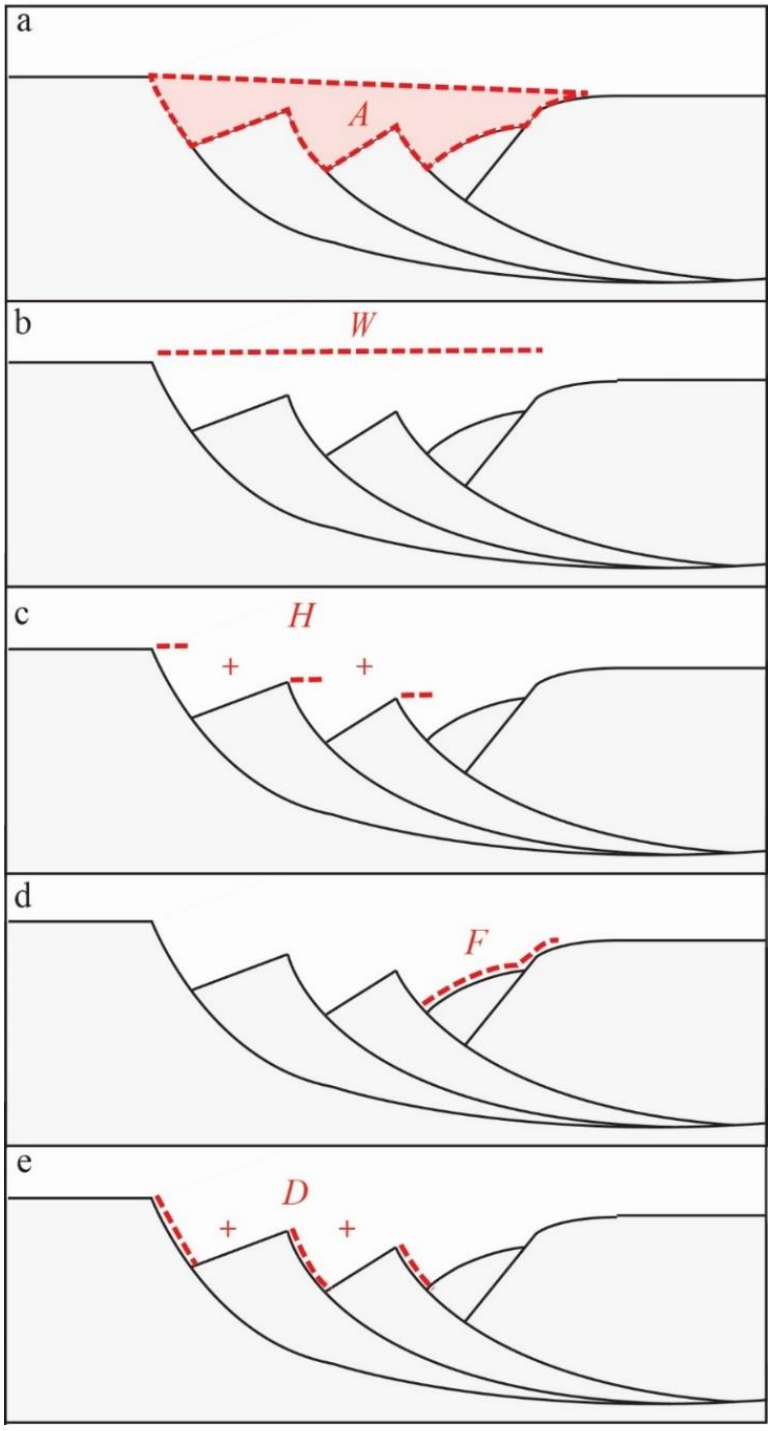

Figure I-12. Diagrams of a listric fault system showing a) the area dropped below the regional surface, b) the width of the listric fault system, c) the heave of the rollover anticline, d) the folded bed length of the rollover anticline, and e) the displacement of the rollover anticline, assuming no shearing.

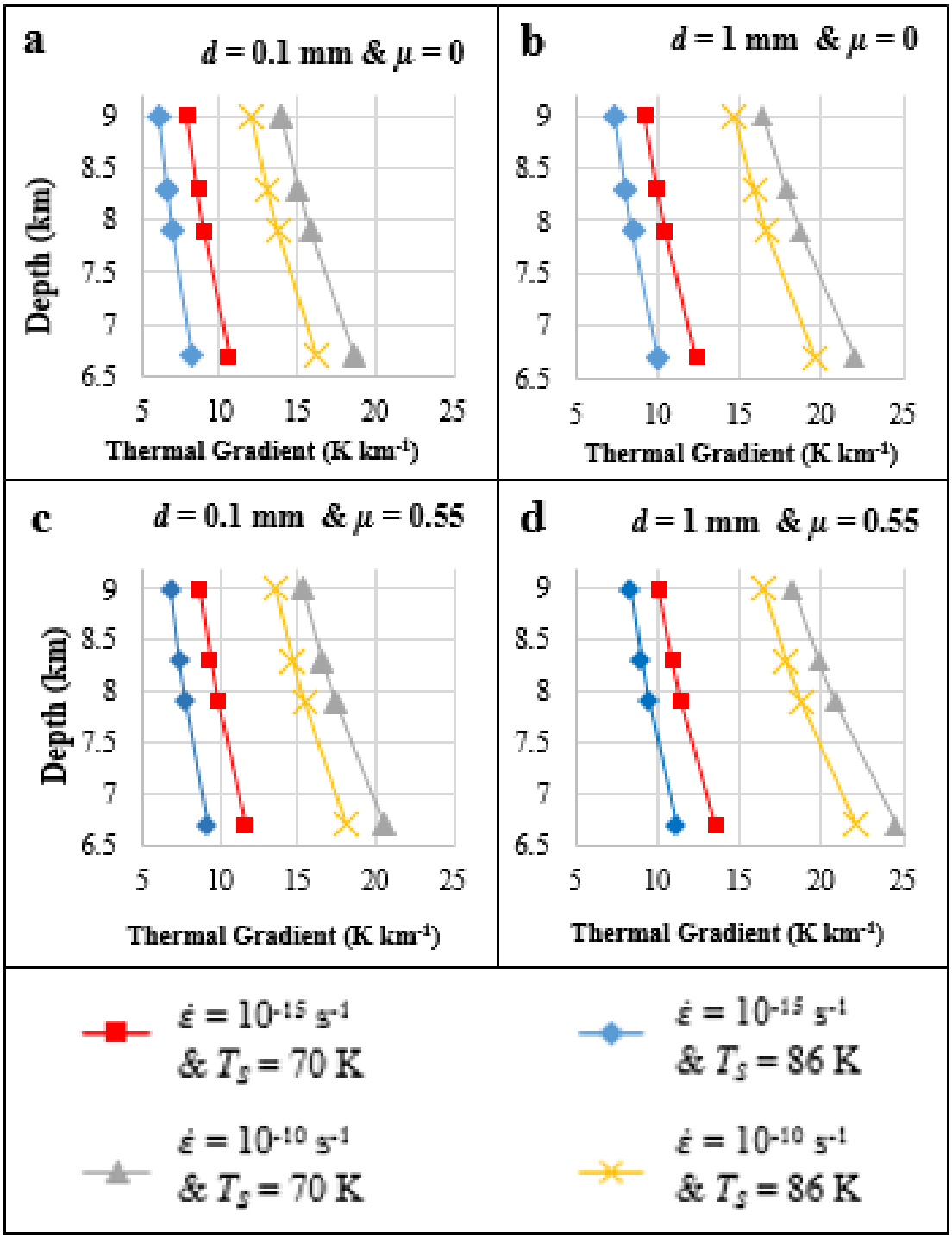

Figure I-13. Results of calculations of the thermal gradient of the Arden Corona boundary region of Miranda.

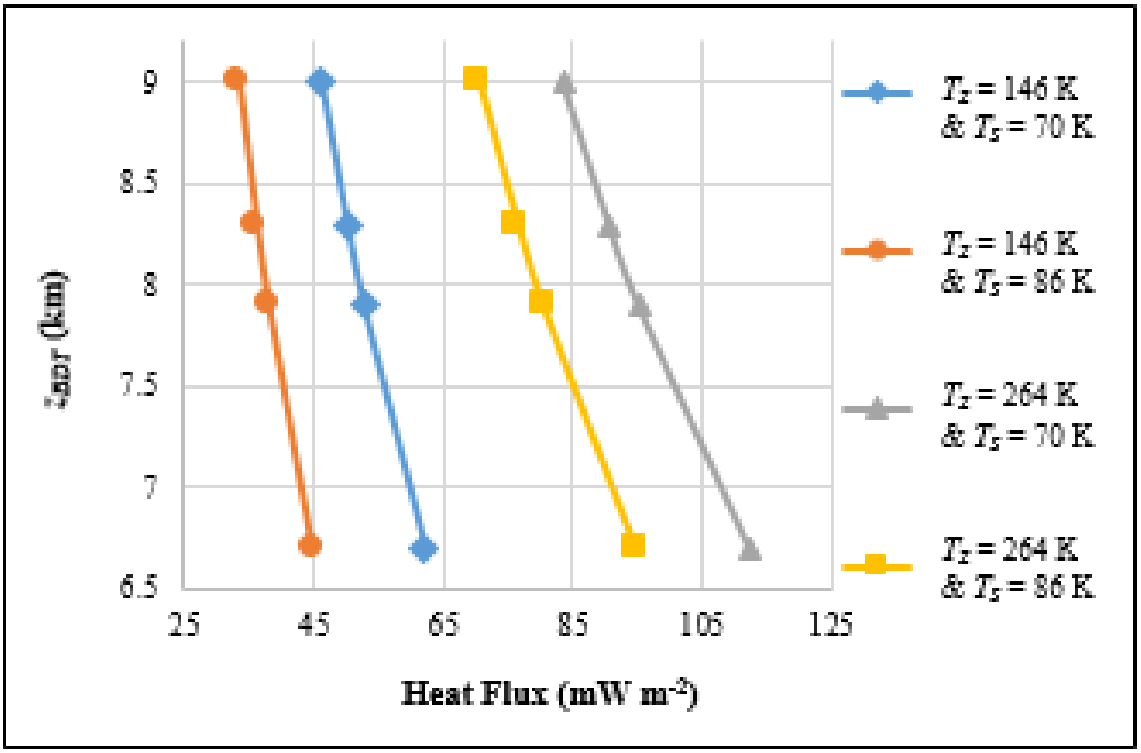

Figure I-14. Results of calculations of the heat flux of the Arden Corona boundary region of Miranda.

Appendix I-A: ISIS Image Processing Steps

Images from the ISS camera onboard the Voyager 2 spacecraft were processed and map-projected using the ISIS software (Anderson et al., 2004). The processing steps used on the images are as follows:

- Eight Voyager 2 ISS images were downloaded from the PDS website (pds.nasa.gov).
- The images were converted from their initial PDS format (.imq files) to ISIS image cubes (.cub files) using ISIS's *pds2isis* command.
- The new image cubes were then associated with a camera model for ISS and augmented with spatial information (geometries of the spacecraft, sun angle geometries, ground positions, etc.) appropriate for the image acquisition time by using ISIS's *spiceinit* command.
- The data number (DN) values of the images were converted to reflectance by using the *voycal* command.
- The images were then projected into a south polar stereographic projection using ISIS's *cam2map* command.

After inspection of the eight processed images, we found that four were usable for our study.

Appendix I-B: Ames Stereo Pipeline Processing Steps and Vertical Accuracy Calculations

The ASP software was used to generate DEMs from Voyager 2 ISS image pairs. A few prepossessing steps using ISIS and one step in ASP were required before generating DEMs using ASP.

ISIS preprocessing steps:

- Reseau points are black, regularly spaced dots on Voyager images that are used to correct for image distortion. Reseau points were identified in each image by using ISIS's *findrx* command, and were then removed from each image by using the *remrx* command. Five samples and five lines were removed around each identified reseau point in each image. We chose these values because five lines and samples is a sufficient area to cut out an entire reseau point, while creating the smallest holes in our final DEMs. The reseau points were replaced with null values.
- Most of the Voyager 2 images used to generate DEMs included the limb of Miranda. To reduce noise in our final DEMs, the pixels beyond the limb of Miranda were removed from images using the *circle* command in ISIS.
- To reduce the effects on the output DEMs from errors in the satellite position and orientation information, the images were bundle adjusted. This adjustment was done using the *bundle_adjust* command in ASP with the Ceres Solver algorithm (http://ceres-solver.org/) (Agarwal and Mierle, 2012).
- The images were then map-projected using ISIS's *cam2map* command for subsequent easy identification of common features in both images by Ames

Stereo Pipeline. The lowest resolution image of each pair was map-projected first, and then the highest resolution image of each pair was projected to the lowest resolution image, so that each image in a pair were projected around the same point in latitude and longitude space. Projecting the highest resolution image to the lowest resolution image was done to prevent stretching of the lowest resolution image, which would have occurred if the images were projected in the opposite order. Polar stereographic projections were used in this step for all image pairs.

ASP processing steps:

- The *stereo* command was used to generate an output TIFF point cloud file from each image pair. Each point cloud file consists of spatial information in three dimensions.
- The *point2dem* command was then used to generate a DEM from each point cloud file in the form of a TIFF file with georeferencing information stored as GeoTIFF tags. During this step, the DEM was projected into a south polar projection for Miranda (IAU2000:70520) with the Geospatial Data Abstraction Library (GDAL) command.
    - For the *point2dem* command, the user can specify a specific post spacing for the final DEM (or final DEM resolution) by using the *--dem-spacing* argument. We used a lower resolution for our output DEMs than the resolution of the input images so that the information in the output DEM better matches the 'true resolution' of the output elevation data. A lower DEM resolution relative to the input images is required due to the unlikelihood that ASP would identify a single pixel correspondence in both of the input images. Multiple pixels in each image are needed to identify surface features that are the same in both images. For all of the DEMs we generated, we used a post spacing of three times the average of the resolutions of the two images used. TIFF files of images showing the intersection error and an orthorectified image of the region of the ISS image covered by the DEM were also generated by the *point2dem* step. All three of these TIFF files (the DEM, the intersection error map, and the orthorectified image) for each stereo image pair were imported into ESRI's ArcMap software for analysis.

Vertical accuracy calculations:

- The vertical accuracy (*VA*) of each DEM (also known as the expected precision) depends on the stereo convergence angle of the image pair, as well as the resolutions of the images as shown by,

$$VA = \rho \, GSD \, \frac{P}{H}, \tag{I-B1}$$

where ρ is the matching accuracy in pixels, *GSD* is the root mean square value of the ground sample distance (image resolution) of the image pair, and *P/H* is the parallax – height ratio.

- The values to use for ρ depend on the quality of the images used in the images pair (A. Howington, personal communication). For image pairs that are comprised of limb images, ρ = 0.3 is used. For non-limb image pairs, ρ = 0.2 is used.
- *P/H* is calculated with

$$\frac{P}{H} = \sqrt{(PX_1 - PX_2)^2 + (PY_1 - PY_2)^2}\,, \tag{I-B2}$$

where PX_1 and PY_1 refers to the parallax in the X and Y directions respectively of one of the stereopair images. PX_2 and PY_2 refer to the parallax in the X and Y directions of the other image:

$$PX = -\tan(EA)\cos(SGA) \tag{I-B3}$$

and

$$PY = \tan(EA)\sin(SGA)\,, \tag{I-B4}$$

where *EA* is the emission angle, and SGA is the subspacecraft ground azimuth.

The *caminfo* command in ISIS was used to generate text files associated with each image, containing image and camera information. The values for EA, SGA, and GSD for each image were collected from this text file, and used to calculate VA (Table I-2).

Appendix I-C: Tables I-C1 through I-C6

Tables I-C1 through I-C6 are given.

Table I-C1. Measurements of scarp dips and back-tilted face slopes. The results of Criterion 1 (progressive decrease in fault dip) and Criterion 2 (progressive increase in back-tilted face slope) are shown. The variation in scarp dip along strike for an individual fault may be due to portions of the fault scarp being mantled by material as a result of mass wasting events. The angle between the fault strike and apparent dip direction of the Arden Corona faults is estimated to be 79˚. This value was used to convert the measured apparent dip to true dip using Equation I-1.

Scarp #	Limb or Profile Line #	Criterion 1: Fault Scarp			Criterion 2: Back-tilted Face		
		Dip	Dip Standard Deviation	Dip Standard Error	Back-tilted Face Slope	Slope Standard Deviation	Slope Standard Error
1	Limb	43˚	3.6˚	1.1˚	14˚	2.7˚	0.9˚
2	Limb	42˚	2.3˚	0.7˚	21˚	2.8˚	0.9˚
3	Limb	32˚	1.9˚	0.6˚	22˚	4.2˚	1.3˚
4	Limb	27˚	4.7˚	1.5˚	30˚	4.2˚	1.3˚
Scarp 5							
	1	37˚	7.3˚	4.2˚	6˚	0.7˚	0.4˚
	2	34˚	8.1˚	5.7˚	4˚	2.4˚	1.4˚
	3	38˚	6.1˚	4.3˚	4˚	2.3˚	1.3˚
	4	42˚	5.7˚	4.0˚	2˚	1.7˚	1.0˚
	5	41˚	6.7˚	4.7˚	2˚	1.7˚	1.0˚
	6	41˚	10.7˚	7.6˚	2˚	1.5˚	0.9˚
	7	19˚	3.6˚	2.1˚	1˚	0.9˚	0.6˚
	8	26˚	3.5˚	2.5˚	4˚	0.2˚	0.2˚
	9	29˚	6.6˚	4.7˚	4˚	1.6˚	1.1˚
	10	31˚	2.0˚	1.4˚	4˚	2.7˚	1.9˚
	11	29˚	4.0˚	2.8˚	1˚	0.3˚	0.2˚
	12	30˚	0.3˚	0.2˚	1˚	0.8˚	0.6˚
	13	28˚	2.8˚	2.0˚	0˚	0.3˚	0.2˚
	14	23˚	3.6˚	2.6˚	3˚	0.2˚	0.1˚
	15	21˚	1.8˚	1.3˚	11˚	1.5˚	1.1˚
Scarp 6							
	1	16˚	2.2˚	1.5˚	6˚	0.6˚	0.3˚
	2	20˚	1.8˚	1.3˚	7˚	0.4˚	0.3˚
	3	11˚	1.2˚	0.6˚	7˚	0.6˚	0.4˚
	4	10˚	1.3˚	0.9˚	6˚	0.0˚	0.0˚
	5	10˚	1.0˚	0.6˚	6˚	0.7˚	0.5˚
	6	17˚	0.3˚	0.2˚	4˚	0.8˚	0.5˚
	7	20˚	0.2˚	0.2˚	4˚	0.8˚	0.6˚
	8	20˚	10.8˚	7.7˚	5˚	0.1˚	0.1˚
	9	15˚	0.2˚	0.1˚	5˚	0.3˚	0.2˚

Table IC-1. Continued.

Scarp #	Limb or Profile Line #	Criterion 1: Fault Scarp			Criterion 2: Back-tilted Face		
		Dip	Dip Standard Deviation	Dip Standard Error	Back-tilted Face Slope	Slope Standard Deviation	Slope Standard Error
	10	13˚	0.9˚	0.6˚	6˚	0.9˚	0.6˚
	11	13˚	1.3˚	0.9˚	7˚	1.0˚	0.6˚
	12	12˚	2.9˚	2.0˚	9˚	2.2˚	1.6˚
	13	12˚	0.3˚	0.2˚	11˚	0.5˚	0.3˚
	14	13˚	1.8˚	1.3˚	12˚	2.0˚	1.2˚
	15	11˚	1.7˚	1.2˚	8˚	1.7˚	1.0˚

Table I-C2. The results of the Shapiro-Wilk test for normality on dip and slope data collected for Criteria 1 and 2.

Scarp #s	Criterion 1: Fault Scarp		Criterion 2: Back-tilted Face	
	Normally Distributed?	p-value	Normally Distributed?	p-value
1	Yes	0.9	Yes	0.7
2	Yes	0.3	Yes	0.8
3	No	0.0	Yes	0.7
4	Yes	0.6	Yes	0.2
5	Yes	0.8	Yes	0.1
6	Yes	0.1	Yes	0.1

Table I-C3. The statistical test results of Criteria 1 and 2.

Scarp #s	Criterion 1: Fault Scarp			Criterion 2: Back-tilted Face		
	Statistical Test Used	**p-value**	**Dips Statistically Different?**	**Statistical Test Used**	**p-value**	**Slopes Statistically Different?**
1 & 2	t-test	0.6	No	t-test	4×10^{-4}	Yes
1 & 3	Mann-Whitney U	1×10^{-5}	Yes	t-test	1×10^{-3}	Yes
1 & 4	t-test	6×10^{-6}	Yes	t-test	7×10^{-6}	Yes
2 & 3	Mann-Whitney U	2×10^{-3}	Yes	t-test	0.6	No
2 & 4	t-test	3×10^{-6}	Yes	t-test	1×10^{-3}	Yes
3 & 4	Mann-Whitney U	5×10^{-4}	Yes	t-test	2×10^{-3}	Yes
5 & 6	t-test	1×10^{-8}	Yes	t-test	4×10^{-4}	Yes

Table I-C4. The results of Criterion 3 (concavity) on Scarps 5 and 6.

Profile Line #	m12 – m13	Standard Deviation	Standard Error
	Scarp 5		
1	0.09	0.08	0.06
2	0.06	0.08	0.05
3	0.00	0.13	0.07
4	0.01	0.28	0.16
5	-0.11	0.10	0.06
6	0.04	0.36	0.21
7	-0.01	0.08	0.05
8	-0.06	0.19	0.11
9	0.05	0.14	0.08
10	0.02	0.13	0.07
11	0.04	0.10	0.06
12	0.00	0.09	0.05
13	0.02	0.11	0.06
14	0.03	0.06	0.04
15	0.03	0.05	0.03
	Scarp 6		
1	-0.01	0.07	0.04
2	0.04	0.09	0.06
3	-0.01	0.01	0.00
4	-0.04	0.03	0.02
5	0.00	0.02	0.01
6	0.00	0.07	0.04
7	0.01	0.10	0.06
8	-0.06	0.14	0.08
9	0.00	0.06	0.03
10	0.00	0.05	0.03
11	0.01	0.05	0.03
12	0.02	0.04	0.02
13	-0.02	0.03	0.02
14	-0.01	0.05	0.04
15	-0.01	0.04	0.03

Table I-C5. The calculated thermal gradient of the region of the Arden Corona boundary at the time of faulting given different surface temperatures, brittle-ductile transition temperatures, strain rates, grain sizes and friction coefficients.

	z_{BDT} = 6.7 km	z_{BDT} = 7.9 km	z_{BDT} = 8.3 km	z_{BDT} = 9.0 km
T_s = 70 K, μ = 0				
$\dot{\varepsilon} = 10^{-15}$ s^{-1}	T_z = 141 K	T_z = 141 K	T_z = 141 K	T_z = 141 K
d = 0.1 mm	ΔT = 11 K km^{-1}	ΔT = 9 K km^{-1}	ΔT = 9 K km^{-1}	ΔT = 8 K km^{-1}
$\dot{\varepsilon} = 10^{-10}$ s^{-1}	T_z = 195 K	T_z = 195 K	T_z = 195 K	T_z = 195 K
d = 0.1 mm	ΔT = 19 K km^{-1}	ΔT = 16 K km^{-1}	ΔT = 15 K km^{-1}	ΔT = 14 K km^{-1}
$\dot{\varepsilon} = 10^{-15}$ s^{-1}	T_z = 153 K	T_z = 153 K	T_z = 153 K	T_z = 153 K
d = 1 mm	ΔT = 12 K km^{-1}	ΔT = 10 K km^{-1}	ΔT = 10 K km^{-1}	ΔT = 9 K km^{-1}
$\dot{\varepsilon} = 10^{-10}$ s^{-1}	T_z = 217 K	T_z = 217 K	T_z = 217 K	T_z = 217 K
d = 1 mm	ΔT = 22 K km^{-1}	ΔT = 19 K km^{-1}	ΔT = 18 K km^{-1}	ΔT = 16 K km^{-1}
$\dot{\varepsilon} = 10^{-15}$ s^{-1}	T_z = 150 K	T_z = 150 K	T_z = 150 K	T_z = 150 K
d = 10 mm	ΔT = 12 K km^{-1}	ΔT = 10 K km^{-1}	ΔT = 10 K km^{-1}	ΔT = 9 K km^{-1}
$\dot{\varepsilon} = 10^{-10}$ s^{-1}	T_z = 196 K	T_z = 196 K	T_z = 196 K	T_z = 196 K
d = 10 mm	ΔT = 19 K km^{-1}	ΔT = 16 K km^{-1}	ΔT = 15 K km^{-1}	ΔT = 14 K km^{-1}
T_s = 86 K, μ = 0				
$\dot{\varepsilon} = 10^{-15}$ s^{-1}	T_z = 141 K	T_z = 141 K	T_z = 141 K	T_z = 141 K
d = 0.1 mm	ΔT = 8 K km^{-1}	ΔT = 7 K km^{-1}	ΔT = 7 K km^{-1}	ΔT = 6 K km^{-1}
$\dot{\varepsilon} = 10^{-10}$ s^{-1}	T_z = 195 K	T_z = 195 K	T_z = 195 K	T_z = 195 K
d = 0.1 mm	ΔT = 16 K km^{-1}	ΔT = 14 K km^{-1}	ΔT = 13 K km^{-1}	ΔT = 12 K km^{-1}
$\dot{\varepsilon} = 10^{-15}$ s^{-1}	T_z = 153 K	T_z = 153 K	T_z = 153 K	T_z = 153 K
d = 1 mm	ΔT = 10 K km^{-1}	ΔT = 8 K km^{-1}	ΔT = 8 K km^{-1}	ΔT = 7 K km^{-1}
$\dot{\varepsilon} = 10^{-10}$ s^{-1}	T_z = 217 K	T_z = 217 K	T_z = 217 K	T_z = 217 K
d = 1 mm	ΔT = 20 K km^{-1}	ΔT = 17 K km^{-1}	ΔT = 16 K km^{-1}	ΔT = 15 K km^{-1}
$\dot{\varepsilon} = 10^{-15}$ s^{-1}	T_z = 150 K	T_z = 150 K	T_z = 150 K	T_z = 150 K
d = 10 mm	ΔT = 10 K km^{-1}	ΔT = 8 K km^{-1}	ΔT = 8 K km^{-1}	ΔT = 7 K km^{-1}
$\dot{\varepsilon} = 10^{-10}$ s^{-1}	T_z = 196 K	T_z = 196 K	T_z = 196 K	T_z = 196 K
d = 10 mm	ΔT = 16 K km^{-1}	ΔT = 14 K km^{-1}	ΔT = 13 K km^{-1}	ΔT = 12 K km^{-1}
T_s = 70 K, μ = 0.55				
$\dot{\varepsilon} = 10^{-15}$ s^{-1}	T_z = 146 K	T_z = 146 K	T_z = 146 K	T_z = 146 K
d = 0.1 mm	ΔT = 12 K km^{-1}	ΔT = 10 K km^{-1}	ΔT = 9 K km^{-1}	ΔT = 9 K km^{-1}
$\dot{\varepsilon} = 10^{-10}$ s^{-1}	T_z = 205 K	T_z = 204 K	T_z = 204 K	T_z = 204 K
d = 0.1 mm	ΔT = 21 K km^{-1}	ΔT = 17 K km^{-1}	ΔT = 17 K km^{-1}	ΔT = 15 K km^{-1}
$\dot{\varepsilon} = 10^{-15}$ s^{-1}	T_z = 159 K	T_z = 159 K	T_z = 159 K	T_z = 158 K
d = 1 mm	ΔT = 14 K km^{-1}	ΔT = 11 K km^{-1}	ΔT = 11 K km^{-1}	ΔT = 10 K km^{-1}
$\dot{\varepsilon} = 10^{-10}$ s^{-1}	T_z = 230 K	T_z = 230 K	T_z = 230 K	T_z = 229 K
d = 1 mm	ΔT = 25 K km^{-1}	ΔT = 21 K km^{-1}	ΔT = 20 K km^{-1}	ΔT = 18 K km^{-1}
$\dot{\varepsilon} = 10^{-15}$ s^{-1}	T_z = 174 K	T_z = 174 K	T_z = 174 K	T_z = 173 K
d = 10 mm	ΔT = 14 K km^{-1}	ΔT = 11 K km^{-1}	ΔT = 11 K km^{-1}	ΔT = 10 K km^{-1}

Table I-C5. Continued**.**

	z_{BDT} = 6.7 km	z_{BDT} = 7.9 km	z_{BDT} = 8.3 km	z_{BDT} = 9.0 km
$\dot{\varepsilon} = 10^{-10}$ s^{-1}	T_z = 264 K	T_z = 263 K	T_z = 263 K	T_z = 262 K
d = 10 mm	Δ = 22 K km^{-1}	Δ = 18 K km^{-1}	Δ = 17 K km^{-1}	Δ = 16 K km^{-1}
T_s = 86 K, μ = 0.55				
$\dot{\varepsilon} = 10^{-15}$ s^{-1}	T_z = 146 K	T_z = 146 K	T_z = 146 K	T_z = 146 K
d = 0.1 mm	ΔT = 9 K km^{-1}	ΔT = 8 K km^{-1}	ΔT = 7 K km^{-1}	ΔT = 7 K km^{-1}
$\dot{\varepsilon} = 10^{-10}$ s^{-1}	T_z = 205 K	T_z = 204 K	T_z = 204 K	T_z = 204 K
d = 0.1 mm	ΔT = 18 K km^{-1}	ΔT = 15 K km^{-1}	ΔT = 15 K km^{-1}	ΔT = 14 K km^{-1}
$\dot{\varepsilon} = 10^{-15}$ s^{-1}	T_z = 159 K	T_z = 159 K	T_z = 159 K	T_z = 158 K
d = 1 mm	ΔT = 11 K km^{-1}	ΔT = 9 K km^{-1}	ΔT = 9 K km^{-1}	ΔT = 8 K km^{-1}
$\dot{\varepsilon} = 10^{-10}$ s^{-1}	T_z = 230 K	T_z = 230 K	T_z = 230 K	T_z = 229 K
d = 1 mm	ΔT = 22 K km^{-1}	ΔT = 19 K km^{-1}	ΔT = 18 K km^{-1}	ΔT = 16 K km^{-1}
$\dot{\varepsilon} = 10^{-15}$ s^{-1}	T_z = 174 K	T_z = 174 K	T_z = 174 K	T_z = 173 K
d = 10 mm	ΔT = 11 K km^{-1}	ΔT = 9 K km^{-1}	ΔT = 9 K km^{-1}	ΔT = 8 K km^{-1}
$\dot{\varepsilon} = 10^{-10}$ s^{-1}	T_z = 264 K	T_z = 263 K	T_z = 263 K	T_z = 262 K
d = 10 mm	ΔT = 19 K km^{-1}	ΔT = 16 K km^{-1}	ΔT = 16 K km^{-1}	ΔT = 14 K km^{-1}

Table I-C6. The calculated heat fluxes of the region of the Arden Corona boundary at the time of faulting given different surface temperatures and brittle-ductile transition temperatures.

	z_{BDT} = 6.7 km	z_{BDT} = 7.9 km	z_{BDT} = 8.3 km	z_{BDT} = 9.0 km
T_s = 70 K T_z = 141 K	59 mW m^{-2}	50 mW m^{-2}	48 mW m^{-2}	44 mW m^{-2}
T_s = 86 K T_z = 141 K	42 mW m^{-2}	35 mW m^{-2}	34 mW m^{-2}	31 mW m^{-2}
T_s = 70 K T_z = 264 K	112 mW m^{-2}	95 mW m^{-2}	91 mW m^{-2}	84 mW m^{-2}
T_s = 86 K T_z = 264 K	95 mW m^{-2}	80 mW m^{-2}	77 mW m^{-2}	71 mW m^{-2}

CHAPTER II
Shallow Normal Fault Slopes on Saturn's Icy Satellites

This chapter is a reformatted version of a paper by the same name under review in the Journal of Geophysical Research by Chloe Beddingfield, Devon Burr, and William Dunne. All data collection and analyses were performed by Chloe Beddingfield.

Abstract

Fault dips are a function of the coefficient of internal friction, μ_i, of the lithospheric material. Laboratory deformation experiments of H_2O ice at conditions applicable to icy bodies yield $0 \leq \mu_i \leq 0.55$ such that normal faults dip between 45° and 59°. We tested the hypothesis that normal faults on icy bodies reflect these values by using digital elevation models to examine geometries of large extensional systems on three Saturnian satellites. Analyzed faults within Ithaca Chasma on Tethys and Avaiki Chasmata on Rhea all exhibit shallower-than-predicted topographic slopes across the fault scarp, which we term 'fault slopes'. A scarp of Padua Chasmata within Dione's Wispy Terrain also has a shallow fault slope, although three others that make up Palatine Chasmata exhibit steeper slopes as predicted. We infer that viscous relaxation is the most viable explanation for these shallow fault slopes, and we model the potential role of viscous relaxation in creating shallow fault slopes. Our modeling results support formation of these normal faults with steep dips consistent with deformation experiments, followed by their relaxation due to lithospheric heating events related to radionuclide decay. The steepest fault slopes in this terrain yield $0 \leq \mu_i \leq 0.73$ for Dione's lithospheric ice, which overlaps the dip range predicted from experiments. Results of this work suggest that viscous relaxation substantially affected fault slopes on Tethys, Rhea, and Dione. By implication, these processes may have also affected fault geometries on other icy satellites.

Introduction

Tectonic structures are nearly ubiquitous on icy satellites throughout the solar system, and analyses of these structures can provide insight into satellite evolution (Collins et al., 2009). From analyses of terrestrial tectonic structures, fault dips are known to be indicators of behaviors that control initial fault geometries or alter pre-existing geometries. For example, normal faults with shallow dips, termed low-angle normal faults (LANFs), can be indicative of specific geologic settings or events (e.g., Proffett, 1977; Spencer and Chase, 1989; Axen, 1992; Parsons and Thompson, 1993).

Icy satellites commonly exhibit large-scale, fault scarps (Figure II-1). Fault geometries measured from these scarps have the potential to provide important information on the tectonic histories of the satellites. It is unclear, however, whether the topographic slope across fault scarps, which we term 'fault slopes', on icy satellites directly reflect dips inferred from laboratory deformation experiments (e.g., Durham et

al., 1983; Beeman et al., 1988; Schulson and Fortt, 2012). In particular, normal fault slopes on icy satellites may be shallower than expected from experiments, indicating the presence of regolith overlying the fault scarps, or indicating LANFs. LANFs may be caused by fault block tilting (e.g., Proffett, 1977; Pappalardo and Greeley, 1995; Regenauer-Lieb et al., 2004), perturbation of the stress-axes due to the application of additional shear stresses in the lithosphere (e.g., Yin, 1989; Spencer and Chase, 1989), material weakening (e.g., Byerlee, 1978; Buck et al., 2005), deposition of regolith over the scarps (e.g., Blackwelder, 1928; Burbank and Anderson, 2011), and/or viscous relaxation (Buck, 1988; Wernicke and Axen, 1988).

In this work, our hypothesis is that dips inferred from laboratory deformation experiments of cryogenic H_2O ice I are directly reflected by normal fault slopes on icy satellites. To test this hypothesis, we compare fault slopes – as a proxy for fault dips – on icy satellites to normal fault dips inferred in laboratory deformation experiments. If laboratory results are directly reflected by icy satellite fault slopes, then these slopes would be analogous to terrestrial faults found within rift systems in rock. The terrains considered in this study are on Saturnian icy satellites, and all exhibit large structures, interpreted by others as sets of normal faults (Figures II-1 and II-2). The selected terrains are two simple fault systems, Ithaca Chasma on Tethys (Moore and Ahern, 1983) and Avaiki Chasmata on Rhea (Thomas, 1988), and a more complex fault system, the Wispy Terrain on Dione (Moore, 1984; Wagner et al., 2006). On Dione, we focus our study on Palatine Chasmata and Padua Chasmata, but for simplicity, we refer to this study area as the Wispy Terrain. These three terrains, well-established by previous work as extensional fault systems, provide landscape-scale data for comparison on appropriate experimental data.

Background

Brittle Deformation Theory

On the surfaces of planetary bodies, including the icy surfaces of Saturn's moons and the rocky surface of Earth, tectonic structures form when differential stress exceeds the strength of a material (e.g., Fossen, 2010). The relative importance of fracturing during structure formation is an outcome of material rheology, intrinsic parameters, and extrinsic conditions at the time of deformation. Fracture-related deformation is the expected behavior for near-surface conditions on icy satellites, where the vertical normal stress is relatively small and the temperature is low (Durham et al., 1983).

In brittle materials, the type of major fault depends on the orientations of the maximum and minimum stresses on and near the surface, which results in some combination of normal, reverse, and strike-slip displacement (Anderson, 1951). For terrestrial examples of brittle normal faults, the orientation of the maximum compressive stress, σ_1, is typically vertical, while the orientations of the intermediate compressive stress, σ_2, and the minimum compressive stress, σ_3, are horizontal, with σ_2 oriented parallel and σ_3 oriented perpendicular to the strike of the fault (Figure II-3) (e.g.,

Anderson, 1942; McGarr and Gay, 1978). In this case, compression is taken to be positive stress and tension is taken to be negative stress.

Static analysis of brittle fault formation in terrestrial crust approximates deformation behavior with the Coulomb failure criterion (e.g., Jaeger and Cook, 1979; Price and Cosgrove, 1990) (Figure II-4). The minimum plane-parallel shear stress, σ_S, required to form a fracture plane is given by

$$\sigma_S = C + \mu_i \sigma_N, \tag{II-1}$$

where C is the cohesion of the material, σ_N is the normal stress on the fracture plane, and μ_i is the material's coefficient of internal friction, equal to $tan\,(\sigma_S/\sigma_N)$. The ratio σ_S/σ_N is the internal friction angle, φ, of the material. The angle of the fracture plane relative to σ_3, θ, is related to φ, by

$$\theta = 45° + \frac{\varphi}{2}. \tag{II-2}$$

Because normal faults initiate with σ_1 in the vertical and σ_3 in the horizontal directions, the normal fault dip, δ_{normal}, is equal to θ. When deformation is brittle, μ_i is related to δ_{normal} (Anderson, 1905) by

$$\delta_{normal} = 45° + \frac{\arctan(\mu_i)}{2}. \tag{II-3}$$

In summary, as μ_i increases, δ_{normal} increases, and the fault dip becomes steeper. As μ_i decreases, δ_{normal} decreases, and the fault dip becomes shallower. Values for μ_i can be inferred from measured δ_{normal} in laboratory brittle deformation experiments for different materials. For H_2O ice I, these experiments have been conducted at a variety of temperatures down to cryogenic conditions, vertical normal stresses, and strain rates.

Brittle Deformation Experiments in Water Ice

H_2O ice I is stable at the surfaces and within the lithospheres of icy satellites (e.g., Durham et al., 1983). To determine μ_i for H_2O ice I, previous investigators conducted a series of deformation experiments at various temperatures, vertical normal stresses, and strain rates. As summarized in Schulson and Fortt (2012), μ_i is dependent on temperature and strain rate. The dependence of μ_i on temperature is complex, and disagreements over this dependence are noted in the literature (e.g., Schulson and Fortt, 2012, 2013). However, μ_i is independent of ice grain size and ice type (granular vs. columnar) at some strain rates and temperatures (Kennedy et al., 2000; Montagnat and Schulson, 2003; Schulson and Fortt, 2012, 2013).

The experimental conditions relevant to the lithospheric environments of Saturn's icy satellites are cryogenic H_2O ice I compositions, low temperatures, and small strain rates (Table II-1). Thus, for this study, we focus on results from experiments under these

conditions (Durham et al., 1983; Beeman et al., 1988; Schulson and Fortt, 2012), which indicate that μ_i ranges from 0 to 0.55 and hence, that δ_{normal} ranges from 45° to 59°.

Causes of Icy Satellite Extensional Tectonics

Evidence for brittle deformation, in the form of tectonic faults, is visible on many icy satellite surfaces in the outer solar system (e.g., Figure II-1). Most of these structures are interpreted as extensional normal faults (e.g., Collins et al., 2009). On a planetary surface, a series of sub-parallel-striking normal faults will create a set of sub-parallel troughs that typically align perpendicular to the direction of extension (Pappalardo and Greeley, 1995). The trough walls are defined by fault scarps that may dip consistently in one direction (Figure II-2a), alternate directions (Figure II-2b), or may exhibit a combination of these patterns (Figure II-2c).

Sources of differential stress at the global and/or local scale can generate these normal fault systems (Collins et al., 2009). Global-scale sources include tides (e.g., Greenberg et al., 1998; Hoppa et al., 1999; Tobie et al., 2005), nonsynchronous rotation (e.g., Helfenstein and Parmentier, 1985; Leith and McKinnon, 1996; Greenberg et al., 1998), polar wander (e.g., Willemann, 1984; Leith and McKinnon, 1996; Matsuyama and Nimmo, 2008), despinning (e.g., Melosh, 1977; Squires and Croft, 1986; Murray and Dermott, 1999), orbital recession (e.g., Melosh, 1980; Helfenstein and Parmentier, 1983), and satellite volume change (e.g., Squyres and Croft, 1986; Kirk and Stevenson, 1987; Mueller and McKinnon, 1988). Local-scale sources of differential stress include convection (e.g., Kirk and Steveson, 1987; Nimmo and Manga, 2002; Showman and Han, 2005; Barr, 2008), lateral pressure gradients (e.g., Ojakangas and Stevenson, 1989; Buck, 1991; Nimmo, 2004), flexure (e.g., Hurford et al., 2005; Hammond et al., 2013), and impact cratering (e.g., McKinnon and Melosh, 1980; Bruesch and Asphaug, 2004; Moore et al., 2004).

Data and Methods

In the Saturnian system, inferred normal faults have been identified on various icy satellites. In some cases, these structures constitute entire terrains including Ithaca Chasma on Tethys, Avaiki Chasmata on Rhea, and the Wispy Terrain on Dione. For this reason, we use these well-established examples of normal fault systems from the Saturnian icy satellites to test our hypothesis. Based on our results, we assess the possibility that various processes could generate the observed fault slopes.

Ithaca Chasma on Tethys, Avaiki Chasmata on Rhea, and the Wispy Terrain on Dione were all imaged by the Imaging Science Subsystem (ISS) onboard the Voyager 2 spacecraft and by the ISS camera onboard the Cassini spacecraft. The sets of normal faults that comprise these terrains were identified by others based on their graben-like geometries (Moore, 1984), the relatively high albedo and spectral signature of freshly exposed H_2O ice of their walls (Wagner et al., 2006, 2007, 2010; Clark et al., 2008;

Stephan et al., 2010, 2012), and the sharpness of their ridges (Moore and Ahern, 1983; Giese et al., 2007). Ithaca Chasma on Tethys and Avaiki Chasmata on Rhea exhibit relatively simple rift-system geometries. The Wispy Terrain on Dione also exhibits rift-system geometries, but with an overall more complex geometry made up of several fossae and chasmata with various orientations.

Ithaca Chasma, Tethys

Closest to Saturn of the three satellites in this study, Tethys, Saturn's third regular satellite, orbits between Enceladus and Dione and has a mean radius of ~531 km (Roatsch et al., 2009; Thomas, 2010). H_2O ice is the primary surface constituent (Morrison et al., 1976; Emery et al., 2005), and the surface temperature averages ~87 K (Hanel et al., 1982; Howett et al., 2010, 2012). Tethys' surface exhibits heavily cratered plains (Smith et al., 1981, 1982; Moore and Ahern, 1983), smooth, less densely cratered plains (Smith et al., 1982), the large impact crater Odysseus (~400 km diameter), and a set of normal faults termed Ithaca Chasma (Smith et al., 1982) (Figures II-5 and II-6).

Ithaca Chasma can be traced more than 1,000 km across the Saturn-facing hemisphere, trends approximately north-south, is 50 - 100 km wide, and ~3 km deep relative to the surrounding plains, as derived from digital elevation models (DEMs) (e.g., Smith et al., 1981; Giese et al., 2007). Based on the sharpness of the topography of Ithaca Chasma, and its graben-like geometry, this set of structures is inferred to be extensional (Moore and Ahern, 1983; Giese et al., 2007).

Different causes for the formation of Ithaca Chasma have been proposed. One explanation is that extension on the surface resulted from global volume expansion resulting from internal freezing of Tethys (Smith et al., 1981), or from radionuclide heating (Hillier and Squyres, 1991). An alternative hypothesis is that Ithaca Chasma formed during the impact event that generated Odysseus crater (Moore and Ahern, 1983; Moore et al., 2004).

Avaiki Chasma, Rhea

Further out in the Saturnian system, Rhea orbits between Dione and Titan, and is Saturn's fifth regular satellite. Larger than Tethys, Rhea is the second largest Saturnian moon (radius ~764 km) (Roatsch et al., 2009; Thomas, 2010). As with Tethys, Rhea's surface composition is mostly H_2O ice (Morrison et al., 1976; Emery et al., 2005; Stephan et al., 2012) with minor amounts of visually dark material of unknown composition on the surface of the trailing hemisphere (e.g., Smith et al., 1982; Buratti et al., 2002; Stephan et al., 2012). The presence of this dark material is associated with a slightly higher trailing hemisphere surface temperature (~88 K) than leading hemisphere surface temperature (~82 K) (Cruikshank et al., 1984; Howett et al., 2010).

A set of tectonic features was initially described as wispy terrain (Smith et al., 1981; Thomas, 1988) and was later termed Avaiki Chasmata by the International Astronomical Union (IAU) Working Group for Planetary System Nomenclature (WGPSN). The structures that comprise Avaiki Chasmata trend approximately north-

south across most of Rhea's northern, trailing hemisphere (Figures II-7 and II-8) (Thomas, 1988). Based on their graben-like cross-sectional geometry, albedo, and the spectral signature of fresh H_2O ice of the trough walls, these features are interpreted as sets of inward-facing normal faults (Moore et al., 1985; Plescia, 1985; Wagner et al., 2007, 2010; Stephan et al., 2012). Avaiki Chasmata may have formed due to global volume expansion associated with an interior heating event (Ellsworth and Schubert, 1983; Hillier and Squyres, 1991).

The Wispy Terrain, Dione

Dione orbits between Tethys and Rhea. With a mean radius of ~561 km (Giese et al., 2006; Roatsch et al., 2009; Thomas, 2010), Dione is slightly larger than Tethys, but smaller than Rhea. In addition to a predominately H_2O ice surface composition, with minor abundances of CO_2 and CN (Morrison et al., 1976; Cruikshank et al., 2005; Clark et al., 2008), the surface includes minor amounts of a visually dark non-ice material of unknown composition that is concentrated on the surface of the trailing hemisphere (Clark et al., 2008; Roatsch et al., 2009; Stephan et al., 2010). Similar to Rhea, this asymmetry in albedo produces an asymmetry in temperature, with an average surface temperature of ~83 K on Dione's leading hemisphere and ~90 K on the trailing hemisphere (Cruikshank et al., 1984; Howett et al., 2010, 2014).

Bright, wispy material (Plescia, 1983; Moore, 1984), termed the "Wispy Terrain", covers a large portion of Dione's trailing hemisphere, and exhibits a series of lineaments. These lineaments are interpreted as extensional with dilational fractures and normal faults arranged in horst and graben geometries (Figures II-9 and II-10). This interpretation is based on the high albedo of the trough walls relative to the surrounding terrain (Wagner et al., 2006), the spectral signature of fresh H_2O ice of these walls (Clark et al., 2008; Stephan et al., 2010), as well as the graben-like geometries of the troughs in cross-section (Moore, 1984). The Wispy Terrain is made up of several fossae and chasmata including Clusium and Carthage Fossae, Drepanum Chasma, and Eurotas, Palatine, Padua, and Aurunca Chasmata. Like Avaiki Chasmata on Rhea, Dione's Wispy Terrain may have also formed during a period of near-global expansion due to a heating event from the decay of long-lived radionuclides (Moore, 1984; Hillier and Squyres, 1991).

Digital Elevation Models

To investigate fault scarp geometries of the three study areas, we generated and analyzed digital elevation models (DEMs) that cover scarps within each area. Each region has overlapping images acquired by the ISS camera onboard the Cassini spacecraft, exhibiting emission angles appropriate for DEM construction. DEMs were constructed with the Softcopy Exploitation Toolkit (SOCET SET). SOCET SET is a BAE Systems' digital mapping software and hardware, which allows for user supervision of automated tie-point generation in overlapping images, enabling reduction in computer-generated DEM error that results from the misidentifications of features in these images.

Overlapping image pairs of Ithaca Chasma, Avaiki Chasmata, and the Wispy Terrain were acquired from the Planetary Data System (PDS) website. These images were processed with the Integrated Software for Imagers and Spectrometers (ISIS) (Anderson et al., 2004), using the steps required for preparing the images to be imported into SOCET SET. The images were then imported into SOCET SET and used to create DEMs. The steps used to process the images in ISIS and generate the DEMs with SOCET SET, as well as the approach for calculating the vertical accuracy of each DEM, are given in Appendix II-A.

A second and more widely available method of generating DEMs from overlapping images uses the Ames Stereo Pipeline (ASP) software (Broxton and Edwards, 2008; Moratto et al., 2010), and was designed to process image pairs acquired by cameras onboard National Aeronautics and Space Administration (NASA) spacecrafts. ASP is freeware made available by NASA to produce DEMs. ASP automatically generates tie-points on overlapping images, but does not provide the user supervision of these tie-point measurements as does SOCET SET. Because SOCET SET allows for user supervision, we favor the results gathered from the DEMs generated with SOCET SET, but compared the output DEMs of both SOCET SET and ASP for completeness.

We used the same image pairs to generate DEMs with SOCET SET and ASP, and compared measurements of fault slopes taken on these different sets of DEMs. We also compared fault slope measurements of the sections of extensional faults that are visible in overlapping SOCET SET DEMs. The steps used to create ASP DEMs are discussed in Appendix II-B, results of the comparison between SOCET SET and ASP DEMs and the comparison of results between overlapping sections of SOCET SET DEMs are given in Appendix II-C.

We generated DEMs using one image pair covering Ithaca Chasma on Tethys (Figure II-6), four image pairs covering Avaiki Chasmata on Rhea (Figure II-8), and one image pair covering the Wispy Terrain on Dione (Figure II-10) (Table II-2). The SOCET SET DEMs used in this work and their associated orthorectified images were exported to the Environmental Systems Research Institute's (ESRI's) ArcMap software for analysis and data collection.

Measurement Techniques

On each DEM overlying its associated orthorectified Cassini ISS image in ArcMap, we mapped normal fault scarps within Ithaca Chasma on Tethys (Figure II-6), Avaiki Chasmata on Rhea (Figure II-8), and the Wispy Terrain on Dione (Figure II-10). Using the measurement tool in ArcMap as a guide, we only mapped scarps that exhibited widths that, in at least some sections of the scarp, are ≥ 2.5 times the DEM resolution to insure that at least two DEM pixels exist across the width of each scarp.

We then generated several profile lines across each fault scarp, with each line crossing the scarp perpendicular to the local strike of the fault and spaced two to five kilometers along strike. We avoided areas along strike where: 1) the visible scarp width is < 2.5 times the DEM resolution; 2) the scarps are in shadows dark enough for the DEM

to have generated error when calculating topography, or where there is an obvious error in the DEM, usually due to dark shadowing of the terrain; and 3) the scarps have been visibly disrupted, either by post-faulting impact events or offset by younger factures that currently cut the scarp.

In the cases where a section of the same fault scarp exists on multiple DEMs, we were careful not to incorporate measurements of a single area multiple times into the results. In those cases, we took measurements on the DEM with the highest vertical accuracy. The data along each profile line were exported from ArcMap to a spreadsheet for fault slope calculations.

From plots of each scarp's topography, we estimated the top and bottom of the scarp in each profile line visually, using the greatest change in slope above and below each sub-planar sloped surface to define the scarp limits (Figure II-11). We then took one fault slope measurement along each profile line by measuring the slope between the pixel directly below the scarp top, and the pixel directly above the scarp bottom.

We derived the uncertainty for each fault slope measurement from the calculated vertical accuracy of each DEM (Appendix II-A). To derive the uncertainty, we subtracted the vertical accuracy value from the height measurement of the bottom of each scarp and added this value to the height measurement of the top of each scarp to find the maximum fault slope values. Similarly, we added the value for vertical accuracy to the bottom of each scarp and subtracted that value from the top of each scarp to find the minimum fault slope values. The average measured fault slope and the average uncertainty, calculated for each fault scarp, were then compared to the laboratory-derived, expected dip range using a set of statistical tests.

Statistical Analysis Techniques

The statistical test used to assess the data collected from each fault slope depended on the distribution of each set of data. To select the appropriate parametric or non-parametric statistical test, we first applied the Shapiro-Wilk test to determine whether a data set is normally distributed or not. The null hypothesis of the Shapiro-Wilk test is that the data are normally distributed. The resulting p-value of a statistical test represents the probability that the null hypothesis is correct. The alpha level is a threshold value used to decide if the null hypothesis of a statistical test is rejected or accepted, and is the probability of rejecting the null hypothesis when the null hypothesis is true. If the resulting p-value of the Shapiro-Wilk test is less than an alpha level of 0.01, then we can say with 99% confidence that the data are not normally distributed, so we rejected the null hypothesis and used a nonparametric test on the data in later analyses. However, if the resulting p-value is greater than an alpha level of 0.01, then we cannot conclude with 99% certainty that the data are normally distributed, so we accepted the null hypothesis and used a parametric test on these data in later analyses.

For normally distributed sets of data, we used the parametric one-sample t-test to determine whether the population mean is equal to a specified value. The nonparametric analogue of the one-sample t-test is the Wilcoxon Signed Ranks test, and was used when analyzing data that are not normally distributed. For both the one-sample t-test and the

Wilcoxon Signed Ranks test, if the resulting p-value is less than an alpha level of 0.01, then we can say that there is a difference between the population mean and the specified value with 99% confidence, and we rejected the null hypothesis for those data. However, if the resulting p-value is greater than 0.01, then we accepted the null hypothesis that there is a similarity between the population mean and the specified value.

Statistical analyses of the collected fault slope measurements were used to determine if the data support our hypothesis that dips inferred from laboratory deformation experiments of cryogenic H_2O ice I are directly reflected in normal fault slopes on icy satellites. If the average measured fault slope of a particular scarp, including the average uncertainty associated with that value, falls within the range of laboratory-derived dip values ($45° \leq \delta_{normal} \leq 59°$), then our hypothesis is supported. If the estimated fault slope and its uncertainty falls partially within and partially outside this range of expected dips, then we performed a statistical test to determine whether the results are different from the laboratory-derived dip range or not. If the average fault slope in combination with its uncertainty is less than the expected range of dips, we then performed a one-sample statistical test, comparing the collected data to the smallest value in the expected range (45°). Alternatively, if the average fault slope, including the uncertainty, is greater than the expected range of dips, then we performed this same test, but compared the data to the largest value in the expected range (59°). However, if the estimated fault slope of a scarp, including the uncertainty, falls completely outside the range of expected dip values, then our hypothesis is not supported.

Results

In the region of Ithaca Chasma on Tethys, the average measured fault slope is 24° ± 3°. The population of fault slopes from Ithaca Chasma ranges from 15° ± 3° to 36° ± 2° (Table II-3, Figures II-12a and II-13). All 10 faults analyzed in this region exhibit fault slopes that fall below the range of expected values inferred from laboratory results ($45° \leq \delta_{normal} \leq 59°$). The results of one-sample t-tests and Wilcoxon Signed Ranks tests show that these fault slopes are less than the lowest value in the expected range (45°) on a statistically significant level (Table II-4).

Similarly, the population of calculated average fault slopes of Avaiki Chasmata on Rhea fall below the expected values inferred from laboratory results. The average measured fault slope within Avaiki Chasmata is 29° ± 8°, and the population of fault slopes in this region ranges from 22° ± 6° to 37° ± 4° (Table II- 3, Figures II-12b and II-14). The results of one-sample t-tests and Wilcoxon Signed Ranks tests also show that fault slopes, for all 12 scarps analyzed are statistically less than the lowest value in the expected range (45°) (Table II-4).

The set of fault slope measurements of normal faults within Dione's Wispy Terrain differ from those gathered from Ithaca Chasma and Avaiki Chasmata. The average fault slope for three of the four scarps analyzed in this region, all within Palatine Chasmata (Scarps A, B, and C), falls within the experimentally inferred dip range (Table

II-3, Figures II-12c and II-15), with fault slopes ranging from 38° ± 12° to 56° ± 7°. Additionally, the results of one-sample statistical tests show that the measured fault slopes of these three faults are similar to the expected range (Table II-4). However, the average fault slope of the scarp within Padu Chasmata (Scarp D), is less than the experimental dip range (Table II-3 and Figure II-15), with a fault slope of only 23° ± 13°. A statistical test shows that this fault slope is not similar to the lowest expected dip range value (45°) (Table II-4).

Thus, our hypothesis that normal fault dips inferred from laboratory experiments are directly reflected on icy satellites is not supported in the region of Ithaca Chasma on Tethys, or Avaiki Chasmata on Rhea. Because fault slopes of the three scarps analyzed in Palatine Chasmata within the Wispy Terrain of Dione fall within the expected dip range, our hypothesis is supported in this region. However, measured fault slopes indicate the presence of one shallow fault slope in Padua Chasmata that is approximately 200 km from the other three scarps (Figure II-10b).

Shallow Fault Slope Development and Icy Satellite Faults

Several causes for the formation of shallow fault slopes have been proposed to account for the smaller than expected dips, and may be applicable to the occurrence of shallow fault slopes on Tethys, Rhea, and Dione.

Fault Rotation during Offset

Faults with an initially steep dip may be later rotated to a shallower angle, creating LANFs. For example, faults may rotate during offset in the case of domino-style fault blocks (Figure II-16) (Proffett, 1977; Wernicke and Burchfiel, 1982; Davis, 1983; Jackson et al., 1988; Pappalardo and Greeley, 1995). Domino-style fault blocks are characterized by having a shallow fault dip as well as a back-tilted face that was initially the sub-horizontal external surface of the fault block. Domino-style faulting has been identified on icy satellites including Miranda (Pappalardo and Greeley, 1995; Pappalardo et al., 1997) and Ganymede (Pappalardo et al., 1998; Collins et al., 1998; Pappalardo and Collins, 2005).

If a LANF is solely the result of domino-style tilting, the sum of the fault slope and the back-tilted face slope should be a value within the experimentally derived dip range. The average sums are 33° and 34° (Table II-5) for the faults of Ithaca Chasma and Avaiki Chasmata, respectively, and thus are not consistent with rotation of faults with initial dips expected for cryogenic H_2O ice I. In addition, the shallow fault slope identified within Padua Chasmata in Dione's Wispy Terrain does not exhibit any evidence of a back-tilted face. These observations indicate that rotation during domino-style faulting is not a viable explanation for the observed shallow fault slopes in the study areas.

Another fault-rotation behavior is caused by hanging-wall translation along listric faults (e.g., Ord and Hobbs, 1989; Regenauer-Lieb et al., 2004) (Figure II-17). Listric faults are curved, concave-up faults that decrease in dip with increased depth, and transition into a sub-horizontal detachment (Suess, 1909; Bally, 1983; Shelton, 1984). Rollover structures related to curved, hanging walls necessitated by the fault surface geometry are common at the margins of listric fault systems in the down-dip region of the systems (Hamblin, 1965; Xiao and Suppe, 1992).

Listric faults can exist on icy satellites, and have been identified on Uranus' icy satellite Miranda (*Beddingfield et al.*, 2015). However, on the three Saturnian fault systems studied here, the normal faults show no evidence of decreasing dip in the down-dip direction of the fault system, and rollover structures down-dip of the faults are not observed. Thus, we dismiss rotation by listric faults as a cause for these observed shallow fault slopes.

Stress-Axis Perturbation

LANFs may form if the stress-axis orientations within the lithosphere were perturbed during faulting so that the orientation of σ_1 deviated from vertical and σ_3 deviated from horizontal. Perturbed stress-axes may exist due to additional shear stress acting in the horizontal direction within the lithosphere (e.g., Pollard and Segall, 1987; Parsons and Thompson, 1993). In response to the applied shear stress, the principal stress-axes rotate to balance this additional stress, causing new stress-axes orientations to form. These additional shear stresses could exist due to the presence of intrusive magmatism (Parsons and Thompson, 1993) or pre-existing topography (Spencer and Chase, 1989). The presence of liquid water within the host material becoming incorporated into the fault system would increase pore pressure and negate a component of the normal stress perpendicular to the fault plane, allowing for LANF formation (Axen, 1992).

Liquid H_2O and/or brines in the near subsurface of Tethys, Rhea, and Dione, today and in the past, is unlikely (e.g., Hussmann et al., 2006), and impact events would only allow short lived surface water to be present. Liquid water oceans may have existed on Tethys, Rhea, and Dione, however they are estimated to have been more than 100 km below the surface. Consequently, liquid water-induced high pore-fluid pressure likely had no influence on structures formed on the surfaces of these satellites. Following this logic, we find that the possibility of stress-axis perturbation resulting from high pore-fluid pressure is not a viable explanation for the observed shallow fault slopes.

With the exception of the fault scarps, the terrains within and surrounding Ithaca Chasma, Avaiki Chasmata, and the Wispy Terrain exhibit roughly uniform topography. In addition, pre-existing features that would have caused more variation in topography, such as large impact basins, are not present. Based on these observations, we conclude that stress-axis perturbation due to the presence of topography is not a viable explanation for the presence of shallow fault slopes in any of these study areas.

In the case of stress-axes perturbation induced by intrusion of warm and buoyant ice, a variation in normal fault dips from fault to fault is expected, because of the

heterogeneous distribution of magmatic bodies (e.g., Parsons and Thompson, 1993). As a result, not all normal faults in an area with intrusive magma would be LANFs. However, within Ithaca Chasma on Tethys and Avaiki Chasmata on Rhea, all faults analyzed exhibit shallow fault slopes. Additionally, although evidence for icy satellite cryovolcanism and diapirism is commonly associated with tectonically deformed terrains on many other icy satellites throughout the solar system (e.g., Smith et al., 1986; Kargel and Strom, 1990; Croft and Soderblom, 1991; Greenberg et al., 1991; Schenk, 1991; Head and Pappalardo, 1999; Porco et al., 2006), evidence for this activity has not yet been directly associated with any of the study areas. Based on these reasons, we do not find intrusion-induced stress-axes perturbation to be a likely explanation for the observed shallow fault slopes in the study areas.

Material Weakening

In terrestrial settings, strain-softening behavior along a fault-zone is another cause for LANFs (Bazant et al., 1984; Buck et al., 2005). In this case, strain-softening reduces the μ_i of the material with increasing displacement, causing the material to weaken. This activity in turn produces faults with lower than expected dips (Huismans et al., 2002).

Strain-softening has been observed in laboratory deformation experiments of cryogenic ice, although this behavior only occurs in specific cases before a steady state has been reached (e.g., Durham et al., 1997; Stern et al., 1997). Additionally, as shown by Equation II-3, the lowest possible dip that could be produced by LANFs formed from material weakening is 45°, with an associated μ_i of 0. Because the shallow fault slopes in the study areas exhibit dips less than 45°, we infer that strain-softening is not a viable explanation for the shallow fault slopes in any of the study areas.

Regolith Deposition

Another possible modifier of fault slopes is the deposition of regolith, either from elsewhere on the satellite and/or from local mass wasting (i.e. from the fault scarps), causing once exposed normal fault scarps to be mantled (e.g., Blackwelder, 1928; Veverka et al., 1986; Moore et al., 2009; Burbank and Anderson, 2011). Over time, this mantling process would fill in topographic lows, such as at the bases of scarps, and reduce initially steep fault slopes to the angle of repose (e.g., Blackwelder, 1928; Burbank and Anderson, 2011). The angle of repose is the maximum slope angle at which a noncohesive granular material can be at rest (Lowe, 1976) and is likely independent of gravitation acceleration (e.g., Atwood-Stone and McEwen, 2013), but see Kleinhans et al. (2011) for an alternative view. The static angle of repose is ~25° for very rounded grains, and ~45° for very angular grains (e.g., Carrigy, 1970; Pohlman et al., 2006).

On the surfaces of icy satellites, regolith may be generated by different processes including meteorite bombardment (Veverka et al., 1986), micrometeorite bombardment (e.g., Moore et al., 1996, 1999; Howard et al., 2012), and/or sublimation (e.g., Sieveka and Johnson, 1982; Moore et al., 1996, 1999). On the basis of satellite size and high impact crater densities (Smith et al., 1982), impact-derived regolith thicknesses have been

estimated from Monte Carlo computer simulations for Tethys, Rhea, and Dione (Veverka et al., 1986). The mean estimated regolith thicknesses range from 1.6 km to 1.7 km on Tethys, 1.9 km to 2.0 km on Rhea, and 740 m to 780 m on Dione (Veverka et al., 1986). The minimum values of these ranges assume an open system, so that ejecta that reached escape velocity were permanently lost, whereas the maximum values of these ranges assume a closed system so that all ejecta returned to the system (Veverka et al., 1986).

As summarized in Table II-6, heights of the analyzed fault slopes within Ithaca Chasma and the Wispy Terrain are much greater than the estimated regolith thicknesses for Tethys and Dione, respectively. Although nearly all analyzed fault slopes in these regions are below the angle of repose, the height data of these fault slopes indicate that regolith deposition is an unlikely explanation for the shallow fault slopes measured in these study areas.

Unlike the results for Ithaca Chasma and the Wispy Terrain, the heights of the analyzed fault slopes of Avaiki Chasmata are comparable to the estimated regolith thickness on Rhea. About half of the analyzed fault slopes exhibit a lesser height than the estimated regolith thickness, while the other half exhibits a greater height. Additionally, the measured fault slopes of Avaiki Chasmata are below the maximum angle of repose.

Thus, although regolith deposition may have contributed to the shallow fault slopes of the smaller faults, regolith deposition cannot not explain the shallow fault slopes of all analyzed faults in this study area. Because regolith deposition does not sufficiently explain the presence of all shallow fault slopes within Avaiki Chasmata, and does not explain any of the faults within Ithaca Chasma or the Wispy Terrain, we do not find that it is a robust explanation for the presence of shallow fault slopes on these bodies.

Mass wasting along scarp faces is another possible modifier of fault slopes (e.g., Blackwelder, 1928; Moore et al., 2009; Burbank and Anderson, 2011). If enough mass wasting has taken place, a fault scarp may be completely covered by locally derived regolith that sits at or below the angle of repose (e.g., Blackwelder, 1928; Burbank and Anderson, 2011). Mass wasting has not been well-studied on Tethys, Rhea or Dione, although it has been inferred on other icy satellites including Europa (e.g., Moore et al., 1996, 1999; Head et al., 1999), Ganymede (e.g., Prockter et al., 1998; Moore et al., 1999), Callisto (e.g., Moore et al., 1999; Chuang and Greeley, 2000), Iapetus (Singer et al., 2012), Miranda (Pappalardo et al., 1997), and Triton (Smith et al., 1989; Moore et al., 1996). On these satellites, evidence for mass wasting include the presence of smooth, semicircular to tongue-shaped lobes of material at the base of slopes. These lobes are estimated to be only tens of meters thick on these satellites (Moore et al., 1999; Chuang and Greeley, 2000), and to average 90 m thick at the bases of highly eroded slopes on Callisto (Chuang and Greeley, 2000).

Inspection of high resolution Cassini ISS images reveals that semicircular and tongue-shaped lobes of material are also present at the base of some slopes on Tethys (Figure II-18a), Rhea (Figure II-18b), and Dione (Figure II-18c). However, these slopes with lobate deposits are confined to crater walls and the talus is not observed to extend up the walls. The lobate mass wasting features are not identifiable in larger scale, lower resolution images of these satellites, including the images used to analyze faults within

the three study areas (Table II-2). This lack of observable lobate features at the bases of analyzed fault slopes in low resolution imagery of Tethys, Rhea, and Dione suggest that mass wasting features only exist at small scales. Because these deposits are not sufficient to cover the fault slopes analyzed, they would not significantly influence our fault slope measurements. In addition, the estimated thicknesses for lobate features on other icy satellites, including the highly eroded surface of Callisto, are only tens of meters, much smaller than the kilometer scale fault slopes analyzed in this work. Thus, we conclude that regolith deposition across fault scarps from mass wasting is an unlikely explanation for the shallow fault slopes in all three study areas.

Viscous Relaxation

Viscous relaxation reduces stresses associated with topographic relief by reducing topography over time (Scott, 1967; Parmentier and Head, 1981; Passey and Shoemaker, 1982; Thomas and Schubert, 1988). Over geologic timescales, viscous relaxation acts to subdue topographic features (e.g., Grimm and Solomon, 1988; Brown and Grimm, 1996; Melosh, 1976) and shallow slopes (Heiskanen and Venig Meinesz, 1958; Spencer, 1984; Buck, 1988; Wernicke and Axen, 1988; Hamilton, 1988).

Viscous relaxation is evidenced by the morphology of ancient impact craters on the surfaces of Tethys (e.g., Schenk, 1989; Schenk and Moore, 2007), Rhea (Schenk, 1989; White et al., 2013), and Dione (Schenk, 1989; Moore et al., 2004; Schenk and Moore, 2007). Before viscous relaxation-related modification takes place, fresh impact craters exhibit depth-diameter ratios that are consistent across the surface of a single body (e.g., *Schenk*, 1991, 2002). However, some craters on the surfaces of Tethys, Rhea, and Dione exhibit smaller depth-diameter ratios. These observations are indicative of crater floor uplift resulting from viscous relaxation. Because noticeable topographic alteration of impact craters via viscous relaxation has been documented on Tethys, Rhea, and Dione, viscous relaxation may have also affected normal fault topography and geometries within Ithaca Chasma, Avaiki Chasmata, and the Wispy Terrain.

Impact craters with larger diameters undergo viscous relaxation at a faster rate than smaller diameter craters (e.g., Cathles, 1975), causing the floors of larger impact craters to uplift faster than those of smaller craters (Solomon et al., 1982). As a result, this activity causes larger impact craters to exhibit smaller depth-diameter ratios than smaller impact craters of the same age. However, the diameter of a sub-circular impact crater affects the rate of viscous relaxation quite differently than the width of a sub-linear graben, as shown by equations derived in Cathles (1975).

Additional evidence for viscous relaxation exists in the form of raised rims bounding both Ithaca Chasma and Avaiki Chasmata. Viscous relaxation can lead to rim uplift if the rims of the rift system are also affected (Karner et al., 2000). The cause of rim uplift is depth-dependent stretching of the lithosphere where the brittle portion of the lithosphere is extended more locally than the underlying ductile portion of the lithosphere (Royden and Keen, 1980; Rowley and Sahagian, 1986). In other words, ductile extension in the subsurface occurs over a larger area than the fault controlled brittle extension in the

near surface, leading to uplift of the rift system flanks (Royden and Keen, 1980; Rowley and Sahagian, 1986).

The raised rim (also called a rift-flank) of Ithaca Chasma on Tethys was analyzed in previous studies (e.g., Smith et al., 1981; Giese et al., 2007). As summarized in Giese et al. (2007), the uplifted rim of Ithaca Chasma is up to 6 km higher than the surrounding terrain. The high topography and concave-up geometry of the Ithaca Chasma's rims are indicative of flexural uplift of the foot wall resulting from unloading of the lithosphere and consequent viscous relaxation (e.g., Weissel and Karner, 1989; Braun and Beaumont, 1989; Brink and Stern, 1992; Mark et al., 2014).

We also analyze and quantify the raised rims along all fault scarps analyzed within Ithaca Chasma. This analysis shows that, in addition to Ithaca Chasma, Avaiki Chasmata exhibits raised rims (Table II-7). Unlike Ithaca Chasma and Avaiki Chasmata, the horst block of the fault within Padua Chasmata of Dione's Wispy Terrain does not appear to have a raised rim. Upon examining all profile lines generated on the DEM across Scarps A, B, C, and D within the Wispy Terrain, the profile lines do not show evidence for positive topography between the fault scarps and the surrounding terrain for the region around any of the analyzed scarps. However, the vertical accuracy and horizontal resolution of the DEM covering Dione's Wispy Terrain may be too coarse, relative to the scale of the faults, to show that evidence of this feature.

The average raised rim height of Ithaca Chasma from our DEM is ~1.4 km, while the maximum rim height measured is ~5.6 km above the surrounding terrain (Table II-7 and Figure II-19). The raised rim height of Avaiki Chasmata on Rhea is smaller than that of Ithaca Chasma. The average height along the analyzed scarps of this fault system is ~590 m and the maximum rim height is ~1.8 km. The presence of these large raised rims and relaxed impact craters supports the interpretation that viscous relaxation played a role in the formation of the shallow fault slopes on Tethys and Rhea.

Model Tests for Shallow Fault Slope Formation by Viscous Relaxation

To further investigate the possible role of viscous relaxation for forming shallow fault slopes in each study area, we consider the estimated ages for each study areas and use basic geophysical modeling.

Calculation Methods

Viscous relaxation magnitude estimates for a set of faults can be quantified from their geometries, the ages of the fault systems, and the material properties of the satellite's lithospheres. As discussed in Cathles (1975), the simplest model is a half space of uniform viscosity η, uniform density ρ, and a uniform gravitational acceleration g. For initial topography, the initial height of a scarp, h_0, that is two-dimensional and regularly spaced, is given by

$$h_0 = h_t e^{\left(\frac{t}{\tau}\right)}, \quad \text{(II-4)}$$

where

$$\tau = \frac{4\pi\eta}{\rho g \lambda}, \quad \text{(II-5)}$$

and where h_t is the height of the fault scarp at $t > 0$, t is the age of the fault, η is the viscosity of the ice, and λ is the width of the graben.

The initial fault dip formed at $t = 0$, $\Theta_{0,}$ is given, in degrees, by

$$\Theta_{0,degrees} = \left|\arctan\left(\frac{h_0}{w}\right)\frac{180°}{\pi}\right|, \quad \text{(II-6)}$$

where w is the width of the scarp, assuming that w, when $t > 0$, is approximately equal to w for $t = 0$.

For the near-surface icy lithospheres of all three study areas, the density, ρ, is taken to be 930 kg m^{-3}. Values for gravitational acceleration, g, are 0.145 m s^{-2} for Tethys, 0.264 m s^{-2} for Rhea, and 0.232 m s^{-2} for Dione (Table II-8). The values for t are taken from age estimates given for Ithaca Chasma (t = 0.4 Ga, t = 3.3 Ga, and t = 4.0 Ga) (Giese et al., 2007), inferred for Avaiki Chasmata based on the estimated ages of the cratered plains which are cut by the chasmata (t < 3.6 Ga and t < 4.2 Ga) (Wagner, 2007), and given for Dione's Wispy Terrain (t > 1 Ga and t > 3.7 Ga) (Wagner et al., 2006) (Table II-8).

We quantify λ, w, and h_t, for each scarp mapped in each study area (Figure II-20). We measure λ by averaging the distance between the top of a scarp and the top of the adjacent, oppositely dipping normal fault scarp that frames the graben for each profile line across that scarp. We estimate w of each scarp by measuring the average horizontal distance across each scarp face in each profile line. Similarly, we derive h_t by averaging the vertical height of each scarp face in each profile line.

The effective viscosity for a material is given by

$$\eta = \left(\frac{d^p}{A}\right)\sigma_{diff}^{1-n}\exp\left(\frac{Q}{RT_Z}\right), \quad \text{(II-7)}$$

where d is the grain size, p, A, and n are empirical constants, σ_{diff} is the differential stress, Q is the activation energy of creep, R = 8.3145 J mol^{-1} K^{-1} is the gas constant, and T_z is the temperature at the base of the satellite's lithosphere (Turcotte and Schubert, 2014).

The grain size of the upper icy lithospheres of Tethys, Rhea, and Dione is unknown, so we use multiple grain sizes for our calculations. We set the smallest grain size used to the smallest estimated grain size for Europa's lithosphere (Geissler et al., 1998; Ruiz, 2005), and then consider grain sizes with an increase of up to two orders of magnitude: d = 0.1 mm, d = 1 mm, and d = 10 mm. The values for σ_{diff} on the surfaces of Tethys, Rhea, and Dione are also unknown, so a range of values are used in our calculations spanning three orders of magnitude. Convection is possible within Tethys, Dione, and Rhea (e.g., Multhaup and Spohn, 2007), so we use the estimated range of σ_{diff} typical of convection on icy satellites (10^{-4}-10^{-3} MPa) (Tobie et al., 2003) as minimum values in our calculations. These satellites may have exhibited higher eccentricities in the

past, and tidal stresses may have been important (e.g. Chen and Nimmo, 2008; Meyer and Wisdom, 2008). To cover all differential stress values possible on icy satellites, the estimated range of σ_{diff} typical of tidal stress for icy satellites (0.01-0.1 MPa) is used as maximum values in our calculations.

Superplastic flow is the dominant creep mechanism for H_2O ice I with grain sizes of d = 0.1 mm and 1 mm, and dislocation creep is dominant when d > 1 mm (McKinnon, 1999; Durham et al., 2001). Q is dependent on the type of deformation that occurs. For superplastic flow, Q = 49 kJ mol^{-1}, A = 3.9 x 10^{-3} MPa^{-n} m^{p} s^{-1}, p = 1.4, and n = 1.8 (Goldsby and Kohlstedt, 2001). For dislocation creep Q = 61 kJ mol^{-1}, A = 1.26 x 10^{5} MPa^{-n}, p = 0 and n = 4 (Durham and Stern, 2001).

T_z is given by

$$T_z = T_s e^{\frac{F z}{k_0}}, \qquad \text{(II-8)}$$

where T_S is the surface temperature, F is the heat flux, z is the lithospheric thickness, and k_0 = 567 W m^{-1} is the coefficient describing the temperature dependence of the thermal conductivity of H_2O ice I (Turcotte and Schubert, 2014). Given the derived values for surface temperatures across these icy bodies the surface temperatures may vary by several degrees over the study areas. This few percent variance in surface temperature would produce a relatively small effect on viscosity (see Equation II-7). Potentially higher surface temperatures in the base are unknown to us. Thus, for this work, we use the average reported surface temperatures for either the Saturn-facing or trailing hemispheres as appropriate. These values are T_s = 87 K for Tethys (Hanel et al., 1982), and the average trailing hemisphere temperatures of 88 K for Rhea (Cruikshank et al., 1984), and 90 K for Dione (Cruikshank et al., 1984) (Table II-8). Estimates for F range from 18 – 30 mW m^{-2} for Tethys (Giese et al., 2007; Chen and Nimmo, 2008), 15 – 30 mW m^{-2} for Rhea (Nimmo et al., 2010; White et al., 2013), and 24 – 90 mW m^{-2} for Dione (Hammond et al., 2013; Phillips, 2014) (Table II-8).

Estimates for z range from 16 – 20 km on Tethys (Giese et al., 2007) and 15 – 28 km on Dione (Forni et al., 1991) (Table II-8). Because z of Rhea has not been estimated, we use the range of estimated elastic thicknesses for Rhea to represent a minimum lithospheric thickness. These estimates range from 5 – 10 km (Nimmo et al., 2010, 2011). Using the estimated range of elastic thicknesses for z will yield minimum magnitudes for the slope changes as shown in Equations II-4 through II-8, and because the elastic thickness of a satellite is never greater than the lithospheric thickness. As shown by the relationship between z and T_Z in Equation II-8, the elastic thickness will give a minimum value for $T_{Z,}$ giving a maximum value for η in Equation II-7, resulting in a minimum value for h_0 in Equation II-4, and so yielding a minimum value for Θ_0 in Equation II-6. If calculation results using elastic thicknesses show viscous relaxation is a viable cause for the observed fault slopes, this result would hold true if the greater values for lithospheric thickness were known and used instead. The calculation results of viscosities of each satellite are shown in Table II-9.

To investigate the possible role of viscous relaxation in modifying scarps in the study areas, Θ_0 for one scarp in each area is calculated. Results of calculations are only

needed for one scarp in each study area to determine if viscous relaxation is a viable explanation for the observed shallow fault slopes. Using Equation II-6, Θ_0 of Scarp A of Ithaca Chasma on Tethys, and Θ_0 of Scarp A of Avaiki Chasmata on Rhea is calculated. We calculate Θ_0 of Scarp D of Padua Chasmata of Dione's Wispy Terrain, since this was the only scarp with a shallow fault slope identified in this study area.

Calculation Results

The calculation results show that viscous relaxation may account for the shallow fault slopes of the analyzed faults in all three study areas (Table II-9 and Figure II-21). The fault slope, Θ_t, for Scarp A within Ithaca Chasma on Tethys is 15° ± 3°. As shown in Figure II-21a, for $\eta = 1.0 \times 10^{23}$ Pa s, Θ_0 for this scarp could have been as steep as ~37° during fault formation if the fault system is 3.3 Ga, or as steep as ~42° if the fault system is 4.0 Ga. With a lower viscosity of $\eta = 1.0 \times 10^{22}$ Pa s, this fault could have been as steep as ~42° if the fault system is only 0.4 Ga, or 90° if the fault system is either 3.3 Ga or 4.0 Ga. For $\eta = 1.0 \times 10^{14}$ Pa s, Θ_0 could have been 90° for all estimated ages of Ithaca Chasma. On the other hand, for $\eta \geq 1.0 \times 10^{24}$ Pa s, Θ_0 would not have increased above ~17° for any age estimated for this fault system.

For Scarp A within Avaiki Chasmata on Rhea, Θ_t is 32° ± 3°. As shown in Figure II-21b, for $\eta = 1.0 \times 10^{23}$ Pa s, Θ_0 for this scarp could have been ~56° or ~60° if the age of Avaiki Chasmata is 3.6 Ga or 4.2 Ga respectively. For $\eta \leq 1.0 \times 10^{22}$ Pa s, Θ_0 could have been 90° for either estimated age of Avaiki Chasmata. Otherwise, for $\eta \geq 1.0 \times 10^{24}$ Pa s, Θ_0 would not have increased above ~34° for either estimated fault system age.

For Scarp D within Padua Chasmata of Dione's Wispy Terrain, Θ_t is 23° ± 13°. If $\eta = 1.0 \times 10^{22}$ Pa s, Θ_0 of this scarp could have been ~35° or 90° if the faults were 1 Ga or 3.7 Ga respectively (Figure II-21c). Instead, if $\eta \leq 1.0 \times 10^{21}$ Pa s, Θ_t could have been 90° for both estimated ages of the Wispy Terrain. If $\eta \geq 1.0 \times 10^{23}$ Pa s, Θ_0 would not have exceeded ~27° for either estimated fault system age.

In summary, we find that viscous relaxation can account for the shallow fault slopes of faults within Ithaca Chasma, Avaiki Chasmata, and Padua Chasmata of the Wispy Terrain. For the fault scarps analyzed, Θ_0 falls within the dip range inferred from laboratory experiments (45° to 59°) when 1.0×10^{22} Pa s $\leq \eta \leq 1.0 \times 10^{23}$ Pa s, for all three study areas. For Ithaca Chasma and Avaiki Chasmata, Θ_0 may have been up to 90° if $\eta = 1.0 \times 10^{22}$ Pa s and the faults are 4.0 Ga and 3.7 Ga respectively. Our results follow a purely viscous formulation, although elastic and plastic effects, under conditions of high heat flow, would cause greater amounts of relaxation (e.g., Dombard and McKinnon, 2006).

Discussion and Implications

Of all the possible drivers known to reduce fault slopes, we find that viscous relaxation is the most viable explanation for the shallow fault slopes in all three study

areas. Our modeling shows that sufficient relaxation could have taken place to account for the observed shallow fault slopes in the study areas. Additional support for viscous relaxation includes the presence of raised rims of Ithaca Chasma and Avaiki Chasmata and relaxed impact craters on Tethys, Dione, and Rhea. Based on these three positive pieces of evidence, we consider viscous relaxation to be the most viable explanation for the observed shallow fault slopes in all three study areas.

If viscous relaxation did shallow the analyzed fault slopes, then Tethys, Rhea, and Dione must have experienced significant global heating events during their histories, because viscous relaxation is dependent on a high heat flux (Consolmagno, 1985; Schenk, 1989; Nimmo et al., 2010; White et al., 2013). The present day shallow fault slopes in each study area would have initially formed with steep dips controlled by μ_i of lithospheric H_2O ice, but subsequently underwent a period of enhanced satellite heating with associated relaxation. Short-lived radionuclide-induced heating events have been suggested to have created heat pulses with peak internal heating and melting at 4.0, 3.1, and 4.1 Ga within Tethys, Rhea, and Dione, respectively (Table II-10) (Consolmagno, 1985). Following these peak melting events, Tethys and Dione likely refroze around 3.4 and 2.1 Ga respectively, while Rhea is likely still not completely frozen (Consolmagno, 1985).

The maximum estimated age of Ithaca Chasma (4.0 Ga), both the minimum and maximum estimated ages of Avaiki Chasmata (3.6 and 4.2 Ga), and the maximum estimated age of the Wispy Terrain (> 3.7 Ga) suggest that the fault formation events pre-date or were concurrent with the estimated peak internal heating and melting events of their respective satellites (Table II-10). These timing relationships show that geometries of faults within all three study areas could have been readily modified by viscous relaxation during these heating events, when the heat flux was the highest.

The variation in measured fault slopes of faults between Palatine and Padua Chasmata within the Wispy Terrain may reflect a series of tectonic events that occurred at different times throughout Dione's history so that viscous relaxation had a more noticeable effect on the older faults than the younger faults. This interpretation is supported by the observation that the shallow fault slope identified within Padua Chasmata trends at a noticeably different azimuth than the three faults with steeper fault slopes analyzed in Palatine Chasmata, and is spatially separated (by ~200 km) from these faults.

Perhaps some Wispy Terrain faults are > 3.7 Ga, and have undergone viscous relaxation during the peak melting event of Dione, while others formed after this event, and have not undergone much viscous relaxation. If portions of the Wispy Terrain postdate this heating event, then some normal faults in this study area exhibit dips that reflect μ_i of Dione's lithospheric ice. Using Equation II-3, we find that the three analyzed faults with steep fault slopes (Table II-3) indicate that $0 \leq \mu_i \leq 0.73$ for Dione's lithospheric H_2O ice. These results are similar to those inferred from laboratory deformation experiments of cryogenic H_2O ice, which show that $0 \leq \mu_i \leq 0.55$ (Table II-1).

Although mass wasting may have contributed to the shallowing of scarp slopes, the results of this work suggest that viscous relaxation has had a substantial effect on

fault geometries within Ithaca Chasma on Tethys, Avaiki Chasmata on Rhea, and the Wispy Terrain on Dione. Viscous relaxation may have also affected fault geometries on other icy satellites.

Summary

In this study, we investigate the hypothesis that inferred normal fault dips from laboratory deformation experiments of H_2O ice I at conditions comparable to icy satellite lithospheres, are reflected in the natural setting. Results of H_2O ice I deformation experiments at cryogenic temperatures and small strain rates, most comparable to those expected in the lithospheres of outer solar system icy satellites, imply that normal fault dips should range from 45° to 59°. However, we find that many natural normal fault slopes in these study areas are much shallower than expected. In the regions of Ithaca Chasma on Tethys, and Avaiki Chasmata on Rhea, none of the analyzed normal faults exhibit fault slopes that fall within the laboratory derived dip range. Within Dione's Wispy Terrain, the analyzed faults of Palatine Chasmata exhibit fault slopes that fall within this range, while only one fault in Padua Chasmata, has a fault slope that falls below this range. Our hypothesis is supported for the Wispy Terrain, but is not supported for Ithaca Chasma or Avaiki Chasmata. The steepest analyzed faults in the Wispy Terrain indicate that the range of μ_i for Dione's lithospheric H_2O ice is similar to values derived for cryogenic H_2O ice in laboratory deformation experiments. Our results provide evidence that viscous relaxation is the most viable explanation for the shallow fault slopes in all three study areas. This evidence includes the relaxed impact craters identified on Tethys, Rhea, and Dione in previous work, and raised rims exhibited by Ithaca Chasma and Avaiki Chasmata. In addition, our calculation results show that viscous relaxation can explain the observed shallow scarp slopes in all three study areas.

The variation in measured fault slopes within Dione's Wispy Terrain may reflect a series of tectonic events sufficiently different in time so that viscous relaxation had a more noticeable effect on the older fault scarps than the younger fault scarps. To further investigate the timing between Wispy Terrain faults, future studies should explore cross-cutting relations of faults and crater age dating of different regions of the Wispy Terrain.

The steepest analyzed faults of Palatine Chasmata within the Wispy Terrain indicate that the range of μ_i for Dione's lithospheric H_2O ice is similar to values derived for cryogenic H_2O ice in laboratory deformation experiments. Viscous relaxation has had a substantial effect on fault geometries of Ithaca Chasma on Tethys, Avaiki Chasmata on Rhea, and the Wispy Terrain on Dione. Future work involving analysis of fault geometry should use caution, since viscous relaxation may have also affected ancient fault systems on other icy satellites.

Acknowledgements

We express gratitude to Annie Howington-Kraus and Ra'ad Saleh for their contribution to the production of SOCET SET DEMs, and to Joshua Emery and Liem Tran for insightful and constructive feedback. We also express gratitude to the National Aeronautics and Space Administration (NASA) and the Cassini Mission team for the Cassini ISS data.

References

Anderson, E. M. (1905), The dynamics of faulting, *Transactions of the Edinburgh Geological Society 8*(3), 387-402, doi:10.1144/transed.8.3.387.

Anderson, E. M. (1942), The dynamics of faulting and dyke formation with application to Britain, *Edinburgh, Oliver and Boyd, 191*.

Anderson, E. M. (1951). The Dynamics of Faulting and Dyke Formation with Application to Britain, *(2nd edn) Oliver and Boyd, Edinburgh*.

Anderson, J. A., S. C. Sides, D. L. Soltesz, T. L. Sucharski, and K. J. Becker (2004), Modernization of the integrated software for imagers and spectrometers, paper presented at *Lunar Planet. Sci. 35*, 2039, The Woodlands.

Atwood-Stone, C., and A. S. McEwen. (2013), Avalanche slope angles in low-gravity environments from active Martian sand dunes, *Geophysical Research Letters*, 40(12), 2929-2934, doi:10.1002/grl.50586.

Axen, G. J. (1992), Pore pressure, stress increase, and fault weakening in low-angle normal faulting, *J. Geophys. Res. 97*, 8979-8991, doi:10.1029/92JB00517.

Barr, A. C. (2008), Mobile lid convection beneath Enceladus' south polar terrain, *J. of Geophys. Res. Planets (1991–2012)*, *113*(E7), doi:10.1029/2008JE003114.

Beddingfield, C. B., D. M. Burr, and J. P. Emery (2015), Fault geometries on Uranus' satellite Miranda: Implications for internal structure and heat flow, *Icarus*, *247*, 35-52, doi:10.1016/j.icarus.2014.09.048.

Beeman, M., W. B. Durham, and S. H. Kirby (1988), Friction of ice, *J. of Geophys. Res. Solid Earth*, *93*(B7), 7625-7633, doi:10.1029/JB093iB07p07625.

Blackwelder, E. (1928), The recognition of fault scarps, *Geology 36(4)*, 289-311.

Braun, J., and C. Beaumont (1989), A physical explanation of the relation between flank uplifts and the breakup unconformity at rifted continental margins, *Geology*, *17.8*, 760-764, doi:10.1130/0091-7613(1989)017.

Brink, U., and T. Stern (1992), Rift flank uplifts and hinterland basins: comparison of the Transantarctic Mountains with the Great Escarpment of southern Africa, *J. of Geophys. Res. Solid Earth*, 97.*B1*, 569-585, doi:10.1029/91JB02231.

Brown, C. D., and R. E. Grimm (1996), Floor subsidence and rebound of large Venus craters. *J. of Geophys. Res. Planets*, *101*(E11), 26057-26067, doi:10.1029/96JE02706.

Bruesch, L. S., and E. Asphaug (2004), Modeling global impact effects on middle-sized icy bodies: Applications to Saturn's moons, *Icarus*, *168*(2), 457-466, doi:10.1016/j.icarus.2003.11.007.

Buck, W. R. (1988), Flexural rotation of normal faults, *Tectonics*, *7*, 959–973, doi:10.1029/TC007i005p00959.

Buck, W. R. (1991), Modes of continental lithospheric extension, *J. of Geophys. Res. Solid Earth 96*(B12), 20161-20178.

Buck, W. R., L. L. Lavier, and A. N. Poliakov (2005), Modes of faulting at mid-ocean ridges.
Nature 434(7034), 719-723, doi:10.1029/91JB01485.

Buratti, B. J., M. D. Hicks, K. A. Tryka, M. S. Sittig, and R. L. Newburn (2002), High-resolution 0.33–0.92 μm spectra of Iapetus, Hyperion, Phoebe, Rhea, Dione, and D-type asteroids: How are they related?, *Icarus*, *155*(2), 375-381, doi: 10.1006/icar.2001.6730.

Burbank, D. W., and R. S. Anderson (2011), Tectonic geomorphology, *John Wiley & Sons*, Hoboken.

Byerlee, J. (1978), Friction of rocks, Pure and Applied Geophysics, 615–626, Springer.

Carrigy, M. (1970), Experiments on the angles of repose of granular materials, *Sedimentology, 14*, 147–158, doi: 10.1111/j.1365-3091.1970.tb00189.x.

Cathles, L. M. (1975), *The viscosity of the Earth's mantle*, 386, Princeton University Press, Princeton.

Chen, E. M. A., and F. Nimmo (2008), Implications from Ithaca Chasma for the thermal and orbital history of Tethys, *Geophys. Res. Lett., 35(19), L19203*, doi: 10.1029/2008GL035402.

Clark, R. N., J. M. Curchin, R. Jaumann, D. P. Cruikshank, R. H. Brown, T. M. Hoefen, K. Stephan, J. M Moore, B. J. Buratti, and K. H. Baines (2008), Compositional mapping of Saturn's satellite Dione with Cassini VIMS and implications of dark material in the Saturn system, *Icarus 193*(2), 372-386, doi:10.1016/j.icarus.2007.08.035.

Collins, G. C., J. W. Head, and R. T. Pappalardo (1998), Formation of Ganymede grooved terrain by sequential extensional episodes: Implications of Galileo observations for regional stratigraphy, *Icarus 135*(1), 345-359, doi:10.1006/icar.1998.5978.

Collins G. C., W. B. McKinnon, J. M. Moore, F. Nimmo, R. T. Pappalardo, L. M. Prockter, P. M. Schenk (2009), Tectonics of the outer planet satellites. In Schultz RA, Watters TR (eds) Planetary tectonics, 264–350, Cambridge University Press, Leiden.

Consolmagno, G. J. (1985), Resurfacing Saturn's satellites: Models of partial differentiation and expansion, *Icarus* 64.3, 401-413, doi:10.1016/0019-1035(85)90064-8.

Croft, S., and L. Soderblom (1991), Geology of the Uranian satellites, Uranus, 561-628, University of Arizona Press, Tucson.

Cruikshank, D. P., J. Veverka, and L. A. Lebofsky (1984), Satellites of Saturn-Optical properties, *Saturn*, *1*, 640-667, University of Arizona Press, Tucson.

Cruikshank, D. P., T. C. Owen, D. Dalle Ore, T. R. Geballe, T. L. Roush, C. de Bergh, S. A. Sandford, F. Poulet, G. K. Benedix, J. P. Emery (2005), A spectroscopic study of the surfaces of Saturn's large satellites: H_2O ice, tholins, and minor constituents, *Icarus, 175*, 268-283, doi:10.1016/j.icarus.2004.09.003.

Chuang, F. C., and R. Greeley (2000), Large mass movements on Callisto. *J. Geophys. Res. Planets*, *105*(E8), 20227-20244, doi:10.1029/2000JE001249.

Davis, G. H. (1983), Shear-zone model for the origin of metamorphic core complexes, *Geology 11*, 342-347, doi:10.1130/0091-7613(1983)11.

Dombard, A. J., and W. B. McKinnon (2006), Elastoviscoplastic relaxation of impact crater topography with application to Ganymede and Callisto, *Journal of Geophysical Research: Planets, 111*(E1), doi: 10.1029/2005je002445.

Durham, W. B., H. C. Heard, and S. H. Kirby (1983), Experimental deformation of polycrystalline H_2O ice at high pressure and low temperature: Preliminary results, *J. Geophys. Res. Solid Earth*, *88*(S01), B377-B392, doi:10.1029/JB088iS01p0B377.

Durham, W. B., S. H. Kirby, and L. A. Stern (1997). Creep of water ices at planetary conditions: A compilation, *Journal of Geophys. Res. Planets*, *102*(E7), 16293-16302, doi:10.1029/97JE00916.

Ellsworth, K., and G. Schubert (1983), Saturn's icy satellites: Thermal and structural models. *Icarus* 54(3), 490-510, doi:10.1016/0019-1035(83)90242-7.

Emery, J. P., D. M. Burr, D. P. Cruikshank, R. H. Brown, and J. B. Dalton (2005), Near-infrared (0.8–4.0 μm) spectroscopy of Mimas, Enceladus, Tethys, and Rhea, *Astron. Astrophys*, *435*, 353-362, doi:10.1051/0004-6361:20042482.

Forni, Olivier, Angioletta Coradini, and Costanzo Federico (1991), Convection and lithospheric strength in Dione, an icy satellite of Saturn, *Icarus, 94(1)*: 232-245, doi:10.1016/0019-1035(91)90153-K.

Fossen, Haakon (2010), *Structural geology*, Cambridge University Press, Cambridge.

Geissler, P., R. Greenberg, G. Hoppa, A. McEwen, R. Tufts, C. Phillips, B. Clark, M. Ockert-Bell, P. Helfenstein and J. Burns (1998), Evolution of lineaments on Europa: Clues from Galileo multispectral imaging observations, *Icarus 135*(1): 107-126, doi:10.1006/icar.1998.5980.

Giese, B., R. Wagner, G. Neukum, P. Helfenstein, and C. C. Porco (2006), Topographic features of Ithaca Chasma, Tethys, paper presented at *Lunar Planet. Sci. 37*, 1749, The Woodlands.

Giese, B., R. Wagner, G. Neukum, P. Helfenstein, P. C. Thomas (2007), Tethys: Lithospheric thickness and heat flux from flexurally supported topography at Ithaca Chasma, *Geophys. Res. Lett.*, *34*(21), doi: 10.1029/2007GL031467.

Greenberg, R., S. Croft, D. Janes, J. Kargel, L. Lebofsky, J. Lunine, R. Marcialis, H. Melosh, G. Ojakangas and R. Strom (1991), Miranda, Uranus, 693-735, University of Arizona Press, Tucson.

Greenberg, R., P. Geissler, G. Hoppa, B. R. Tufts, D. D. Durda, R. Pappalardo, J. W. Head, R. Greeley, R. Sullivan, and M. H. Carr (1998), Tectonic processes on Europa: Tidal stresses, mechanical response, and visible features, *Icarus 135(1)*, 64-78, doi:10.1006/icar.1998.5986.

Grimm, R. E., and S. C. Solomon (1988), Viscous relaxation of impact crater relief on Venus: Constraints on crustal thickness and thermal gradient, *J. Geophys. Res. Solid Earth*, *93*(B10), 11911-11929, doi:10.1029/JB093iB10p11911.

Hamilton, W. (1988), Detachment faulting in the Death Valley region, California and Nevada, *U.S. Geol. Surv. Bull., 1790*, 51-85.

Hammond, N. P., C. B. Phillips, F. Nimmo, and S. A. Kattenhorn (2013), Flexure on Dione: Investigating subsurface structure and thermal history, *Icarus, 223*(1), 418-422, doi:10.1016/j.icarus.2012.12.021.

Hanel, R., B. Conrath, F. Flasar, V. Kunde, W. Maguire, J. Pearl, J. Pirraglia, R. Samuelson, D. Cruikshank and D. Gautier (1982), Infrared observations of the Saturnian system from Voyager 2, *Science 215*(4532), 544-548, doi:10.1126/science.215.4532.544.

Head, J. W., and R. T. Pappalardo (1999), Brine mobilization during lithospheric heating on Europa: Implications for formation of chaos terrain, lenticula texture, and color variations, *J. Geophys. Res. Planets, 104*(E11), 27143-27155, doi:10.1029/1999JE001062.

Head, J. W., R. T. Pappalardo, and R. Sullivan (1999), Europa: Morphological characteristics of ridges and triple bands from Galileo data (E4 and E6) and assessment of a linear diapirism model, *J. of Geophys. Res. Planets* 104.E10, 24223-24236, doi:10.1029/1998JE001011.

Heiskanen, W. A., and F. A. Vening-Meinesz (1958), The Earth and its Gravity Field, *McGraw-Hill*, New York.

Helfenstein, P., and Parmentier E. M. (1983), Patterns of fracture and tidal stresses on Europa, *Icarus*, *53*(3), 415-430, doi:10.1016/0019-1035(83)90206-3.

Helfenstein, P., and E. M. Parmentier (1985), Patterns of fracture and tidal stresses due to nonsynchronous rotation: Implications for fracturing on Europa, *Icarus*, *61*(2), 175-184, doi:10.1016/0019-1035(85)90099-5.

Hillier, J., and Squyres, S. W. (1991), Thermal stress tectonics on the satellites of Saturn and Uranus, *Journal of Geophysical Research: Planets*, *96*(E1), 15665-15674, doi:10.1029/91JE01401.

Hoppa, G., B. R. Tufts, R. Greenberg, and P. Geissler (1999), Strike–slip faults on Europa: Global shear patterns driven by tidal stress, *Icarus*, *141*(2), 287-298, doi:10.1006/icar.1999.6185.

Howard, A. D., J. M. Moore, P. M. Schenk, O. L. White, and J. Spencer (2012), Sublimation-driven erosion on Hyperion: Topographic analysis and landform simulation model tests, *Icarus*, *220*(1), 268-276, doi:10.1016/j.icarus.2012.05.013.

Hurford, T. A., R. A. Beyer, B. Schmidt, B. Preblich, A. R. Sarid, and R. Greenberg (2005), Flexure of Europa's lithosphere due to ridge-loading, *Icarus*, *177*(2), 380-396, doi:10.1016/j.icarus.2005.06.019.

Hussmann, H., F. Sohl, and T. Spohn (2006), Subsurface oceans and deep interiors of medium-sized outer planet satellites and large trans-neptunian objects, *Icarus*, *185*(1), 258-273, doi:10.1016/j.icarus.2006.06.005.

Jackson, J. A., N. J. White, Z. Garfunkel, H. Anderson (1988), Relations between normal-fault geometry, tilting and vertical motions in extensional terrains: an example from the southern Gulf of Suez, *Journal of Structural Geology*, *10*(2), 155-170, doi:10.1016/0191-8141(88)90113-7.

Jaeger, J. and N. Cook (1979), Fundamentals of rock mechanics, *Chapman & Hall*, London.

Kargel, J. S., and R. G. Strom (1990), Cryovolcanism on triton, paper presented at Lunar Planet. Sci., 21, 599, The Woodlands.

Karner G, B. Byamungu, C. Ebinger, A. Kampunzu, R. Mukasa, J. Nyakaana, E. Rubondo, N. Upcott (2000), Distribution of crustal extension and regional basin architecture of the Albertine rift system, East Africa, *Marine and Petroleum Geology, 17*, 1131–1150, doi:10.1016/S0264-8172(00)00058-1.

Kennedy, F. E., E. M. Schulson, and D. E. Jones (2000), The friction of ice on ice at low sliding velocities, *Philosophical Magazine A. 80*(5), 1093-1110, doi:10.1080/01418610008212103.

Kirk, R. L., and D. J. Stevenson (1987), Thermal evolution of a differentiated Ganymede and implications for surface features, *Icarus*, *69*(1), 91-134, doi:10.1016/0019-1035(87)90009-1.

Kirk, R. L., E. Howington-Kraus, B. Redding, D. Galuszka, T. M. Hare, B. A. Archinal, L. A. Soderblom, and J. M. Barrett (2003), High-resolution topomapping of candidate MER landing sites with Mars Orbiter Camera narrow-angle images. *J. Geophys. Res. Planets, 108*(E12), 713-722, doi:10.1029/2003JE002131.

Kleinhans, M. G., H. Markies, S. J. De Vet, and F. N. Postema (2011), Static and dynamic angles of repose in loose granular materials under reduced gravity, *J. Geophys. Res. Planets (1991–2012), 116*(E11), doi:10.1029/2011JE003865.

Leith, A. C., and W. B. McKinnon (1996), Is there evidence for polar wander on Europa?, *Icarus, 120*(2), 387-398, doi:10.1006/icar.1996.0058.

Lowe, D. (1976), Grain flow and grain flow deposits, *J. Sed. Pet., 46*, 188–199.

Mark, C., S. Gupta, A. Carter, D. F. Mark, C. Gautheron, and A. Martín (2014), Rift flank uplift at the Gulf of California: No requirement for asthenospheric upwelling, *Geology*, *42*(3), 259-262, doi:10.1130/G35073.1.

Matsuyama, I., and F. Nimmo (2008), Tectonic patterns on reoriented and despun planetary bodies, *Icarus*, *195*(1), 459-473, doi:10.1016/j.icarus.2007.12.003.

McGarr, A., and N. C. Gay (1978), State of stress in the earth's crust, *Annual Review of Earth and Planetary Sciences, 6*, 405, doi:10.1146/annurev.ea.06.050178.002201.

McKinnon, W. B. (1999), Convective instability in Europa's floating ice shell, *Geophys. Res. Lett. 26*(7), 951-954, doi:10.1029/1999GL900125.

McKinnon, W. B., and H. J. Melosh (1980), Evolution of planetary lithospheres: Evidence from multiringed structures on Ganymede and Callisto, *Icarus*, *44*(2), 454-471, doi:10.1016/0019-1035(80)90037-8.

Melosh, H. J. (1976), On the origin of fractures radial to lunar basins, paper presented at *Lunar Planet. Sci*., *7*, 2967-2982, The Woodlands.

Melosh, J. H. (1977), Global tectonics of a despun planet, *Icarus*, *31*(2), 221-243, doi:10.1016/0019-1035(77)90035-5.

Melosh, H. J. (1980), Tectonic patterns on a tidally distorted planet, *Icarus*, *43*(3), 334-337, doi:10.1016/0019-1035(80)90178-5.

Meyer, J., and J. Wisdom (2008), Tidal evolution of Mimas, Enceladus, and Dione, *Icarus* 193(1), 213-223, doi:10.1016/j.icarus.2007.09.008.

Moore, J. M. (1984), The tectonic and volcanic history of Dione, *Icarus 59*(2), 205-220, doi:10.1016/0019-1035(84)90024-1.

Moore, J. M., and J. L. Ahern (1983), The geology of Tethys, *J. Geophys. Res. Solid Earth, 88(S02),* A577-A584.

Moore, J. M., V. M. Horner, and R. Greeley (1985), The geomorphology of Rhea: Implications for geologic history and surface processes, *J. Geophys. Res. Solid Earth, 90(S02)*, C785-C795.

Moore, J. M., M. T. Mellon, and A. P. Zent (1996), Mass wasting and ground collapse in terrains of volatile-rich deposits as a Solar System-wide geological process: The pre-Galileo view, *Icarus, 122*, 63–78, doi:10.1006/icar.1996.0109.

Moore, J. M., E. Asphaug, D. Morrison, J. R. Spencer, C. R. Chapman, B. Bierhaus, R. J. Sullivan, F. C. Chuang, J. E. Klemaszewski, and R. Greeley (1999), Mass Movement and Landform Degradation on the Icy Galilean Satellites: Results of the Galileo Nominal Mission. *Icarus, 140(2),* 294-312, doi:10.1006/icar.1999.6132.

Moore, J. M., P. M. Schenk, L. S. Bruesch, E. Asphaug, and W. B. McKinnon (2004), Large impact features on middle-sized icy satellites, *Icarus, 171(2)*, 421-443, doi:10.1016/j.icarus.2004.05.009.

Morrison, D., G. Rieke, D. Cruikshank, and C. Pilcher (1976), Surface compositions of the satellites of Saturn from infrared photometry, *The Astrophysical Journal, 207*, L213-L216.

Mueller, S., and W. B. McKinnon (1988), Three-layered models of Ganymede and Callisto: Compositions, structures, and aspects of evolution, *Icarus*, *76*(3), 437-464, doi:10.1016/0019-1035(88)90014-0.

Multhaup, K., and T. Spohn (2007), Stagnant lid convection in the mid-sized icy satellites of Saturn., *Icarus* 186(2), 420-435, doi:10.1016/j.icarus.2006.09.001.

Murray, C. D., and S. F. Dermott (1999), *Solar system dynamics*, Cambridge University Press, Cambridge.

Nimmo, F. (2004), Non-Newtonian topographic relaxation on Europa, *Icarus*, *168*(1), 205-208, doi:10.1016/j.icarus.2003.11.022.

Nimmo, F., and M. Manga (2002), Causes, characteristics and consequences of convective diapirism on Europa, *Geophys. Res. Lett.*, *29*(23), 24-1, doi:10.1029/2002GL015754.

Nimmo, F., B. Bills, P. Thomas, and S. Asmar (2010), Geophysical implications of the long-wavelength topography of Rhea, *J. Geophys. Res. 115*(E10), E10008, doi:10.1029/2010JE003604.

Nimmo, F., B. G. Bills, and P. C. Thomas (2011), Geophysical implications of the long-wavelength topography of the Saturnian satellites, *J. Geophys. Res. Planets* 116(E11), doi: 10.1029/2011JE003835.

Ojakangas, G. W., and D. J. Stevenson (1989), Thermal state of an ice shell on Europa, *Icarus, 81*(2), 220-241, doi:10.1016/0019-1035(89)90052-3.

Pappalardo, R. T., and G. C. Collins (2005), Strained craters on Ganymede. *Journal of structural geology, 27*(5), 827-838, doi:10.1016/j.jsg.2004.11.010.

Pappalardo, R. T., and R. Greeley, R. (1995), A review of the origins of subparallel ridges and troughs: Generalized morphological predictions from terrestrial models, *J. Geophys. Res. Planets, 100*(E9), 18985-19007, doi:10.1029/94JE02638.

Pappalardo, R. T., S. J. Reynolds, and R. Greeley (1997), Extensional tilt blocks on Miranda: Evidence for an upwelling origin of Arden Corona, *J. Geophys. Res. Planets, 102*(E6), 13369-13379, doi:10.1029/97JE00802.

Pappalardo, R. T., J. W. Head, G. C. Collins, R. L. Kirk, G. Neukum, J. Oberst, B. Giese, R. Greeley, C. R. Chapman and P. Helfenstein (1998), Grooved terrain on Ganymede: First results from Galileo high-resolution imaging, *Icarus, 135*(1), 276-302, doi:10.1006/icar.1998.5966.

Parmentier, E. M., and J. W. Head (1981), Viscous relaxation of impact craters on icy planetary surfaces: Determination of viscosity variation with depth, *Icarus, 47*(1), 100-111, doi:10.1016/0019-1035(81)90095-6.

Parsons, T., and G. A. Thompson (1993), Does magmatism influence low-angle normal faulting?, *Geology, 21*, 247-250, doi:10.1130/0091-7613(1993)021.

Passey, Q. R., and E. M. Shoemaker (1982), Craters and basins on Ganymede and Callisto: Morphological indicators of crustal evolution, In Satellites of Jupiter (D. Morrison, Ed.), 379–434. University of Arizona Press, Tucson.

Phillips, C. B. (2014), Stereo topography and subsurface thermal profiles on icy satellites of Saturn, Workshop on the Habitability of Icy Worlds, LPI Contributions, Pasadena, California.

Plescia, J. B. (1983), The geology of Dione, *Icarus*, *56*(2), 255-277, doi:10.1016/0019-1035(83)90038-6.

Plescia, J. B. (1985), Geology of Rhea, paper presented at *Lunar Planet. Sci.*, *16*, 665-666, The Woodlands.

Pohlman, N., B. Severson, J. Ottino, and R. Lueptow (2006), Surface roughness effects in granular matter: Influence on angle of repose and the absence of segregation, *Phys. Rev. E, 73*(3), 031304, doi:10.1103/PhysRevE.73.031304.

Pollard, D. D., and P. Segall (1987), Theoretical displacements and stresses near fractures in rock: with applications to faults, joints, veins, dikes, and solution surfaces, Fracture mechanics of rock, 277-349, Academic Press, London.

Porco, C. C., P. Helfenstein, P. C. Thomas, A. P. Ingersoll, J. Wisdom, R. West, G. Neukum, T. Denk, R. Wagner, T. Roatsch, S. Kieffer, E. Turtle, A. McEwen, T. V. Johnson, J. Rathbun, J. Veverka, D. Wilson, J. Perry, J. Spitale, A. Brahic, J. A. Burns, A. D. DelGenio, L. Dones, C. D. Murray, S. Squyres (2006), Cassini observes the active south pole of Enceladus, *Science* 311(5766), 1393-1401, doi:10.1126/science.1123013.

Price, N. J., and J. W. Cosgrove (1990), Analysis of geological structures, *Cambridge University Press*, Cambridge.

Prockter, L. M., J. W. Head, R. T. Pappalardo, D. A. Senske, G. Neukum, R. Wagner, U. Wolf, J. Oberst, B. Giese, J. M. Moore, C. R. Chapman, P. Helfenstein, R. Greeley, H. H. Breneman, and M. J. S. Belton (1998), Dark terrain on Ganymede: Geological mapping and interpretation of Galileo Regio at high resolution, *Icarus*, 135(1), 317-344, doi:10.1006/icar.1998.5981.

Proffett, J. M. (1977), Cenozoic geology of the Yerington District, Nevada, and implications for nature and origin of Basin and Range faulting, *Geological Society of America Bulletin*, *88*, 247–266, doi:10.1130/0016-7606(1977)88.

Roatsch, T., R. Jaumann, K. Stephan, and P. Thomas (2009), Cartographic mapping of the icy satellites using ISS and VIMS data, Saturn from Cassini-Huygens, 763-781, Springer Science & Business Media.

Rowley D. B., D. Sahagian (1986), Depth-dependent stretching: a different approach, *Geology* 14, 32–35, doi: 10.1130/0091-7613(1986)14.

Royden, L., C. E. Keen (1980), Rifting process and thermal evolution of the continental margin of eastern Canada determined from subsidence curves, *Earth Planet Sci. Lett.*, *51*, 343–36, doi:10.1016/0012-821X(80)90216-2.

Schenk, P. M. (1989), Crater formation and modification on the icy satellites of Uranus and Saturn: Depth/diameter and central peak occurrence, *J. Geophys. Res. Solid Earth*, *94*(B4), 3813-3832, doi:10.1029/JB094iB04p03813.

Schenk, P. M. (1991), Fluid volcanism on Miranda and Ariel: Flow morphology and composition, *J. Geophys. Res. Solid Earth 96*(B2), 1887-1906, doi:10.1029/90JB01604.

Schenk, P.M. (2002), Thickness constraints on the icy shells of the Galilean satellites from a comparison of crater shapes, *Nature 417*, 419–421, doi:10.1038/417419a.

Schenk, P. M., and J. M. Moore (2007), Impact crater topography and morphology on saturnian mid-sized satellites, paper presented at Lunar Planet. Sci., 38, 2305, The Woodlands.

Schulson, E. M., and A. L. Fortt (2012), Friction of ice on ice, *J. Geophys. Res. Solid Earth*, *117*(B12), doi:10.1029/2012JB009219.

Schulson, E. M., and A. L. Fortt (2013), Static strengthening of frictional surfaces of ice, *Acta Materialia*, *61*(5), 1616-1623, doi:10.1016/j.actamat.2012.11.038.

Scott, R. F. (1967), Viscous flow of craters, *Icarus* 7.1, 139-148, doi:10.1016/0019-1035(67)90058-9.

Showman, A. P., and L. Han (2005), Effects of plasticity on convection in an ice shell: Implications for Europa, *Icarus*, *177*(2), 425-437, doi:10.1016/j.icarus.2005.02.020.

Sieveka, E. M., and R. E. Johnson (1982), Thermal-and plasma-induced molecular redistribution on the icy satellites, *Icarus* 51.3, 528-548.

Singer, K. N., W. B. McKinnon, P. M. Schenk, and J. M. Moore (2012), Massive ice avalanches on Iapetus mobilized by friction reduction during flash heating, *Nature Geoscience*, *5*(8), 574-578, doi:10.1016/0019-1035(82)90144-0.

Smith, B. A., L. Soderblom, R. Beebe, J. Boyce, G. Briggs, A. Bunker, S. A. Collins, C. J. Hansen, T. V. Johnson and J. L. Mitchell (1981), Encounter with Saturn: Voyager 1 imaging science results, *Science 212(4491)*, 163-191, doi:10.1126/science.212.4491.163.

Smith, B. A., L. Soderblom, R. Batson, P. Bridges, J. Inge, H. Masursky, E. Shoemaker, R. Beebe, J. Boyce and G. Briggs (1982), A new look at the Saturn system: The Voyager 2 images, *Science 215(4532)*, 504-537, doi:10.1126/science.215.4532.504.

Smith, B. A., L. A. Soderblom, R. F. Beebe, K. Bollinger, J. M. Boyce, A. Brahic, G. A. Briggs, R. H. Brown, C. Chyba, S. A. Collins, A. F. Cook, S. K. Croft, D. Cruikshank, J. N. Cuzzi, G. E. Danielson, M. E. Davies, T. E. Dowling, D. Godfrey, C. J. Hansen, C. Harris, C. P. Helfenstein, G. E. Hunt, A. P. Ingersoll, T. V. Johnson, R. J. Krauss, H. Masursky, D. Morrison, T. Owen, J. B. Plescia, J. B. Pollack, C. C. Porco, K. Rages, C. Sagan, J. Schwartz, E. M. Shoemaker, L. A. Sromovsky, C. Stoker, R. G. Strom, V. E. Suomi, S. P. Synott, R. J. Terrile, P. Thomas, W. R. Thompson, J. Veverka (1986), Voyager 2 in the Uranian system: imaging science results, *Science 233(4759)*, 43–64, doi:10.1126/science.233.4759.43.

Spencer, J. E. (1984), Role of tectonic denudation in warping and uplift of low-angle normal faults, *Geology*, *12(2)*, 95-98, doi:10.1130/0091-7613(1984)12.

Spencer, J. E., and Chase, C. G. (1989), Role of crustal flexure in initiation of low angle normal faults and implications for structural evolution of the Basin and Range province, *J. Geophys. Res.*, *94*, 1765–1775, doi:10.1029/JB094iB02p01765.

Squyres, S. W., and S. K, Croft (1986), The tectonics of icy satellites, In Satellites, 293-341, University of Arizona Press, Tucson.

Stephan, K., R. Jaumann, R. Wagner, R. N. Clark, D. P. Cruikshank, C. A. Hibbitts, T. Roatsch, H. Hoffmann, R. H. Brown, and G. Filiacchione (2010), Dione's spectral and geological properties, *Icarus 206(2)*, 631-652, doi:10.1016/j.icarus.2009.07.036.

Stephan, K., R. Jaumann, R. Wagner, R. N. Clark, D. P. Cruikshank, B. Giese, C. A. Hibbitts, T. Roatsch, K. Matz, R. H. Brown, G. Filacchione, F. Cappacioni, F. Scholten, B. J. Buratti, G. B. Hansen, P. D. Nicholson, K. H. Baines, R. M. Nelson, D. L. Matson (2012), The Saturnian satellite Rhea as seen by Cassini VIMS, *Planetary and Space Science 61*(1), 142-160, doi:10.1016/j.pss.2011.07.019.

Thomas, P. G. (1988), The tectonic and volcanic history of Rhea as inferred from studies of scarps, ridges, troughs, and other lineaments, *Icarus 74(3)*, 554-567, doi:10.1016/0019-1035(88)90121-2.

Thomas, P. (2010), Sizes, shapes, and derived properties of the saturnian satellites after the Cassini nominal mission, *Icarus 208(1)*, 395-401, doi:10.1016/j.icarus.2010.01.025.

Thomas, P. J., and G. Schubert (1988), Power law rheology of ice and the relaxation style and retention of craters on Ganymede, *J. Geophys. Res. Solid Earth, 93(B11)*, 13755-13762, doi: 10.1029/JB093iB11p13755.

Tobie, G., G. Choblet, C. Sotin (2003), Tidally heated convection: Constraints on Europa's ice shell thickness, *J. Geophys. Res. 108*(E11), doi:10.1029/2003JE002099.

Tobie, G., A. Mocquet, and C. Sotin (2005), Tidal dissipation within large icy satellites: Applications to Europa and Titan, *Icarus, 177*(2), 534-549, doi:10.1016/j.icarus.2005.04.006.

Turcotte, D. L., and G. Schubert (2014), *Geodynamics*, Cambridge University Press, Cambridge.

Veverka, J., P. Thomas, T. V. Johnson, D. Matson, and K. Housen (1986), The physical characteristics of satellite surfaces, In Satellites, 342-402, University of Arizona Press, Tucson.

Wagner, R., G. Neukum, B. Giese, T. Roatsch, U. Wolf, T. Denk, and C. I. Team (2006), Geology, Ages and Topography of Saturn's Satellite Dione Observed by the Cassini ISS Camera, paper presented at Lunar Planet. Sci., 37, 1805, The Woodlands.

Wagner, R., G. Neukum, B. Giese, T. Roatsch, and U. Wolf (2007), The global geology of Rhea: Preliminary implications from the Cassini ISS data, paper presented at Lunar Planet. Sci., 38, 1958, The Woodlands.

Wagner, R., G. Neukum, B. Giese, T. Roatsch, T. Denk, U. Wolf, and C. Porco (2010), The Geology of Rhea: A First Look at the ISS Camera Data from Orbit 121 (Nov. 21, 2009) in Cassini's Extended Mission, paper presented at *Lunar Planet. Sci., 41, 1672*, The Woodlands.

Weissel, J. K., and G. D. Karner (1989), Flexural uplift of rift flanks due to mechanical unloading of the lithosphere during extension, *J. Geophys. Res. Solid Earth, 94(B10)*, 13919-13950, doi:10.1029/JB094iB10p13919.

Wernicke, B., and G. J. Axen (1988), On the role of isostasy in the evolution of normal fault systems, *Geology, 16*, 848–851, doi:10.1130/0091-7613(1988)016.

Wernicke, B., and B. C. Burchfiel (1982), Modes of extensional tectonics, *J. Struct. Geol., 4*, 105-115, doi:10.1016/0191-8141(82)90021-9.

White, O. L., Paul M. S., and A. J. Dombard (2013), Impact basin relaxation on Rhea and Iapetus and relation to past heat flow, *Icarus 223(2)*, 699-709, doi:10.1016/j.icarus.2013.01.013.

Willemann, R. J. (1984), Reorientation of planets with elastic lithospheres, *Icarus, 60*(3), 701-709, doi:10.1016/0019-1035(84)90174-X.

Yin, A. (1989), Origin of regional rooted low-angle normal faults: A mechanical model and its implications, *Tectonics, 8*, 469–482, doi:10.1029/TC008i003p00469.

Appendix II

Table II-1. Values used and empirically derived in H_2O ice deformation experiments. Values are shown for the coefficient of internal friction of cryogenic H_2O ice I, and normal fault dips associated with those values, from laboratory deformation experiments. These laboratory studies were conducted under the conditions most relevant to icy satellite near-surface and surface conditions, at low temperatures and strain rates.

Reference	**Temperature**	**Strain Rate**	**Vertical Normal Stress**	**Coefficient of Internal Friction (μ_i)**	**Normal Fault Dip (δ_{normal})**
Durham et al. (1983)	77 K to 258 K	3.5×10^{-6} s^{-1} to 3.5×10^{-4} s^{-1}	0.1 MPa to 350 MPa	~0	~45°
Beeman et al. (1988)	77 K to 115 K	3×10^{-7} s^{-1} to 3×10^{-5} s^{-1}	0.3 MPa to 250 MPa	0.2 to 0.55	51° to 59°
Schulson and Fortt (2012)	98 K	5×10^{-8} s^{-1}	$\leq$ 0.098 MPa	0.29 to 0.44	53° to 57°

Table II-2. The image pairs used to make the DEMs in this study. Details about each resultant SOCET SET DEM, including details about the relevance of the off-nadir angles, number of tie points, root mean square (RMS) values, emission angles, and subspacecraft ground azimuth (SGA) values for each DEM as well as the derivation of the DEM resolutions and vertical accuracies are discussed in Appendix II-A.

Image Pair Numbers	Image Res.	DEM Res.	Off-nadir Angle	Number of Tie Points	RMS Value	Emission Angle	SGA	Vertical Accuracy
Ithaca Chasma, Tethys								
N1489061272 & N1489061678	497 m/px 497 m/px	1.4 km/px	0.025 rad 0.028 rad	44	0.489 px	3.91° 4.37°	346° 349°	83 m
Avaiki Chasmata, Rhea								
N1637519574 & N1637520407	306 m/px 171 m/px	510 m/px	0.453 rad 0.771 rad	30	0.139 px	15.79° 28.33°	160° 133°	175 m
N1637519392 & N1637520350	150 m/px 169 m/px	480 m/px	0.269 rad 0.504 rad	10	0.122 px	9.18° 19.49°	115° 111°	198 m
N1637519986 & N1637520407	161 m/px 171 m/px	550 m/px	0.789 rad 0.711 rad	10	0.140 px	29.78° 28.33°	157° 133°	58 m
N1637519768 & N1637520407	156 m/px 171 m/px	520 m/px	0.681 rad 0.711 rad	10	0.113 px	24.65° 28.33°	127° 133°	71 m
The Wispy Terrain, Dione								
N1662199979 & N1662200068	237 m/px 475 m/px	1.1 km/px	0.206 rad 0.204 rad	9	0.083 px	14.89° 14.78°	320° 320°	283 m

Table II-3. Results of fault slope measurements for each analyzed fault in each study area. These results show that the average fault slopes of the scarps of Ithaca Chasma, Avaiki Chasmata, and Padu Chasmata of the Wispy Terrain fall below the expected dip range from laboratory experiments, although the faults of Palatine Chasmata of the Wispy Terrain fall within the expected dip range.

Scarp Name	Number of Measurements	Maximum Fault Slope (± Uncertainty)	Average Fault Slope (± Uncertainty)	Relationship to Expected Dip Range
Ithaca Chasma, Tethys				
A	20	29° ± 3°	15° ± 3°	Below
B	10	27° ± 3°	16° ± 2°	
C	8	23° ± 3°	18° ± 2°	
D	25	24° ± 3°	18° ± 3°	
E	14	39° ± 2°	21° ± 2°	
F	29	51° ± 1°	36° ± 2°	
G	19	27° ± 3°	24° ± 3°	
H	19	58° ± 2°	34° ± 5°	
I	8	46° ± 3°	35° ± 3°	
J	9	27° ± 3°	21° ± 3°	
	Total: 161	Average: 35° ± 3°	Average: 24° ± 3°	
Avaiki Chasmata, Rhea				
A	28	42° ± 3°	32° ± 3°	Below
B	5	27° ± 3°	25° ± 2°	
C	25	48° ± 2°	33° ± 5°	
D	23	64° ± 8°	37° ± 4°	
E	8	26° ± 16°	23° ± 12°	
F	9	28° ± 4°	23° ± 5°	
G	25	31° ± 5°	22° ± 6°	
H	6	32° ± 6°	29° ± 6°	
I	9	35° ± 9°	29° ± 10°	
J	13	40° ± 10°	32° ± 13°	
K	5	36° ± 11°	29° ± 12°	
L	6	34° ± 17°	31° ± 13°	
	Total: 162	Average: 37° ± 8°	Average: 29° ± 8°	
The Wispy Terrain, Dione (Palatine Chasmata)				
A	17	72° ± 3°	56° ± 7°	Above
B	13	66° ± 6°	38° ± 12°	
C	8	64° ± 6°	49° ± 10°	

Table II-3. Continued.

Scarp Name	Number of Measurements	Maximum Fault Slope (± Uncertainty)	Average Fault Slope (± Uncertainty)	Relationship to Expected Dip Range
The Wispy Terrain, Dione (Padu Chasmata)				
D	9	34° ± 10°	23° ± 13°	Below
	Total: 52	Average: 55° ± 7°	Average: 35° ± 11°	

Table II-4. Results of the Shapiro-Wilk and one-sample statistical tests. These results show the results of the Shapiro-Wilk tests for a normal distribution for scarp slope measurements of each scarp analyzed. The one-sample t-test and the Wilcoxon Signed Ranks test results show if the data are similar to the expected fault dip range inferred from laboratory deformation experiments in cryogenic H_2O ice. Our hypothesis that laboratory inferred normal fault dips are reflected on icy satellites is not supported for any scarps within Ithaca Chasma or Avaiki Chasmata, but is supported for faults within Palatine Chasmata within Dione's Wispy Terrain.

Scarp Name	**Shapiro-Wilk Test**		**One-Sample t-test / Wilcoxon Signed Ranks Test**			**Hypothesis supported?**
	Normally distributed?	**p-value**	**Test Used**	**Statistically similar to 45° / 59°?**	**p-value**	
Ithaca Chasma, Tethys						
A	No	0.001	Wilcoxon Signed Ranks	No (45°)	< 0.001	No
B	Yes	0.707	One-sample t-test			
C		0.388				
D		0.193				
E		0.287				
F		0.560				
G		0.587				
H	No	0.001	Wilcoxon Signed Ranks		0.002	
I	Yes	0.380	One-sample t-test		0.005	
J		0.600			< 0.001	
Avaiki Chasmata, Rhea						
A	Yes	0.879	One-sample t-test	No (45°)	< 0.001	No
B		0.777				
C		0.579				
D		0.672			0.004	
E		0.928			< 0.001	
F		0.363				
G		0.794				
H		0.421				
I		0.314				
J		0.678				
K		0.400			0.003	
L		0.814			< 0.001	

Table II-4. Continued.

Scarp Name	Shapiro-Wilk Test		One-Sample t-test / Wilcoxon Signed Ranks Test			Hypothesis supported?
	Normally distributed?	**p-value**	**Test Used**	**Statistically similar to 45° / 59°?**	**p-value**	
The Wispy Terrain, Dione (Palatine Chasmata)						
A	Yes	0.329	One-sample t-test	Yes (59°)	0.272	Yes
B		0.190		Yes (45°)	0.156	
C		0.922			0.327	
The Wispy Terrain, Dione (Padu Chasmata)						
D	No	0.030	Wilcoxon Signed Ranks	No (45°)	0.008	No

Table II-5. Summary of evidence for back-tilted faces in the study areas. These results show that the sum of the fault slope and the back-tilted face slope for each scarp analyzed do not fall within the experimentally derived dip range for most faults analyzed in each study area. The back-tilted face and fault slope uncertainties were derived from the vertical accuracy of the relevant DEM (Appendix II-A). The back-tilted face slope and uncertainties were measured using the same method to measure the fault slope. There is little relief immediately outside the study areas at the resolution of the DEMs used, so accounting for background topography was unnecessary. Overall, these results show that fault block tilting is not a viable explanation for the shallow fault slopes within Ithaca Chasma, Avaiki Chasmata, or the Wispy Terrain.

Scarp Name	Average Back-Tilted Face Slope (± Uncertainty)	Sum of Fault Slope and Back-Tilted Face Slope (± Uncertainty)	Consistent with Fault Rotation as a Cause for Shallow Fault Slope Formation?
Ithaca Chasma, Tethys			
A	13° ± 3°	28° ± 6°	No
B	7° ± 4°	23° ± 6°	
C	9° ± 4°	27° ± 6°	
D	10° ± 4°	28° ± 7°	
E	8° ± 3°	29° ± 5°	
F	14° ± 2°	50° ± 4°	Yes
G	11° ± 4°	37° ± 7°	No
H	5° ± 1°	39° ± 6°	Inconclusive (uncertainty falls within range)
I	8° ± 3°	43° ± 6°	
J	6° ± 4°	27° ± 7°	No
	Average: 9° ± 4°	Average: 33° ± 6°	Overall: No
Avaiki Chasmata, Rhea			
A	5° ± 5°	37° ± 9°	Inconclusive (uncertainty falls within range)
B	0° ± 0°	25° ± 2°	No
C	8° ± 4°	41° ± 9°	Inconclusive (uncertainty falls within range)
D	6° ± 3°	43° ± 7°	
E	10° ± 4°	33° ± 16°	
F	5° ± 3°	28° ± 8°	No
G	0° ± 0°	22° ± 6°	
H	6° ± 4°	35° ± 10°	Inconclusive (uncertainty falls within range)
I	4° ± 4°	33° ± 14°	
J	6° ± 9°	38° ± 22°	
K	6° ± 12°	35° ± 24°	
L	7° ± 5°	38° ± 18°	

Table II-5. Continued.

Scarp Name	Average Back-Tilted Face Slope (± Uncertainty)	Sum of Fault Slope and Back-Tilted Face Slope (± Uncertainty)	Consistent with Fault Rotation as a Cause for Shallow Fault Slope Formation?
	Average: 5° ± 5°	Average: 34° ± 12°	Overall: Inconclusive (uncertainty falls within range)

Table II-6. Analysis of evidence for regolith deposition. The average fault slope heights are compared to estimates for regolith thickness on the appropriate satellite, and the average fault slopes are compared to the maximum angle of repose (AOR). Consistency with regolith deposition (last column) requires both that fault slope heights be at/below regolith thickness and that fault slopes be at/below the angle of repose. These results show that regolith deposition across fault scarps is not a viable explanation for the shallow fault slopes within any of the study areas.

Scarp Name	Comparing Fault Slope Heights to the Estimated Regolith Thickness		Comparing Fault Slopes to the Angle of Repose for Angular Grains		Consistent with Regolith Deposition on Fault Scarps?
	Average Fault Slope Height	Height Relation to Regolith Thickness	Average Fault Slope	Fault Slope Relation to AOR	
			Ithaca Chasma, Tethys		
A	2.0 km ± 181 m	Above	15° ± 3°	Below	No
B	2.2 km ± 157 m		16° ± 2°		
C	2.6 km ± 82 m		18° ± 2°		
D	2.4 km ± 103 m		18° ± 3°		
E	2.8 km ± 257 m		21° ± 2°		
F	6.6 km ± 1.3 km		36° ± 2°		
G	2.6 km ± 152 m		24° ± 3°		
H	3.2 km ± 262 m		34° ± 5°		
I	3.3 km ± 260 m		35° ± 3°		
J	3.2 km ± 82 m		21° ± 3°		
	Average: 3.1 km ± 378 m	Overall: Above	Average: 24° ± 3°	Overall: Below	Overall: No
			Avaiki Chasmata, Rhea		
A	2.4 ± 131 m	Above	32° ± 3°	Below	No
B	2.3 ± 228 m		25° ± 2°		
C	2.1 ± 77 m		33° ± 5°		
D	2.5 ± 82 m		37° ± 4°		
E	1.2 ± 15 m	Below	23° ± 12°		Yes
F	1.4 ± 103 m		23° ± 5°		
G	1.1 ± 47 m		22° ± 6°		
H	1.7 ± 120 m		29° ± 6°		
I	1.8 ± 53 m		29° ± 10°		
J	2.0 ± 112 m	Same	32° ± 13°		
K	1.1 ± 35 m	Below	29° ± 12°		
L	2.2 ± 56 m	Above	31° ± 13°		No
	Average: 1.8 ± 148 m	Overall: Inconclusive	Average: 29° ± 8°	Overall: Below	Overall: Inconclusive

Table II-6. Continued.

Scarp Name	Comparing Fault Slope Heights to the Estimated Regolith Thickness		Comparing Fault Slopes to the Angle of Repose for Angular Grains		Consistent with Regolith Deposition on Fault Scarps?
	Average Fault Slope Height	Height Relation to Regolith Thickness	Average Fault Slope	Fault Slope Relation to AOR	
The Wispy Terrain, Dione					
A	2.9 km ± 196 m	Above	56° ± 7°	Above	No
B	2.9 km ± 168 m		38° ± 12°	Below	
C	2.0 km ± 100 m		49° ± 10°	Above	
D	1.1 km ± 55 m		23° ± 13°	Below	
	Average: 2.2 km ± 252 m	Overall: Above	Average: 35° ± 11°	Overall: Below	Overall: No

Table II-7. Summary of evidence for raised rims in each study area. The associated average and maximum rim heights are given for each scarp, where a raised rim is present. The presence of raised rims of Avaiki Chasmata and Ithaca Chasma are indicative of viscous relaxation. The uncertainty given for the average raised rim heights is the sum of the vertical accuracy of the DEM used and the standard error of the measurements (Appendix II-A). The uncertainty given for the maximum raised rim heights is the vertical accuracy of the DEM used.

Scarp Name	Raised Rim Present? (Evident for ≥ 50% of Profile Lines)	Average Raised Rim Height (± Uncertainty)	Maximum Rim Height (± Uncertainty)	Consistent with Viscous Relaxation?
Ithaca Chasma, Tethys				
A	Yes	1.3 km ± 220 m	2.7 km ± 83 m	Yes
B		630 m ± 170 m	1.0 km ± 83 m	
C		3.1 km ± 150 m	3.3 km ± 83 m	
D		3.4 km ± 370 m	5.6 km ± 83 m	
E		610 m ± 200 m	3.1 km ± 83 m	
F		1.3 km ± 260 m	3.3 km ± 83 m	
G		750 m ± 140 m	1.1 km ± 83 m	
H		890 m ± 150 m	1.3 km ± 83 m	
I		920 m ± 410 m	1.5 km ± 83 m	
J		610 m ± 210 m	1.3 km ± 83 m	
	Overall: Yes	Average: 1.4 km ± 230 m	Maximum: 5.6 km ± 83 m	Overall: Yes
Avaiki Chasmata, Rhea				
A	Yes	360 m ± 110 m	690 m ± 58 m	Yes
B	No	-		No
C	Yes	580 m ± 110 m	870 m ± 58 m	Yes
D		560 m ± 170 m	1.1 km ± 58 m	
E		1.1 km ± 330 m	1.5 km ± 175 m	
F		380 m ± 110 m	560 m ± 71 m	
G	No	-		No
H	Yes	260 m ± 90 m	340 m ± 71 m	Yes
I		470 m ± 230 m	800 m ± 175 m	
J		490 m ± 240 m	640 m ± 198 m	
K		470 m ± 260 m	610 m ± 198 m	
L		1.3 km ± 310 m	1.8 km ± 198 m	
	Overall: Yes	Average: 590 m ± 200 m	Maximum: 1.8 km ±198 m	Overall: Yes
The Wispy Terrain, Dione				
A	No	-		No
B				

Table II-7. Continued.

Scarp Name	Raised Rim Present? (Evident for ≥ 50% of Profile Lines)	Average Raised Rim Height (± Uncertainty)	Maximum Rim Height (± Uncertainty)	Consistent with Viscous Relaxation?
C				
D				
	Overall: No			Overall: No

Table II-8. Summary of values used for variables given in Equations II-4, II-5, and II-8. See text for derivation of values.

	Ithaca Chasma, Tethys	**Avaiki Chasmata, Rhea**	**The Wispy Terrain, Dione**
g	0.145 m s^{-2}	0.264 m s^{-2}	0.232 m s^{-2}
t	0.4 Ga 3.3 Ga 4.0 Ga	< 3.6 Ga < 4.2 Ga	> 1 Ga > 3.7 Ga
T_S	87 K	88 K	90 K
F	18 – 30 mW m^{-2}	15 – 30 mW m^{-2}	24 – 90 mW m^{-2}
z	16 – 20 km	15 – 28 km	5 – 10 km

Table II-9. Initial fault slope (Θ_0) and the change in fault slope ($\Theta_0 - \Theta_t$) of scarps in each study area. These calculations were done using the calculated values for viscosity (η) (Equation II-7), including the maximum and minimum viscosities calculated, shown here, and different age estimates for each study area (t). These results show that viscous relaxation can account for the shallow fault slopes of faults within all three study areas.

Study Area	Viscosity (η)	Age (t)	Initial Dip (Θ_0)	Change in Fault Slope ($\Theta_0 - \Theta_t$)
Ithaca Chasma, Tethys Scarp A	1.0×10^{22} Pa s	0.4 Ga	43° ± 9°	28°
		3.3 Ga	90° ± 0°	75°
		4.0 Ga		
	1.0×10^{23} Pa s	0.4 Ga	17° ± 6°	2°
		3.3 Ga	37° ± 9°	22°
		4.0 Ga	43° ± 9°	28°
	1.0×10^{24} Pa s	0.4 Ga	15° ± 5°	0°
		3.3 Ga	16° ± 6°	1°
		4.0 Ga	17° ± 6°	2°
Avaiki Chasmata, Rhea Scarp A	1.0×10^{23} Pa s	3.6 Ga	56° ± 6°	24°
		4.2 Ga	60° ± 6°	28°
	1.0×10^{24} Pa s	3.6 Ga	34° ± 6°	2°
		4.2 Ga	35° ± 6°	3°
The Wispy Terrain, Dione (Padua Chasmata) Scarp D	1.0×10^{22} Pa s	1.0 Ga	35° ± 8°	12°
		3.7 Ga	90° ± 5°	67°
	1.0×10^{23} Pa s	1.0 Ga	24° ± 6°	1°
		3.7 Ga	27° ± 7°	4°

Table II-10. Summary of estimated satellite peak melting events and fault systems formation events.

Satellite	Peak Melting	Fault System Age Estimates				Is Fault Age ≥ Heating Age?
		Study Area	Minimum	Intermediate	Maximum	
Tethys	4.0 Ga	Ithaca Chasma	0.4 Ga	3.3 Ga	4.0 Ga	Yes, for the maximum age estimate
Rhea	3.1 Ga	Avaiki Chasmata	3.6 Ga	-	4.2 Ga	Yes, for both age estimates
Dione	4.1 Ga	The Wispy Terrain	> 1.0 Ga	-	> 3.7 Ga	Yes, for the maximum age estimate

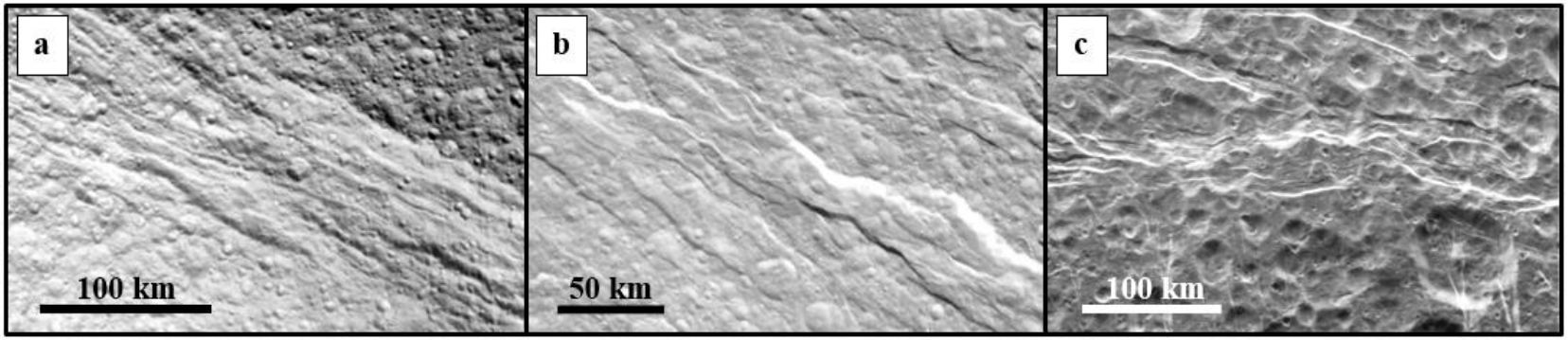

Figure II-1. Close up Cassini ISS images of normal faults on Tethys, Rhea, and Dione. a) Image N1716178094 of Ithaca Chasma on Tethys. Illumination is from the bottom left. b) Image N1637520407 of Avaiki Chasmata on Rhea. Illumination is from the bottom. c) Image N1662199979 of the Wispy Terrain on Dione. Illumination is from the top.

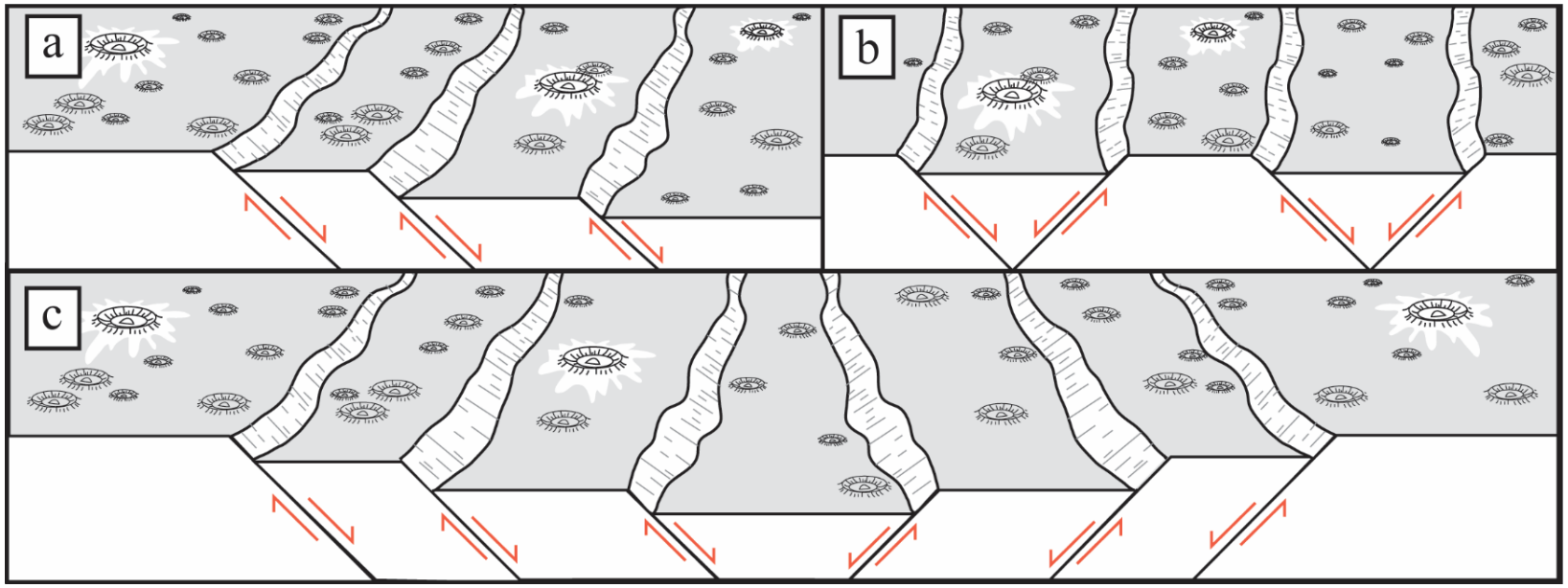

Figure II-2. Idealized sketches of extensional terrain with sets of normal faults that a) exhibit tilted fault blocks with faults that are dipping in a single direction, b) normal faults that alternate dip direction, in the form of horsts and grabens, and c) sets of normal faults that exhibit that, in some areas, dip in a consistent direction, and in other areas, dip in opposite directions.

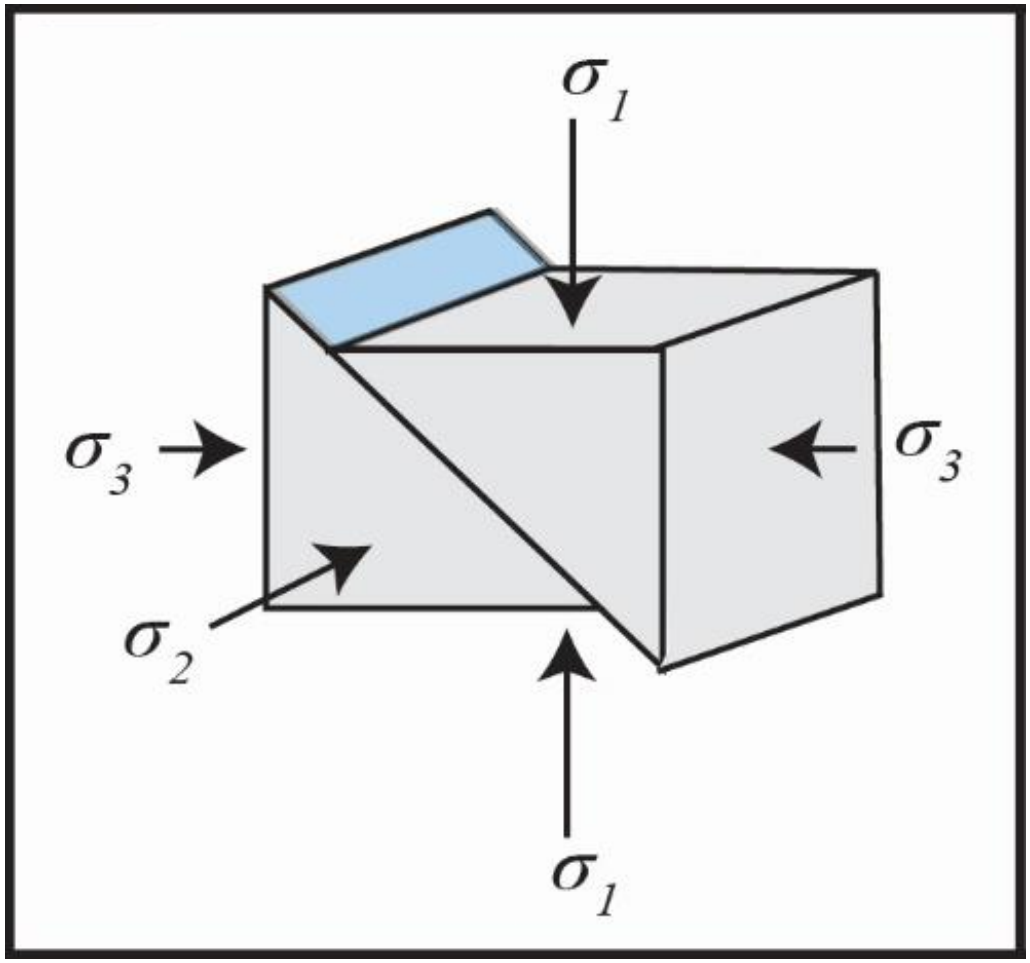

Figure II-3. Orientations of the principle stresses associated with normal faults are shown. σ_1 is the maximum principle stress, σ_2 is the intermediate principle stress, and σ_3 is the minimum principle stress. Arrow lengths are proportional to the relative stress magnitude.

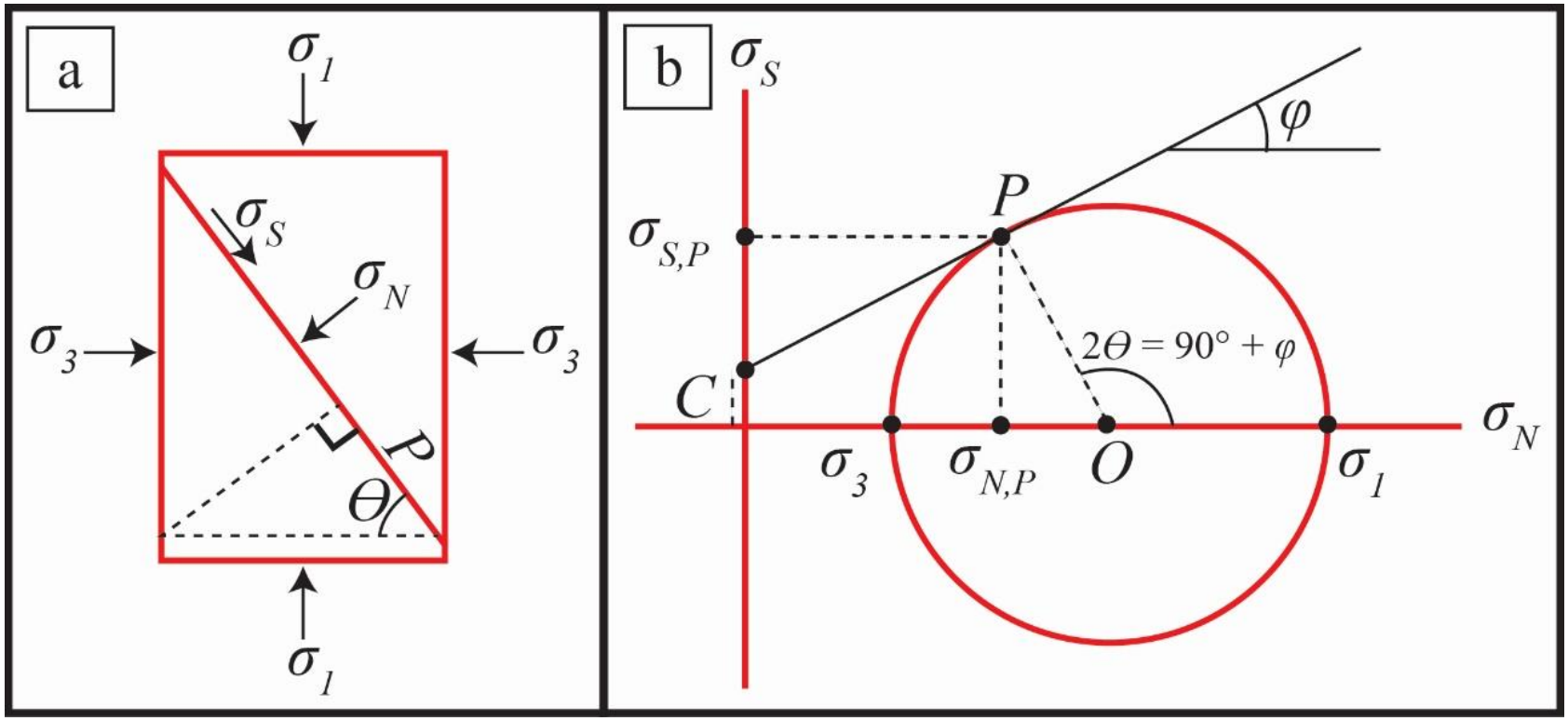

Figure II-4. The distribution of stresses on a material (a) with its associated Mohr's circle (b). σ_1 is the maximum principle stress, σ_3 is the minimum principle stress, σ_N is the normal stress, σ_S is the shear stress, P is the fracture plane, and θ is angle of P relative to σ_3. $\sigma_{S,P}$ is the shear required to form P, and $\sigma_{N,P}$ is the normal stress required to form P. φ is the material's internal friction angle, C is the compressive strength of the material, and O is the average of σ_1 and σ_3.

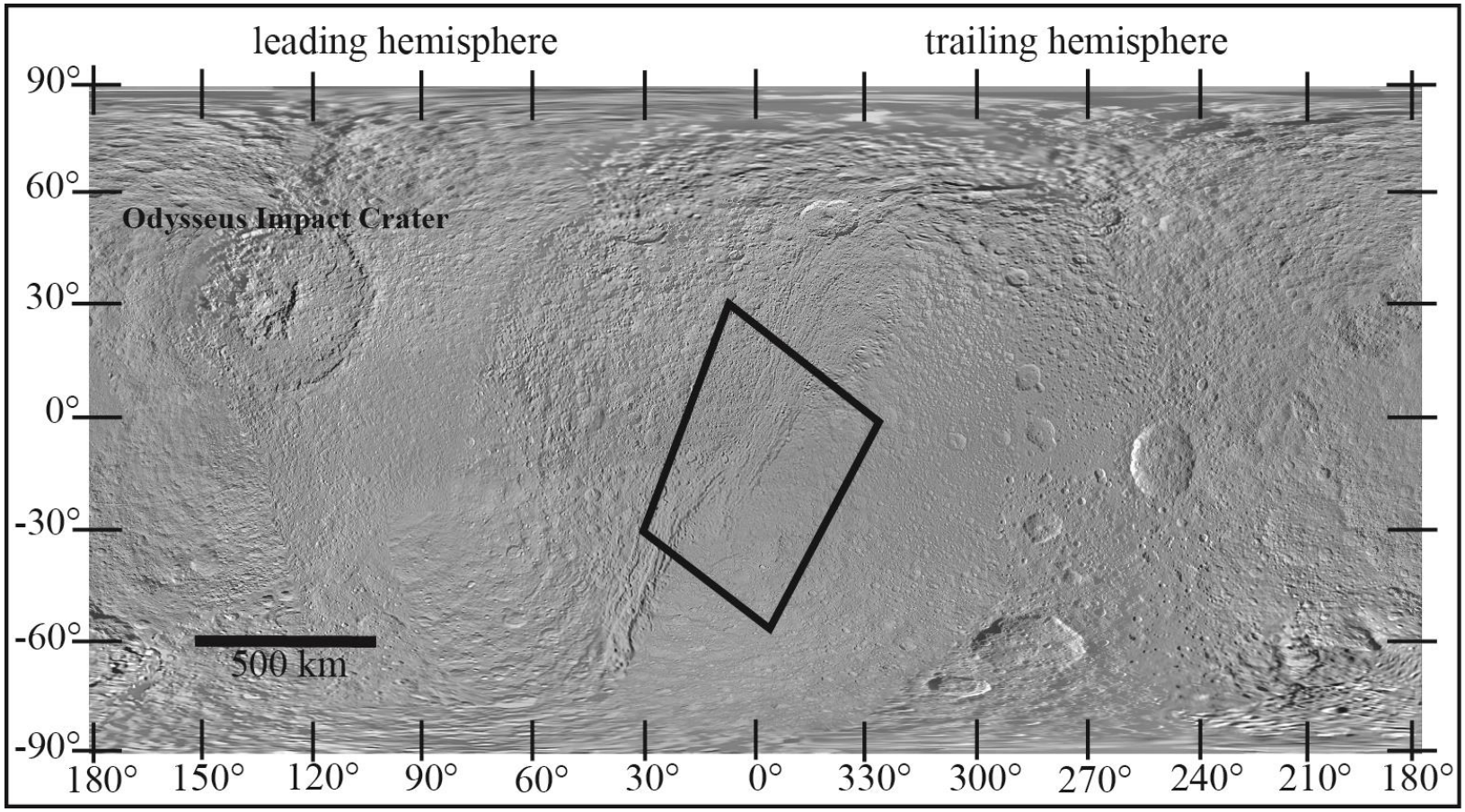

Figure II-5. Mosaic of Tethys with the region covered by the DEM (Figure II-6) outlined. The mosaic is a Mercator projection and is made up of Cassini ISS images.

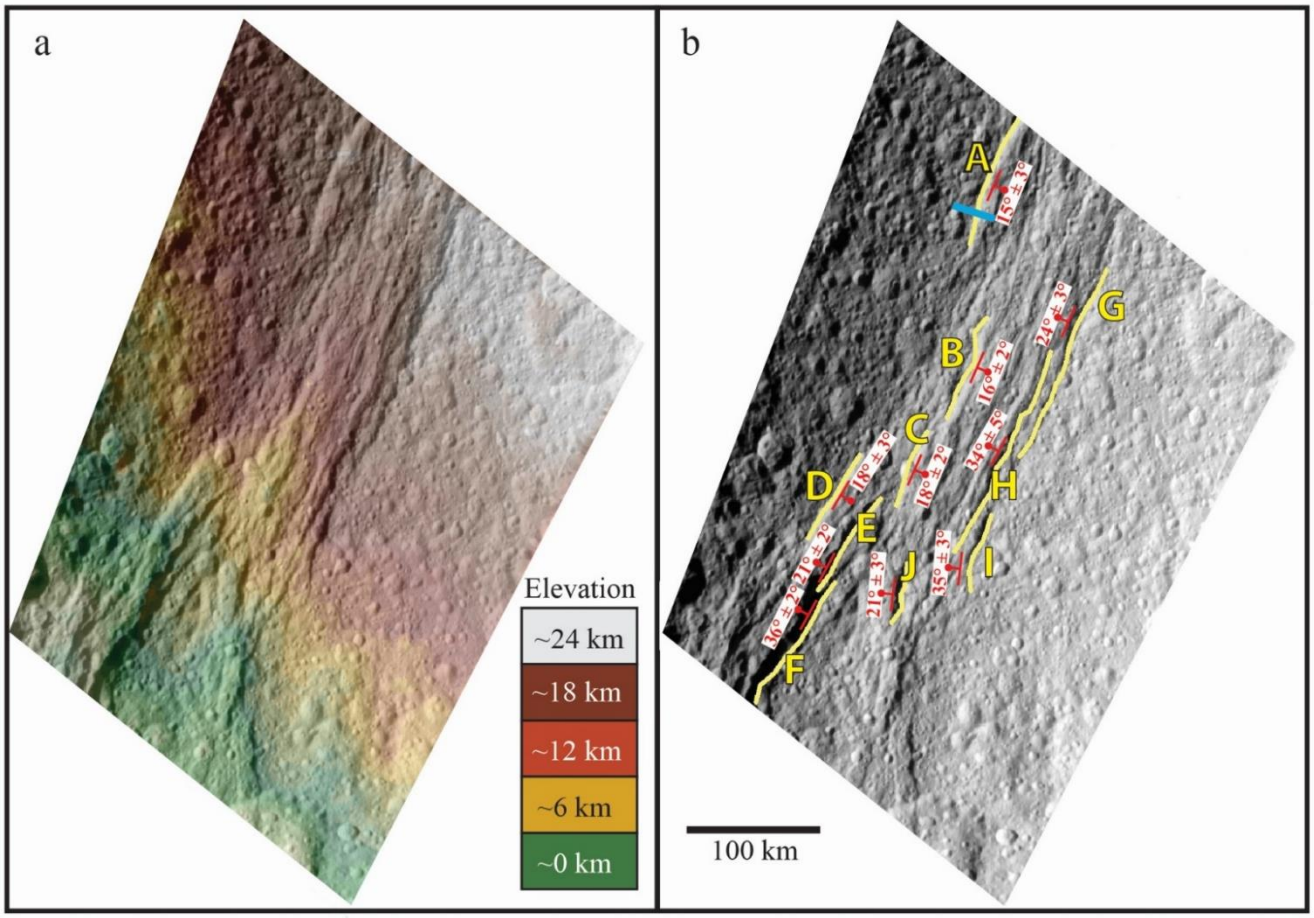

Figure II-6. a) The SOCET SET DEM generated of a section of Ithaca Chasma on Tethys. b) The orthorectified image associated with the DEM in a). The blue line is the location of the topographic profile shown in Figure II-19a. The DEM and orthorectified image was generated using a Cassini ISS image pair.

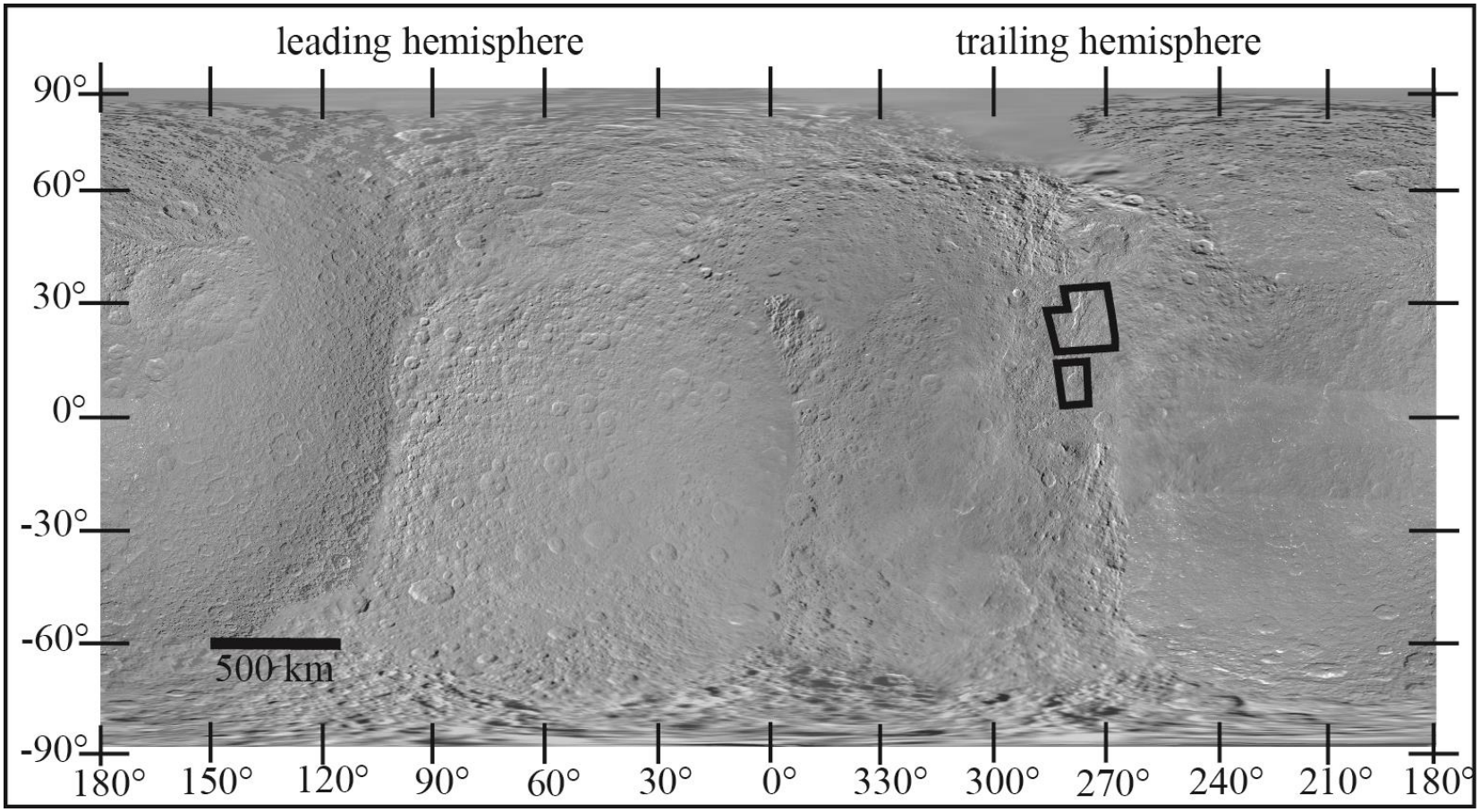

Figure II-7. Mosaic of Rhea, with the region covered by the DEMs (Figure II-8) outlined. The mosaic is a Mercator projection and is made up of Cassini ISS images.

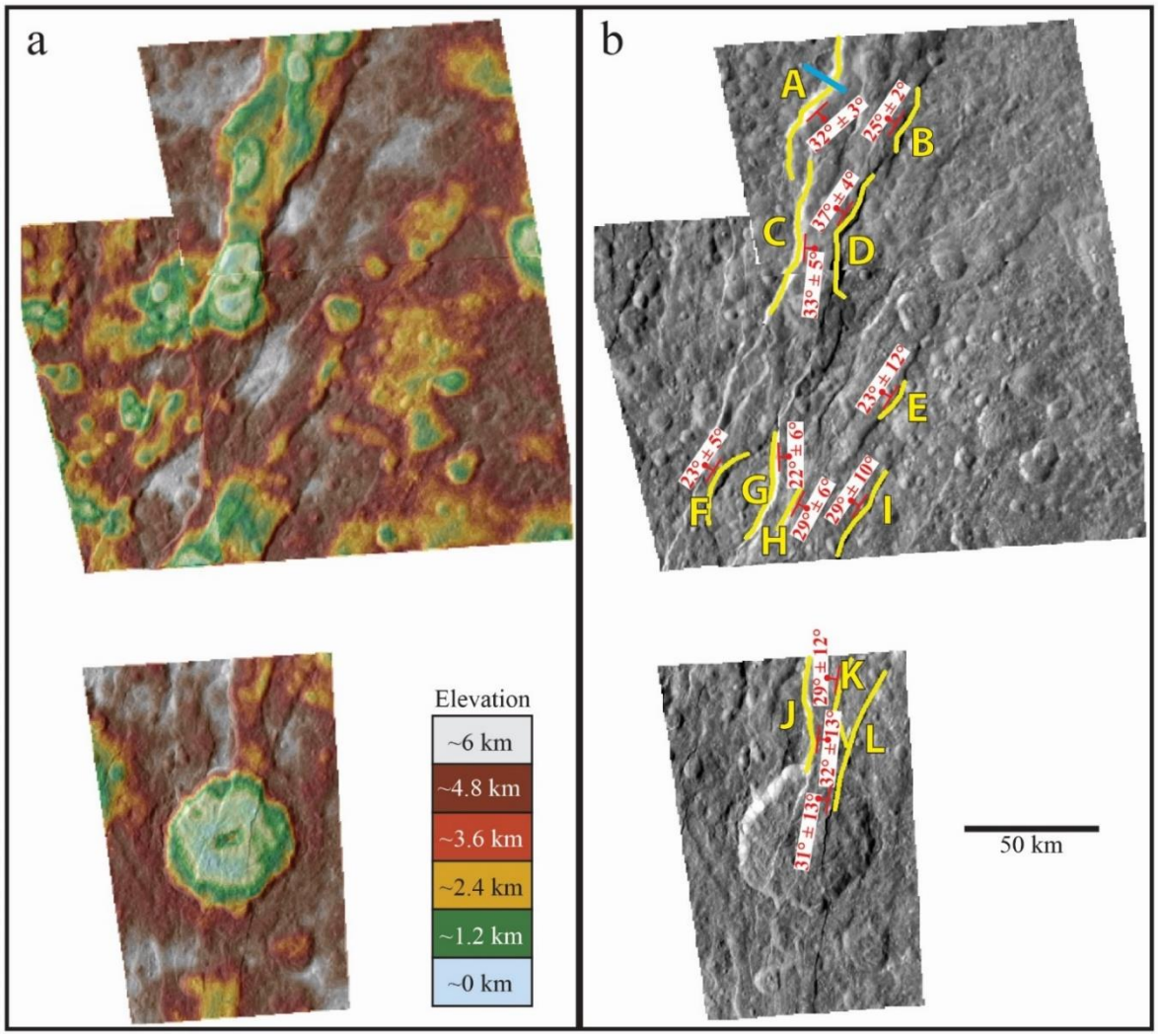

Figure II-8. a) The SOCET SET DEMs used covering of sections of Avaiki Chasmata on Rhea. b) The orthorectified image associated with the DEM in a). The blue line is the location of the topographic profile shown in Figure II-19b. The DEM and orthorectified image was generated using Cassini ISS image pairs.

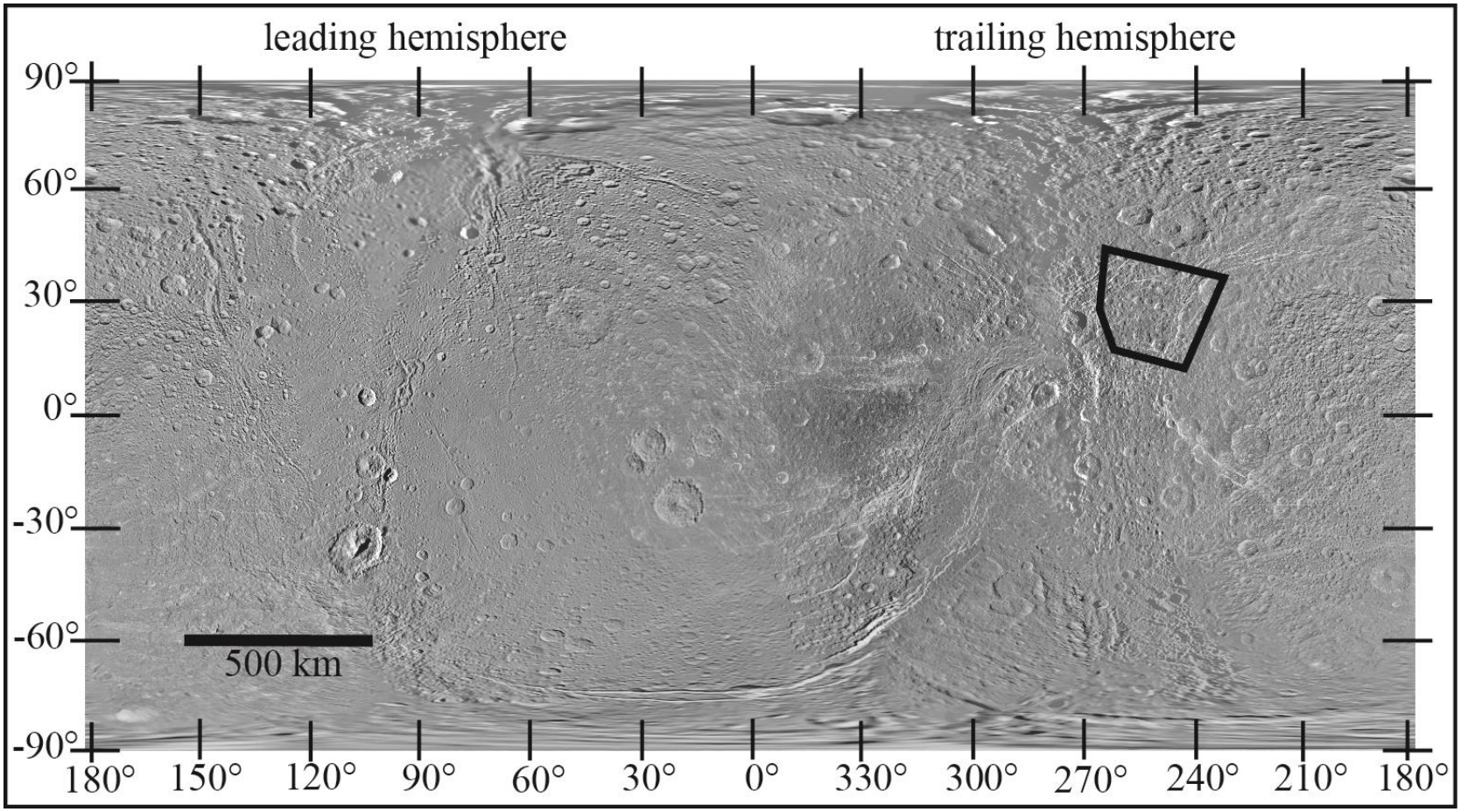

Figure II-9. Mosaic of Dione, with the region covered by the DEM (Figure II-10) outlined. The mosaic is a Mercator projection and is made up of Cassini ISS images.

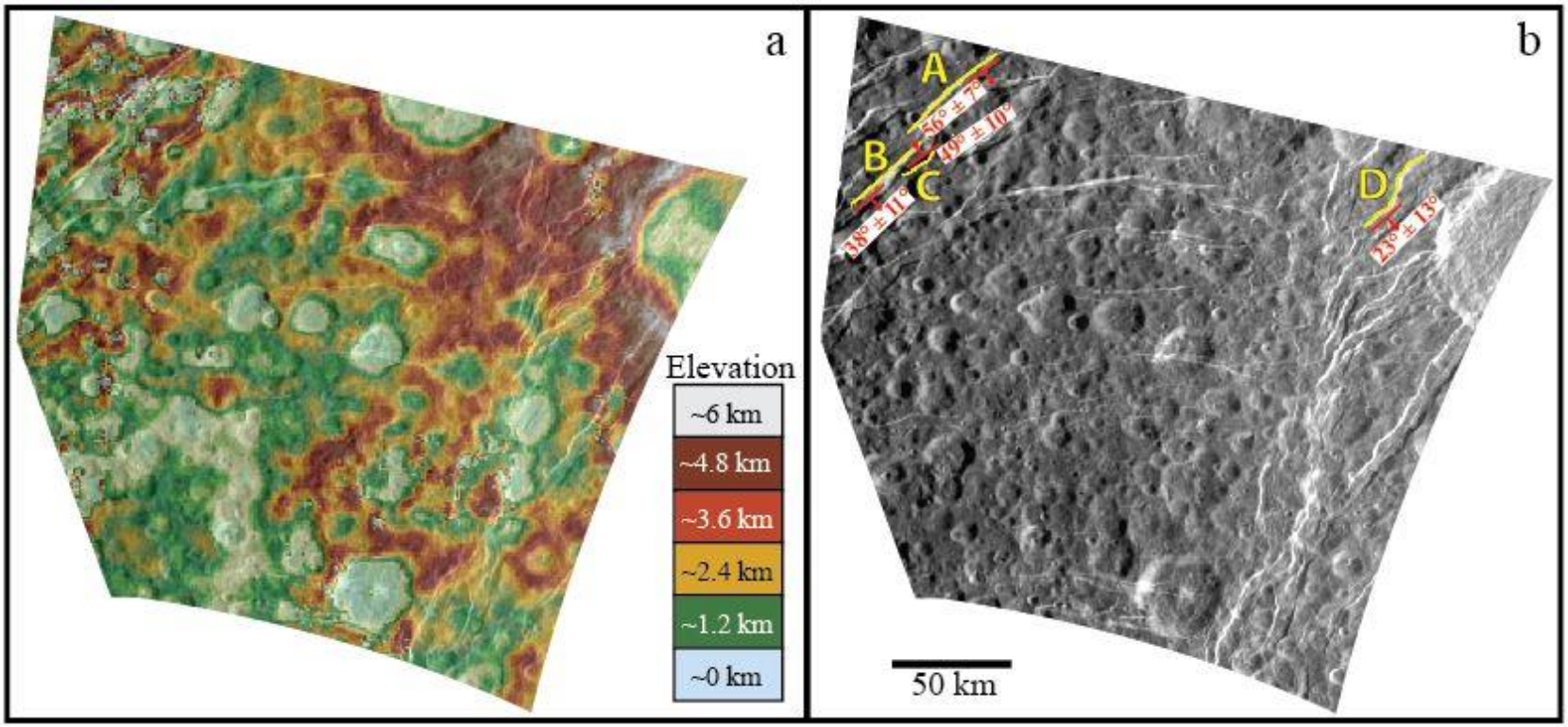

Figure II-10. a) The SOCET SET DEM generated of a section of the Wispy Terrain on Dione. b) The orthorectified image associated with the DEM in a). The DEM and orthorectified image was generated using a Cassini ISS image pair.

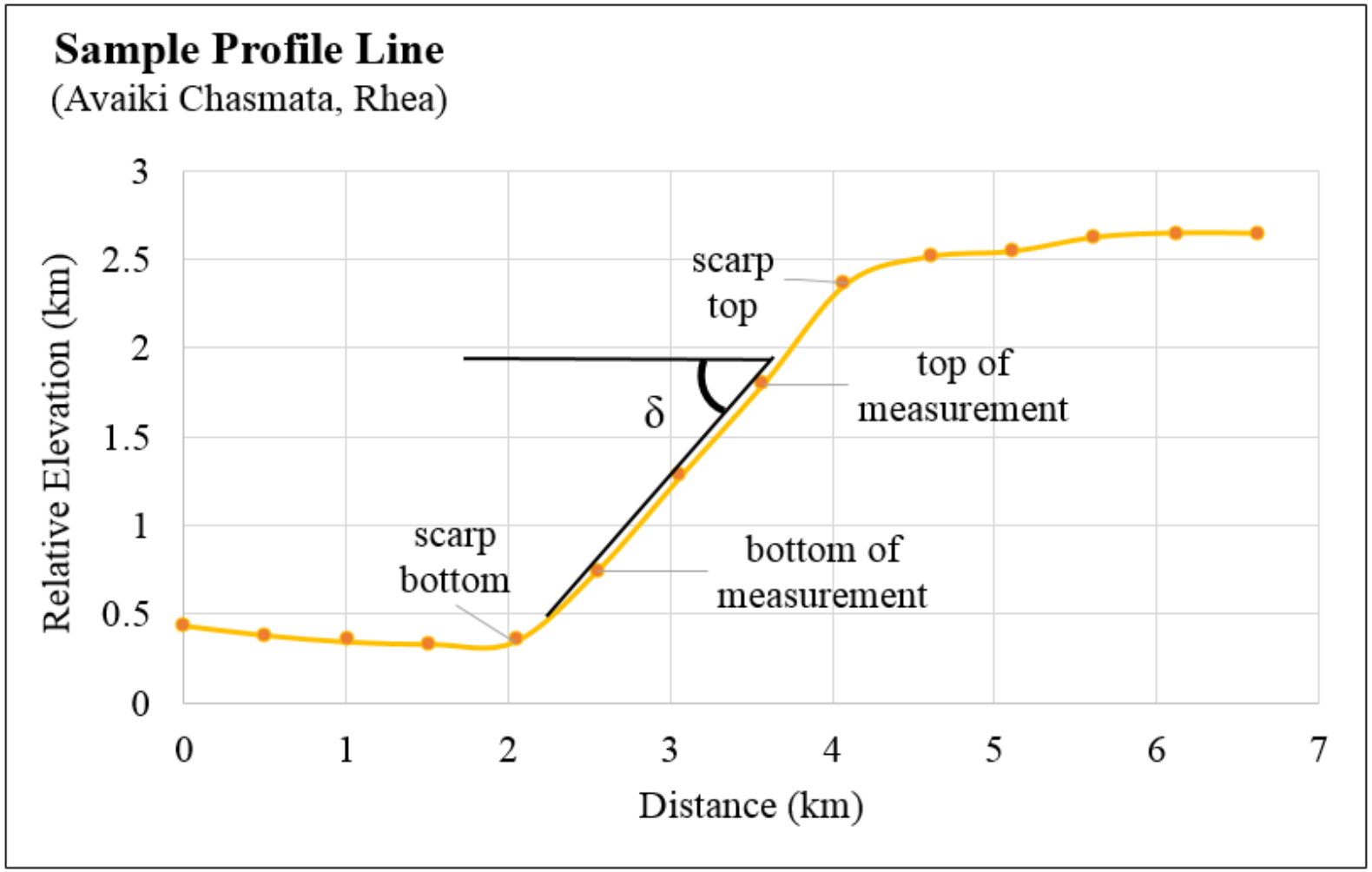

Figure II-11. An example of a profile line across Avaiki Chasmata on Rhea. The method of taking scarp slope measurements is illustrated.

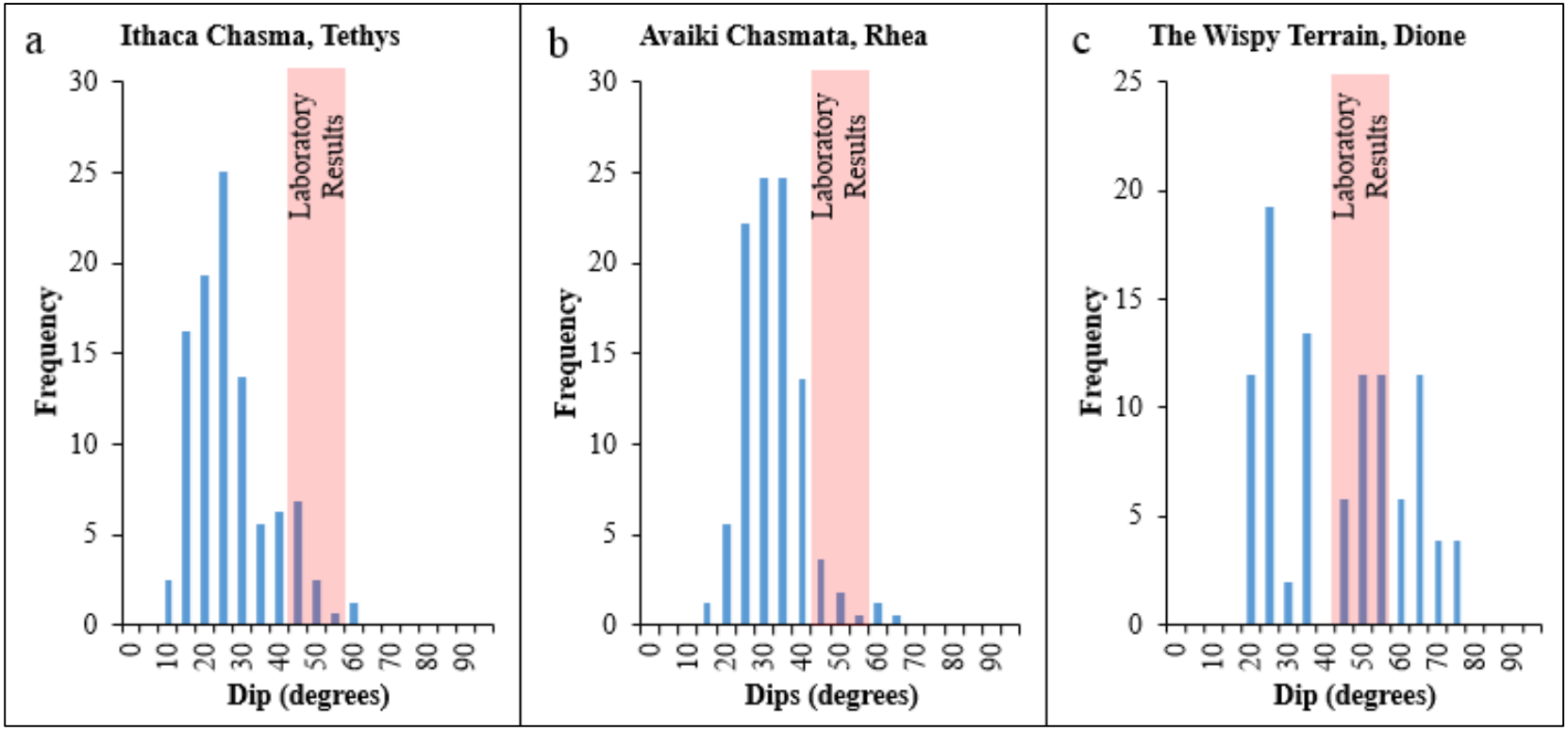

Figure II-12. Histograms of dip measurements with annotated hypothesized dip range derived from laboratory studies of a) Ithaca Chasma on Tethys, b) the Wispy Terrain on Dione, and c) Avaiki Chasmata on Rhea.

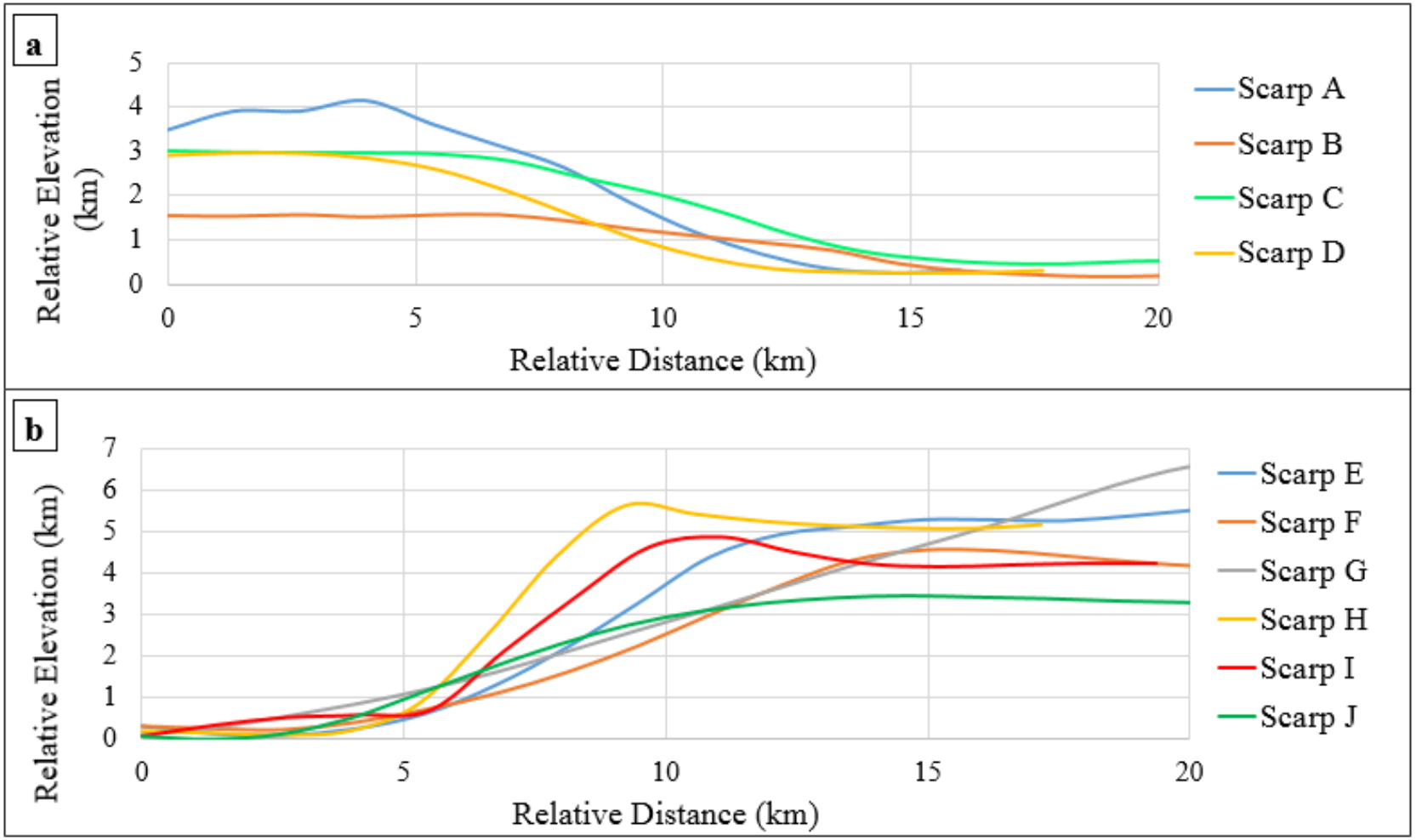

Figure II-13. Example profile lines from each scarp analyzed in Ithaca Chasma on Tethys. For simplicity, these profile lines are separated into a) east dipping fault scarps and b) west dipping fault scarps.

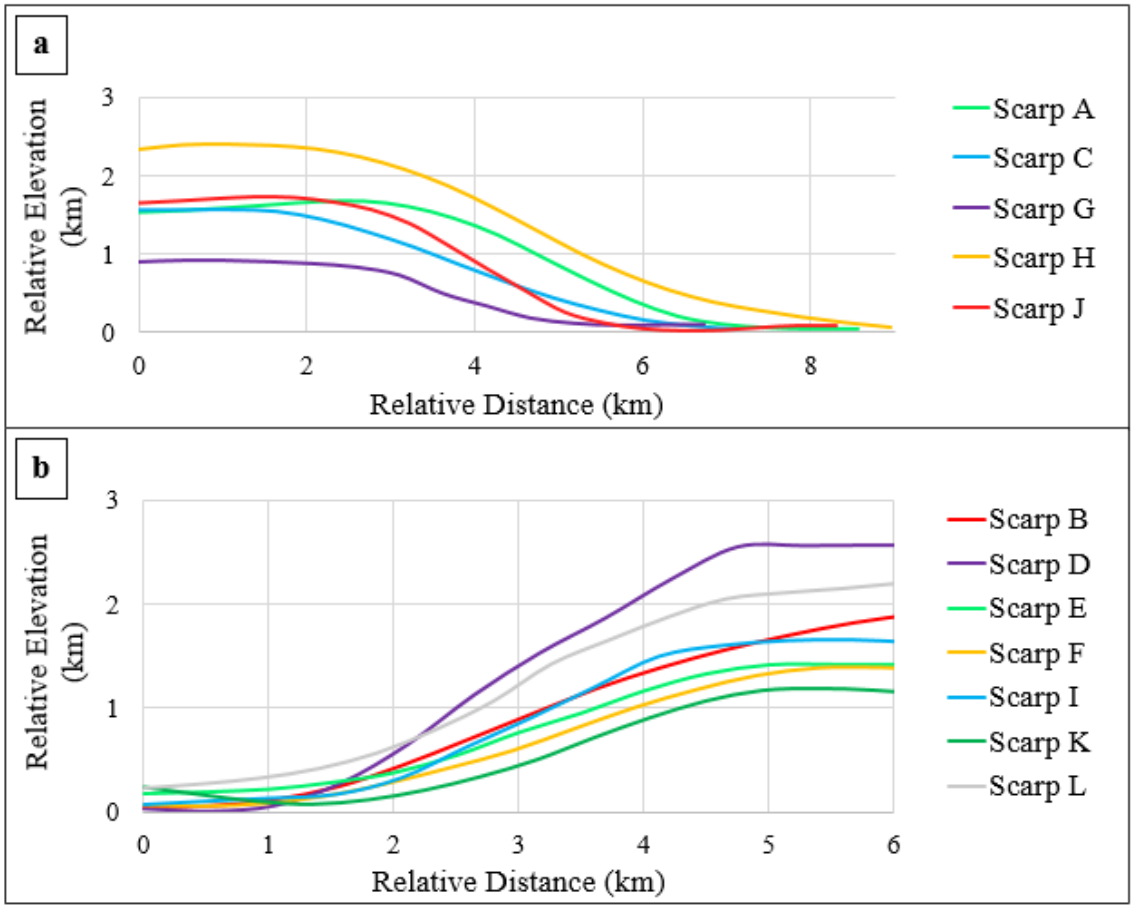

Figure II-14. Example profile lines from each scarp analyzed in Avaiki Chasmata on Rhea. For simplicity, these profile lines are separated into a) southeast dipping fault scarps and b) northwest dipping fault scarps.

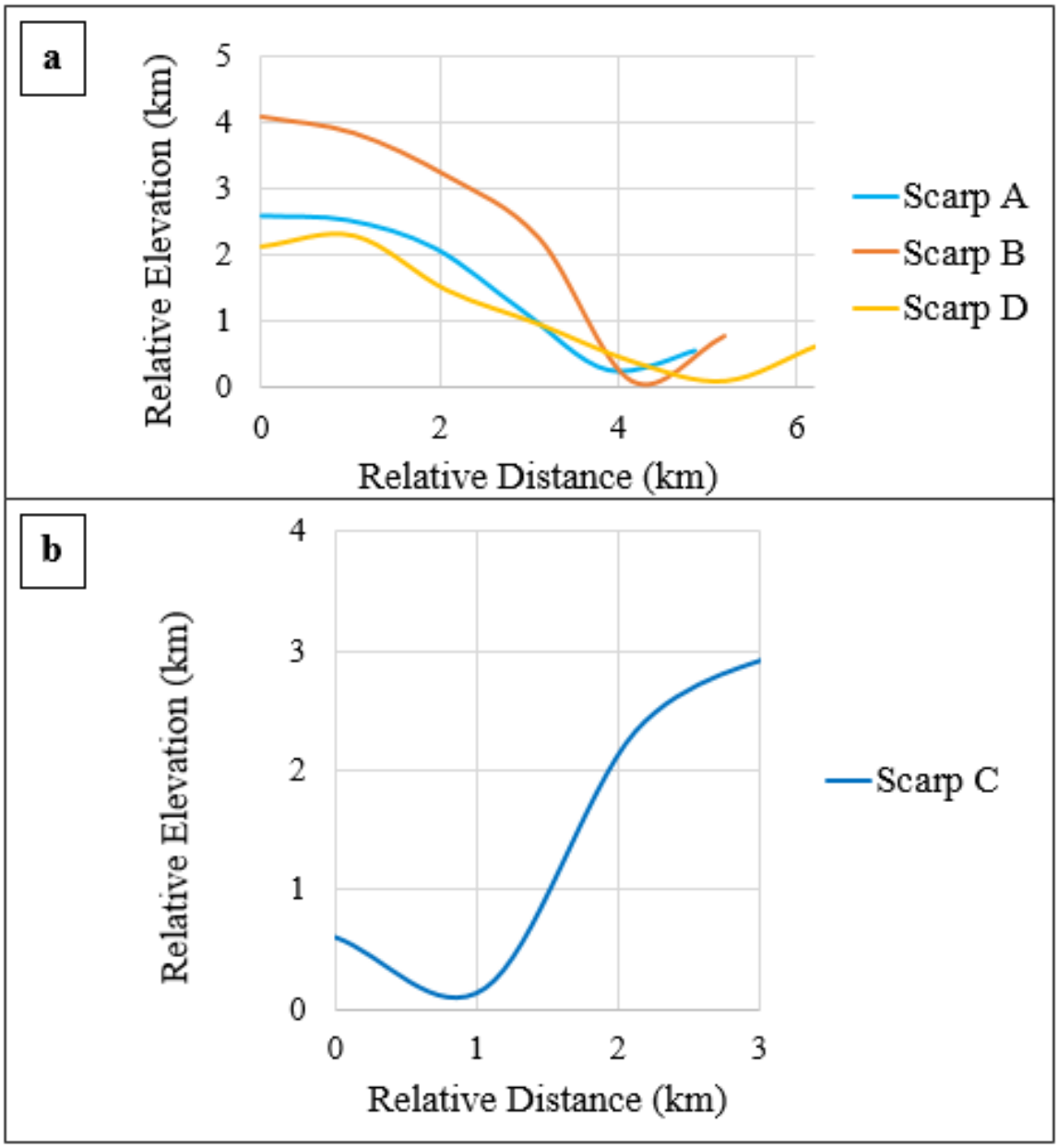

Figure II-15. Example profile lines from each scarp analyzed in the Wispy Terrain on Dione. For simplicity, these profile lines are separated into a) east dipping fault scarps and b) west dipping fault scarps.

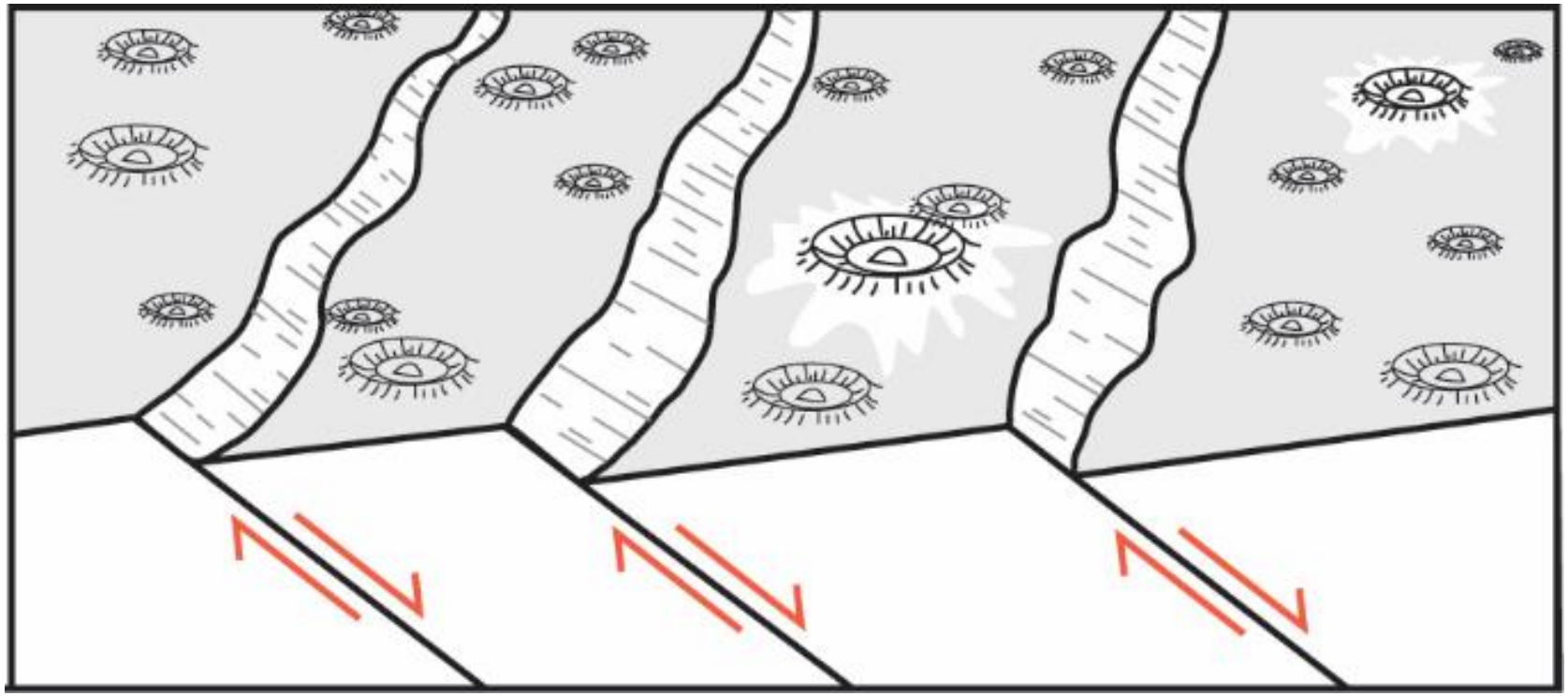

Figure II-16. Idealized illustration of "domino style" fault blocks. Each fault block is bound by normal faults dipping in a single direction. Each block exhibits a fault scarp and a back-tilted face slope (to the left of each fault). Displacement along each fault is shown by the red arrows.

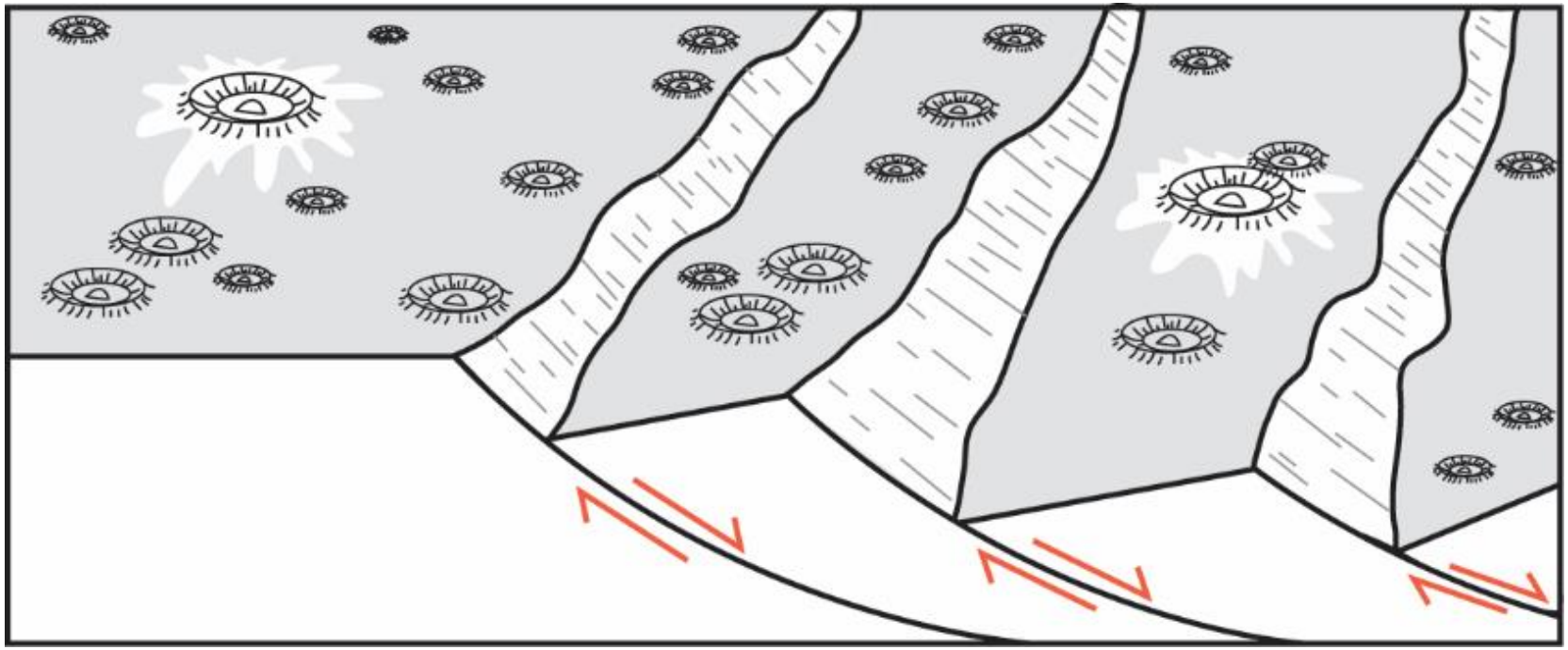

Figure II-17. Idealized illustration of listric normal faults. Listric faults are curved, concave-up faults that decrease in dip with increasing depth. This fault geometry causes a progressive decrease in surface fault dip in the down-dip direction of the fault system. Displacement along each fault is shown by the red arrows.

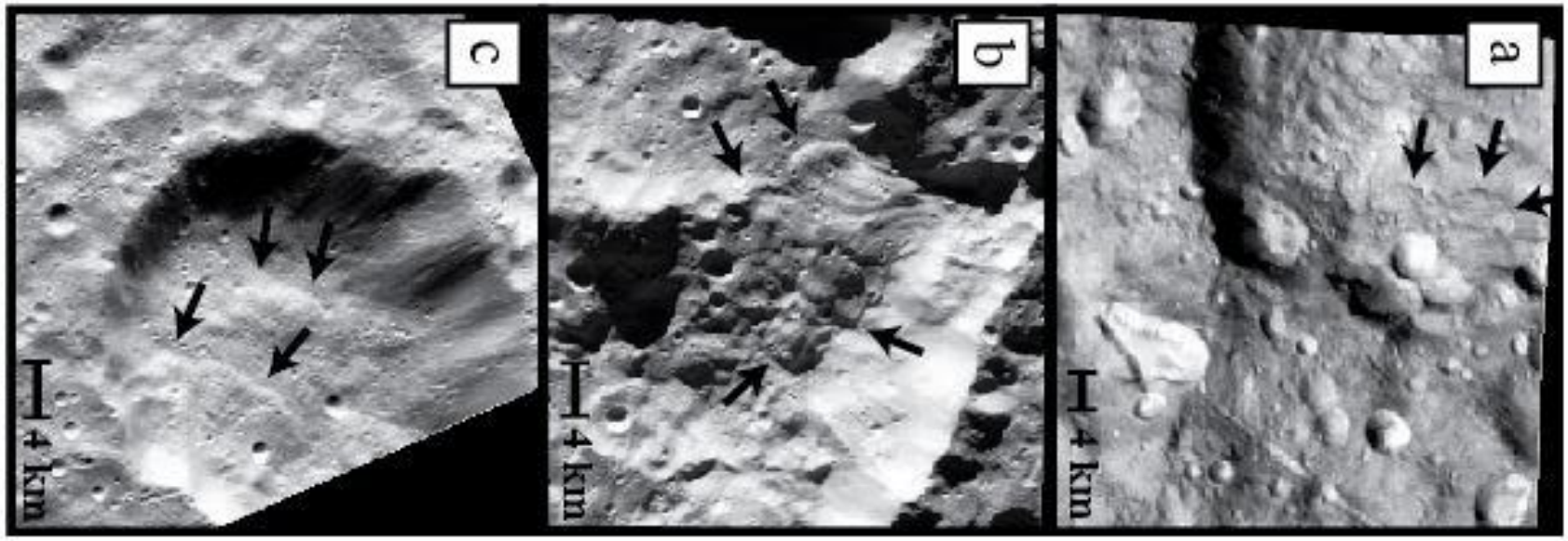

Figure II-18. Evidence for mass wasting in Cassini ISS imagery of Tethys, Dione, and Rhea. Semicircle to tongue-shaped lobes of material are present at the base of impact crater rims. Lobe edges are shown by black arrows. a) Lobes on Tethys shown in image N1506220559 (110 m px^{-1}). b) Lobes on Rhea shown in image N1567129584 (38 m px^{-1}). c) Lobes on Dione shown in image N1714684069.

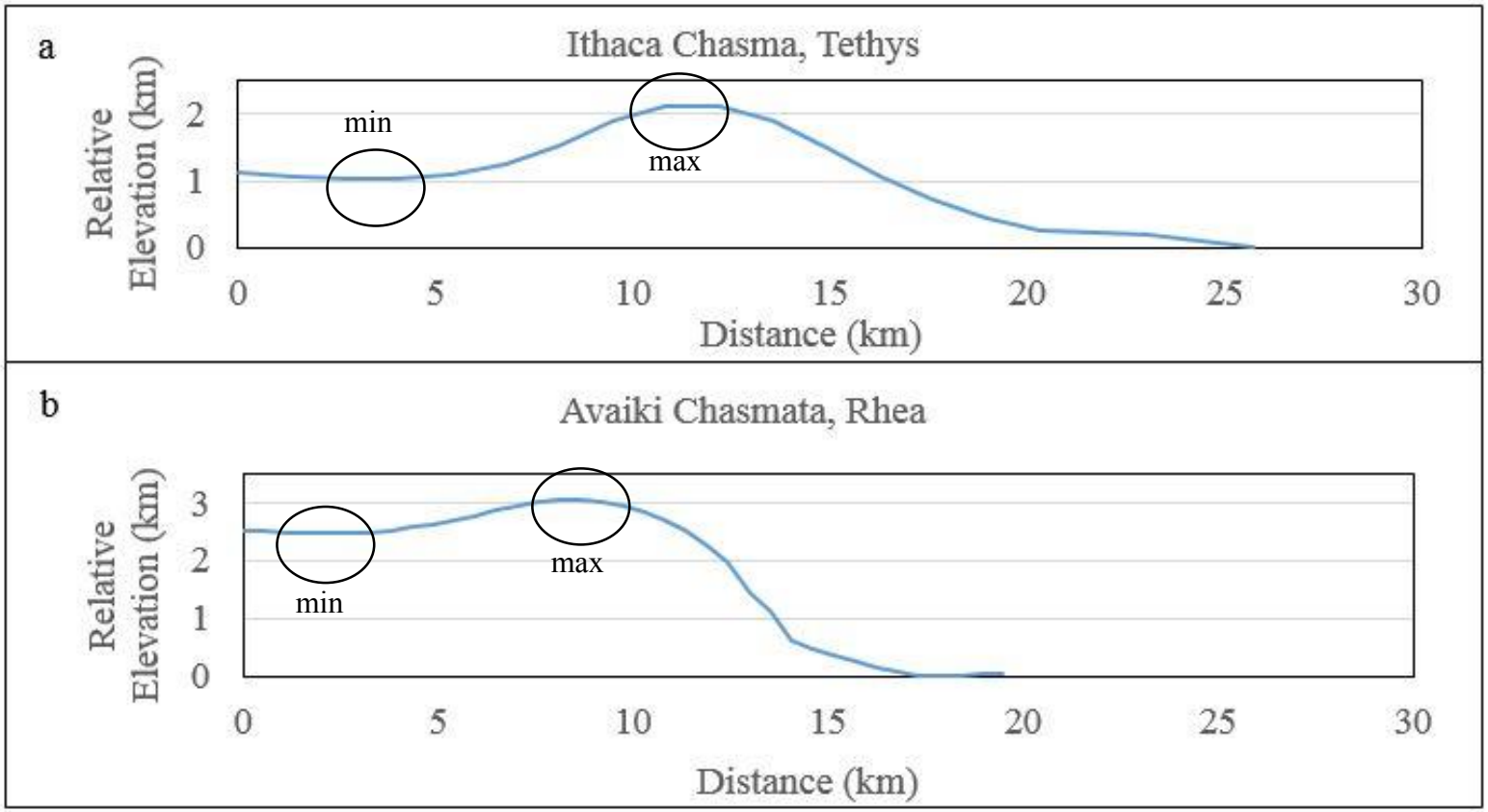

Figure II-19. Examples of raised rim topographic profiles (vertical exaggeration ~2). a) The topographic profile of Scarp A of Ithaca Chasma on Tethys is given. The location of this profile is shown in Figure II-6b. b) The topographic profile of Scarp A of Avaiki Chasmata on Rhea is given. This profile location is shown in Figure II-8b. For each profile line that exhibited a raised rim, the minim elevation was subtracted from the maximum elevation outside the fault system. The slope on the right side of each profile line is the scarp slope. The slope to the left of each profile line is not associated with a scarp, and makes up the raised rim. There is little topography immediately outside the study areas at the resolution of the digital elevation models used, so accounting for background topography was unnecessary.

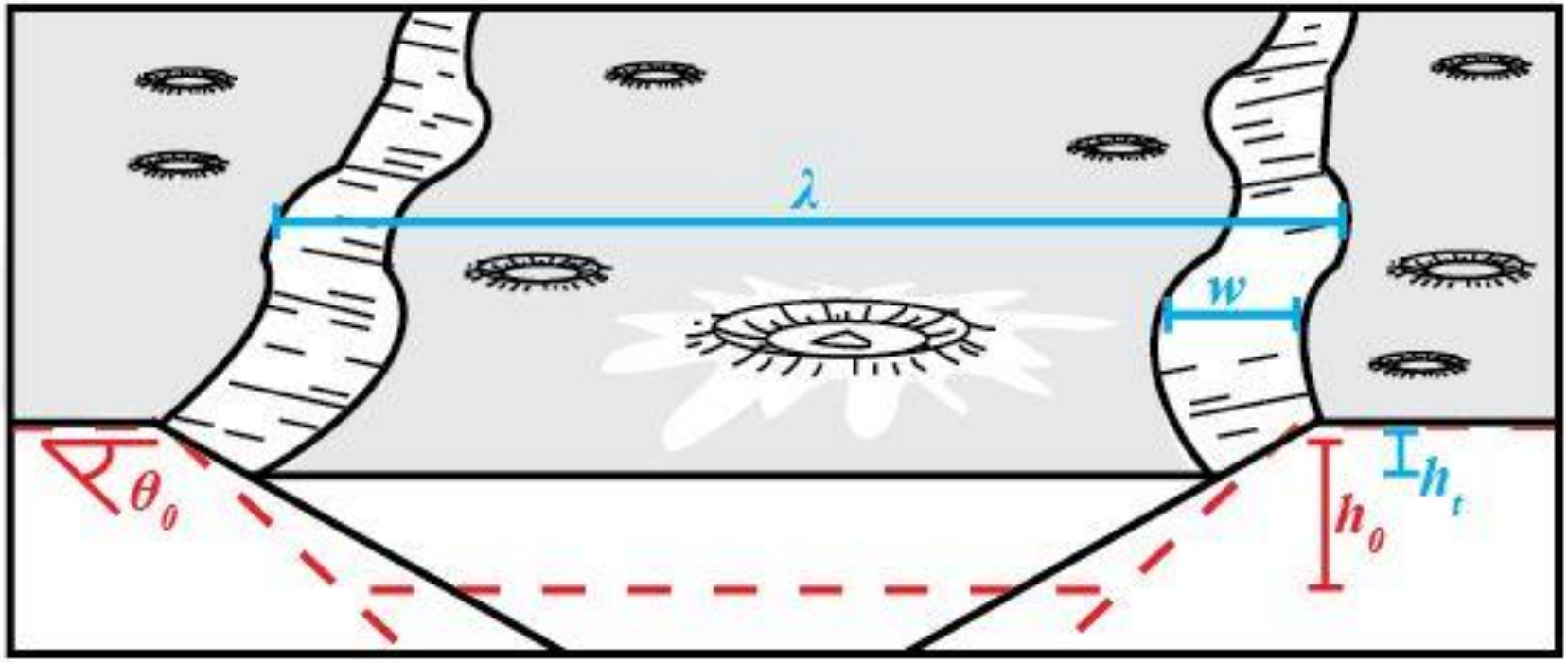

Figure II-20. Idealized illustration of viscous relaxation of normal faults. The dashed line represents the initial topographic profile and the solid line represents the present topography. The height of the current topography, h_t, the width of the graben, λ, the width of the scarp, w, the height of the initial topography, h_0, and the initial scarp dip angle, θ_0, are annotated.

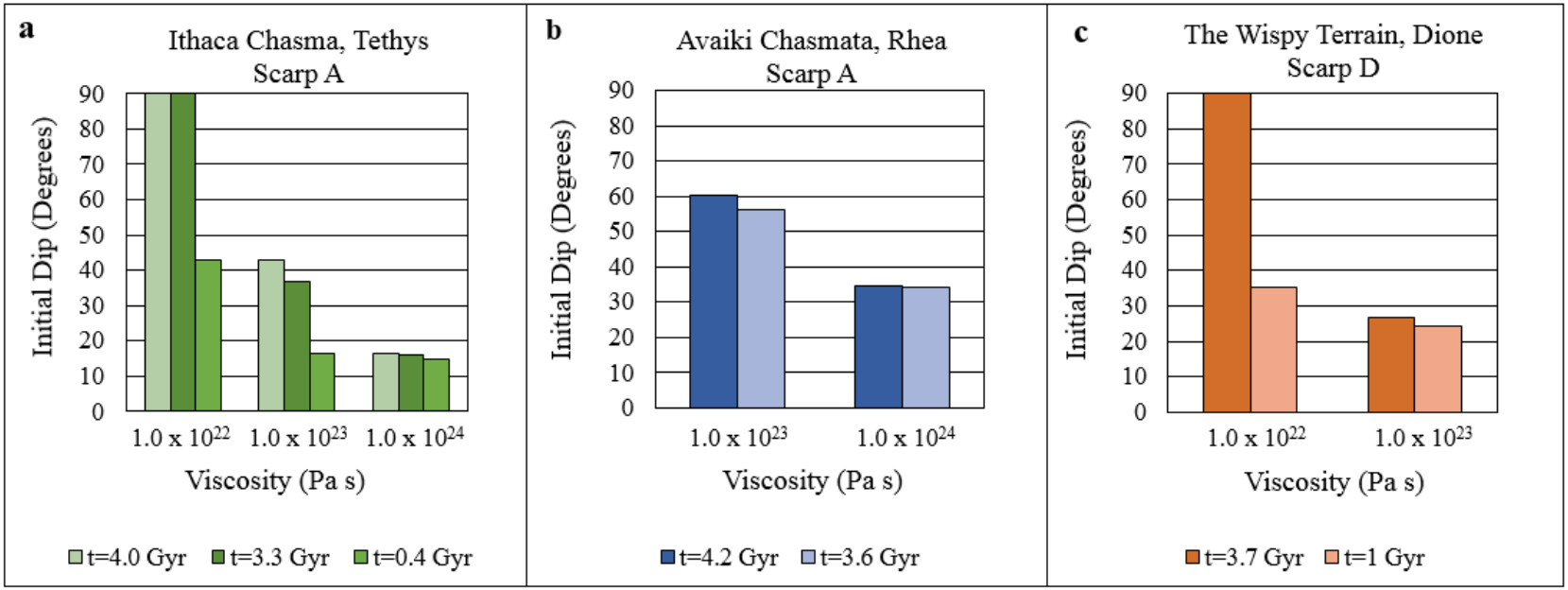

Figure II-21. Illustrations of viscous relaxation calculation results. The results are shown for the different age and mantle viscosity estimates for a) Ithaca Chasma on Tethys, b) Avaiki Chasmata on Rhea, and c) the Wispy Terrain on Dione.

Appendix II-A: SOCET SET DEM Generation

- All DEMs used in this study were generated with the SOCET SET located at the Astrogeology Branch of the USGS in Flagstaff, Arizona. The Cassini Imaging Science Subsystem (ISS) images used to generate the Softcopy Exploitation Toolkit (SOCET SET) DEMs were downloaded from the Planetary Data System (PDS) website (pds.nasa.gov).
- The images were first processed with the Integrated Software for Imagers and Spectrometers 3 (ISIS 3) (*Anderson et al*., 2004) in order to prepare them for import into SOCET SET. The following ISIS commands were run on all images in the order that they are listed. More details about specific ISIS commands can be found on the ISIS website (http://isis.astrogeology.usgs.gov/).
    - The *ciss2isis* command was used to convert the original PDS files (.img and .lbl files) of each image into an ISIS cube file (.cub files).
    - The new image cubes were then associated with a camera model for ISS and augmented with spatial information (geometries of the spacecraft, sun angle geometries, ground positions, etc.) appropriate for the image acquisition time by using ISIS's *spiceinit* command.
    - The *cisscal* command was used to convert the data number (DN) values of the images to reflectance.
    - The *noisefilter* command was used to apply a noise filter to a cube. In this step, the noise within the images was replaced and average DN value of the surrounding pixels.
    - The *campt* command was run in order to compute the geometric and photometric information about each image. The ground pixel resolution and off nadir angle of each image is needed in order to generate the final DEMs with SOCET SET in later steps.
    - The *socetframesettings* command was then run in order generated settings files (.set files) for each image, which is required for importation of the images into SOCET SET.
    - The *enlarge* command was used to enlarge the pixel dimensions of each image using cubic convolution.
    - The *bit2bit* command was used to change the bit-type of each cube to an 8-bit image, necessary for importation into SOCET SET.
- Separate projects were created, each including one or multiple stereo pairs that overlapped significantly and that had images with similar resolutions. Two projects were created for stereo image pairs that cover Ithaca Chasma, Tethys. Four projects were created for Avaiki Chasmata on Rhea, and three projects were created for the stereo pairs that cover the Wispy Terrain on Dione.
    - The information for each coordinate system of each satellite was taken from the information available from the Gazetteer of Planetary Nomenclature developed by the International Astronomical Union (IAU) Working Group for Planetary System Nomenclature (WGPSN). (Specific information about each coordinate system is regularly updated and can be found at the following

website: http://planetarynames.wr.usgs.gov/TargetCoordinates) The available coordinate system information for each satellite in this study at the time these DEMs were generated (January, 2014) are:

- Tethys: Spherical with a radius of 536.3 km
- Rhea: Spherical with a radius of 764.2 km
- Dione: Spherical with a radius of 562.5 km

- Multi-Sensor Triangulation (MST)
  - The purpose of MST is to orient and register overlapping images to each other by performing bundle adjustment in order to improve matching of identical features in each image of a stereo pair (in later steps) during digital elevation model generation. Bundle adjustment is performed by improving the values for the camera parameters of the Cassini spacecraft that were estimated during imaging. The nadir-most image (stated in the output files from the ISIS *campt* command explained above) was not changed, and the position and pointing of the other images were adjusted to the centermost image. The nadir-most image was chosen as a reference for the other system in order to make the resulting DEMs as horizontal relative to the true satellite surface as possible.
  - The accuracy values of the initial estimates for each math model parameter used for MST were attuned specifically for the Cassini spacecraft. The purpose of the accuracy values are to prevent SOCET SET from changing the camera parameters more than a realistic amount. All images other than the nadir-most image in each project were allowed to adjust. The accuracy values used for each parameter that was allowed to adjust for these images are as follows:
    - Camera X M,Ft (spacecraft position in the in-track axis): 2000 meters
    - Camera Y M,Ft (spacecraft position in the cross-track axis): 2000 meters
    - Camera Z M,Ft (spacecraft position in the axis radial to the planet (vertical axis)): 500 meters
    - Omega Deg (rolling of the spacecraft from side to side): 0.00001 degrees
    - Phi Deg (pitch of the spacecraft): 0.00001 degrees
    - Kappa Deg (twist around the axis of the spacecraft): 0.001 degrees
  - Interactive Point Measurement (IPM) was used to generate tie points and z-only points between multiple overlapping images. A few z-only points were added around the edges of the DEMs to avoid tilted of the resulting DEMs. Enough tie points were made so that the y-parallax distortion was minimized for all images in each project and so that the root mean square (RMS) residual errors of the adjustment were below 0.6 pixels (Table II-2).
    - If the resulting RMS value of a project was above 0.6 pixels, then the residual tie-points and/or z-only points were re-measured until an acceptable RMS value was achieved.
- Epipolar (Pairwise) Rectification was then performed on all of the image pairs in order to enhance the stereo visualization of the stereo image pairs, allowing for more

accurate matching during the DEM generation process (next step). Pairwise rectification works by resampling each image in a stereo pair so that they have the same image resolutions.

- The Next Generation Automatic Terrain Extraction (NGATE) was then used to generate a digital elevation model (DEM) by correlating overlapping pixels in one stereo pair image with pixels in the other image.
    - The user can specify a specific post spacing (resolution) for the final DEM during this step. For all of the DEMs we generated, we used a post spacing of approximately three times the average of the resolutions of the two images used (Table II-2). We used lower resolutions for the DEMs than the input image resolutions because of the unlikelihood that NGATE would identify single pixel correspondences in both of the input images. Multiple pixels in each image are needed to identify surface features that are the captured in both images of a stereo image pair.
    - Because the images used were of low resolution, the NGATE strategy file was altered so that only three passes (instead of the seven passes used for high resolution imagery) were performed.
- The Automatic Extraction (AATE) program was then used in order to fix any blocky texture in the output NGATE DEMs. The adaptive.strat strategy file was used when running AATE on all the NGATE DEMs.
- Orthorectified images were generated for each DEM, both at the nominal image resolution and at the resolution of its associated DEM. The purpose of producing orthorectified images is to remove distortions due to terrain relief and obliquity of the spacecraft so that more accurate measurements can be taken.
- All of the resulting DEMs and orthorectified images were exported from SOCET SET and were converted into an ISIS and ArcMap compatible cube (.cub file).
- The DEM and orthorectified image cube files were then imported into ESRI's ArcMap software for analysis and data collection. Equidistant cylindrical projections were used for all ArcMap projects.
- Vertical accuracy calculation (*Kirk et al*., 2003)
    - The vertical accuracy (*VA*) of each DEM (also known as the expected precision) depends on the stereo convergence angle of the image pair, as well as the resolutions of the images as shown by,

$$VA = \rho GSD \frac{P}{H} \qquad \text{(II-A1)}$$

      where ρ is the matching accuracy in pixels, *GSD* is the root mean square value of the ground sample distance (image resolution) of the image pair, and *P/H* is the parallax – height ratio.
    - The values to use for ρ depends on the quality of the images used in the images pair (personal communication with Annie Howington). For image pairs that are comprised of limb images, ρ = 0.3 is used. For non-limb image pairs, ρ = 0.2 is used.

- *P/H* is calculated with
- *P/H* is calculated with

$$\frac{P}{H} = \sqrt{(PX_1 - PX_2)^2 + (PY_1 - PY_2)^2} \quad \text{(II-A2)}$$

where PX_1 and PY_1 refers to the parallax in the X and Y directions respectively of one of the stereopair images. PX_2 and PY_2 refers to the parallax in the X and Y directions of the other image.

$$PX = -\tan(EA)\cos(SGA) \quad \text{(II-A3)}$$

and

$$PY = \tan(EA)\sin(SGA) \quad \text{(II-A4)}$$

where *EA* is the emission angle, and SGA is the subspacecraft ground azimuth.

- The *caminfo* command in ISIS was used to generate text files associated with each image, containing image and camera information. The values for EA, SGA, and GSD for each image were collected from this text file, and used to calculate VA (Table II-2).

Appendix II-B: ASP DEM Generation

- DEMs were generated with the Ames Stereo Pipeline (ASP) software (Broxton and Edwards, 2008; Moratto et al., 2010).
- Images from the ISS camera onboard the Cassini spacecraft were processed and map-projected using the ISIS software (Anderson et al., 2004). The processing steps used on the images are as follows:
  - Cassini ISS images were downloaded from the PDS website (pds.nasa.gov).
  - The images were converted from their initial PDS format (.lbl and .img files) to ISIS image cubes (.cub files) using ISIS's *ciss2isis* command.
  - The new image cubes were then associated with a camera model for ISS and augmented with spatial information (geometries of the spacecraft, sun angle geometries, ground positions, etc.) appropriate for the image acquisition time by using ISIS's *spiceinit* command.
  - The data number (DN) values of the images were converted to reflectance by using the *cisscal* command.
    - The *noisefilter* command was used to apply a noise filter to a cube. In this step, the noise within the images was replaced and average DN value of the surrounding pixels.

- The images were then projected into an equirectangular projection using ISIS's *cam2map* command.
- The images were map-projected using ISIS's *cam2map* command for subsequent easy identification of common features in both images by ASP. The lowest resolution image of each pair was map-projected first, and then the highest resolution image of each pair was projected to the lowest resolution image, so that each image in a pair were projected around the same point in latitude and longitude space. Projecting the highest resolution image to the lowest resolution image was done to prevent stretching of the lowest resolution image, which would have occurred if the images were projected in the opposite order.

ASP processing steps:

- The *stereo* command was used to generate an output TIFF point cloud file from each image pair. Each point cloud file consists of spatial information in three dimensions.
- The *point2dem* command was then used to generate a DEM from each point cloud file in the form of a TIFF file with georeferencing information stored as GeoTIFF tags. During this step, the DEM was projected with the Geospatial Data Abstraction Library (GDAL) command.
    - For the *point2dem* command, the user can specify a specific post spacing for the final DEM (or final DEM resolution) by using the *--dem-spacing* argument. We used a lower resolution for the DEMs than the resolution of the input images because of the unlikelihood that ASP would identify a single pixel correspondence in both of the input images, meaning that multiple pixels in each image are needed to identify surface features that are the same in both images. For all of the DEMs we generated, we used a post spacing of three times the average of the resolutions of the two images used.
    - TIFF files of the DEMs and orthorectified images of the region of the ISS image covered by the DEM were generated by the *point2dem* step. These TIFF files (the DEM, the intersection error map, and the orthorectified image) for each stereo image pair were imported into ESRI's ArcMap software for analysis.

Appendix II-C: DEM Comparisons

- To further analyze the accuracy of the SOCET SET DEMs used in this study, we compare the average dip values collected on the DEMs used in this study with DEMs generated using the same image pairs with ASP.
- For each DEM, we analyzed the dips of a single scarp. We chose the scarp with the most dip measurements in the DEM used in this study.
- We took the same number of scarp slope measurements on the ASP DEM as the SOCET SET DEMs used in this study.

- As shown in Table II-C1, we compared the set of collected data on each ASP DEM with the associated SOCET SET DEM by using a two-sample statistical test. To determine if a nonparamentric Mann-Whitney U test or a parametric one-sample t-test should be used, we tested each set of collected data for normality using the Shapiro-Wilk test. Because all sets of data collected were normally distributed, we use the one-sample t-test for all analyses.
- To further analyze the accuracy of the SOCET SET DEMs, we compare the average dip values collected on the DEMs used in this study with another DEMs covering the sample locations generated by SOCET SET, but using different image pairs.
    - Ithaca Chasma, Tethys – a DEM generated using a different set of image pairs was used (Table II-C2)
    - Avaiki Chasmata, Rhea – Two of the SOCET SET DEMs used in this study overlap. We compare the average dip values in the overlapped section of these two DEMs.
    - The Wispy Terrain, Dione - We were unable to find image pairs of the region that we analyzed, so the SOCET SET DEM used was not compared to another SOCET SET DEM.
  - Similar to the method used in Appendix II-C, we analyzed the dips of a single scarp within the coverage of each DEM. We chose the scarp with the most scarp slope measurements covered by the DEM used in this study.
  - We took the same number of scarp slope measurements on both SOCET SET DEMs.
  - As shown in Table II-C3, we compared the set of collected data of each scarp analyzed, covered in the two different DEMs by using a two-sample statistical test. To determine if a nonparamentric Mann-Whitney U test or a parametric one-sample t-test should be used, we tested each set of collected data for normality using the Shapiro-Wilk test.

Table II-C1. Comparison between SOCET SET and ASP DEMs. The Cassini ISS image pairs, the difference in average scarp slope measured, and results of statistical tests are shown.

Image Pair	**Difference in Fault Slope (SOCET SET vs. ASP)**	**Shapiro-Wilk Test**	**T-test**	
		ASP p-value	***Statistically Similar?***	***p-value***
Ithaca Chasma, Tethys				
Scarp F				
N1489061272 & N1489061678	1°	0.269	Yes	0.554
Avaiki Chasmata, Rhea				
Scarp A				
N1637519986 & N1637520407	1°	0.711	Yes	0.412
Scarp G				
N1637519768 & N1637520407	5°	0.391	No	< 0.001
Scarp I				
N1637519574 & N1637520407	4°	0.460	No	0.03
Scarp J				
N1637519392 & N1637520350	2°	0.752	Yes	0.413
The Wispy Terrain, Dione				
Scarp B				
N1662199979 & N1662200068	5°	0.458	Yes	0.333

Table II-C2. The image pairs used to make additional SOCET SET DEMs. These DEMs were not used in this study, but cover the same areas as the SOCET SET DEMs used in this study.

Image Pair Product IDs	Image Resolution	DEM Resolution	Off-nadir Angle	Number of Tie Points	RMS Value	Vertical Accuracy
Ithaca Chasma, Tethys						
N1489061272 & N1489062260	497 m/px	1.4 km/px	0.025 rad	44	0.489 px	402 m
	498 m/px		0.028 rad			621 m

Table II-C3. Comparison between SOCET SET DEMs. The SOCET SET DEMs used in this study were compared with other overlying SOCET SET DEMs not used in this study.

Image Pairs	Average Fault Slope Difference	Shapiro-Wilk Test	t-test	
		p-value (2nd DEM) / Test Used	Statistically Similar?	p-value
Ithaca Chasma, Tethys				
Scarp F				
N1489061272 & N1489061678 / N1489061272 & N1489062260	1°	0.142 t-test	Yes	0.848
Avaiki Chasmata, Rhea				
Scarp G				
N1637519768 & N1637520407 / N1637519574 & N1637520407	4°	0.036 Mann-Whitney U Test	No	0.02

Chapter III
Polygonal Impact Craters on Dione: Evidence for Tectonic Structures outside the Wispy Terrain

This chapter is a reformatted version of a paper by the same name in preparation for submission to Icarus by Chloe Beddingfield, Devon Burr, and Liem Tran. All data collection and analyses were performed by Chloe Beddingfield.

Abstract

Plan-view impact crater geometries can be indicative of pre-impact structures within the target material. Impact events that occur on a pre-fractured surface generate craters exhibiting large scale straight rim segments with intervening angles, termed polygonal impact craters (PICs). Impact craters that appear to be PICs are abundant on the surface of Saturn's icy satellite, Dione, both within Dione's Wispy Terrain, a region with large visible fractures, and also outside the Wispy Terrain (the 'Non-Wispy Terrain'), where less evidence for fracturing has been observed. In the Non-Wispy Terrain, subtle lineaments are hypothesized to be NE-SW, NW-SE, and E-W trending fractures, suggesting that tectonism may have been an important process in this terrain.

Results of previous studies have shown that PIC straight rim segment azimuths (PIC azimuths) commonly parallel pre-impact fracture azimuths, although disagreements about this relationship exist in the literature. We investigated the hypothesis that fractures, either subtle or not visible with available spacecraft images, are present within Dione's Non-Wispy Terrain. Our first step was to assess the relationship between PICs and pre-existing fracture azimuths in the Wispy Terrain. Our results from this initial assessment show a parallel relationship between PIC azimuths and fracture azimuths. Based on this correlation in the Wispy Terrain, we accept that this relationship would hold true in the Non-Wispy Terrain if PICs are present.

We tested for PICs using crater rim azimuth data collected from randomly distributed study locations throughout the Non-Wispy Terrain. From these data, we identify widespread PICs in this terrain, which supports the hypothesis that subtle fractures are also present. Analysis of the PIC crater rim azimuth data yield a pattern for these inferred fractures across Dione's surface that is consistent with the hypothesized global deformation that would result from a combination of satellite despinning and volume expansion. Our results provide evidence of previously hypothesized events in Dione's history and demonstrate that mapping PICs and their azimuths a useful tool for investigating subtle fractures on solar system bodies.

Introduction

Impact craters commonly exhibit circular plan-view geometries (Figure III-1a), and are inferred to result from impact events in homogenous target material (e.g.,

Melosh, 1989). However, where pre-existing fractures exist in the target material, impact craters commonly exhibit plan-view geometries with straight rim segments, creating polygonal plan-view geometries (Figure III-1b) (e.g., Fielder, 1961a, 1961b; Kopal, 1966; Shoemaker, 1962, 1963; Roddy, 1978; Öhman et al., 2005a, 2005b). Whereas other types of impact crater morphologies, including those with non-circular plan view geometries, are caused by various conditions other than pre-existing fractures, the only known cause for the formation of PICs is the influence of pre-existing sub-vertical structures within the target material (e.g., Öhman, 2009). These structures include faults, joint sets, and lithologic boundaries (e.g., Fielder, 1965; Eppler et al., 1983; Öhman et al., 2005a, 2005b; Öhman, 2009; Aittola et al., 2010). For simplicity, we refer to these sub-vertical structures as fractures. Consequently, these circular impact craters (CICs) (Figure III-2a) and polyongal impact craters (PICs) (Figure III-2c) may be useful tools to distinguish between homogenous and tectonized terrains on the surfaces of planetary bodies.

Multiple PIC formation models predict that azimuths of PIC straight rim segments, which we term 'PIC azimuths', parallel surrounding target fracture azimuths (Eppler et al., 1983; Kumar and Kring, 2008; Poelchau et al., 2008, 2009; Öhman, 2009). This relationship is agreed upon in the literature for complex PICs, although not for simple PICs (Eppler et al., 1983; Kumar and Kring, 2008). One of the three proposed PIC formation models for simple craters predicts a 45º offset between PIC azimuths and controlling fracture azimuths (Eppler et al., 1983). However, more recent studies show that evidence better supports a parallel PIC-fracture azimuth relationship (Kumar and Kring, 2008; Öhman et al., 2008). In support of this parallel relationship, simple and complex PIC azimuths have been found to be indistinguishable in the same study areas (Öhman et al., 2008), contradicting findings by Eppler et al. (1983).

Both CICs and PICs are widespread throughout the Solar System, existing on both rocky and icy planetary bodies (e.g., Öhman, 2009). On Saturn's icy satellite, Dione, apparent CICs (Figure III-1a) and PICs (Figure III-1b) are visible in both Voyager Imaging Science Subsystem (ISS) (Plescia, 1983; Moore, 1984) and Cassini ISS imagery, and those appearing to be PICs seem to be widespread across the satellite. Dione's surface also exhibits a region of heavily tectonized terrain, termed the Wispy Terrain (Figure III-3a) (Plescia, 1983; Moore, 1984), and less discernably tectonized terrain elsewhere, which we term the 'Non-Wispy Terrain' (Figure III-3b). Evidence for tectonism within Dione's Non-Wispy Terrain is ambiguous, although subtle features termed 'lineaments' have been identified and are hypothesized to be subtle fractures (Moore, 1983, 1984). If these lineaments are fractures, then they may provide insight into Dione's tectonic and orbital history. We further examine the interpretation of the Non-Wispy Terrain lineaments as fractures by investigating the presence of PICs within this region.

Background

Impact Processes

An impact event is a complex process that can be divided into a contact and compression stage, an excavation stage, and a modification stage (e.g., Gault et al., 1968). During the contact and compression stage, the projectile impacts the target body (e.g., Melosh, 1989; French, 1998), and a compressional shock wave is produced at the point of contact between the projectile and the target (e.g., Gault et al., 1968). During the excavation stage, a tensile, rarefaction wave (also called a release wave or a decompression wave) forms in response to the compressional shock wave passing through the free surface of the trailing end of the projectile. A resulting excavation flow of material upwards and outwards from the impact site creates a transient crater and ejecta (e.g., Shoemaker, 1960; Dence, 1968; Gault et al., 1968; Grieve, 1987; Melosh, 1989; French, 1998). The excavation of ejecta during this stage can lead to the formation of nearby secondary impact craters (e.g., Roberts, 1964), characterized by their small sizes, irregular plan view geometries, shallow floors, and occurrences in chains and clusters (e.g., Shoemaker, 1962; Oberbeck and Morrison, 1973). During the modification stage, significant alteration of the crater occurs within the first few minutes following the excavation stage, although further crater modification can take place for millions of years (e.g., French, 1998; Osinski and Pierazzo, 2012). Little collapse of the crater rims takes place for simple craters, whereas complex craters form central uplift structures and terraces along the rim (Gault et al., 1968).

Controls on Impact Crater Size and Morphology

Differences in properties of both the impactor and target material affect the resulting impact crater morphology. As summarized in De Pater and Lissauer (2010), for a given impactor and impact velocity, the diameter of an impact crater will be larger on planets and satellites with low gravity and low target material density, such as Dione. Higher velocity impacts will form craters with larger diameters, as will an increase in density or size of the impactor. Impact crater geometries also depend on the angle of impact (e.g., Herrick and Forsberg-Taylor, 2003), whether or not impacts are clustered (e.g., O'Keef and Ahrens, 1982; Schultz and Gault, 1985a; Cochrane and Ghail, 2006), projectile shape (Schultz and Gault, 1985b, 1986), topography of the target area (e.g., Gifford and Maxwell, 1979), layering of the target material (Quaide and Oberbeck, 1968), erosion (Ronca and Salisbury, 1966), post-impact tectonic modification (e.g., Pappalardo and Collins, 2005; Watters and Johnson, 2010), and the presence of pre-existing sub-vertical structures within the target material (e.g., Eppler et al., 1983; Kumar and Kring, 2008).

While many variables affect the resulting morphologies of impact craters, PICs only form when pre-existing sub-vertical structures are present within the target material (e.g., Schultz, 1976; Öhman, 2009). These sub-vertical structures include normal, thrust, and strike-slip faults, joint sets, and lithologic boundaries (Fielder, 1965; Eppler et al.,

1983; Öhman et al., 2005a, 2005b; Öhman, 2009; Aittola et al., 2010), and for simplicity, we refer to all of these structures as fractures. Nonetheless, CICs may also form in pre-fractured target material if the fractures are very widely or very closely spaced, the fracture system is highly complex, or when the target material is covered by a thick layer of non-cohesive sediment (e.g., Fulmer and Roberts, 1963).

Models of PIC Formation

A total of four PIC formation models are given in the literature, and each requires the target material to contain pre-existing fractures. For simplicity, we break these models up into Models A, B, C, and D (Figure III-4). Model A (Figure III-4a) is equivalent to Model 1 in Eppler et al. (1983), and is only applicable for simple PICs. According to this model, simple PICs are structurally controlled during the excavation stage of the transient crater (e.g. Schultz, 1976; Eppler et al., 1983). The cavity expands in a direction oriented 45° to the surrounding fracture azimuths, forming PICs with azimuths that are offset by 45° to azimuths of the controlling fractures. This model is based on observations of two orthogonal fracture sets trending 45° to the straight crater rim segments of Meteor Crater in Arizona, USA (Shoemaker, 1960, 1963; Gault et al., 1968; Schultz, 1976; Roddy, 1978; Poelchau et al., 2008, 2009).

In contradiction to Eppler et al. (1983), Kumar and Kring (2008) found three unmapped prominent pre-impact joint sets in the target material of Meteor Crater that are generally oriented parallel to the sides of the crater's straight rim segments. These authors proposed a new simple PIC formation model, which we refer to as Model B (Figure III-4b). According to this model, the geometry of a simple PIC is defined during the excavation stage, like that proposed for Model A. However, in this model, the crater shape forms as excavation flow preferentially overturns material along pre-existing fractures, causing the crater to preferentially expand in a direction perpendicular to the fracture azimuths. Unlike Model A, Model B predicts final PIC azimuths that parallel surrounding fracture azimuths.

Model C (Figure III-4c), equivalent to Model 2 described by Eppler et al. (1983), proposes that complex PIC geometries are determined during the modification stage (e.g., Schultz, 1976; Eppler et al., 1983). In this model, the crater's straight rim segments are a result of the transient crater walls slumping, via modification-related normal faulting along pre-existing target structures along the crater wall. As a consequence, the crater expands in a direction parallel to surrounding fracture azimuths. Like Model B for simple PICs, this activity results in a parallel PIC-fracture azimuth relationship.

In Model D (Figure III-4d), applicable to both simple and complex craters, PICs inherit their geometries from thrust faulting of material along pre-existing structures during the excavation stage (Öhman, 2009). Like Models B and C, Model D predicts that the final PIC azimuths parallel surrounding fracture azimuths. Model D is supported by some observational evidence of an association of thrust faults with PIC crater rims (Gault et al., 1968; Reimold et al., 1998).

PICs throughout the Solar System

PICs have been identified throughout the Solar System, as summarized in Table III-1, and relationships between PIC azimuths and controlling fracture azimuths have been investigated on many Solar System bodies (Öhman, 2009; Öhman et al., 2010). PIC azimuths on Mercury (Melosh and Dzurisin, 1978; Strom and Sprague, 2003) and Venus (Aittola et al., 2007, 2008, 2010; Öhman, 2009), have been found to parallel azimuths of surrounding linear structures. On Earth, many PICs have also been identified and their orientations have been compared to those of surrounding structures for both simple craters (e.g., Shoemaker, 1960; Öhman, 2009) and complex craters (e.g., Morrison, 1984).

Earth's moon also exhibits PICs (e.g., Elger, 1895; Alter, 1956; Fielder, 1961b; Fulmer and Roberts, 1963; Baldwin, 1963, 1964; Kopal, 1966; Davydov, 1968; Chadderton et al., 1969; Melosh, 1976; Schultz, 1976; Scott et al., 1977; Eppler et al., 1983; Spudis, 1993), and their azimuths parallel those of surrounding fracture azimuths (Baldwin, 1963; Melosh, 1976; Schultz, 1976; Scott et al., 1977; Eppler et al., 1983). Similarly, Martian PICs have been associated with the presence of pre-existing target structures (Thomas and Allemand, 1993; Watters, 2006, 2009; Watters and Zuber, 2009). PICs are also present on the surfaces of asteroids (Belton et al., 1994; Veverka et al., 1997; Thomas et al., 1999; Zuber et al., 2000; Prockter et al., 2002), on the nucleus of a comet (Basilevsky and Keller, 2006), and on icy satellites (Smith et al., 1981; Plescia, 1983; Porco et al., 2005; Denk et al., 2005; Helfenstein et al., 2005) including Dione (Plescia, 1983). Based on our qualitative observation of Cassini ISS imagery, craters appearing to be PICs are numerous across the surface of Dione, and are present in both the pervasively fractured Wispy Terrain and the less apparently fractured Non-Wispy Terrain.

The Geology of Dione

Dione orbits Saturn between neighboring satellites Tethys and Rhea. Dione is small, with a mean radius of only ~561 km (Giese et al., 2006; Roatsch et al., 2009; Thomas, 2010). In addition to H_2O ice (e.g., McCord et al., 1971; Fink et al., 1976), minor abundances of volatile CO_2 and CN (Morrison et al., 1976; Clark et al., 2008) are present. Dione's surface also displays a low albedo non-ice material of unknown composition concentrated on the trailing hemisphere (Clark et al., 2008; Roatsch et al., 2009; Stephan et al., 2010). Low albedo material on Dione is estimated to be centimeters thick (e.g., Clark et al., 2008), and may result from charged particle interactions with surface ice (e.g., Cassidy et al., 2010), micrometeorite bombardment (e.g., Bottke et al., 2010), and/or radiation darkening (e.g., Cassidy et al., 2010). Charged particle bombardment can drive surface chemistry including albedo alterations that are enhanced on trailing hemispheres of synchronously locked icy satellites, like Dione, due to magnetic field interactions (e.g., Noll et al., 1997; Bennett et al., 2013; Cartwright et al., 2015). Dione's variation in surface albedo is reflected by a surface temperature variation, with an average temperature of ~83 K on the leading hemisphere and ~90 K on the trailing hemisphere (Cruikshank et al., 1984).

The Wispy Terrain covers a large portion of Dione's trailing hemisphere (Figure III-3a), and is interpreted as sets of extensional fractures (Plescia and Boyce, 1982; Moore, 1984; Stephan et al., 2010). This interpretation is based on the graben-like geometries of the troughs (Moore, 1984) and the high albedo and the ice-rich spectral class of the trough walls, which may result from the exposure of fresh ice during normal faulting due to the exposure of the fault scarp and/or mass wasting along fault related topography (Wagner et al., 2006; Stephan et al., 2010). The Wispy Terrain overprints a region that is covered with a thin layer of low albedo non-ice material (Stephan et al., 2010). The age of the terrain is estimated to be >3.7 Ga, based on a lunar-like impact flux model (Boyce and Plescia, 1985; Neukum, 1985), or >1 Ga, based on a constant impact flux model (Zahnle et al., 2003).

In the Non-Wispy Terrain, several subtle linear features, termed lineaments, have been observed and are speculated to be fractures (Plescia, 1983; Moore, 1983, 1984; Wagner et al., 2006; Clark et al., 2008; Stephan et al., 2010). These lineaments exhibit dominant trends of NE-SW and NW-SE and a less dominant trend of E-W (Moore, 1984). Multiple formation mechanisms have been proposed for the fractures sets comprising Dione's Wispy Terrain and for the lineaments observed in the Non-Wispy Terrain. The Wispy Terrain was initially thought to have been formed by pyroclastic events based on interpretations of features shown in Voyager imagery (Moore 1984), although later analysis of higher resolution Cassini imagery does not show evidence for pyroclastic flows in the region. Alternatively, the Wispy Terrain may have formed during a period of near-global expansion due to a heating event from the decay of long-lived radionuclides (Moore, 1984). The impact craters Aeneas and Dido near the center of the Wispy Terrain (Smith et al., 1981) may have directly generated a system of radial fractures (Plescia, 1983). Alternatively, they may have acted as a stress concentrator, allowing fracturing produced by other mechanisms to have preferentially formed in this region (Plescia, 1983). Proposed formation mechanisms for the Non-Wispy Terrain lineaments as fractures include despinning (Moore, 1983, 1984) or a combination of orbital recession and despinning (Moore, 1983, 1984). Volume expansion, perhaps as the result of internal freezing (Moore, 1983) or a radionuclide-induced heating event (Moore, 1984), may also have contributed to lineament formation. It has also been hypothesized that both the Wispy Terrain fractures and the Non-Wispy Terrain lineaments formed from nonsynchronous rotation (Collins, 2010). Global stress mechanisms are discussed further under section 5 below.

If the Non-Wispy Terrain lineaments are fractures, their presence may have controlled the formation of the craters resembling PICs observed by Plescia (1983) in Voyager imagery. Based on our qualitative assessment of craters resembling PICs on Dione using higher resolution Cassini imagery, these craters seem to be numerous and widespread. Consequently, we investigate the hypothesis that subtle fractures exist within Dione's Non-Wispy Terrain.

Data and Methods

We developed a methodology to first identify PICs and investigate their azimuth relationships – whether parallel or having a 45º offset – to observable fracture azimuths within Dione's Wispy Terrain, and then to identify PICs and investigate their azimuths within the Non-Wispy Terrain (Figure III-5). Fractures are both visible and measureable within the Wispy Terrain, and some craters overprint these fractures without being overprinted by other fractures or craters. Of these craters, we identified PICs by statistically analyzing rim azimuth distributions of individual craters (Figure III-6). Once PICs were identified, we statistically compared PIC azimuths to surrounding fracture azimuths (Figure III-7). We then extrapolated the observed PIC-fracture azimuth relationship to the Non-Wispy Terrain to infer azimuths of subtle and/or nonvisible fractures based on azimuths of PICs identified in this region.

Measurement Techniques

To conduct this study, we first divided a global mosaic of Dione into the Wispy and Non-Wispy Terrains, with terrain boundaries based on mapping by Stephan et al. (2010). Multiple tools in ESRI's ArcMap software were utilized to determine random study locations (Appendix III-A). Five random study locations were created within the Wispy Terrain (Table III-E1), and 30 locations were created within the Non-Wispy Terrain (Table III-E2). These numbers of study locations provide a sample size large enough for meaningful statistical analysis while at the same time leaving sufficient space so that the study locations do not overlap each other. Fewer points were generated within the Wispy Terrain because the terrain covers a smaller area than the Non-Wispy Terrain. Each study location was named for organizational purposes, with the Wispy Terrain location names ranging from WT-1 to WT-5, and the Non-Wispy Terrain location names ranging from NWT-1 to NWT-30. Each crater analyzed in this study was also uniquely identified by appending a number to the end of the name.

The highest resolution Cassini Imaging Science Subsystem (ISS) images covering these study locations were acquired from the Planetary Data System (PDS) website (pds.nasa.gov). We utilized these images for measurements in ArcMap. Processing and projection of these images were conducted with the Integrated Software for Imagers and Spectrometers 3 (ISIS 3) (Anderson et al., 2004) (Appendix II-B).

We incorporated into our study the five closest impact craters to each Wispy Terrain study location and the 10 closest impact craters to each Non-Wispy Terrain study location (Figure III-8). These quantities of impact craters provide a robust sample without causing areas of analysis around study locations to overlap. PICs are easier to recognize by eye in images with low illumination angles that create prominent shadows of the crater's rims. However, studies show that, when rim azimuths are measured quantitatively, neither image resolution nor solar illumination effects due to lighting geometry have a strong effect on whether or not a crater is identified as a PIC (Binder and McCarthy, 1972; Öhman et al., 2006). Measured rim azimuth distributions of impact craters taken on images with low illumination angles have been shown to be statistically

similar to those taken on images with high illumination angles (Öhman et al., 2006). For this reason, we included imagery with a variation of illumination angles in this study.

Because post-faulting across impact craters alters their morphology, we disregarded craters with rims visibly cut by faults, and also craters with rims visibly overprinted by other craters. To avoid analyzing secondary impact craters, we diregarded craters that make up chains and clusters. Additionally, impact craters too small to be confidently measured were not incorporated into this study (diameters ≤10 times the image resolution). We analyzed the azimuths of the closest fractures to the impact craters analyzed in each study location. Any fracture with a length too small to be confidently measured (lengths ≤10 times the image resolution) was disregarded.

For each impact crater selected to be analyzed in each study location, we determined the crater rim azimuth distribution using multiple ArcMap tools (Appendix III-C) (Figure III-2). First, each impact crater rim was manually traced. To create an accurate azimuth distribution, each recorded azimuth must represent a common rim length. Each traced crater rim was normalized to the pixel length of the image used, then the azimuth associated with each of these lengths was included in the rim azimuth distribution for that crater (see Figure III-2a,c).

PIC Identification

We identified PICs by using a series of statistical tests to analyze rim azimuth distributions for each crater (Figure III-6 and Appendix III-C). Our PIC identification technique was conservative because each crater analyzed was required to pass all statistical tests to be classified as a PIC, so that a single test could have excluded it from this classification.

We first tested for a uniform azimuth distribution for each analyzed impact crater by applying the Pearson's Chi-Squared test (e.g., Burt et al., 2009). In this test, we selected an alpha level of 0.01. The alpha level is the maximum threshold used in conjunction with the calculated p-value to decide if the null hypothesis in a statistical test should be rejected. It represents the probability of a false negative, or rejecting the null hypothesis when that hypothesis is true. In other words, if the resulting p-value of the Pearson's Chi-Squared test was less than the alpha level of 0.01, then we could say with 99% confidence that the data are not uniformly distributed (i.e., we rejected the null hypothesis). In this case, the crater was considered a PIC candidate, and was further analyzed in later steps. If the test failed to reject the null hypothesis that the azimuth distribution of an impact crater rim is uniform, the crater was classified as a CIC.

A subsequent test was then applied to exclude degraded CICs that may be falsely classified as PICs due to non-uniform rim azimuth distributions. Fractures are typically present in a set with consistent azimuths between or among fractures, which may be reflected by overprinting PICs. Therefore, true PICs, i.e., those formed by interaction with tectonic fractures, would likely exhibit rim azimuth distributions similar to PICs near-by, reflecting these fracture azimuths. For this subsequent testing to exclude degraded CICs, we used the Kolmogorov-Smirnov test, which tests for similarity between distributions of two sets of data; the null hypothesis is that the two data sets have

a similar distribution. For this work, the Kolmogorov-Smirnov test was performed on PIC candidates at the alpha value of 0.01 and the null hypothesis is that the rim azimuth distribution of each crater is similar to that of other non-uniform craters nearby (i.e., the PIC under consideration is still a PIC candidate). If the Kolmogorov-Smirnov test was significant (p-value < 0.01), we rejected the null hypothesis and classified the crater as a CIC. Otherwise, the crater was retained as a PIC candidate and further tests were carried out.

The prominent rim azimuth(s) was (were) then determined for all remaining PIC candidates. The prominent rim azimuth(s) of each crater is (are) reflected by the mode(s) of the rim azimuth distributions. Because true PICs may exhibit plan view geometries that reflect multiple sets of controlling fractures with various azimuths, the modality, either unimodal or multimodal, of the rim azimuth distribution for each PIC candidate was determined using the Dip test (Hartigan and Hartigan, 1985). The null hypothesis of the Dip test is that a set of data is unimodal. If the resulting p-value of the Dip test was less than the alpha level of 0.01, then the result was significant, the null hypothesis was rejected, and we could say with 99% confidence that the set of data is multimodal. Otherwise, the data were taken to be unimodal. For the unimodal azimuth distributions, the mode was recorded for that PIC candidate. For multimodal distributions, the first and second modes were recorded, as the Dip test result could not determine whether any modes over the second mode were significant. Consequently, each crater could reflect a maximum of two fracture sets with different azimuths. However, nearby craters could add to the number of fracture sets reflected in a study location.

The collections of crater rim azimuth modes for each study location were then analyzed. Over distances similar to the inter-crater distances within study locations, azimuths of fractures vary by approximately 5º to 10º. To group PIC candidates with similar azimuths, a conservative (minimum) value of 5º was used as a threshold difference between crater rim modes of PICs within a study location. If a PIC candidate in a study location exhibits a rim azimuth mode within 5º of another PIC candidate, then both craters were classified as PICs, otherwise the crater was classified as a CIC.

Comparing PIC and Fracture Azimuths

Within Dione's Wispy Terrain, we compared the distributions of the prominent rim azimuths of the identified PICs to the distributions of proximal fracture azimuths in each study location using a series of statistical tests (Figure III-7 and Appendix III-D). The azimuthal data are circular, meaning that they lack a designated zero and the designation of high and low values is arbitrary. For this reason, common statistical tests used for linear data cannot be applied to these data, and specialized circular statistical tests must be utilized instead (e.g., Fisher, 1953, 1995; Jammalamadaka and Sengupta, 2001).

To determine the appropriate circular statistical test for the set of data in each study location, we applied the Watson's goodness of fit test to each PIC azimuth distribution (e.g., Stephens, 1970; Jammalamadaka and SenGupta, 2001). Application of the Watson's goodness of fit test allowed us to determine whether or not each set of data

follows a circular normal distribution (also called the von Mises distribution or Tikhonov distribution). The circular normal distribution is a continuous probability distribution on a circle and is the circular analogue to the linear normal distribution (e.g., Von Mises, 1918; Gumbel et al., 1953). The null hypothesis of the Watson's goodness of fit test is that a set of data follows a circular normal distribution. If the resulting p-value of the test was less than the alpha level of 0.01, then we could say with 99% confidence that the data do not follow a circular normal distribution (i.e., we rejected the null hypothesis). Alternatively, we accepted the null hypothesis that the data set follows a circular normal distribution. If they follow a circular normal distribution, the data are parametric, and in that case the Watson-Williams two-sample test (Watson and Williams, 1956; Stephens, 1969) was utilized to compare means between PIC and fracture azimuths. The Watson-Williams two-sample test is the circular analogue of the linear two-sample t-test, and was conducted to test the null hypothesis that the mean directions of two sets of data are statistically similar. If the data do not follow a circular normal distribution, we instead employed the analogous non-parametric Watson-Wheeler two-sample test (also called the Mardia-Watson-Wheeler test or Uniform Score test) (Batschelet, 1981; Zar, 1999). For either test, if the resulting p-value was less than the alpha level of 0.01, then we could say that there is a difference between the two sets of data with 99% confidence (i.e., we rejected the null hypothesis). However, if the resulting p-value was greater than 0.01, then we accepted the null hypothesis that there is a similarity between the sets of data.

If the result of either test failed to reject the null hypothesis, then the PICs and fractures were considered to have a similar azimuth distribution. In that case, the interpretation that PIC azimuths parallel surrounding fracture azimuths would be supported in Dione's Wispy Terrain. A parallel relationship between PIC and fracture azimuths in the Wispy Terrain would enable us to estimate azimuths of subtle and/or nonvisible fractures inferred from PIC azimuths within the Non-Wispy Terrain, if and where PICs are present. We used the PIC identification technique (Figure III-6) (Appendix III-C) to test the hypothesis that subtle fractures exist within Dione's Non-Wispy Terrain. If any PICs were present in a single Non-Wispy Terrain study location, then the hypothesis would be supported for that location.

Results

Wispy Terrain Results

All five Wispy Terrain study locations (Appendix III-E and Table III-E1) exhibit evidence for PICs (Tables III-2, III-F1, III-F2, and III-F3, Figure III-9). In the Wispy Terrain, 76% of the impact craters analyzed were classified as PICs, while 24% were classified as CICs. Out of the five impact craters analyzed in each study location, five were identified as PICs in WT-5, four were identified as PICs in study locations WT-1 and WT-4, and three were identified as PICs in WT-2 and WT-3. Thus, a total of six of the 25 analyzed craters do not show evidence for being PICs. These CICs may be present in the pervasively fractured Wispy Terrain because the local fractures are either very

widely spaced, very closely spaced, or highly complex. Additionally, the craters may predate the surrounding fractures, or the craters may have formed in a region where a thick layer of non-cohesive sediment is present.

Results of two-sample statistical tests fail to reject the null hypothesis, showing that both simple PIC azimuths and complex PIC azimuths parallel nearby fracture azimuths in all five Wispy Terrain study locations (Tables III-2, III-F4, and III-F5). The fracture azimuths and the PIC azimuths are the most complicated in study location WT-1. Both PICs and fractures in this area exhibit prominent rim segments with various azimuths (Figure III-10, Table III-F6). Study locations WT-2 through WT-5 tend to be much simpler tectonically, and the relationships between PIC azimuths and nearby fracture azimuths are clear (Figure III-10c-j, Tables III-2 and III-F6). Based on these results, we conclude that if PICs are present within Dione's Non-Wispy Terrain, their azimuths would parallel those of the inferred subtle fracture azimuths.

Non-Wispy Terrain Results

Location information of the randomly generated Non-Wispy Terrain study locations is given in Appendix II-E (Table III-E2). Results of crater analyses in these widespread locations show that PICs are abundant (Tables III-3, III-F7, III-F8, and III-F9), supporting our hypothesis that subtle and/or nonvisible fractures are present within Dione's Non-Wispy Terrain. PICs were identified in 21 of the 30 Non-Wispy Terrain study locations (Table III-3), indicating that subtle fractures are present within these regions. The percentages of craters classified as PICs varies for each study location, and in some locations are as high as 80%. Most PICs within these 21 study locations exhibit one set of prominent rim azimuths, suggesting the influence of a single fracture set. However, other Non-Wispy Terrain study locations exhibit PICs with two or three prominent rim azimuths, suggesting multiple fracture sets.

Global prominent inferred fracture orientations are reflected by the mode(s) of the PIC azimuths across the study locations in the Wispy Terrain (Figure III-10) and Non-Wispy Terrain (Figure III-11) where PICs were identified. Three modes of PIC azimuths are present across Dione's surface (Figure III-12, Tables III-3 and III-4). The Dip test was used to quantify this observation and determine the modality of this global distribution of PIC azimuths (Table III-4). Because the results of the Dip test only determine if a set of data is exhibits either a unimodal distribution or a multimodal distribution, and cannot discern between data that are bimodal or trimodal, two dip tests were used to determine if the sets of data exhibit three modes. The first Dip test was used to analyze all PIC azimuths that fall within the range of 0° to 100°, and the second Dip test was used to analyze all PIC azimuths that fall within the range of 80° to 180° (Table III-4). The results of the Dip tests show that three modes, representing prominent PIC azimuths, are present across the surface of Dione. The modes are 110°, 90°, and 52°, which correspond to three inferred fracture orientations of NW-SE, E-W, and NE-SW (Table III-4).

Implications for the Tectonic History of Dione

The hypothesis, that subtle fractures are present within Dione's Non-Wispy Terrain, is supported for 70% (21 out of 30) of the study locations. Within all study locations analyzed in the Non-Wispy Terrain, 35% (104 out of 300) of impact craters analyzed were classified as PICs. For comparison, PICs were identified to make up 16% of impact craters on Mercury (Wood et al., 1977), 22% on Venus (Aittola et al., 2010), and 17% in the Argyre region on Mars (Öhman, 2009). This large proportion of PICs on Dione, with a significant number in the Non-Wispy Terrain, implies that subtle and/or nonvisible fractures are widespread across this icy satellite, including in the Non-Wispy Terrain (Figure III-9).

Seven of the nine study locations in the Non-Wispy Terrain that do not exhibit PICs are on the trailing hemisphere near the Wispy Terrain. This absence of PICs in these study locations could indicate either that fractures are present but did not influence the crater morphology, as is suggested by CICs in the Wispy Terrain study locations, or that fractures are not present. Fractures may not be present in the study locations without identified PICs because the region has been in a state of compression, possibly in compensation for the formation of the Wispy Terrain extensional fractures. Because polycrystalline H_2O ice increases in strength with compressional stress, contractional structures (i.e., thrust faults) require a larger differential stress (the difference between the greatest and the least compressive stresses) than extensional structures (i.e., normal faults) or shear structures (i.e., strike-slip faults) (e.g., Gold, 1977; Hobbs, 1974; Haynes, 1978). Deformation only occurs if and where the differential stress exceeds that of the lithospheric strength. Therefore, it is possible for a stress-field to be present without manifesting fractures, and this scenario would be more likely.

Fracturing may be caused by various events that would alter the satellite's shape (e.g., Murray and Dermott, 1999; Matsuyama and Nimmo, 2008; Collins et al., 2009). As summarized by Collins et al. (2009), stress fields that lead to fracturing on icy satellites can be produced by orbital recession or decay (e.g., Melosh, 1980a; Helfenstein and Parmentier, 1983), diurnal tides (e.g., Greenberg et al., 1998; Hoppa et al., 1999; Tobie et al., 2005), true polar wander (e.g., Melosh, 1980b; Willemann, 1984; Leith and McKinnon, 1996; Matsuyama and Nimmo, 2008), nonsynchronous rotation (e.g., Helfenstein and Parmentier, 1985; Leith and McKinnon, 1996; Greenberg et al., 1998), spin-up or despinning (e.g., Squyres and Croft, 1986; Murray and Dermott, 1999), and volume expansion or contraction (e.g., Squyres and Croft, 1986; Kirk and Stevenson, 1987; Mueller and McKinnon, 1988). Stress events hypothesized to have taken place on Dione include orbital recession (Moore, 1983, 1984), spin-up (Plescia, 1983), despinning (Plescia, 1983; Moore, 1983, 1984), volume expansion (Stevenson, 1982; Moore, 1983, 1984; Consolmagno, 1985), volume contraction (Stevenson, 1982; Moore 1984; Consolmagno, 1985), and nonsynchronous rotation (Collins, 2010).

The pattern of visible fractures within Dione's Wispy Terrain and inferred fractures within the Non-Wispy Terrain could be a useful tool in identifying the stress mechanisms relevant to Dione's tectonic and orbital history. Theoretical maps of global stress patterns have been derived for various mechanisms (e.g., Collins et al., 2009, and

references therein). However, a rigorous comparison of the visible and inferred fractures with global stress patterns would require deformation maps for the various stress patterns, and only some corresponding deformation maps are available in the literature. We compare our inferred fracture map to the available deformation maps to hypothesize about global stress events on Dione including orbital recession, spin-up, despinning, volume contraction, and volume expansion.

Orbital Recession

Orbital recession describes the slow migration of a satellite away from its primary planet (e.g., De Pater and Lissauer, 2010), increasing the radius of its orbit. The satellite's increase in distance from the planet acts to decrease the amplitude of the satellite's tidal bulges. This increased distance also causes the satellite to reduce its rotation rate (e.g., De Pater and Lissauer, 2010), which further decreases the amplitude of the satellite's equatorial bulge. To conserve volume and mass, shortening in the satellite's equatorial region causes elongation in the polar regions.

The satellite's shape change associated with orbital recession may create a deformation field that includes the following regions (Melosh, 1980b; Helfenstein and Parmentier, 1983; Collins et al., 2009): 1) a region of N-S trending thrust faults around the planet-facing and anti-planet points on the satellite; 2) NE-SW and NW-SE oriented strike-slip faults within the mid-latitudes and in the equatorial regions on the lead and trailing hemispheres; 3) normal faults oriented from the planet-facing to the anti-planet hemispheres around the north and south poles.

This deformation field pattern is not consistent with the inferred fracture pattern on Dione's surface. There is no evidence in PIC orientations of N-S trending thrust faults in Dione's equatorial region (Figures III-9 and III-13), and no evidence for latitudinal orientations of normal faults in Dione's polar regions.

Spin-up

Spin-up is the speeding up of a satellite's rotational velocity so that it is no longer in synchronous rotation. Spin-up of an icy satellite may take place if differentiation within the satellite creates torque that overcomes the torque of despinning (e.g. Collins et al., 2009) or as an effect of large impact events, as has been proposed for Dione (Plescia, 1983). During spin-up, the satellite's equatorial bulge increases in amplitude as rotation velocity increases (e.g. Matsuyama and Nimmo 2008), causing elongation in the equatorial regions and shortening in the polar regions. In the case of a satellite with a uniform lithospheric thickness, the deformation field may include the following (Matsuyama and Nimmo, 2008; Beuthe, 2010): 1) normal faults that trend N-S in the equatorial region; 2) thrust faults trending E-W in the polar regions. 3) in the mid-latitudes, NE-SW and NW-SE trending strike-slip faults.

In the case of a satellite with a thinner lithospheric thickness in the equatorial region and a thicker lithosphere near the poles, the pattern of deformation would be different (Beuthe, 2010). In this case, the equatorial region of normal faulting would not be present. Instead, the equatorial region would and NE-SW and NW-SE trending strike-slip faults would instead be present.

On Dione, many of the observed and inferred fracture systems (Figures III-9 and III-13) are consistent with patterns expected for spin-up of a satellite with a thin equatorial lithosphere and a thick polar lithosphere. Inferred and visible fractures trend NE-SW and NW-SE within Dione's mid-latitudes and in the equatorial regions. In the polar regions, E-W trending fractures are also visible and inferred. However, some inconsistencies are present. The visible E-W trending fractures within the Wispy Terrain in the southern hemisphere show characteristics of normal faults (Moore, 1984; Wagner et al., 2006), not thrust faults. Similarly, fractures within a small branch of the Wispy Terrain near the north polar region also shows characteristics of normal faults (Moore, 1984; Wagner et al., 2006), instead of thrust faults.

Because thrust faults require a higher differential stress to form than normal faults or strike-slip faults (e.g., Gold, 1977; Hobbs, 1974; Haynes, 1978), spin-up may have occurred without creating thrust faults in the polar regions. If spin-up did occur and cause fracturing on Dione, at least one other mechanism must have created the extensional fractures within the Wispy Terrain.

Despinning

The opposite process of spin-up is despinning, by which satellites that are initially rotating too fast to be synchronous with their primary planet reduce their rotation velocities, or despin, until synchronous rotation is achieved (e.g., Murray and Dermott, 1999). This process causes the equatorial bulge to subside and the spin-axis to elongate as rotation slows (e.g., Murray and Dermott, 1999). In the case of a satellite with a uniform global lithospheric thickness, this change in satellite shape creates a unique global stress field and deformation field. The regions within these fields would be opposite of the fields induced by spin-up, and would include the following (Melosh, 1977; Collins et al., 2009): 1) Thrust faults would be present in the equatorial region and would trend N-S. 2) Normal faults may form in the polar regions, and would trend E-W. 3) In the mid-latitudes, strike-slip faults may be present and would trends of NE-SW and NW-SE.

In the case of a satellite with a thinner lithosphere in the equatorial region and a thicker lithosphere near the poles, the pattern of deformation would be different (Melosh, 1977; Beuthe, 2010). In this case, the equatorial region of N-S trending thrust faults would not be present. Instead, in the mid-latitude regions, NE-SW and NW-SE trending strike-slip faults would be present in the equatorial region.

Dione's visible and inferred fractures are consistent with some patterns expected for despinning of a satellite with a thin equatorial lithosphere and a thick polar lithosphere. Inferred fractures trend NE-SW or NW-SE in Dione's mid-latitudes and equatorial regions and E-W in the north polar and south polar regions. However, the presence and orientation of inferred fractures that trend E-W near Dione's equatorial region does not fit with the expected despinning-induced global deformation pattern.

Volume Contraction

Volume contraction of an icy satellite may occur as a result of global cooling (e.g., Ellsworth and Schubert, 1983) or internal melting (e.g. Consolmagno, 1985). Both of these mechanisms are thought to have taken place on Dione (Stevenson, 1982;

Consolmagno, 1985; Moore, 1984). Additionally, a decrease in satellite volume may occur as a result of the change of water to a high-pressure, high density, ice phase (Squyres, 1980; Showman et al., 1997). Volume contraction leads to a decrease in satellites surface area and compressional stresses. For a satellite with a constant lithospheric thickness, these stresses would be evenly distributed across the satellite surface. If faulting were to occur within this global stress field, the surface would exhibit an even distribution of thrust faults with various orientations. If the satellite has a thinner lithosphere in the equatorial region than in the polar regions, then the expected deformation pattern is different (Beuthe, 2010). In this case, the thrust faults would be localized near the equator, and would exhibit E-W trends.

On Dione, inferred fractures that trend E-W along the equatorial region are present, however, visible sections of visible E-W trending fractures within a branch of the Wispy Terrain in the equatorial region shows characteristics of normal faults (Moore, 1984; Wagner et al., 2006), and not thrust faults. Consequently, we find that volume contraction is not a viable formation mechanism for the inferred fractures on Dione. Although contraction is thought to have played a role in Dione's history (Stevenson, 1982; Moore, 1984; Consolmagno 1985), our results suggest that few or no thrust faults formed during this event.

Volume Expansion

The opposite process to volume contraction is volume expansion, which may be caused by several different drivers (e.g., Squyres and Croft 1986; Kirk and Stevenson, 1987; Mueller and McKinnon, 1988; Collins, 2009). Internal differentiation of a satellite can lead to volume expansion as high pressure ice in the interior is displaced by silicates (Squyres, 1980; Mueller and McKinnon, 1988). H_2O ice transformation from high-pressure to low-pressure phases may also result in volume expansion (Ellsworth and Schubert, 1983). In addition, warming of a satellite may cause silicates within the interior to become dehydrated, which in turn can also lead to further volume expansion (e.g., Dobson et al., 2002). Volume expansion is thought to have occurred on Dione. This event may have been the result of freezing of a subsurface ocean, or partially liquid interior (Moore, 1984; Consolmagno, 1985). In addition, once already frozen, Dione may have later warmed, leading to volume expansion (Consolmagno 1985). This warming event may have been the result of radioactive decay or tidal heating (Moore, 1984).

Volume expansion causes to an increase in satellite surface area, leading to a global distribution of tensional stress across the surface. For a satellite with a constant lithospheric thickness, the resulting pattern of deformation would be evenly distributed and randomly oriented normal faults across the surface. Based on modeling results by Beuthe (2010), volume expansion of a satellite with a thinner equatorial lithosphere and a thicker polar lithosphere, would generate E-W trending normal faults that preferentially form in the equatorial region. Inferred and visible fractures along Dione's equatorial region, matches the volume expansion induced global fracture pattern, and shows evidence for being normal faults (Moore, 1984; Wagner et al., 2006). For this reason we find that volume expansion is a likely formation mechanism for this fracture system.

In summary, we qualitatively compare Dione's inferred fracture pattern with the available hypothetical deformation maps associated with proposed stress events on Dione. Our comparison suggests that Dione's inferred fracture orientations are most consistent with patterns expected for a combination of despinning and volume expansion. If despinning and volume expansion took place during separate events, then the expected global fracture pattern would simply be a combination of those two expected fracture patterns. Based on modeling results by Beuthe (2010), this combined fracture pattern would develop as follows (Figure III-13): 1) Despinning-induced normal faults would form in the polar regions, and would trend E-W. 2) Despinning-induced strike-slip faults would be present in the mid-latitudes, and in the equatorial region, and would trend NE-SW and NW-SE in both locations. 3) Volume expansion-induced normal faults would also be present in the equatorial region, and would trend E-W. In future work, a quantitative comparison between the spatial distribution of visible and inferred fracture patterns on Dione and hypothetical deformation maps induced by various global stress events would provide a quantitative test of this qualitative assessment.

Conclusions

Our methodology provides a quantitative approach for the identification of PICs in satellite imagery. Studies by others have used a PIC identification method that is based on the visual inspection of impact crater plan view geometries (e.g., Öhman et al., 2005a, 2005b, 2006; Aittola et al., 2010). For example, impact craters with multiple straight rim segments and notable angles between these segments may be classified as being a PIC if at least two researchers agree on this classification (e.g., Öhman et al., 2006). In contrast, the technique outlined in this study for identifying PICs is more objective, consistent, and efficient, allowing for a quick identification of PICs even when analyzing a large number of craters. The flowcharts provided (Figures III-5, III-6, and III-7) can be used for coding/programing purposes (e.g., writing codes of statistical tests in R language to automate the process).

Our results support the hypothesis that subtle and/or nonvisible fractures are present within Dione's Non-Wispy Terrain. Analysis of our results indicates that: 1) PICs are widespread and reflect subtle and/or nonvisible fractures in Dione's Non-Wispy Terrain, supporting interpretations of lineaments as subtle fractures. 2) Inferred systems of fractures reflected by PICs exhibit three common orientations (NE-SW, NW-SE, and E-W), and are consistent with lineament orientations. 3) The presence of widespread PICs with consistent azimuths likely reflects fractures associated with global stress deformation mechanisms. These large scale fracture systems likely formed during a global stress event which may have been induced by despinning and volume expansion. Our work shows that the identification of PICs and their azimuths is a useful tool in identifying the presence and azimuths of controlling subtle fractures on icy satellites. This technique could be useful in future studies investigating subtle fractures on both Dione and other small solar system bodies. Other small bodies exhibit impact craters that

appear to be PICs including Iapetus (Porco et al., 2005; Denk et al., 2005), Enceladus (Helfenstein et al., 2005), Rhea (Smith et al., 1981), Tethys, Ceres, and Vesta.

Acknowledgements

We express gratitude to William Dunne, Joshua Emery, and Simon Kattenhorn for insightful and constructive feedback.

References

Abels, A., 2003. *Investigation of impact structures in Finland (Söderfjärden, Lumparn, Lappajärvi) by digital integration of multidisciplinary geodata.* Ph.D. thesis, Westfälische Wilhelms-Universität, Münster, Germany.

Agostinelli, C., Lund, U., 2013. R package 'circular': Circular Statistics (version 0.4-7). URL https://r-forge.r-project.org/projects/circular/

Aittola, M., Öhman, T., Leitner, J.J., Raitala, J., 2007. The characteristics of polygonal impact craters on Venus. *Earth, Moon, and Planets*, *101*(1-2), 41-53.

Aittola, M., Öhman, T., Leitner, J.J., Raitala, J., Kostama, V.P., Törmänen, T., 2008. The association of venusian polygonal impact craters with surrounding tectonic structures. *The Lunar and Planetary Science Conference*, *39*, 2137.

Aittola, M., Öhman, T., Leitner, J.J., Kostama, V.P., Raitala, J., 2010. The structural control of venusian polygonal impact craters. *Icarus*, *205*(2), 356-363, doi:10.1016/j.icarus.2009.08.004.

Alter, D., 1956. The nature of the typical lunar mountain walled plains. *Publications of the Astronomical Society of the Pacific*, *68*(404), 437–443.

Amstutz, G. C., 1965. Tectonic and petrographic observations on polygonal structures in Missouri. *Annals of the New York Academy of Sciences, 123*(2), 876–894, doi: 10.1111/j.1749-6632.1965.tb20406.

Anderson, J.A., Sides, S.C., Soltesz, D.L., Sucharski, T.L., Becker, K.J., 2004. Modernization of the Integrated Software for Imagers and Spectrometers. *The Lunar and Planetary Science Conference, 35*, 2039.

Baldwin, R.B., 1963. The Measure of the Moon. *The University of Chicago Press, Chicago*.

Baldwin, R.B., 1964. The Moon. *Annual Review of Astronomy and Astrophysics, 2*, 73-94.

Basilevsky, A.T., Keller, H.U., 2006, Comet nuclei: Morphology and implied processes of surface modification, *Planetary and Space Science, 54*, 808-829, doi:10.1016/j.pss.2006.05.001.

Batschelet, E., 1981. Circular Statistics in Biology, *Academic Press, London.*

Belton, M.J.S., Chapman, C.R., Veverka, J., Klaasen, K.P., Harch, A., Greeley, R., Greenberg, R., Head, J.W., McEwen, A., Morrison, D., Thomas, P., Davies, M.E., Carr, M.H., Neukum, G., Fanale, F.P., Davis, D.R., Anger, C., Gierasch, P.J., Ingersoll, A.P., and Pilcher, C.B., 1994. First images of Asteroid 243 Ida. *Science, 265*, 1543-1547, doi:0.1126/science.265.5178.1543.

Bennett, C.J., Pirim, C., Orlando, T.M., 2013. Space-weathering of solar system bodies: a laboratory perspective. *Chemical reviews*, *113*(12), 9086-9150, doi:10.1021/cr400153k.

Beuthe, M., 2010. East–west faults due to planetary contraction. *Icarus*, *209*(2), 795-817, doi:10.1016/j.icarus.2010.04.019.

Binder, A.B., McCarthy, D.W., 1972. Mars: The lineament systems, *Science, 176*, 279-281, doi:10.1I26/science.176.4032.279.

Bottke, W.F., Nesvorný, D., Vokrouhlický, D., Morbidelli, A., 2010. The irregular satellites: The most collisionally evolved populations in the Solar System. *The Astronomical Journal, 139*(3), 994, doi:10.1088/0004-6256/139/3/994.

Boyce, J.M., Plescia J.B., 1985. Chronology of surface units on the icy satellites of Saturn. *Ices in the solar system*, Springer, Netherlands, 791-804.

Burt, J.E., Barber, G.M., Rigby, D.L., 2009. *Elementary statistics for geographers*. Guilford Press, New York.

Cassidy, T., Coll, P., Raulin, F., Carlson, R.W., Johnson, R.E., Loeffler, M.J., Hand, K.P., Baragiola, R.A., 2010. Radiolysis and photolysis of icy satellite surfaces: experiments and theory. *Space science reviews, 153*(1-4), 299-315, doi:10.1007/s11214-009-9625-3.

Cartwright, R.J., Emery, J.P., Rivkin, A.S., Trilling, D.E., Pinilla-Alonso, N., 2015. Distribution of CO_2 ice on the large moons of Uranus and evidence for compositional stratification of their near-surfaces, *Icarus*, *257*, 428-456, doi: 10.1016/j.icarus.2015.05.020.

Chadderton, L.T., Krajenbrink, F.G., Katz, R., Poveda, A., 1969. Standing waves on the Moon. *Nature, 223*(5203), 259–263.

Clark, R.N., Curchin, J.M., Jaumann, R., Cruikshank, D.P., Brown, R.H., Hoefen, T.M., Stephan, K., Moore, J.M., Buratti, B.J., Baines, K.H., 2008. Compositional mapping of Saturn's satellite Dione with Cassini VIMS and implications of dark material in the Saturn system. *Icarus 193*(2), 372-386, doi:10.1016/j.icarus.2007.08.035.

Cochrane, C.G., Ghail, R.C., 2006. Topographic constraints on impact crater morphology on Venus from high-resolution stereo synthetic aperture radar digital elevation models. *Journal of Geophysical Research - Planets*, *111(*E04007), doi:10.1029/2005JE002570.

Collins, G.C., McKinnon, W.B., Moore, J.M., Nimmo, F., Pappalardo, R.T., Prockter, L.M., Schenk, P.M., 2009. Tectonics of the outer planet satellites. *Planetary Tectonics*, Cambridge University Press, Cambridge.

Collins, G.C., 2010. Testing candidate driving forces for faulting on Dione: Implications for nonsynchronous rotation and a freezing ocean. *American Geophysical Union Conference*, P24A-08.

Consolmagno, G.J., 1985. Resurfacing Saturn's satellites: Models of partial differentiation and expansion. *Icarus, 64*(3), 401-413, doi:10.1016/0019-1035(85)90064-8.

Cruikshank, D.P., Veverka, J., Lebofsky, L.A., 1984. Satellites of Saturn-Optical properties. *Saturn*, University of Arizona Press, Tucson, 640-667.

Davydov, V.D., 1968. On the question of polygonality and irregularity of the shape of certain craters on the Moon. ST-LPS-LS-10697, Goddard Space Flight Center, National Aeronautics and Space Administration, 4.

Dence, M.R., 1968. Shock zoning at Canadian craters: petrography and structural implications. *Shock Metamorphism of Natural Materials*, Mono Book Corp., Baltimore, 169–184.

Denk, T., Neukum, G., Helfenstein, P., Thomas, R.C., Turtle, E.P., McEwen, A.S., Roatsch, T., Veverka, J., Johnson, T.Y., Perry, J.E., Owen, W.M., Wagner, R.J., Porco, C.C.,

and the Cassini ISS Team, 2005. The first six months of Iapetus observations by the Cassini ISS camera, *The Lunar and Planetary Science Conference, 36*, 2262.

De Pater, I., Lissauer, J.J., 2010. *Planetary Sciences*. Cambridge University Press, Cambridge.

Dobson, D. P., Meredith, P. G., and Boon, S. A. (2002). Simulation of subduction zone seismicity by dehydration of serpentine. *Science*, **298**, 1407–1410, 10.1126/science.1075390.

Elger, T.G., 1895. *The Moon: A Full Description and Map of Its Principal Physical Features.* George Philip & Son, London.

Ellsworth, K. and Schubert, G. (1983). Saturn's icy satellites: Thermal and structural models. *Icarus*, **54**, 490–510, doi:10.1016/0019-1035(83)90242-7.

Elo, S., Jokinen, T., Soininen, H., 1992. Geophysical investigations of the Lake Lappajärvi impact structure, western Finland. *Tectonophysics, 216*, 99-109, doi:10.1016/0040-1951(92)90158-3.

Eppler, D.T., Ehrlich, R., Nummedal, D., Schultz, P.H., 1983. Sources of shape variation in lunar impact craters: Fourier shape analysis. *Geological Society of America Bulletin, 94*, 274–291, doi:10.1130/0016-7606(1983)94<274:SOSVIL>2.0.CO;2.

Fielder, G., 1961a. The contraction and expansion of the moon. *Planetary and Space Science, 8*(1), 1-8.

Fielder, G., 1961b. *Structure of the moon's surface*. Pergamon Press, New York.

Fielder, G., 1965. *Lunar geology*, Lutterworth Press, London.

Fink, U., Larson, H.P., Gautier, T.N., III., Treffers, R.R., 1976. Infrared spectra of the satellites of Saturn-Identification of water ice on Iapetus, Rhea, Dione, and Tethys. *The Astrophysical Journal*, *207*, L63-L67.

Fisher, R., 1953. *Dispersion on a Sphere*. Proceedings of the Royal Society of London A: Mathematical, Physical and Engineering Sciences, 217(1130), 295-305, doi:10.1098/rspa.1953.0064.

Fisher, N.I., 1995. *Statistical Analysis of Circular Data*. Cambridge University Press, Cambridge.

Floran, R.J., Dence, M.R., 1976. Morphology of the Manicouagan ring-structure, Quebec, and some comparisons with lunar basins and craters. *The Lunar Science Conference, 7*, 2845–2865.

French, B.M., 1998. Traces of Catastrophe − A Handbook of Shock-Metamorphic Effects in Terrestrial Meteorite Impact Structures. *LPI Contribution, 954*, 120.

Fulmer, C.V., Roberts, W.A., 1963. Rock induration and crater shape. *Icarus, 2*, 452-465, doi:10.1016/0019-1035(63)90073-3.

Gault, D.E., Quaide, W.L., and Oberbeck, Y.R., 1968. Impact cratering mechanics and structures, *Shock Metamorphism of Natural Materials*, Mono Book Corp., Baltimore, 87-99.

Giese, B., Wagner, R., Neukum, G., Helfenstein, P., Porco, C.C., 2006, Topographic features of Ithaca Chasma, Tethys, *The Lunar and Planetary Science Conference, 37*, 1749.

Gifford, A.W., Maxwell, T.A., 1979. Asymmetric terracing of lunar highland craters: influence of pre-impact topography and structure. *The Lunar and Planetary Science Conference, 10*, 2597-2607.

Gold, L.W., 1977. Engineering properties of freshwater ice. *Journal of Glaciology, 19*, 197-212.

Greenberg, R., Geissler, P., Hoppa, G., Tufts, B.R., Durda, D.D., Pappalardo, R., Head, J.W., Greeley, R., Sullivan, R., and Carr, M.H., 1998. Tectonic processes on Europa: Tidal stresses, mechanical response, and visible features. *Icarus, 135,* 64–78, doi:10.1006/icar.1998.5986.

Grieve, R.A.F., 1987. Terrestrial impact structures. *Annual Review of Earth and Planetary Sciences, 15*, 245–270.

Grieve, R.A.F., Wood, C.A., Garvin, J.B., McLoughlin, G., McHone, J.F., 1988. Astronaut's Guide to the Terrestrial Impact Craters. *LPI Technical Report 88-03*, 89.

Gumbel, E.J., Greenwood, J.A., and Durand, D., 1953. The circular normal distribution: Theory and tables. *Journal of the American Statistical Association, 48*(261), 131-152, doi:10.1080/01621459.1953.10483462.

Hartigan, J.A., Hartigan, P.M., 1985. The dip test of unimodality. *The Annals of Statistics*, 70-84.

Haynes, F.D., 1978. *Effect of Temperature on the Strength of Snow-Ice,* CRREL Report 78-27. U.S. Army Cold Regions Research and Engineering Laboratory, Hanover, N.H.

Helfenstein, P., Parmentier, E.M., 1983. Patterns of fracture and tidal stresses on Europa. *Icarus, 53*, 415–430, doi:10.1016/0019-1035(83)90206-3.

Helfenstein, P., Parmentier, E.M., 1985. Patterns of fracture and tidal stresses due to nonsynchronous rotation: Implications for fracturing on Europa. *Icarus, 61*, 175-184, doi:10.1016/0019-1035(85)90099-5.

Helfenstein, P., Thomas, P.C., Veverka, J., Squyres, S., Rathbun, J.A., Denk, T., Neukum, G., Roatsch, T., Wagner, R., Perry, J., Turtle, E., McEwen, A.S., Johnson, T.Y., Porco, C., the Cassini ISS Team, 2005, Geological features and terrains on Enceladus as seen by Cassini ISS, *Bulletin of the American Astronomical Society, 37*, 701.

Herrick, R.R., Forsberg-Taylor, N.K, 2003. The shape and appearance of craters formed by oblique impact on the Moon and Venus. *Meteoritics & Planetary Science, 38*(11), 1551–1578, doi:10.1111/j.1945-5100.2003.tb00001.x.

Hobbs, P.V., 1974. *Ice Physics.* Oxford University Press, London.

Hoppa, G.V., Tufts, B.R., Greenberg, R., Geissler, P., 1999. Strike-slip faults on Europa: Global shear patterns driven by tidal stress. *Icarus, 141*, 287–298, doi:10.1006/icar.1999.6185.

Jammalamadaka, S.R., SenGupta, A., 2001. *Topics in Circular Statistics*, World Scientific Press, Singapore.

Kenkmann, T., 2002. Folding within seconds. *Geology, 30(3)*, 231–234, doi:10.1130/0091-7613(2002)030<0231:FWS>2.0.CO;2.

Kirk, R.L., Stevenson, D.J., 1987. Thermal evolution of a differentiated Ganymede and implications for surface features. *Icarus*, *69*, 91-134, doi:10.1016/0019-1035(87)90009-1.

Kopal, Z., 1966. *An Introduction to the Study of the Moon.* Astrophysics and Space Science Library, Dordrecht.

Kring, D.A., 2007. *Guidebook to the Geology of Barringer Meteorite Crater, Arizona (a.k.a. Meteor Crater)*. LPI Contribution, *1355*.

Kumar, P.S., Kring, D.A., 2008. Impact fracturing and structural modification of sedimentary rocks at Meteor crater, Arizona, *Journal of Geophysical Research-Planets*, *113*, E09009, doi:10.1029/2008JE003115.

Leith, A.C., McKinnon, W.B., 1996. Is there evidence for polar wander on Europa?. *Icarus*, *120*, 387–398, doi:10.1006/icar.1996.0058.

Matsuyama, I., Nimmo, F., 2008. Tectonic patterns on reoriented and despun planetary bodies. *Icarus*, *195*, 459–473, doi:10.1016/j.icarus.2007.12.003.

McCord, T.B., Johnson, T.V., Elias, J.H., 1971. Saturn and its satellites: Narrow band spectrophotometry (0.3-1.1 mum). *The Astrophysical Journal*, *165*, 413-424.

Maechler M., 2013. diptest: Hartigan's dip test statistic for unimodality – corrected code. R package version 0.75-5 http://CRAN.R-project.org/package=diptest

Melosh, H.J., 1976. On the origin of fractures radial to lunar basins. *The Lunar Science Conference*, *7*, 2967–2982.

Melosh, H.J., 1980a. Tectonic patterns on a tidally distorted planet. *Icarus*, *43*, 334–337, doi:10.1016/0019-1035(80)90178-5.

Melosh, H.J., 1980b. Tectonic patterns on a reoriented planet: Mars. *Icarus*, *44*, 745–751, doi:10.1016/0019-1035(80)90141-4.

Melosh, H.J., 1989. *Impact cratering: a geologic process.* Oxford University Press, New York.

Melosh, H.J., Dzurisin, D., 1978. Mercurian global tectonics: a consequence of tidal despinning? *Icarus*, *35*, 227-236, doi:10.1016/0019-1035(78)90007-6.

Moore, J.M., 1983. The tectonic and volcanic history of Dione as interpreted from studies of its terrains, lineaments and other landforms. *The Lunar and Planetary Science Conference*, *14*.

Moore, J.M., 1984. The tectonic and volcanic history of Dione. *Icarus 59*(2), 205-220, doi:10.1016/0019-1035(84)90024-1.

Morrison, G.G., 1984. Morphological features of the Sudbury structure in relation to an impact origin. *The Geology and Ore Deposits of the Sudbury Structure*, *1*, 513–520.

Morrison, D., Rieke, G., Cruikshank, D., Pilcher, C., 1976. Surface compositions of the satellites of Saturn from infrared photometry. *The Astrophysical Journal*, *207*, L213-L216.

Mueller, S., McKinnon, W.B., 1988. Three-layered models of Ganymede and Callisto: Compositions, structures, and aspects of evolution. *Icarus*, *76*, 437–464, doi:10.1016/0019-1035(88)90014-0.

Murray, C.D., Dermott, S.F., 1999. *Solar System Dynamics*. Cambridge University Press, New York.

Neukum, G., 1985. Cratering records of the satellites of Jupiter and Saturn. *Advances in Space Research, 5*(8), 107-116, doi:10.1016/0273-1177(85)90247-9.

Noll, K.S., Roush, T.L., Cruikshank, D.P., Johnson, R.E., Pendleton, Y.J., 1997. Detection of ozone on Saturn's satellites Rhea and Dione. *Nature, 388*(6637), 45-47.

Oberbeck, V.R., Morrison, R.H., 1973. On the formation of lunar herringbone pattern. *The Lunar Science Conference, 4*, 107-23.

Öhman, T., 2002. *The Indications of Cratering Process in Saarijärvi Impact Crater, Northern Finland.* Unpublished M.Sc. thesis, Institute of Geosciences, University of Oulu, Finland.

Öhman, T., 2007. The origin and tectonic modification of the Saarijärvi impact structure, northern Finland. *Bridging the Gap II: Effect of Target Properties on the Impact Cratering Process. LPI Contribution, 1360*, 85–86.

Öhman, T., 2009. *The structural control of polygonal impact craters*. Ph.D. dissertation, Res Terrae, Publications of the Department of Geosciences, University of Oulu, Finland.

Öhman, T., Pesonen, L.J., Elo, S., Uutela, A., Tuisku, P., Raitala, J., 2003. The origin and evolution of the Saarijärvi impact structure. *Meteoritics & Planetary Science, 38*(7), A52.

Öhman, T., Aittola, M., Kostama, V.P., and Raitala, L., 2005a. *The preliminary analysis of polygonal impact craters within greater Hellas region, Mars*. Impact Tectonics, Springer, Berlin, 131-160, doi:10.1007/3-540-27548-7_5.

Öhman, T, Aittola, M., Kostama, V.P., Raitala, J., and Kortenierni. L., 2005b. Polygonal impact craters in Argyre region, Mars: Implications for geology and cratering mechanics. *Meteoritics & Planetary Science*, 43, 1605-1628.

Öhman, T., Aittola, M., Kostama, V.P., Hyvarinen, M., Raitala., J., 2006. Polygonal impact craters in the Argyre region, Mars: Evidence for influence of target structure on the final crater morphology. *Meteoritics & Planetary Science*, 41, 1163-1173, doi:10.1111/j.1945-5100.2008.tb00632.x.

Öhman T., Aittola M., Kostama V.P., Raitala, J., and Korteniemi, J., 2008. Polygonal impact craters in Argyre region, Mars: Implications for geology and cratering mechanics. *Meteoritics & Planetary Science, 43*, 1605–1628, doi:10.1111/j.1945-5100.2008.tb00632.x.

Öhman, T., Aittola, M., Korteniemi, J., Kostama, V.P., Raitala, J., 2010. Polygonal impact craters in the solar system: Observations and implications. *Geological Society of America Special Papers, 465*, 51-65, doi:10.1130/2010.2465(04).

O'Keefe, J.D., Ahrens, T.J., 1982. Cometary and meteorite swarm impact on planetary surfaces. *Journal of Geophysical Research, 87*(B8), 6668–6680, doi:10.1029/JB087iB08p06668.

Osinski, G.R., Pierazzo, E., 2012. *Impact cratering: processes and products*. John Wiley & Sons, Oxford.

Pappalardo, R.T., Collins, G.C., 2005. Strained craters on Ganymede. *Journal of structural geology, 27*(5), 827-838, doi:10.1016/j.jsg.2004.11.010.

Plescia, J.B., 1983. The geology of Dione. *Icarus, 56*, 255–277, doi:10.1016/0019-1035(83)90038-6.

Plescia, J.B., Boyce, J.M., 1982. Crater densities and geological histories of Rhea, Dione, Mimas and Tethys. *Nature, 295*, 285-290.

Poelchau, M.H., Kenkmann, T. Kring, D.A., 2008. Structural aspects of Meteor Crater and their effect on cratering. *Large Meteorite Impacts and Planetary Evolution, 4*(1423), 176-177.

Poelchau, M.H., Kenkmann, T., Kring, D.A., 2009. Rim uplift and crater shape in Meteor crater: The effects of target heterogeneities and trajectory obliquity, *Journal of Geophysical Research, 114*, EIIJI06, doi:10.102912008JE003235.

Porco, C.C., Baker, E., Barbara, L., Beurle, K., Brahie, A., Burns, J.A., Charnoz, S., Cooper, N., Dawson, D.O., Del Genio, A.D., Denk, L., Dones., L., Dyudina, U., Evans, M.W., Giese, B., Grazier, K., Helfenstein. P., Ingersoll, A.P., Jacobson, R.A., Johnson, T.V., McEwen, A., Murray, E.O., Neukum, G., Owen, W.M., Perry, L., Roatsch, T., Spitale, L., Squyres, S., Thomas, P.C., Tiscareno, M., Turtle, E., Vasavada, A.R., Veverka, J., Wagner, R., West, R., 2005. Cassini imaging science: Initial results on Phoebe and Iapetus, *Science, 307*, 1237-1242, doi:10.1126/science.1107981.

Prockter, L., Thomas, P., Robinson, M., Joseph, J., Milne, A., Bussey, B., Veverka, L., Cheng, A., 2002. Surface expressions of structural features on Eros. *Icarus, 155*, 75-93, doi:10.I006Iicar.211111.6770.

Quaide, W.L., Oberbeck, V.R., 1968. Thickness determinations of the lunar surface layer from lunar impact craters. *Journal of Geophysical Research, 73*(16), 5247−5270, doi:10.1029/JB073i016p05247.

Reimold, W.U., Brandt, D., Koeberl, C., 1998. Detailed structural analysis of the rim of a large, complex impact crater: Bosumtwi crater, Ghana. *Geology 26*(6), 543-546, doi:10.1130/0091-7613(1998)026<0543:DSAOTR>2.3.CO;2.

Roatsch, T., Jaumann, R., Stephan, K., Thomas, P., 2009. Cartographic mapping of the icy satellites using ISS and VIMS data. *Saturn from Cassini-Huygens*, Springer, Netherlands, 763-781.

Roberts, W.A., 1964. Secondary craters. *Icarus*, *3*(4), 348-364, doi:10.1016/0019-1035(64)90045-4.

Roddy, D.J., 1977. Large-scale impact and explosion craters: comparisons of morphological and structural analogs. *Impact and Explosion Cratering*, Pergamon Press, New York, 185-246.

Roddy, D.J., 1978. Pre-impact geologic conditions, physical properties, energy calculations, meteorite and initial crater dimensions and orientations of joints, faults and walls at Meteor Crater, Arizona. *The Lunar and Planetary Science Conference*, *9*, 3891–3930.

Ronca, L.B., Salisbury, J.W., 1966. Lunar history as suggested by the circularity index of lunar craters. *Icarus, 5*, 130–138, doi:10.1016/0019-1035(66)90016-9.

Rossi, A.P., Baliva, A., Piluso, E., 2003. New evidences of an impact origin for Temimichat crater, Mauritania. *The Lunar and Planetary Science Conference, 34*, 1882.

Schultz, P.H., 1976. *Moon morphology: Interpretations based on Lunar Orbiter photography*. The University of Texas Press, Austin.

Schultz, P.H., Gault, D.E., 1985a. Clustered impacts: experiments and implications. *Journal of Geophysical Research – Solid Earth, 90*(B5), 3701-3732, doi:10.1029/JB090iB05p03701.

Schultz, P.H., Gault, D.E., 1985b. The effect of projectile shape in cratering efficiency and crater profile in granular targets. *The Lunar and Planetary Science Conference, 16*, 742–743.

Schultz, P.H., Gault, D.E., 1986. Experimental evidence for non-proportional growth of large craters. *The Lunar and Planetary Science Conference, 17*, 777–778.

Scott, D.H., Diaz, J.M., Watkins, J.A., 1977. Lunar farside tectonics and volcanism. *The Lunar and Planetary Science Conference, 8*, 1119–1130.

Shoemaker, E.M., 1960. Penetration mechanics of high velocity meteorites illustrated by Meteor crater, Arizona. *Structure of the Earth's Crust and Deformation of Rocks, Copenhagen*, 418-434.

Shoemaker, E.M., 1962. Interpretation of lunar craters. *Physics and Astronomy of the Moon*, Academic Press, New York, 283-359.

Shoemaker, E.M., 1963. Impact mechanics at Meteor Crater, Arizona. *The Moon, Meteorites and Comets*, The University of Chicago Press, Chicago, 301-336.

Showman, A. P., Stevenson, D. J., and Malhotra, R. (1997). Coupled orbital and thermal evolution of Ganymede. *Icarus*, **129**, 367–383, doi:10.1006/icar.1997.5778.

Smith, B.A., Soderblom, L., Beebe, R., Boyce, J., Briggs, G., Bunker, A., Collins, S.A., Hansen, C.J., Johnson, T.V., Mitchell, J.L., Terrile, R.J., Carr, M., Cook, A.F., Cuzzi, J., Pollack, J.B., Danielson, G.E., Ingersoll, A., Davies, M.E., Hunt, G.E., Masursky, H., Shoemaker, E., Morrison, D., Owen, T., Sagan, C., Veverka, J., Strom, R., Suomi, V.E., 1981. Encounter with Saturn: Voyager 1 imaging science results, *Science, 212*, 163-191, doi:10.1126/science.212.4491.163.

Spudis, P.D., 1993. *The Geology of Multi-ring Impact Basins*. Cambridge University Press, Cambridge.

Squyres, S. W. (1980). Volume changes in Ganymede and Callisto and the origin of grooved terrain. *Geophys. Res. Lett.*, **7**, 593–596, doi:10.1029/GL007i008p00593.

Squyres, S.W., Croft, S.K., 1986. The tectonics of icy satellites. *Satellites*, University Arizona Press, Tucson, 293–341.

Stephan, K., Jaumann, R., Wagner, R., Clark, R.N., Cruikshank, D.P., Hibbitts, C.A., Roatsch, T., Hoffmann, H., Brown, R.H., Filiacchione, G., 2010. Dione's spectral and geological properties. *Icarus, 206*(2), 631-652, doi:10.1016/j.icarus.2009.07.036.

Stephens, M.A., 1969. Multi-Sample Tests for the Fisher Distribution for Directions. *Biometrika, 56*(1), 169-181, doi:10.1093/biomet/56.1.169.

Stephens, M., 1970. Use of the Kolmogorov-Smirnov, Cramer-von Mises and related statistics without extensive tables. *Journal of the Royal Statistical Society, B32*, 115-122.

Stevenson, D.J., 1982. Volcanism and igneous processes in small icy satellites, *Nature*, 298, 142-144, doi:10.1038/298142a0.

Strom, R.G., Sprague, A.L., 2003. *Exploring Mercury: The Iron Planet.* Springer-Verlag & Praxis Publishing, Berlin.

Thomas, P., 2010. Sizes, shapes, and derived properties of the saturnian satellites after the Cassini nominal mission. *Icarus, 208(1),* 395-401, doi:10.1016/j.icarus.2010.01.025.

Thomas, P.G., Allemand, P., 1993. Quantitative analysis of the extensional tectonics of Tharsis bulge, Mars: geodynamic implications. *Journal of Geophysical Research, 98*(E7), 13097–13108, doi:10.1029/93JE01326.

Thomas, P.C., Veverka, J., Bell, J.F., III, Clark, B.E., Carcich, B., Joseph, J., Robinson, M., McFadden, L.A., Malin, M.C., Chapman, C.R., Merline, W., Murchie, S., 1999. Mathilde: size, shape, and geology. *Icarus, 140*, 17–27, doi:10.1006/icar.1999.6121.

Tobie, G., Mocquet, A., Sotin, C., 2005. Tidal dissipation within large icy satellites: Applications to Europa and Titan. *Icarus*, *177*(2), 534-549, doi:10.1016/j.icarus.2005.04.006.

Trenc, N., Morgan, K.M., Donovan, R.N., Busbey, A.B., 1999. Remote sensing analysis of selected terrestrial impact craters and a suspected impact structure in South Korea using space shuttle photographs. *Geologia Croatica, 52*(2), 203–215.

Veverka. J., Thomas, P., Harch, A., Clark, B., Bell, J.F, III, Carcich, B., Joseph, J., Chapman, C., Merline, W., Robinson, M., Malin, M., Mcfadden, L.A., Murchie, S., Hawkins, S.E., III, Farquhar, R., Izenberg, N., and Cheng, A., 1997. NEAR's flyby of 253 Mathilde: Images of a C asteroid, *Science*, *278*, 2109-2114, doi:10.1126/science.278.5346.2109.

Von Mises, R., 1918. Ueber die Ganzzahligkeit der Atomgewichte und verwandte Fragen. *Phys. Z.*, 19, 490-500.

Wagner, R., Neukum, G., Giese, B., Roatsch, T., Wolf, U., Denk, T., Team, C.I., 2006. Geology, Ages and Topography of Saturn's Satellite Dione Observed by the Cassini ISS Camera. *The Lunar and Planetary Science Conference*, *37*, 1805.

Watson, G.S., Williams E.J., 1956. On the Construction of Significance Tests on the Circle and the Sphere. *Biometrika, 43*, 344-352, doi:10.2307/2332913.

Watters, W.A., 2006. Structure of polygonal impact craters at Meridiani Planum, Mars, and a model relating target structure to crater shape. *The Lunar and Planetary Science Conference, 37*, 2163.

Watters, W. A., 2009. Hypervelocity impacts and the evolution of planetary surfaces and interiors. *Doctoral dissertation, Massachusetts Institute of Technology*.

Watters, T.R., Johnson, C.L., 2010. Lunar tectonics. *Planetary Tectonics.* Cambridge University Press, Cambridge, 121-182.

Watters, W.A., Zuber, M.T., 2009. Relating target properties to the planimetric shape of simple impact craters, *The Lunar and Planetary Science Conference, 40,* 2556.

Willemann, R.J., 1984. Reorientation of planets with elastic lithospheres. *Icarus, 60,* 701–709, doi:10.1016/0019-1035(84)90174-X.

Wood, C. A., J. W. Head, M. J. Cintala, 1977. Crater degradation on Mercury and the moon-Clues to surface evolution. In *Lunar and Planetary Science Conference Proceedings*, 8, 3503-3520.

Zahnle, K., Schenk, P., Levison, H., Dones, L., 2003. Cratering rates in the outer Solar System. *Icarus, 163*(2), 263-289, doi:10.1016/S0019-1035(03)00048-4.

Zar, J.H., 1999. *Biostatistical analysis*, Pearson Education, India.

Zimmermann, R.A., Amstutz, G.C., 1965. The polygonal structure at Decaturville, Missouri: new tectonic observations. *Neues Jahrbuch für Mineralogie, Monatshefte*, 9-11, 288–307.

Zuber, M.T., Smith, D.E., Cheng, A.F., Garvin, J.B., Aharonson, O., Cole, T.D., Dunn, P.J., Guo, Y., Lemoine, F.G., Neumann, G.A., Rowlands, D.D., Torrence, M.H., 2000. The shape of 433 Eros from the NEAR-Shoemaker laser rangefinder. *Science, 289*, 2097–2101, doi:10.1126/science.289.5487.2097.

Appendix III

Table III-1. Documented PICs throughout the Solar System. These studies and observations include PICs on the terrestrial planets, asteroids, a comet, icy satellites, and a dwarf planet.

Impact Structure Name	Geographic Location	Crater Class	Reference(s)
Mercury			
Multiple craters	Global	Unspecified	Melosh and Dzurisin (1978), Strom and Sprague (2003)
Venus			
Multiple craters	Global	Unspecified	Aittola et al. (2007, 2008, 2010), Öhman (2009)
Earth			
Saarijärvi	Finland	Simple	Öhman (2002, 2007), Öhman et al. (2003)
Meteor Crater in Arizona	Arizona, USA	Simple	Shoemaker (1960, 1963), Kring (2007), Kumar and Kring (2008)
Charlevoix	Québec, Canada	Complex	Morrison (1984)
Lappajärvi	Finland	Complex	Elo et al. (1992)
Bigach	Kazakhstan	Complex	Roddy (1977), Grieve et al. (1988), Reimold et al. (1998)
Crooked Creek	Missouri, USA	Complex	Amstutz (1965), Zimmermann and Amstutz (1965), Kenkmann (2002)
Decaturville	Missouri, USA	Complex	Amstutz (1965), Zimmermann and Amstutz (1965), Kenkmann (2002)
Temimichat	Mauritania	Complex	Rossi et al. (2003)
Manicouagan	Québec, Canada	Complex	Floran and Dence (1976), Trenc et al. (1999)
Söderfjärden	Finland	Complex	Abels (2003)
Earth's Moon			
Ptolemaeus	Central Southern Near-side Highlands	Complex	Elger (1895)

Table III-1. Continued.

Impact Structure Name	Geographic Location	Crater Class	Reference(s)
Crisium	Northern Near-Side	Basin	Kopal (1966), Chadderton et al. (1969)
Copernicus	Eastern Oceanus Procellarum	Complex	Elger, (1895)
Multiple craters	Central Southern Near-Side Highlands	Simple and Complex	Öhman et al. (2010)
Mars			
Endurance	Meridiani Planum	Simple	Watters (2006), Watters (2009)
Multiple craters	The Argyre Region	Simple and Complex	Öhman et al. (2006)
Multiple craters	Unspecified	Simple	Watters and Zuber (2009)
Asteroids			
Multiple craters	433 Eros	Unspecified	Zuber et al. (2000), Prockter et al. (2002)
Multiple craters	253 Mathilde	Unspecified	Veverka et al. (1997), Thomas et al. (1999)
Multiple craters	243 Ida	Unspecified	Belton et al. (1994)
Multiple craters	Vesta	Unspecified	This work, based on observations of Dawn Spacecraft images
Comets			
Multiple craters	81P/Wild-2	Unspecified	Basilevsky and Keller (2006)
Icy Satellites			
Multiple craters	The anti-Saturn hemisphere, Iapetus	Unspecified	Porco et al. (2005), Denk et al. (2005)
Multiple craters	Enceladus	Unspecified	Helfenstein et al. (2005)

Table III-1. Continued.

Impact Structure Name	Geographic Location	Crater Class	Reference(s)
Multiple craters	Rhea	Unspecified	Smith et al. (1981)
Multiple craters	Dione	Unspecified	Plescia (1983)
Multiple craters	Tethys	Unspecified	This work, based on observations of Cassini Spacecraft images
Dwarf Planets			
Multiple craters	Ceres	Unspecified	This work, based on observations of Dawn Spacecraft images

Table III-2. Information about PICs identified within Dione's Wispy Terrain. In all five Wispy Terrain study locations, PIC azimuths are statistically similar to the surrounding fracture azimuths, supporting a parallel relationship between PIC and fracture azimuths, as shown in Models B, C, and D (Figure III-4).

Study Location ID	Coordinates (Latitude, Longitude)	Number of PICs Identified / Craters Analyzed	PIC Azimuths Statistically Similar to Fracture Azimuths?
WT-1	77.1°, 12.1°	4/5 (80%)	Yes
WT-2	59.5°, -8.4°	3/5 (60%)	Yes
WT-3	94.5°, 24.6°	3/5 (60%)	Yes
WT-4	116.8°, 26.8°	4/5 (80%)	Yes
WT-5	71.2°, 27.6°	5/5 (100%)	Yes

Table III-3. Information about PICs identified within Dione's Non-Wispy Terrain. PICs were identified in 21 of the 30 Non-Wispy Terrain study locations.

Study Location ID	Coordinates (Latitude, Longitude)	Location Description	PICs Identified?	Number of PICs Identified / Craters Analyzed
NWT-1	127.7º, 9.6º	East Trailing Hemisphere Equatorial Region	Yes	4/10 (40%)
NWT-2	84.3º, -33.5º	Central Trailing Hemisphere Equatorial Region	No	0/10 (0%)
NWT-3	-161.3º, 61.0º	Northwest Leading Hemisphere	Yes	8/10 (80%)
NWT-4	-128.7º, 51.2º	Northwest Leading Hemisphere	Yes	4/10 (40%)
NWT-5	174.6º, -55.2º	Southeast Trailing Hemisphere	Yes	7/10 (70%)
NWT-6	-62.2º, 1.2º	East Leading Hemisphere Equatorial Region	Yes	5/10 (50%)
NWT-7	-89.8º, -22.1º	Central Leading Hemisphere Equatorial Region	Yes	5/10 (50%)
NWT-8	108.7º, -44.6º	South Central Trailing Hemisphere	Yes	6/10 (60%)
NWT-9	-11.9º, -44.6º	Southeast Leading Hemisphere	Yes	6/10 (60%)
NWT-10	31.4º, 29.2º	Northwest Trailing Hemisphere	Yes	2/10 (20%)
NWT-11	-39.7º, 18.6º	East Trailing Hemisphere Equatorial Region	Yes	5/10 (50%)
NWT-12	-157.4º, -22.4º	West Leading Hemisphere Equatorial Region	Yes	8/10 (80%)
NWT-13	110.7º, -22.9º	Central Trailing Hemisphere Equatorial Region	No	0 / 10 (0%)

Table III-3. Continued.

Study Location ID	Coordinates (Latitude, Longitude)	Location Description	PICs Identified?	Number of PICs Identified / Craters Analyzed
NWT-14	-142.5º, 14.2º	West Leading Hemisphere Equatorial Region	Yes	3/10 (30%)
NWT-15	-14.7º, 8.2º	East Leading Hemisphere Equatorial Region	Yes	5/10 (50%)
NWT-16	147.0º, 32.2º	Northeast Trailing Hemisphere	Yes	5/10 (50%)
NWT-17	-11.9º, 43.1º	Northeast Leading Hemisphere	Yes	3/10 (30%)
NWT-18	-112.2º, -3.9º	Central Leading Hemisphere Equatorial Region	Yes	2/10 (20%)
NWT-19	-64.5º, -46.8º	Southeast Leading Hemisphere	No	0/10 (0%)
NWT-20	169.8º, -38.6º	Southeast Trailing Hemisphere	No	0/10 (0%)
NWT-21	178.3º, -9.6º	East Trailing Hemisphere Equatorial Region	Yes	4/10 (40%)
NWT-22	180.0º, 11.4º	East Trailing Hemisphere Equatorial Region	No	0/10 (0%)
NWT-23	38.8º, 40.3º	Northwest Trailing Hemisphere	No	0/10 (0%)
NWT-24	147.4º, 76.0º	Northeast Trailing Hemisphere	Yes	4/10 (40%)
NWT-25	-135.3º, 29.9º	West Leading Hemisphere	Yes	7/10 (70%)
NWT-26	137.5º, -26.1º	East Trailing Hemisphere Equatorial Region	No	0/10 (0%)
NWT-27	105.4º, 62.8º	North Central Trailing Hemisphere	Yes	8/10 (80%)

Table III-3. Continued.

Study Location ID	Coordinates (Latitude, Longitude)	Location Description	PICs Identified?	Number of PICs Identified / Craters Analyzed
NWT-28	96.3º, -4.4º	Central Trailing Hemisphere Equatorial Region	No	0/10 (0%)
NWT-29	17.0º, -1.9º	West Trailing Hemisphere Equatorial Region	Yes	3/10 (30%)
NWT-30	-166.0º, 72.3º	Northwest Leading Hemisphere	No	0/10 (0%)

Table III-4. Modes of inferred fractures of all Non-Wispy Terrain and Wispy Terrain study locations were determined by using the Dip test. The modes correspond to three inferred fracture orientations of NW-SE, E-W, and NE-SW.

Prominent Inferred Fracture Azimuths				
PIC Azimuth Range	**Dip Test p-value**	**Modality (α = 0.05)**	**Azimuth Modes**	**Inferred Fracture Orientations**
0° - 100°	1.3×10^{-4}	Multimodal	110°, 90°, 52°	NW-SE, E-W, NE-SW
80° - 180°	2.2×10^{-16}	Multimodal		

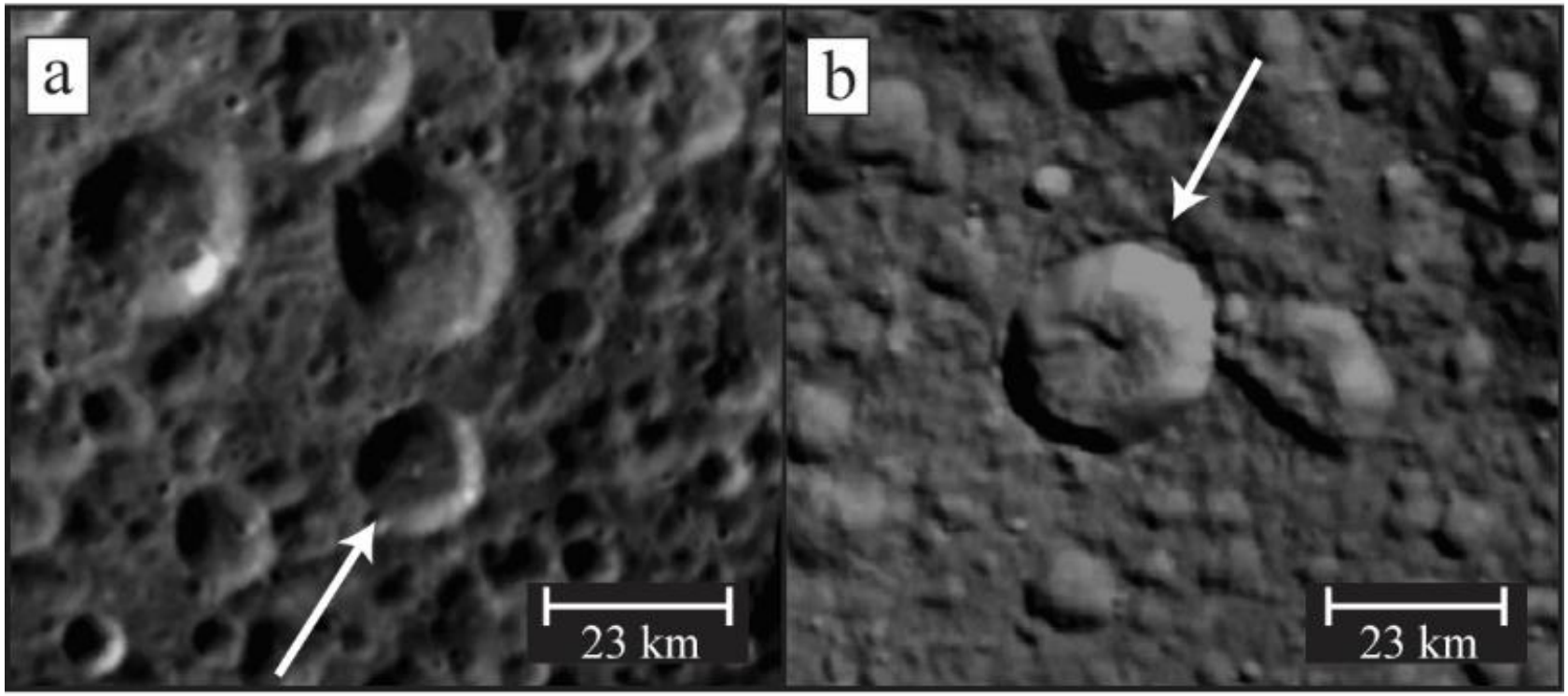

Figure III-1. Cassini images of craters with different plan-view geometries. a) Cassini image N1662197108_1 of a circular impact crater (CIC) in Dione's Non-Wispy Terrain. b) Cassini image N1507741460 of a polygonal impact crater (PIC) in Dione's Non-Wispy Terrain. PICs exhibit large scale straight rim segments with intervening angles (see Figure III-2).

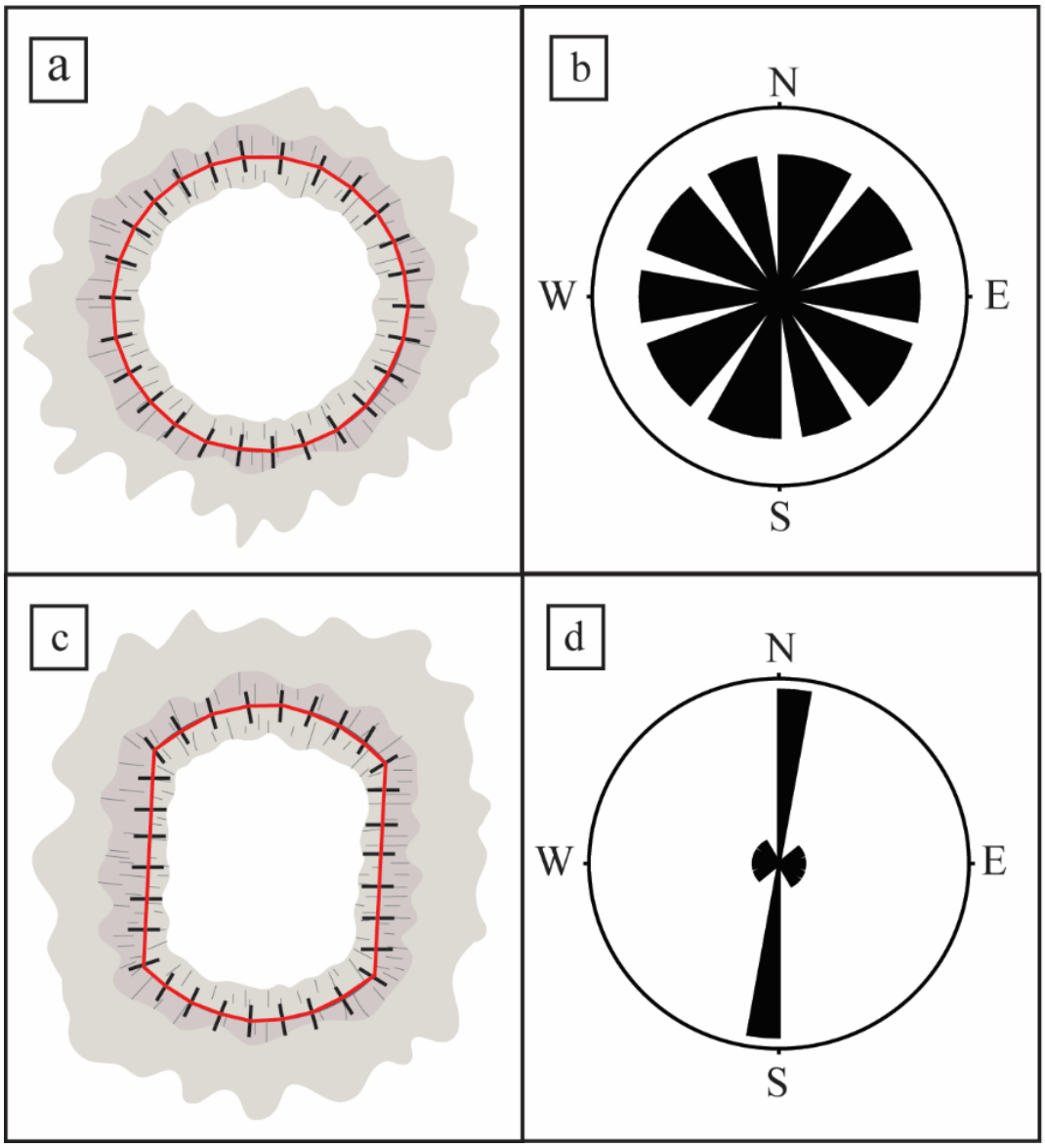

Figure III-2. Plan view geometries of impact craters, showing how the crater rims were traced (red) and normalized to equal lengths (bounded by black tick marks), and the associated rose diagrams of their rim azimuth distributions. a) A circular impact crater (CIC). b) The CIC rose diagram, which shows a uniform crater rim azimuth distribution. c) A polygonal impact crater (PIC). PICs exhibit large scale straight rim segments with intervening angles. d) The PIC rose diagram, which shows a non-uniform rim azimuth distribution, and a PIC azimuth of 0º to 10º.

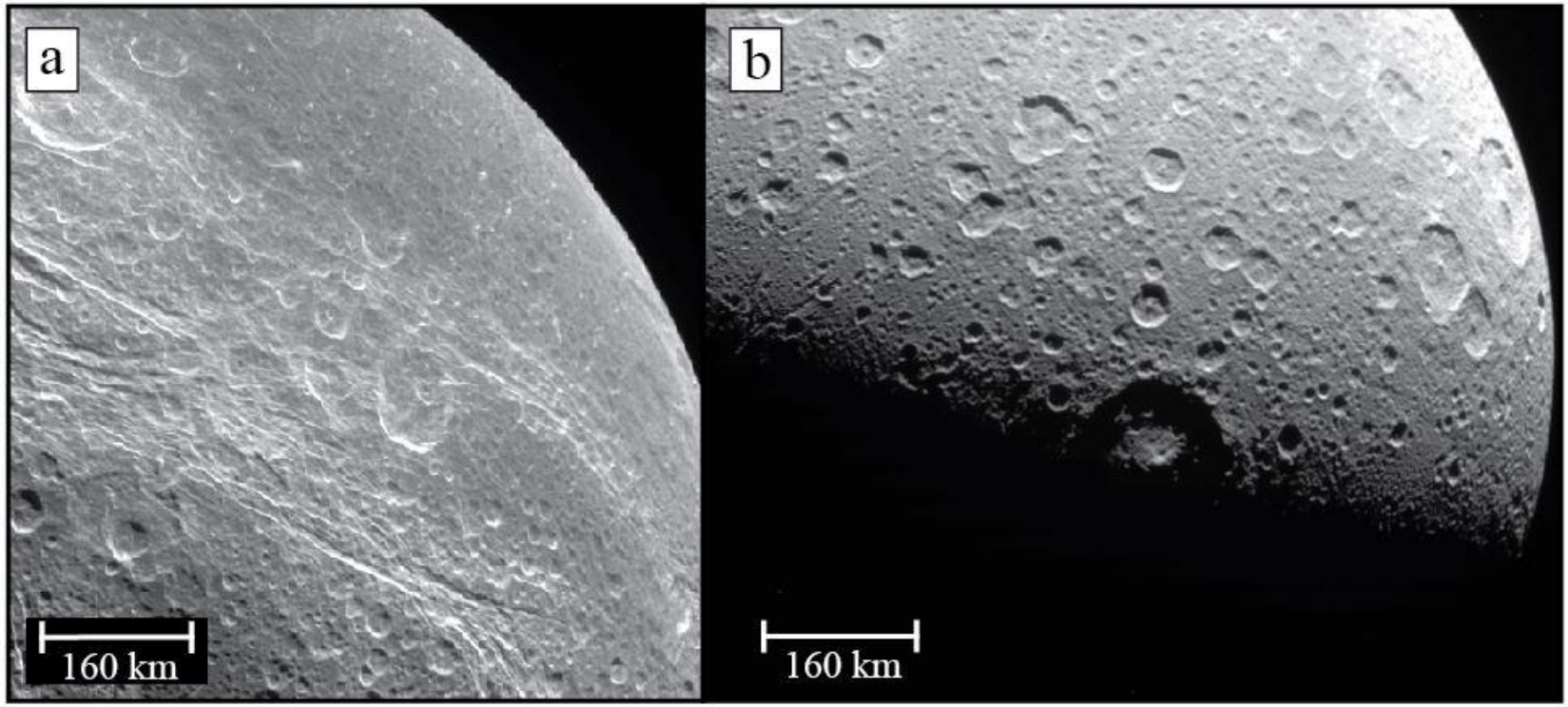

Figure III-3. Cassini images of the Wispy and Non-wispy Terrains. a) Cassini ISS image N1481767088_1 (432 m px^{-1}) of Dione's Wispy Terrain (lower left corner) on the trailing hemisphere. b) Cassini ISS image N1578081030_1 (765 m px^{-1}) of Dione's Non-Wispy Terrain on the leading hemisphere.

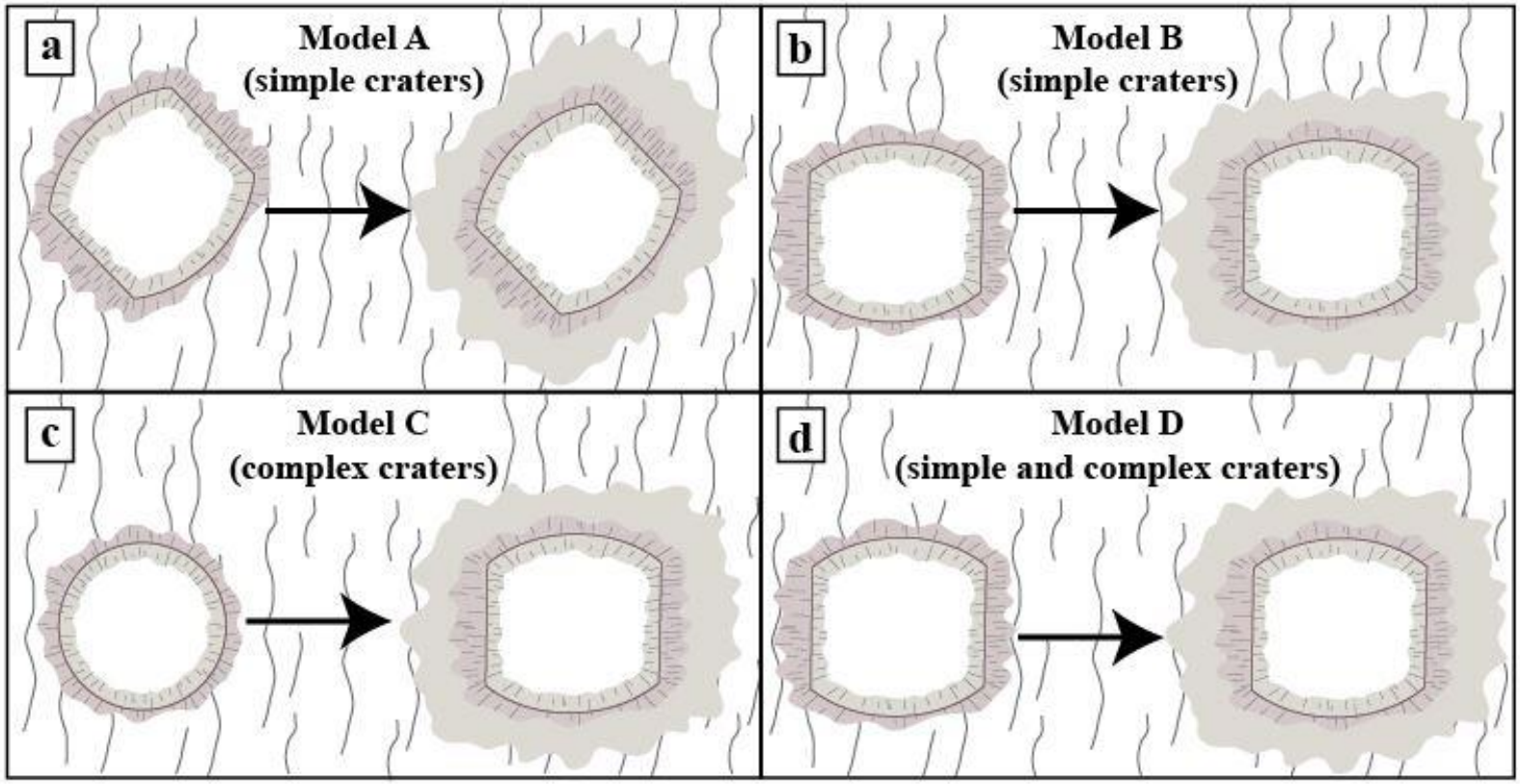

Figure III-4. PIC formation models proposed in the literature. Each diagram shows the progression from the excavation stage (left) to modification stage (right). a) Model A is equivalent to Model 1 proposed by Eppler et al. (1983) for simple PICs. b) Model B was proposed by Kumar and Kring (2008). c) Model C is equivalent to Model 2 proposed by Eppler et al. (1983) for complex PICs. d) Model D was proposed by Öhman (2009). Model A predicts a final PIC azimuths at a 45º angle to the surrounding fractures. Models B, C, and D predicts final PIC azimuths that parallel surrounding fractures.

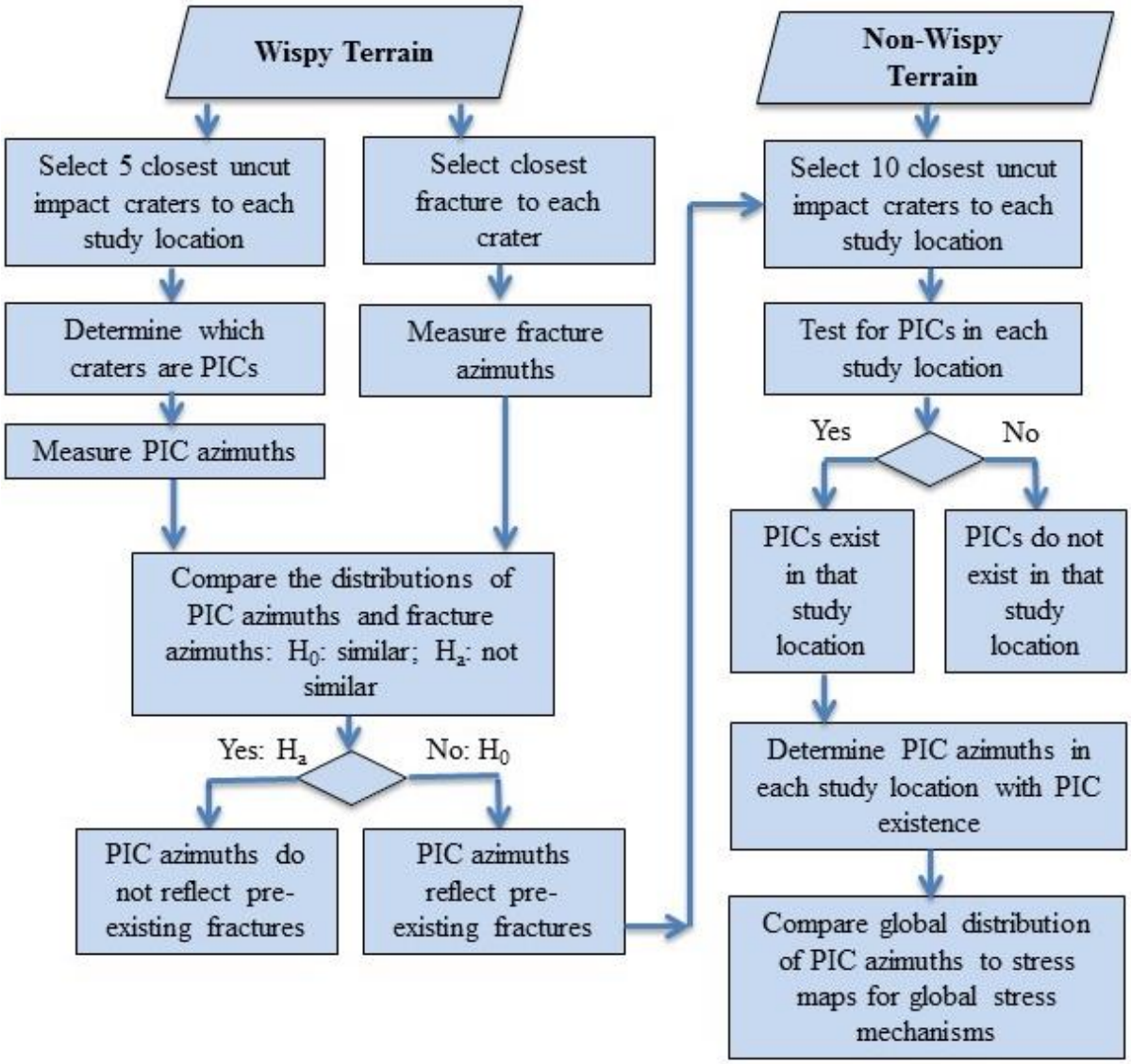

Figure III-5. The methodology used to test our hypothesis and investigate potential implications if the hypothesis is supported.

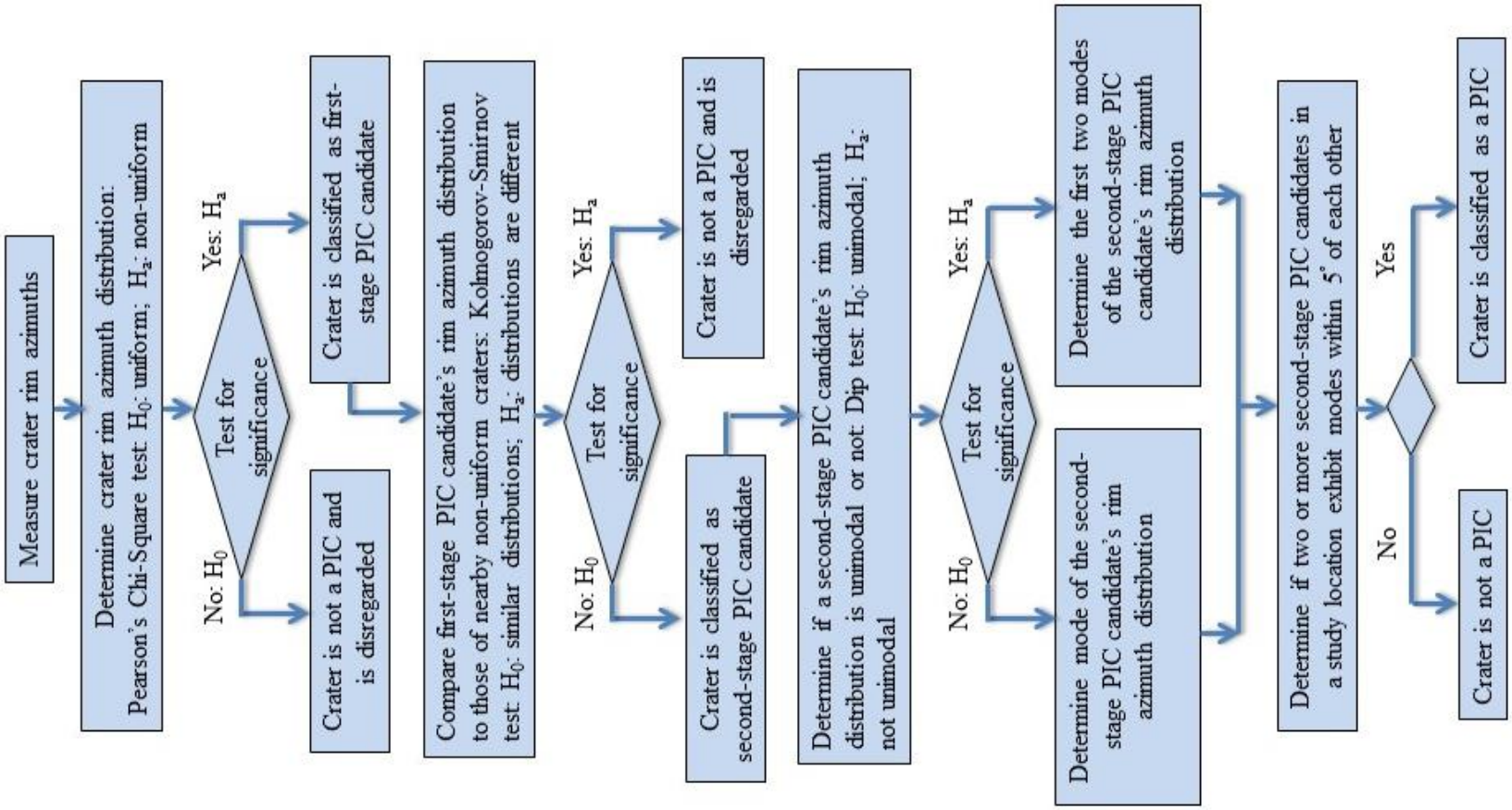

Figure III-6. The methodology used for identifying PICs. This methodology was used for PIC identification in both the Wispy and Non-Wispy Terrains.

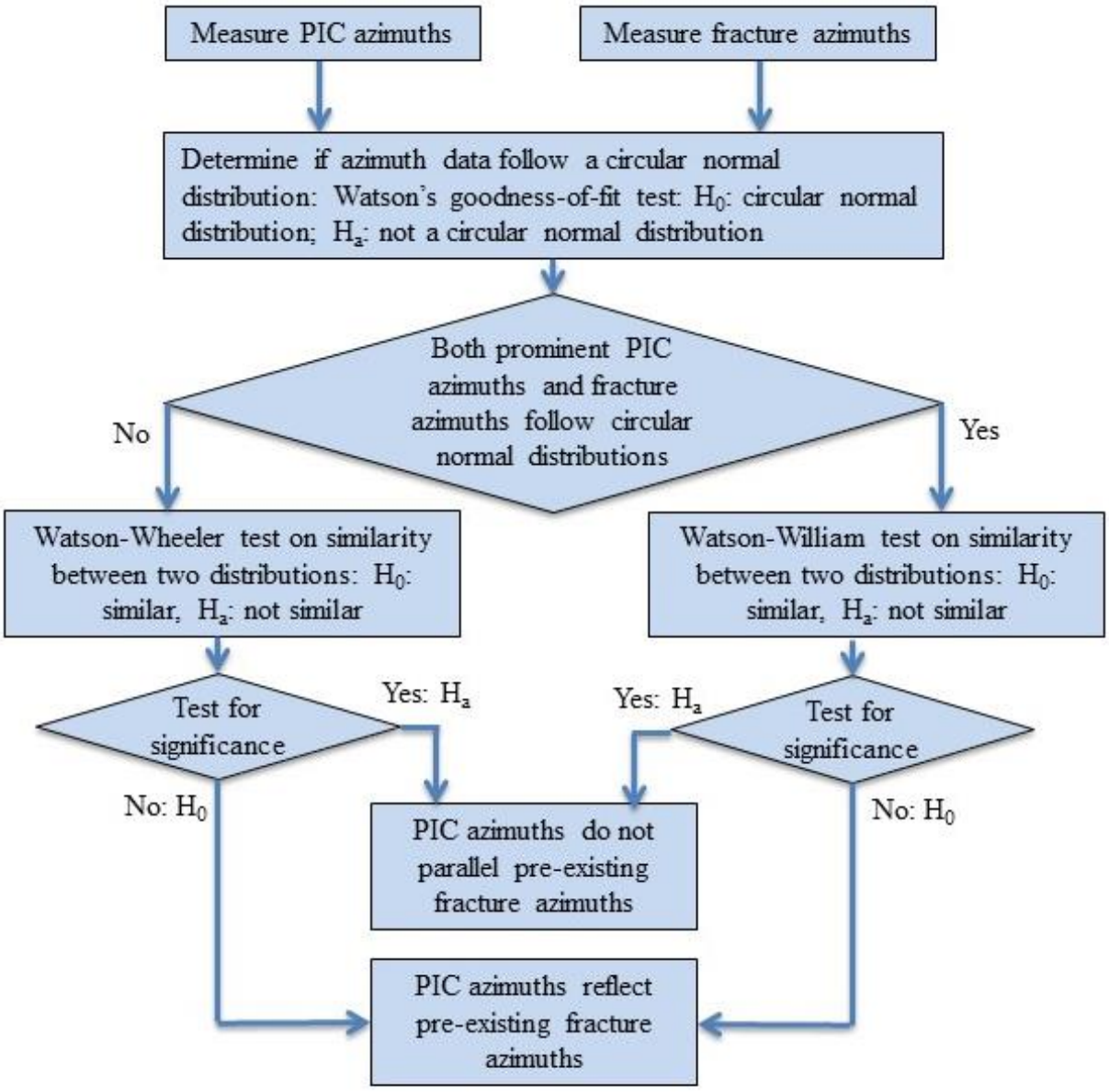

Figure III-7. The methodology used for statistically comparing PIC azimuths with fracture azimuths in Dione's Wispy Terrain.

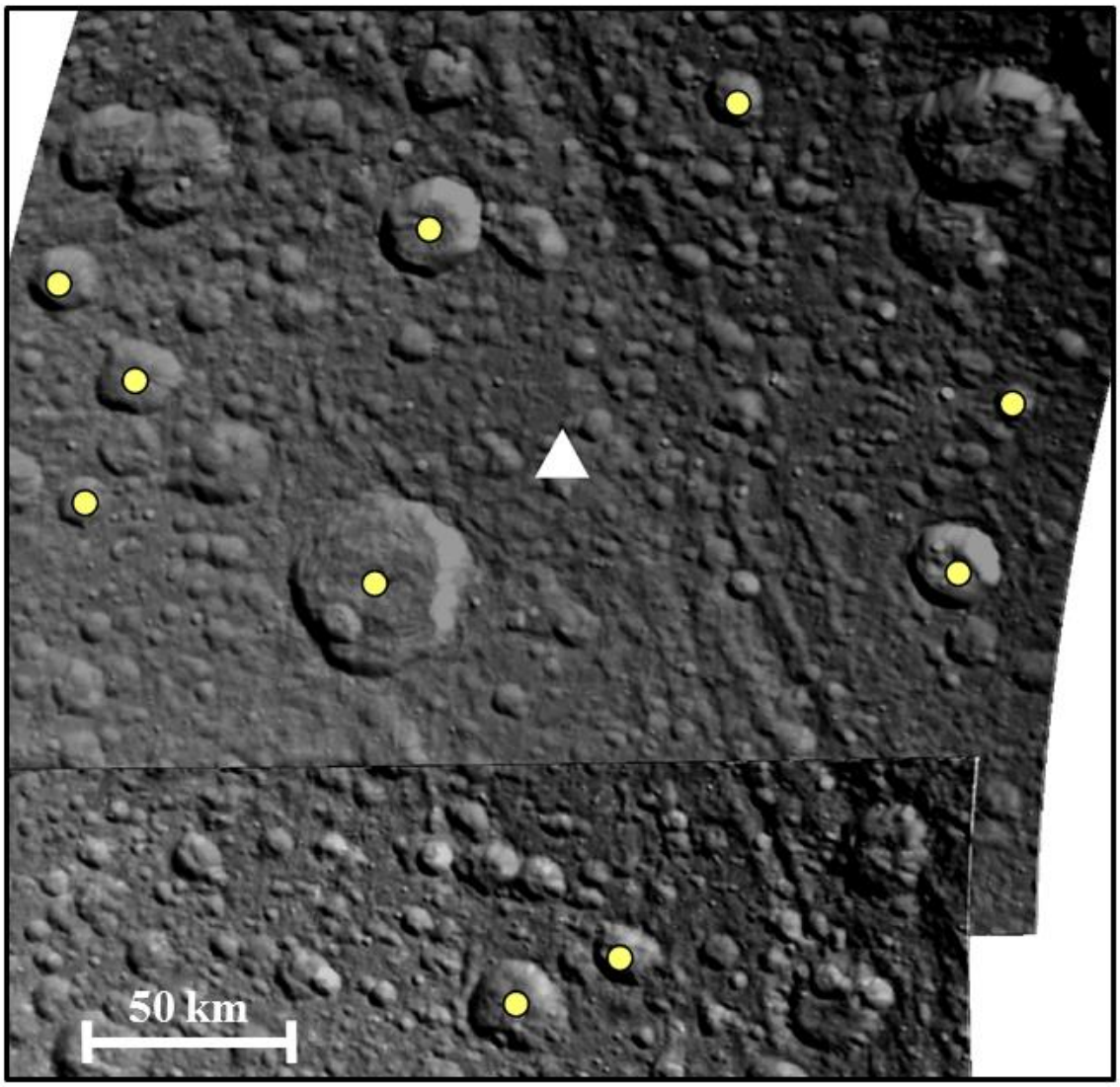

Figure III-8. An example of impact craters within a study location in the Non-Wispy Terrain (NWT-14). We incorporated the 10 closest impact craters (yellow circles) to each Non-Wispy Terrain study location (white triangle) into our study. We disregarded craters that are visibly cut by faults, overprinted by other craters, form chains and clusters of secondaries, or have diameters less than 10 times the image resolution (See Section 3.1). The Cassini ISS images shown are N1507741300_2 (top) and N1507741460_2 (bottom).

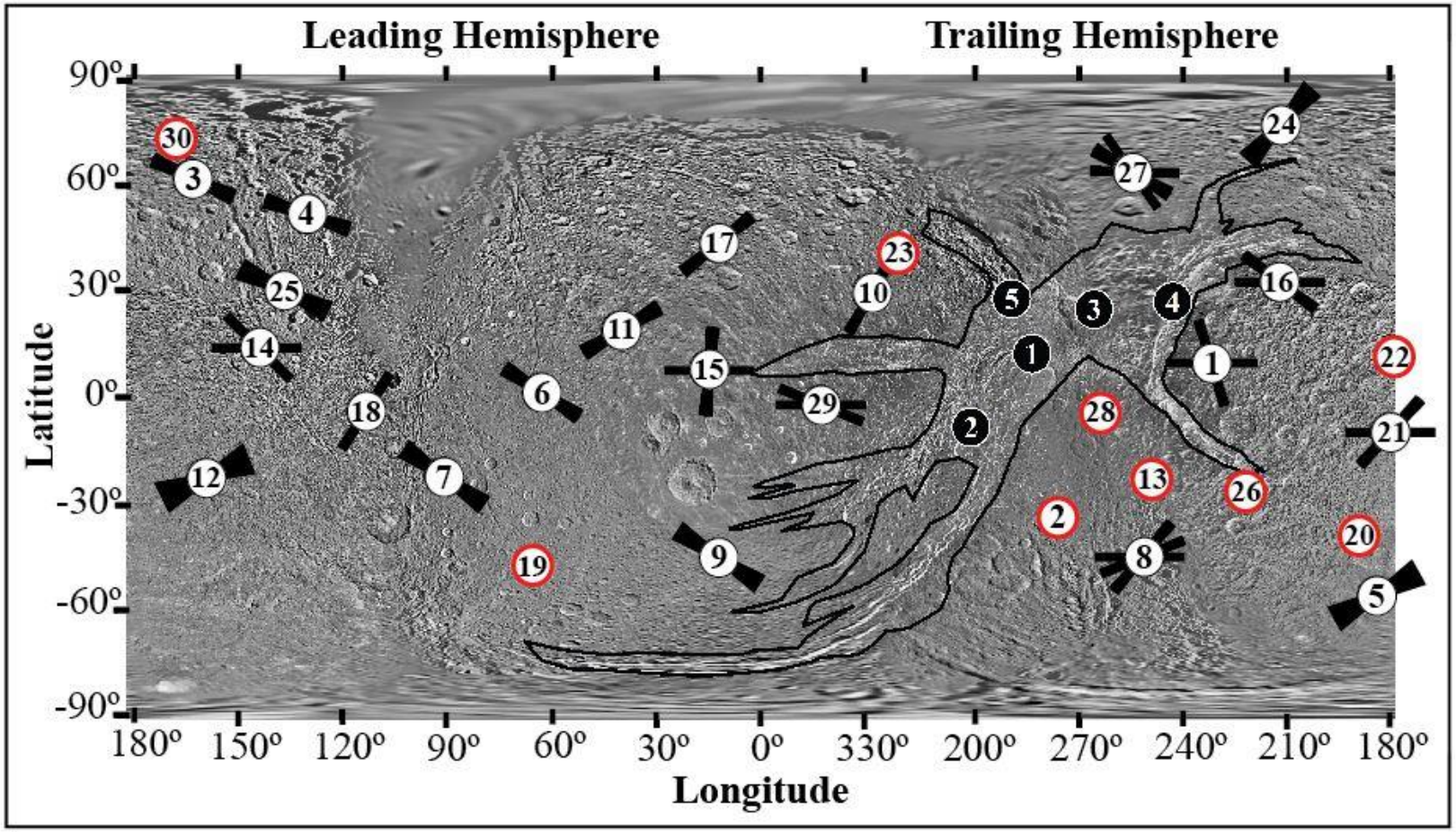

Figure III-9. Rose diagrams of Non-Wispy Terrain PIC azimuths across the surface of Dione. Both Wispy Terrain Study Locations (WT-1 through WT-5 in black), and Non-Wispy Terrain study locations (NWT-1 through NWT-30 in white) are shown. Study locations with bold red borders are locations where no PICs were identified. The presence of PICs imply that subtle fractures are present throughout Dione's Non-Wispy Terrain.

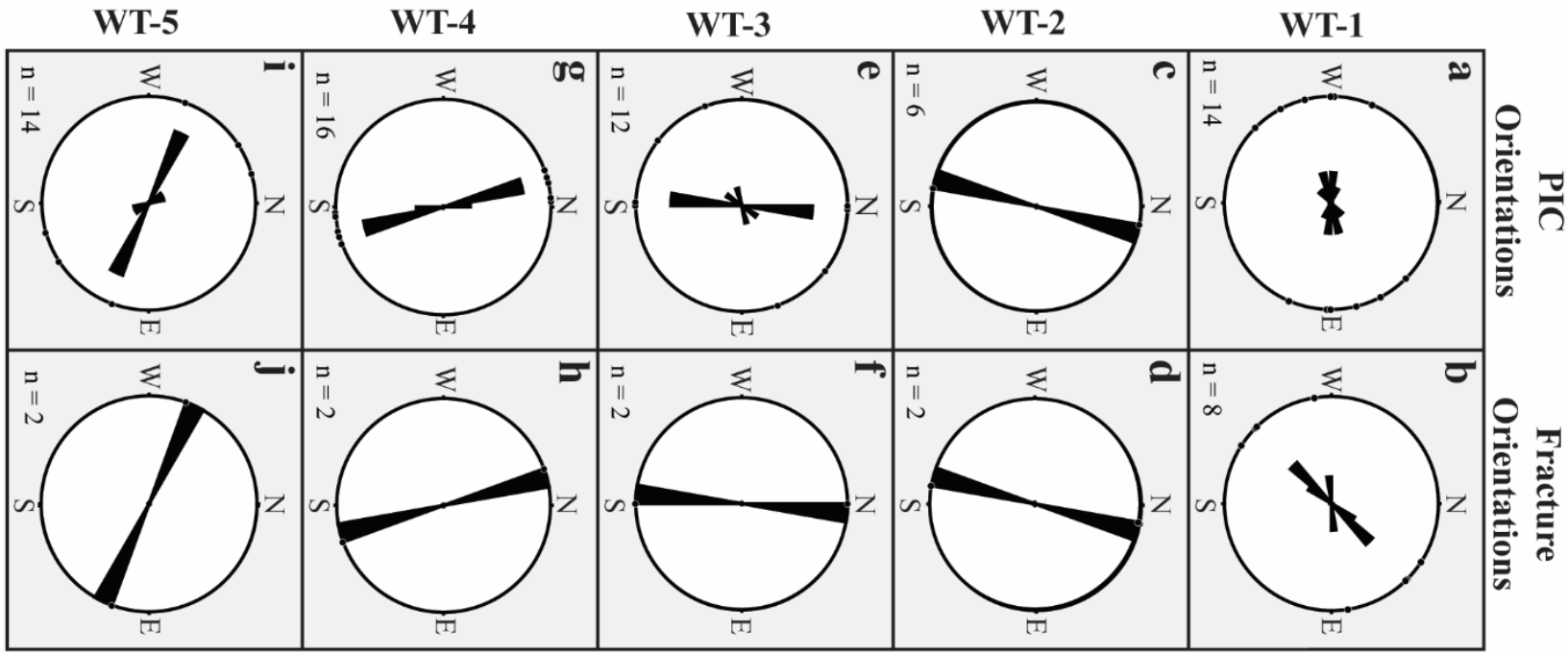

Figure III-10. Rose diagrams showing PIC azimuths and co-located fracture azimuths in each Wispy Terrain study location. The locations of these data are shown as black circles in Figure III-9. The radii of each rose diagram represents 50% of the total data in that diagram.

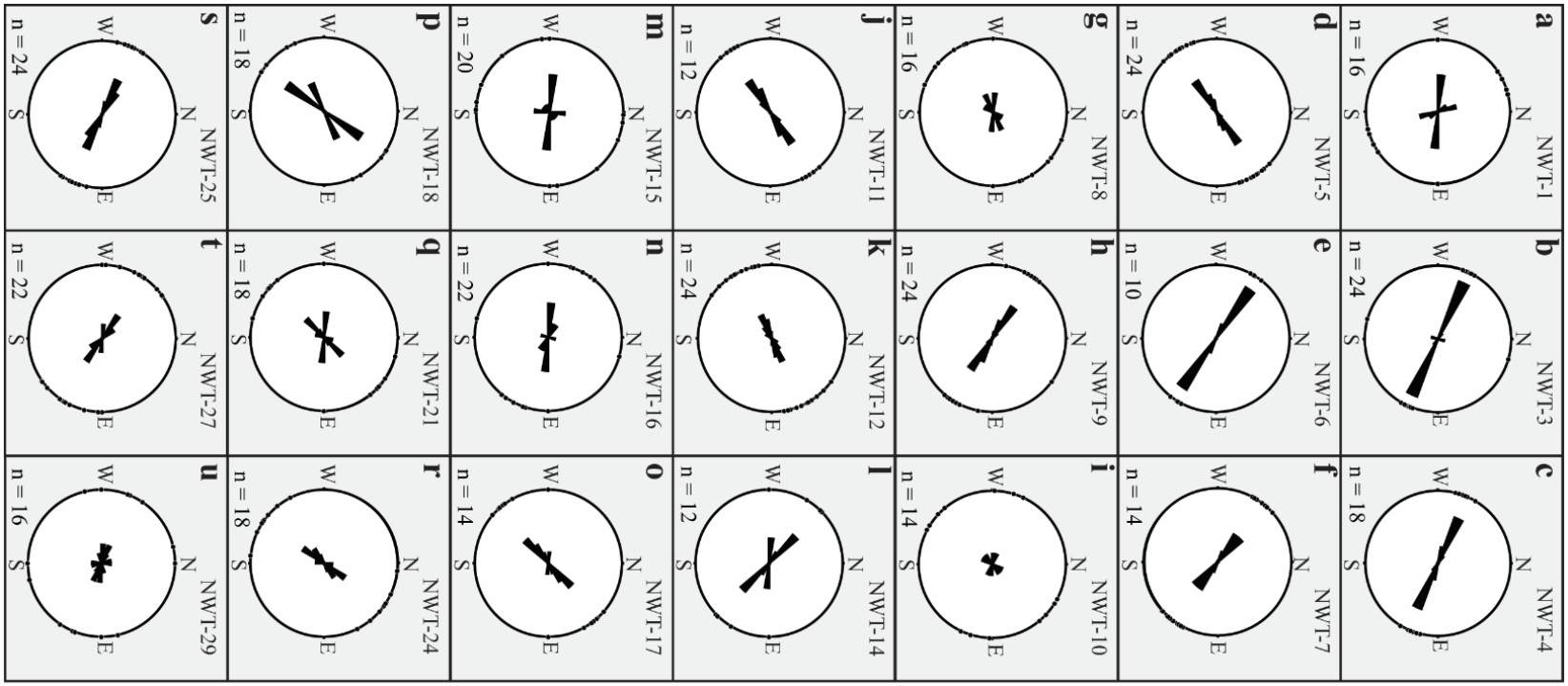

Figure III-11. Rose diagrams showing PIC azimuths in each Non-Wispy Terrain study location where PICs are identified. The locations of these data are shown as white circles in Figure III-9.

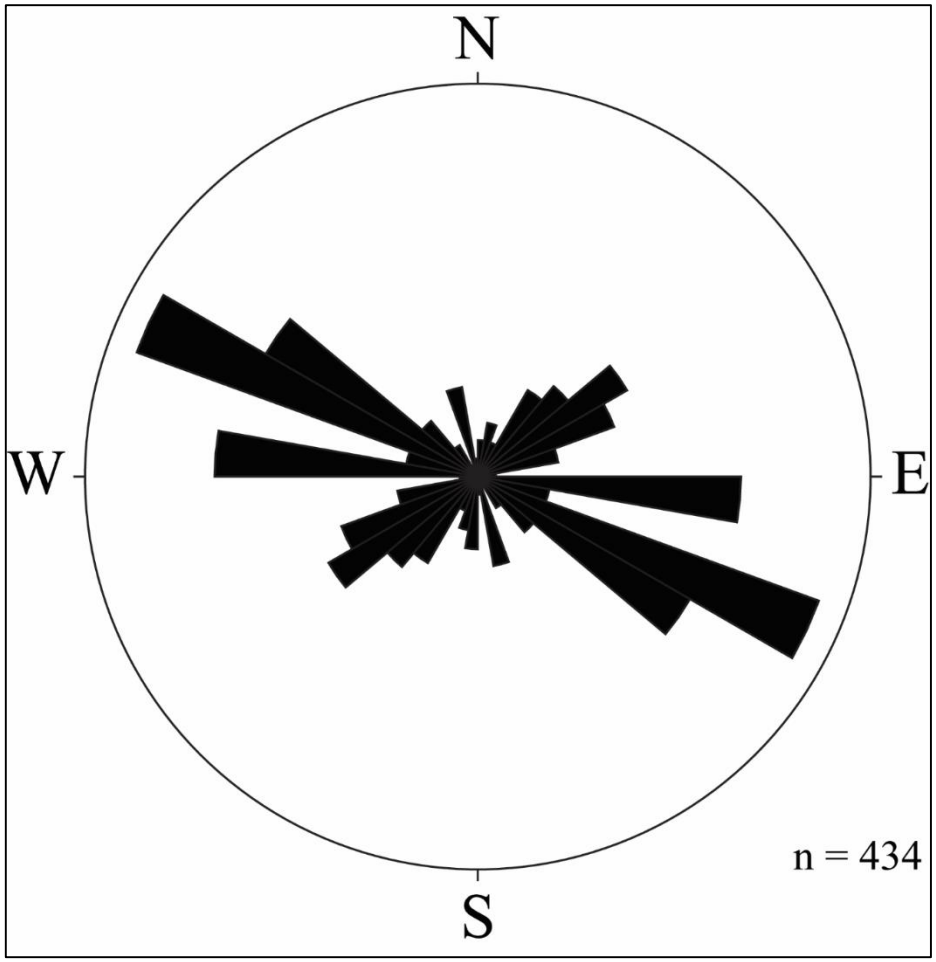

Figure III-12. Rose diagram showing the global distribution of PIC azimuths (from both the Wispy Terrain and Non-Wispy Terrain study locations). Three prominent modes in this data are apparent, as substantiated by dip test results (Table III-4). These modes are 110°, 90°, and 52° corresponding to inferred fracture orientations of NW-SE, E-W, and NE-SW respectively.

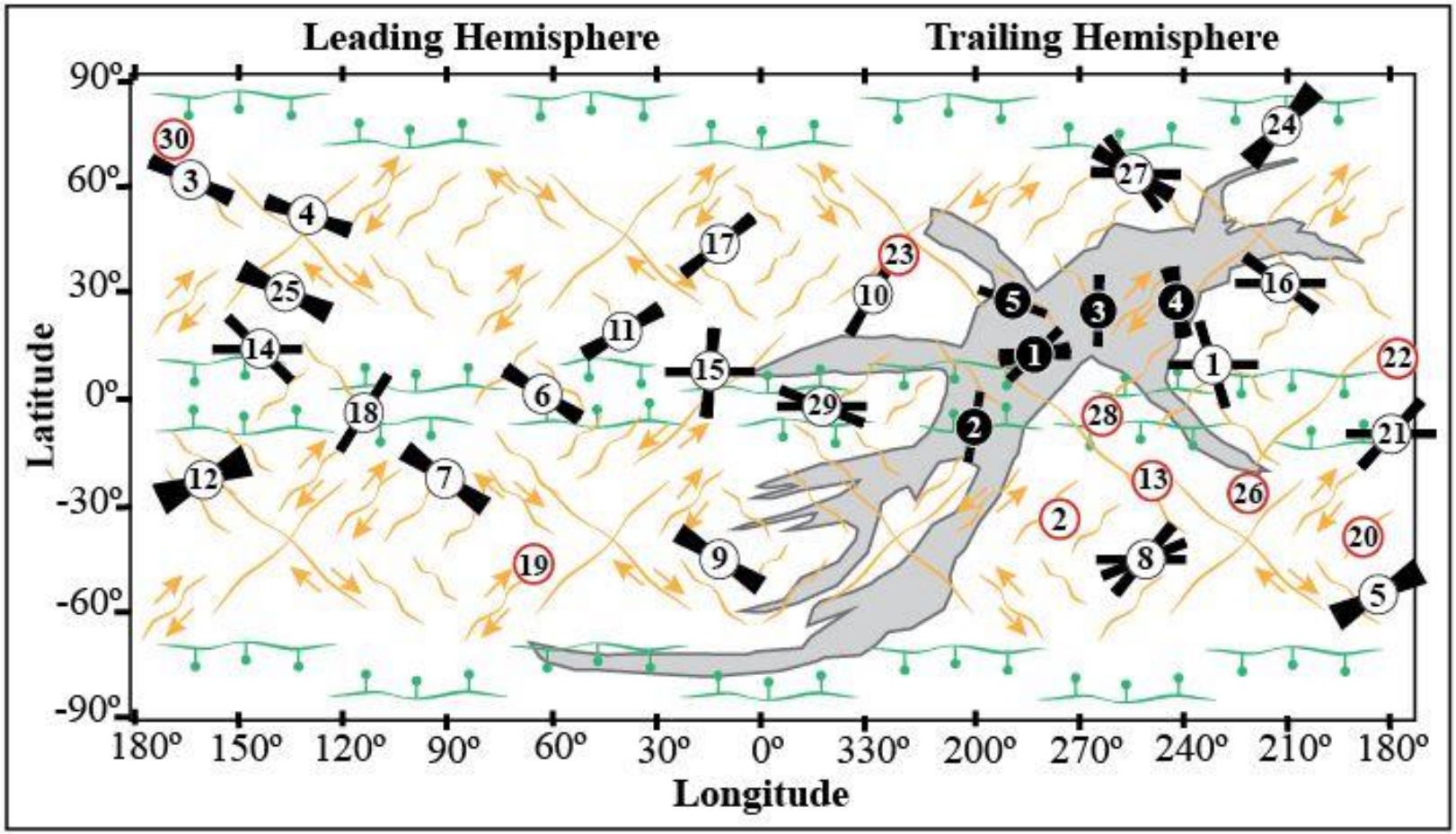

Figure III-13. The deformation pattern, including normal faults (green) and strike-slip faults (orange), associated with separate occurrences of satellite volume expansion and despinning for a satellite with a thinner lithosphere in the equatorial region and a thicker lithosphere in the polar regions (Beuthe, 2010). Rose diagrams of inferred fractures for Wispy and Non-Wispy Terrain study locations are also shown.

Appendix III-A: Determining Study Locations

Random study locations for data collection were generated using multiple tools in ESRI's ArcMap Software. The following steps and tools were utilized in the order listed.

- The Dione global mosaic base map, with attached latitude and longitude information, was acquired through ArcGIS online. The map was provided by the United States Geological Survey (USGS).
- The global mosaic of Dione was divided into two terrains. These terrains are the Wispy Terrain and all other regions on Dione, grouped into what we call the 'Non-Wispy Terrain'. The boundary of these terrains was determined using mapping by Stephan et al. (2010) as a guide.
- New polygon feature classes were created for the Wispy Terrain and Non-Wispy Terrain.
- The *Erase* tool was applied to subtract the Wispy Terrain polygon from the Non-Wispy Terrain polygon.
- Boundaries of the Wispy Terrain and the Non-Wispy Terrain were created using the *Polygon to Line* tool to convert the polygons of these two terrains to lines.
- The *Buffer* tool was utilized to create a 100 km boundary around each unit boundary. The purpose of this step is to allow the randomly generated study locations, discussed in a later step, to be far enough away from each terrain boundary so that a sufficient number of measurements can be taken around each point.
- The buffered regions were then subtracted from the original terrain polygons using the *Erase* tool.
- The *Create Random Points* tool was used to generate 5 points with random locations within the Wispy Terrain, and 30 points with random locations within the Non-Wispy Terrain. More points were generated within the Non-Wispy Terrain because the terrain covers a larger area than the Wispy Terrain. The points were specified to be ≥100 km apart so that a sufficient number of measurements could be taken around each point without analyzed areas overlapping each other.
- The latitudes and longitudes of each point were then added to the layer's attribute table using the *Add XY Coordinates* tool.
- The 30 closest impact craters were analyzed around each point generated. Any impact crater too small to measure was ignored. We disregarded any impact crater with a diameter <10 times the resolution of the image analyzed. Within the Wispy Terrain, the 30 closest fractures with lengths ≥10 times the image resolution were also measured, and those with lengths ≤10 times the image resolution were disregarded.

Appendix III-B: ISIS Image Processing Steps

Images from the Imaging Science Subsystem (ISS) camera onboard the Cassini spacecraft were processed and map-projected using the Integrated Software for Imagers and Spectrometers 3 (ISIS 3) (Anderson et al., 2004). The following ISIS commands were run on all images in the order listed. More details about specific ISIS commands can be found on the ISIS website (http://isis.astrogeology.usgs.gov/).

- The *ciss2isis* command was employed to convert the original PDS files (.img and .lbl files) of each image into an ISIS cube file (.cub files).
- The new image cubes were then associated with a camera model for Cassini ISS and augmented with spatial information (geometries of the spacecraft, sun angle geometries, ground positions, etc.) appropriate for the image acquisition time by using ISIS's *spiceinit* command.
- The *cisscal* command was used to convert the data number (DN) values of the images to reflectance.
- The *cam2map* command was utilized to map-project the images.

Appendix III-C: Classifying PICs

Our approach to classifying PICs is conservative, where some craters that may actually be affected by pre-existing sub-vertical structures within the target material may not be classified as a PIC. Impact craters were classified as PICs, and their rim azimuth distributions were determined using multiple tools in ESRI's ArcMap Software. In later steps, these azimuth distributions were exported to the R software for calculations and statistical analyses. The results of the statistical analyses were used to distinguish between CICs and PICs, and PIC azimuths were calculated. The following steps and tools were done in ESRI's ArcMap Software in the order listed.

- The rims of each crater were manually traced, using shadowing of the surface, as an indicator of topography.
- The resultant crater polygons were then converted to lines by using the *Polygon to Line* tool.
- Each line tracing a crater rim, was converted to sets of multi-lines by splitting the continuous line at its vertices. To do this, the *Split Line at Vertices* tool was used.
- Before the next step, a column was created in the multi-line attribute table called "RimSegmentID". This column was created using the *Add Field* tool. The field calculator was utilized to insert unique values from the OBJECTID column, already included in the attribute table, into this new column.
- For each set of multi-lines, the azimuths of each individual multi-line segment was calculated and added to the multi-line's attribute table. This step requires the *Linear Directional Mean* tool. For the "Case Field" option of this tool, the column termed "RimSegmentID" was used to provide a unique ID number to each multi-line segment. The resulting attribute table gives two piece of

information employed in the next steps. The column called "CompassA" is the azimuth of each multi-line segment given in degrees and measured clockwise from north. The column named "AveLen" is the average length of each multi-line segment.

- For each impact crater, each set of traced multi-line segment azimuths and their associated multi-line lengths were exported to the R software for calculations and analysis.

The following steps and tools were done in the R software using both the base functions, as well as functions provided in the R package 'diptest' (Maechler, 2013) in the order listed.

- For each impact crater trace, the set of multi-line segment azimuths and lengths were utilized to test for a uniform distribution of crater rim azimuths, normalized for the lengths of each measurement, by using a Pearson's Chi-Square test (e.g., Burt et al., 2009). This test was performed by using R's *chisq.test* function.
    - If the results of the Pearson's Chi-Square failed to reject the null hypothesis, then the azimuth distribution of a particular impact crater trace is uniform. The crater shows evidence for being a CIC and no further tests were done on these craters.
    - If instead, the Pearson's Chi-Square test is significant, then the distribution of azimuths is not uniform. In this case, the crater was marked as showing evidence for being a PIC, and further tests were performed on these craters.
- Kolmogorov-Smirnov tests were performed on all craters showing evidence for being a PIC. This test was conducted to investigate if a statistical similarity exists between a crater's rim azimuth distribution and that of nearby craters that also show evidence for being a PIC.
    - The Kolmogorov-Smirnov test was run in R by using the *ks.test* function.
    - If the test was significant, then there is not similarity in the crater's rim azimuth distribution with that of any nearby non-uniform craters. In this case, the crater shows evidence for being a CIC. These craters were not included in further statistical tests.
    - If the tests failed to reject the null hypothesis, then there is similarity in azimuth distributions between craters. The crater shows evidence for being a PIC, and further tests were carried out.
- Prominent modes were identified for each identified PIC using the Dip test (Hartigan and Hartigan, 1985).
    - Modality was determined using R's *dip.test* function, and the modes were also calculated in R.
    - If the dip test results show the set of data is unimodal, the first mode was recorded for that crater.
    - If the dip test results show the set of data is multi-modal, the first and second modes were recorded for that crater.

- If two or more craters in a study location exhibit a mode within 5º of each other, then the crater is identified as a PIC.

Appendix III-D: Comparing Visible Wispy Terrain Fractures to PICs

The following steps and tools were done using the R software and the functions provided in the R package 'circular' (Agostinelli and Lund, 2013). For Dione's Wispy Terrain, we tested for a statistical similarity between PIC azimuths and surrounding fracture azimuths. We employed the Watson's goodness of fit test (e.g., Stephens, 1970; Jammalamadaka and SenGupta, 2001) to determine if each set of data follow a circular normal distribution by using the *watson.test* command. If the data follow a circular normal distribution, then they are parametric. In this case, we applied the Watson-Williams two-sample test (Watson and Williams, 1956; Stephens, 1969) by using the *watson.williams.test* command. If the data do not follow a circular normal distribution, then they are nonparametric. In this case, we applied the Watson-Wheeler two-sample test (Batschelet, 1981; Zar, 1999) by using the *watson.wheeler.test* command.

Appendix III-E: Study Location IDs, Coordinates, and Images Utilized

The coordinates of the center of each study location are given for both the Wispy Terrain (Table III-E1) and the Non-Wispy Terrain (Table III-E2). The coordinates and diameters of the center of each impact crater analyzed are given for all Wispy Terrain Study Locations (Table III-E1) and Non-Wispy Terrain Study Locations (Table III-E2). The image ID of the highest resolution Cassini ISS image available to date (March, 2015) that covers each impact crater, and used to analyze crater are also given in both of these tables.

Table III-E1. Information on impact craters analyzed in each Wispy Terrain study location.

Crater ID	Coordinates (Latitude, Longitude)	Crater Diameter	Image Used (ID Number)	Image Resolution (m/px)
Wispy Terrain Study Location 1 (WT-1) Coordinates: 77.1°, 12.1°				
WT-1-1	6.9°, 79.9°	76.3 ± 2.2 km	N1569815436_1	398
WT-1-2	17.8°, 80.0°	11.4 ± 1.1 km	N1569827906_1	285
WT-1-3	18.4°, 78.0°	12.7 ± 1.0 km	N1569827906_1	285
WT-1-4	2.5°, 69.8°	26.2 ± 2.1 km	N1569815436_1	398
WT-1-5	17.3°, 75.5°	11.8 ± 0.9 km	N1569827906_1	285
Wispy Terrain Study Location 2 (WT-2) Coordinates: 59.5°, -8.4°				
WT-2-1	-16.1°, 60.7°	70.0 ± 6.8 km	N1481767088_1	432
WT-2-2	-10.3°, 65.8°	24.9 ± 0.8 km	N1481767088_1	432
WT-2-3	-13.0°, 69.5°	18.3 ± 1.2 km	N1481767088_1	432
WT-2-4	-3.4°, 72.5°	10.2 ± 1.2 km	N1569815436_1	398
WT-2-5	-19.6°, 69.1°	13.6 ± 1.2 km	N1481767088_1	432
Wispy Terrain Study Location 3 (WT-3) Coordinates: 94.5°, 24.6°				
WT-3-1	22.2°, 95.2°	19.1 ± 1.5 km	N1662198718_1	236
WT-3-2	24.0°, 94.8°	9.4 ± 0.7 km	N1662198718_1	236
WT-3-3	25.2°, 87.8°	64.1 ± 2.0 km	N1662198718_1	236
WT-3-4	19.0°, 110.8°	35.2 ± km	N1662199979_1	237
WT-3-5	18.2°, 99.6°	14.3 ± 1.0 km	N1662200149_1	239
Wispy Terrain Study Location 4 (WT-4) Coordinates: 116.8°, 26.8°				
WT-4-1	33.4°, 127.0°	91.1 ± 2.9 km	N1662200906_1	250
WT-4-2	29.0°, 110.9°	21.0 ± 1.9 km	N1662199979_1	237
WT-4-3	27.0°, 112.6°	13.4 ± 1.6 km	N1662199979_1	237
WT-4-4	20.1°, 117.9°	11.9 ± 0.2 km	N1662199979_1	237
WT-4-5	30.6°,108.4°	18.2 ± 0.8 km	N1662199979_1	237
Wispy Terrain Study Location 5 (WT-5) Coordinates: 71.2°, 27.6°				
WT-5-1	25.4°, 71.6°	9.6 ± 0.7 km	N1662198128_1	243
WT-5-2	25.5°, 72.3°	45.7 ± 3.3 km	N1662198128_1	243
WT-5-3	36.8°, 69.2°	21.5 ± 1.2 km	N1662198128_1	243
WT-5-4	37.4°, 61.7°	16.6 ± 1.0 km	N1662198128_1	243
WT-5-5	21.8°, 65.5°	8.4 ± 0.3 km	N1662198128_1	243

Table III-E2. Information on impact craters analyzed in each Non-Wispy Terrain study location.

Crater ID	Coordinates (Latitude, Longitude)	Crater Diameter	Image Used (ID Number)	Image Resolution (m/px)
Non-Wispy Terrain Study Location 1 (NWT-1) Coordinates: 127.7º, 9.6º				
NWT-1-1	10.6°, 119.3°	10.6 ± 0.7 km	N1662200736_2	247
NWT-1-2	9.0°, 123.6°	13.8 ± 0.8 km	N1662200736_2	247
NWT-1-3	6.0°, 140.0°	11.8 ± 0.8 km	N1662200736_2	247
NWT-1-4	14.0°, 122.0°	9.2 ± 0.4 km	N1662200736_2	247
NWT-1-5	12.6°, 122.3°	10.6 ± 0.5 km	N1662200736_2	247
NWT-1-6	3.9°, 130.4°	21.3 ± 1.4 km	N1662200736_2	247
NWT-1-7	12.4°, 137.9°	39.1 ± 1.8 km	N1662200736_2	247
NWT-1-8	15.9°, 135.2°	13.8 ± 0.5 km	N1662200736_2	247
NWT-1-9	13.5°, 132.7°	26.5 ± 2.2 km	N1662200736_2	247
NWT-1-10	13.5°, 132.7°	14.2 ± 1.6 km	N1662200736_2	247
Non-Wispy Terrain Study Location 2 (NWT-2) Coordinates: 84.3º, -33.5º				
NWT-2-1	-35.3°, 72.3°	11.9 ± 0.9 km	N1569814805_1	414
NWT-2-2	-26.7°, 91.8°	10.4 ± 1.2 km	N1569814968_1	410
NWT-2-3	-34.7°, 83.8°	10.5 ± 0.6 km	N1569814968_1	410
NWT-2-4	-21.9°, 92.3°	18.2 ± 1.7 km	N1569814968_1	410
NWT-2-5	-32.4°, 86.0°	11.6 ± 0.9 km	N1569814968_1	410
NWT-2-6	-30.0°, 86.5°	19.5 ± 1.3 km	N1569814968_1	410
NWT-2-7	-33.1°, 76.5°	18.2 ± 2.5 km	N1569814805_1	414
NWT-2-8	-37.2°, 88.1°	12.2 ± 0.7 km	N1569814968_1	410
NWT-2-9	-36.0°, 86.1°	7.7 ± 0.3 km	N1569814968_1	410
NWT-2-10	-34.9°, 86.2°	7.9 ± 0.2 km	N1569814968_1	410
Non-Wispy Terrain Study Location 3 (NWT-3) Coordinates: -161.3º, 61.0º				
NWT-3-1	59.6°, 193.4°	10.4 ± 0.4 km	N1662201249_1	257
NWT-3-2	61.3°, 190.3°	18.7 ± 3.3 km	N1662201249_1	257
NWT-3-3	58.6°, 184.5°	12.1 ± 0.7 km	N1662201249_1	257
NWT-3-4	61.4°, 166.8°	10.1 ± 0.5 km	N1662201249_1	257
NWT-3-5	57.5°, 187.5°	8.4 ± 0.4 km	N1662201249_1	257
NWT-3-6	63.4°, 209.4°	13.8 ± 0.8 km	N1662201249_1	257
NWT-3-7	55.1°, 198.8°	11.8 ± 0.3 km	N1662201249_1	257
NWT-3-8	59.0°, 175.2°	26.0 ± 0.8 km	N1662201249_1	257
NWT-3-9	57.8°, 201.3°	15.9 ± 1.5 km	N1662201249_1	257
NWT-3-10	53.3°, 204.7°	27.2 ± 1.6 km	N1662201249_1	257

Table III-E2. Continued.

Crater ID	Coordinates (Latitude, Longitude)	Crater Diameter	Image Used (ID Number)	Image Resolution (m/px)
Non-Wispy Terrain Study Location 4 (NWT-4) Coordinates: -128.7º, 51.2º				
NWT-4-1	51.6°, 236.0°	10.9 ± 0.4 km	N1665974345_1	222
NWT-4-2	47.6°, 241.4°	15.5 ± 1.6 km	N1665974517_1	225
NWT-4-3	57.8°, 218.7°	17.5 ± 1.2 km	N1665974345_1	222
NWT-4-4	48.5°, 223.1°	11.8 ± 0.8 km	N1665974345_1	222
NWT-4-5	49.0°, 217.5°	10.1 ± 0.5 km	N1665974345_1	222
NWT-4-6	49.6°, 234.0°	8.4 ± 0.4 km	N1665974345_1	222
NWT-4-7	56.6°, 243.6°	13.0 ± 0.9 km	N1665974345_1	222
NWT-4-8	54.0°, 215.9°	11.8 ± 0.7 km	N1665974345_1	222
NWT-4-9	45.0°, 223.0°	11.4 ± 0.9 km	N1665974345_1	222
NWT-4-10	61.7°, 218.5°	11.7 ± 0.4 km	N1665974345_1	222
Non-Wispy Terrain Study Location 5 (NWT-5) Coordinates: 174.6º, -55.2º				
NWT-5-1	-50.8°, 175.8°	12.0 ± 0.7 km	N1507739776_2	341
NWT-5-2	-55.1°, 161.1°	10.7 ± 0.5 km	N1507739776_2	341
NWT-5-3	-57.0°, 150.5°	10.6 ± 1.2 km	N1507739776_2	341
NWT-5-4	-44.9°, 198.6°	19.2 ± 0.4 km	N1507739776_2	341
NWT-5-5	-56.8°, 189.2°	3.5 ± 0.4 km	N1507743729_2	124
NWT-5-6	-51.1°, 196.8°	10.8 ± 5 km	N1507739776_2	341
NWT-5-7	-48.7°, 163.4°	16.5 ± 1.4 km	N1507739776_2	341
NWT-5-8	-48.8°, 157.1°	18.0 ± 0.6 km	N1507739776_2	341
NWT-5-9	-46.2°, 161.3°	8.5 ± 0.2 km	N1507739776_2	341
NWT-5-10	-56.9°, 150.5°	10.1 ± 0.6 km	N1507739776_2	341
Non-Wispy Terrain Study Location 6 (NWT-6) Coordinates: -62.2º, 1.2º				
NWT-6-1	-4.2°, -61.6°	29.8 ± 1.9 km	N1696197091_1	939
NWT-6-2	0.2°, -67.0°	34.8 ± 1.4 km	N1696197091_1	939
NWT-6-3	-26.9°, -66.8°	26.9 ± 1.3 km	N1696197091_1	939
NWT-6-4	-20.9°, -56.3°	15.9 ± 0.7 km	N1696197091_1	939
NWT-6-5	-33.7°, -66.2°	42.8 ± 2.8 km	N1696197091_1	939
NWT-6-6	-1.5°, -52.4°	16.2 ± 1.0 km	N1696197091_1	939
NWT-6-7	-16.9°, -62.6°	17.0 ± 1.4 km	N1696197091_1	939
NWT-6-8	22.9°, -71.3°	25.4 ± 0.9 km	N1696197091_1	939
NWT-6-9	-18.4°, -77.8°	35.5 ± 0.9 km	N1696197091_1	939
NWT-6-10	-10.9°, -46.6°	21.9 ± 1.5 km	N1696197091_1	939

Table III-E2. Continued.

Crater ID	Coordinates (Latitude, Longitude)	Crater Diameter	Image Used (ID Number)	Image Resolution (m/px)
Non-Wispy Terrain Study Location 7 (NWT-7) Coordinates: -89.8º, -22.1º				
NWT-7-1	-24.4°, -80.9°	47.2 ± 1.5 km	N1696197091_1	939
NWT-7-2	-19.5°, -92.5°	20.3 ± 1.2 km	N1696197091_1	939
NWT-7-3	-19.1°, -94.6°	17.1 ± 1.4 km	N1696197091_1	939
NWT-7-4	-16.0°, -99.6°	38.4 ± 2.0 km	N1696197091_1	939
NWT-7-5	-17.9°, -81.6°	13.3 ± 1.2 km	N1696197091_1	939
NWT-7-6	-37.2°, -90.0°	25.3 ± 2.0 km	N1696197091_1	939
NWT-6-7	-37.2°, -90.0°	82.3 ± 2.6 km	N1696197091_1	939
NWT-7-8	15.6°, -84.8°	26.3 ± 1.5 km	N1696197091_1	939
NWT-7-9	-31.7°, -71.2°	11.2 ± 0.6 km	N1696197091_1	939
NWT-7-10	-4.4°, -88.1°	17.0 ± 2.9 km	N1696197091_1	939
Non-Wispy Terrain Study Location 8 (NWT-8) Coordinates: 108.7º, -44.6º				
NWT-8-1	-38.2°, 106.0°	9.2 ± 0.2 km	N1569814968_1	410
NWT-8-2	-45.5°, 100.1°	24.2 ± 1.1 km	N1569814968_1	410
NWT-8-3	-42.2°, 102.0°	22.2 ± 1.2 km	N1569814968_1	410
NWT-8-4	-48.7°, 115.1°	26.7 ± 0.9 km	N1569814968_1	410
NWT-8-5	-39.4°, 113.0°	12.2 ± 0.7 km	N1569814968_1	410
NWT-8-6	-38.9°, 110.0°	11.9 ± 0.9 km	N1569814968_1	410
NWT-8-7	-36.6°, 106.6°	12.8 ± 0.9 km	N1569814968_1	410
NWT-8-8	-44.0°, 113.7°	7.7 ± 0.3 km	N1569814968_1	410
NWT-8-9	-48.7°, 100.8°	10.0 ± 0.4 km	N1569814968_1	410
NWT-8-10	-37.1°, 109.3°	11.2 ± 0.5 km	N1569814968_1	410
Non-Wispy Terrain Study Location 9 (NWT-9) Coordinates: -11.9º, -44.6º				
NWT-9-1	-45.8°, -22.0°	16.6 ± 1.2 km	N1649318460_1	364
NWT-9-2	-41.9°, -23.6°	13.8 ± 0.3 km	N1649318460_1	364
NWT-9-3	-48.0°, -16.7°	16.0 ± 0.8 km	N1649318460_1	364
NWT-9-4	-41.2°, -32.8°	20.0 ± 0.8 km	N1649318460_1	364
NWT-9-5	-42.6°, 8.4°	23.6 ± 1.2 km	N1649318247_1	352
NWT-9-6	-45.4°, -6.4°	26.4 ± 0.9 km	N1649318247_1	352
NWT-9-7	-42.9°, -29.2°	22.7 ± 0.8 km	N1649318460_1	364
NWT-9-8	-52.7°, -18.7°	10.5 ± 0.9 km	N1649318460_1	364
NWT-9-9	-41.1°, 4.0°	16.1 ± 0.8 km	N1649318247_1	352
NWT-9-10	-49.6°, -33.1°	18.0 ± 1.6 km	N1649318460_1	364

Table III-E2. Continued.

Crater ID	Coordinates (Latitude, Longitude)	Crater Diameter	Image Used (ID Number)	Image Resolution (m/px)
Non-Wispy Terrain Study Location 10 (NWT-10) Coordinates: 31.4º, 29.2º				
NWT-10-1	26.5°, 37.5°	21.4 ± 0.5 km	N1569827799_1	283
NWT-10-2	31.0°, 39.0°	13.4 ± 0.9 km	N1569827799_1	283
NWT-10-3	33.8°, 35.2°	11.6 ± 0.3 km	N1569827799_1	283
NWT-10-4	32.0°, 29.5°	15.1 ± 0.6 km	N1569827692_1	281
NWT-10-5	31.6°, 22.6°	10.8 ± 0.7 km	N1569827692_1	281
NWT-10-6	34.0°, 32.1°	12.9 ± 0.6 km	N1569827692_1	281
NWT-10-7	27.1°, 40.4°	10.1 ± 0.6 km	N1569827799_1	283
NWT-10-8	22.1°, 39.2°	26.1 ± 1.5 km	N1569827799_1	283
NWT-10-9	28.5°, 24.3°	23.9 ± 1.7 km	N1569827692_1	281
NWT-10-10	24.7°, 38.5°	7.9 ± 0.4 km	N1569827799_1	283
Non-Wispy Terrain Study Location 11 (NWT-11) Coordinates: -39.7º, 18.6º				
NWT-11-1	17.4°, -32.4°	24.6 ± 0.8 km	N1696197091_1	939
NWT-11-2	11.7°, -43.7°	28.8 ± 1.3 km	N1696197091_1	939
NWT-11-3	26.0°, -47.1°	152.1 ± 4.2 km	N1696197091_1	939
NWT-11-4	8.4°, -38.8°	16.0 ± 0.8 km	N1696197091_1	939
NWT-11-5	9.9°, -39.3°	15.0 ± 0.6 km	N1696197091_1	939
NWT-11-6	26.6°, -30.6°	39.6 ± 2.2 km	N1696197091_1	939
NWT-11-7	35.2°, -40.4°	23.9 ± 1.2 km	N1696197091_1	939
NWT-11-8	36.0°, -34.3°	20.4 ± 1.0 km	N1696197091_1	939
NWT-11-9	20.5°, -35.6°	28.5 ± 0.9 km	N1696197091_1	939
NWT-11-10	26.0°, -27.0°	20.9 ± 0.6 km	N1696197091_1	939
Non-Wispy Terrain Study Location 12 (NWT-12) Coordinates: -157.4º, -22.4º				
NWT-12-1	-20.9°, 214.5°	15.1 ± 0.5 km	N1507741569_2	483
NWT-12-2	-25.9°, 199.1°	16.8 ± 1.6 km	N1507741669_2	472
NWT-12-3	-28.1°, 205.6°	17.6 ± 2.1 km	N1507741569_2	483
NWT-12-4	-28.7°, 186.5°	25.3 ± 1.9 km	N1507741669_2	472
NWT-12-5	-21.9°, 191.3°	13.9 ± 0.4 km	N1507741669_2	472
NWT-12-6	-16.6°, 205.2°	12.0 ± 0.9 km	N1507741569_2	483
NWT-12-7	-19.7°, 195.4°	13.4 ± 0.8 km	N1507741669_2	472
NWT-12-8	-26.1°, 196.0°	13.3 ± 1.0 km	N1507741669_2	472
NWT-12-9	-19.8°, 199.6°	11.5 ± 1.7 km	N1507741669_2	472
NWT-12-10	-24.6°, 204.3°	10.0 ± 0.7 km	N1507741669_2	472

Table III-E2. Continued.

Crater ID	Coordinates (Latitude, Longitude)	Crater Diameter	Image Used (ID Number)	Image Resolution (m/px)
Non-Wispy Terrain Study Location 13 (NWT-13) Coordinates: 110.7º, -22.9º				
NWT-13-1	-23.1°, 107.2°	26.8 ± 1.8 km	N1662200319_1	241
NWT-13-2	-22.0°, 114.8°	54.0 ± 1.0 km	N1662200319_1	241
NWT-13-3	-16.9°, 115.7°	17.8 ± 8.8 km	N1662200319_1	241
NWT-13-4	-18.9°, 110.3°	8.0 ± 0.7 km	N1662200319_1	241
NWT-13-5	-30.4°, 107.8°	11.2 ± 0.8 km	N1662200319_1	241
NWT-13-6	-29.4°, 110.3°	11.7 ± 0.7 km	N1662200319_1	241
NWT-13-7	-12.5°, 111.3°	19.6 ± 1.2 km	N1662200319_1	241
NWT-13-8	-27.4°, 111.0°	15.4 ± 1.5 km	N1662200319_1	241
NWT-13-9	-23.4°, 102.7°	17.7 ± 1.2 km	N1662200319_1	241
NWT-13-10	-17.3°, 111.5°	16.8 ± 1.6 km	N1662200319_1	241
Non-Wispy Terrain Study Location 14 (NWT-14) Coordinates: -142.5º, 14.2º				
NWT-14-1	10.8°, 228.7°	24.1 ± 0.8 km	N1507741300_2	256
NWT-14-2	10.3°, 212.5°	47.1 ± 1.8 km	N1507741300_2	256
NWT-14-3	16.0°, 205.3°	21.3 ± 1.0 km	N1507741300_2	256
NWT-14-4	15.2°, 230.3°	10.6 ± 0.4 km	N1507741300_2	256
NWT-14-5	12.6°, 204.3°	13.6 ± 0.8 km	N1507741300_2	256
NWT-14-6	18.5°, 202.8°	19.1 ± 1.1 km	N1507741300_2	256
NWT-14-7	23.5°, 221.9°	15.8 ± 0.9 km	N1507741300_2	256
NWT-14-8	20.1°, 213.4°	27.2 ± 0.8 km	N1507741300_2	256
NWT-14-9	-1.2°, 216.7°	24.4 ± 1.6 km	N1507741460_2	247
NWT-14-10	0.2°, 219.6°	17.1 ± 1.0 km	N1507741460_2	247
Non-Wispy Terrain Study Location 15 (NWT-15) Coordinates: -14.7º, 8.2º				
NWT-15-1	1.9°, 0.5°	27.0 ± 2.0 km	N1569828482_1	293
NWT-15-2	23.7°, -13.9°	41.7 ± 2.0 km	N1569828360_1	291
NWT-15-3	4.5°, -19.8°	34.8 ± 0.8 km	N1569828482_1	293
NWT-15-4	27.6°, -17.7°	22.8 ± 1.3 km	N1569828360_1	291
NWT-15-5	14.6°, -10.2°	20.6 ± 0.7 km	N1569828360_1	291
NWT-15-6	1.5°, -4.7°	38.5 ± 2.0 km	N1569828482_1	293
NWT-15-7	3.1°, -12.4°	34.6 ± 1.1 km	N1569828482_1	293
NWT-15-8	7.7°, -11.7°	44.0 ± 4.5 km	N1569828482_1	293
NWT-15-9	-6.1°, -9.6°	76.3 ± 1.0 km	N1569828482_1	293
NWT-15-10	12.7°, -20.7°	16.1 ± 0.2 km	N1569828360_1	291

Table III-E2. Continued.

Crater ID	Coordinates (Latitude, Longitude)	Crater Diameter	Image Used (ID Number)	Image Resolution (m/px)
Non-Wispy Terrain Study Location 16 (NWT-16) Coordinates: 147.0º, 32.2º				
NWT-16-1	34.2°, 146.2°	15.5 ± 0.7 km	N1662200906_1	250
NWT-16-2	30.0°, 148.7°	11.8 ± 0.9 km	N1662200906_1	250
NWT-16-3	36.0°, 142.3°	18.4 ± 0.7 km	N1662200906_1	250
NWT-16-4	37.8°, 153.9°	12.0 ± 0.7 km	N1662201078_1	253
NWT-16-5	36.9°, 146.1°	18.7 ± 1.8 km	N1662201078_1	253
NWT-16-6	26.5°, 141.1°	16.7 ± 0.8 km	N1662200906_1	250
NWT-16-7	20.7°, 146.1°	23.3 ± 1.3 km	N1662200906_1	250
NWT-16-8	24.2°, 145.2°	12.4 ± 6.4 km	N1662200906_1	250
NWT-16-9	23.9°, 153.0°	12.3 ± 5.9 km	N1662201668_1	267
NWT-16-10	31.2°, 156.4°	13.8 ± 4.6 km	N1662201668_1	267
Non-Wispy Terrain Study Location 17 (NWT-17) Coordinates: -11.9º, 43.1º				
NWT-17-1	33.7°, -7.2°	64.7 ± 5.5 km	N1569828360_1	291
NWT-17-2	39.8°, -14.6°	39.4 ± 6.0 km	N1569839110_1	610
NWT-17-3	47.6°, -19.8°	31.6 ± 1.6 km	N1578081030_1	765
NWT-17-4	46.1°, 10.2°	36.2 ± 2.0 km	N1569828131_4	288
NWT-17-5	51.9°, 3.2°	18.1 ± 1.2 km	N1569828131_4	288
NWT-17-6	42.0°, -1.2°	17.4 ± 0.4 km	N1569827692_1	281
NWT-17-7	49.3°, 6.5°	15.3 ± 1.2 km	N1569828131_4	288
NWT-17-8	48.8°, 2.1°	15.8 ± 1.1 km	N1569828131_4	288
NWT-17-9	35.6°, 1.3°	26.9 ± 5.5 km	N1569827692_1	281
NWT-17-10	52.1°, -10.0°	15.2 ± 1.3 km	N1649317673_1	322
Non-Wispy Terrain Study Location 18 (NWT-18) Coordinates: -112.2º, -3.9º				
NWT-18-1	4.8°, 255.2°	48.5 ± 1.8 km	N1665972106_1	190
NWT-18-2	14.2°, 249.3°	12.1 ± 0.1 km	N1665974689_1	229
NWT-18-3	-1.2°, 247.7°	13.2 ± 0.7 km	N1665972106_1	190
NWT-18-4	-3.5°, 250.7°	19.1 ± 1.5 km	N1665972106_1	190
NWT-18-5	-5.5°, 250.4°	13.8 ± 0.9 km	N1665972106_1	190
NWT-18-6	-11.3°, 248.5°	10.6 ± 0.3 km	N1665972106_1	190
NWT-18-7	-5.3°, 254.8°	19.9 ± 0.8 km	N1665972106_1	190
NWT-18-8	-8.9°, 257.1°	13.4 ± 0.5 km	N1665972106_1	190
NWT-18-9	-14.7°, 243.6°	20.1 ± 0.6 km	N1507734092_2	665
NWT-18-10	-7.5°, 249.3°	7.6 ± 0.2 km	N1665972106_1	190

Table III-E2. Continued.

Crater ID	Coordinates (Latitude, Longitude)	Crater Diameter	Image Used (ID Number)	Image Resolution (m/px)
Non-Wispy Terrain Study Location 19 (NWT-19) Coordinates: -64.5º, -46.8º				
NWT-19-1	-34.5°, -53.4°	36.6 ± 1.6 km	N1556123061_1	722
NWT-19-2	-55.2°, -45.1°	20.9 ± 1.1 km	N1556123061_1	722
NWT-19-3	-43.3°, -86.6°	28.0 ± 1.8 km	N1556123061_1	722
NWT-19-4	-42.7°, -55.6°	11.4 ± 0.5 km	N1649318460_1	364
NWT-19-5	-41.7°, -51.8°	8.9 ± 0.4 km	N1649318460_1	364
NWT-19-6	-40.4°, -57.5°	10.2 ± 0.8 km	N1649318460_1	364
NWT-19-7	-41.9°, -45.8°	17.5 ± 2.1 km	N1649318460_1	364
NWT-19-8	-47.8°, -63.2°	13.9 ± 0.3 km	N1649318460_1	364
NWT-19-9	-38.4°, -46.3°	15.6 ± 0.3 km	N1649318460_1	364
NWT-19-10	-37.4°, -86.8°	25.6 ± 1.2 km	N1556123061_1	722
Non-Wispy Terrain Study Location 20 (NWT-20) Coordinates: 169.8º, -38.6º				
NWT-20-1	-36.4°, 173.5°	11.4 ± 0.5 km	N1507743058_2	160
NWT-20-2	-38.3°, 162.4°	17.2 ± 2.1 km	N1507743058_2	160
NWT-20-3	-43.5°, 174.2°	80.9 ± 3.2 km	N1507739776_2	341
NWT-20-4	-34.6°, 164.6°	11.2 ± 0.4 km	N1507743058_2	160
NWT-20-5	-34.0°, 166.2°	9.7 ± 0.5 km	N1507743058_2	160
NWT-20-6	-39.9°, 159.8°	1.1 ± 0.1 km	N1507745820_2	20
NWT-20-7	-36.9°, 161.9°	15.5 ± 1.2 km	N1507743058_2	160
NWT-20-8	-31.7°, 170.0°	8.4 ± 0.1 km	N1507743058_2	160
NWT-20-9	-26.7°, 161.7°	14.5 ± 0.5 km	N1507743058_2	160
NWT-20-10	-33.7°, 169.7°	6.1 ± 0.3 km	N1507743058_2	160
Non-Wispy Terrain Study Location 21 (NWT-21) Coordinates: 178.3º, -9.6º				
NWT-21-1	-13.1°, 183.0°	21.3 ± 1.4 km	N1507741973_2	219
NWT-21-2	-14.7°, 173.6°	14.2 ± 0.6 km	N1507742919_2	167
NWT-21-3	-8.7°, 186.6°	11.8 ± 0.7 km	N1507741973_2	219
NWT-21-4	-7.3°, 192.6°	12.5 ± 0.6 km	N1507741973_2	219
NWT-21-5	-5.0°, 174.8°	50.7 ± 5.1 km	N1507742761_2	176
NWT-21-6	-10.0°, 193.3°	16.1 ± 0.6 km	N1507741973_2	219
NWT-21-7	0.8°, 186.9°	15.4 ± 5.0 km	N1507742134_3	210
NWT-21-8	-5.1°, 178.5°	24.5 ± 0.4 km	N1507742761_2	176
NWT-21-9	-15.1°, 190.3°	23.5 ± 0.6 km	N1507741973_2	219
NWT-21-10	-1.1°, 184.4°	34.6 ± 0.8 km	N1507741973_2	219

Table III-E2. Continued.

Crater ID	Coordinates (Latitude, Longitude)	Crater Diameter	Image Used (ID Number)	Image Resolution (m/px)
Non-Wispy Terrain Study Location 22 (NWT-22) Coordinates: 180.0º, 11.4º				
NWT-22-1	9.7°, 189.8°	23.8 ± 0.9 km	N1507742134_3	210
NWT-22-2	10.7°, 170.1°	32.8 ± 2.7 km	N1507742601_2	185
NWT-22-3	8.4°, 185.3°	14.7 ± 0.6 km	N1507742134_3	210
NWT-22-4	2.6°, 173.5°	16.4 ± 0.8 km	N1507742601_2	185
NWT-22-5	3.3°, 167.9°	33.5 ± 1.4 km	N1507742601_2	185
NWT-22-6	2.3°, 171.1°	16.2 ± 1.2 km	N1507742601_2	185
NWT-22-7	11.2°, 182.7°	12.1 ± 0.9 km	N1507742134_3	210
NWT-22-8	9.8°, 183.9°	20.5 ± 2.0 km	N1507742134_3	210
NWT-22-9	12.8°, 185.0°	15.1 ± 1.1 km	N1507742134_3	210
NWT-22-10	17.0°, 186.2°	14.4 ± 0.4 km	N1507742134_3	210
Non-Wispy Terrain Study Location 23 (NWT-23) Coordinates: 38.8º, 40.3º				
NWT-23-1	38.3°, 44.9°	8.4 ± 0.6 km	N1662197108_1	263
NWT-23-2	37.1°, 45.6°	7.1 ± 0.2 km	N1662197108_1	263
NWT-23-3	35.0°, 45.5°	12.9 ± 0.4 km	N1662197108_1	263
NWT-23-4	34.8°, 51.6°	12.2 ± 1.0 km	N1662197108_1	263
NWT-23-5	33.1°, 44.4°	10.3 ± 0.4 km	N1662197108_1	263
NWT-23-6	36.6°, 43.7°	19.1 ± 1.1 km	N1662197108_1	263
NWT-23-7	34.8°, 41.1°	18.2 ± 0.6 km	N1662197108_1	263
NWT-23-8	48.4°, 33.9°	13.2 ± 0.4 km	N1662197108_1	263
NWT-23-9	37.1°, 50.3°	14.3 ± 0.7 km	N1662197108_1	263
NWT-23-10	41.2°, 37.5°	43.1 ± 4.0 km	N1662197108_1	263
Non-Wispy Terrain Study Location 24 (NWT-24) Coordinates: 147.4º, 76.0º				
NWT-24-1	82.3°, 169.2°	13.8 ± 0.4 km	N1662199058_1	234
NWT-24-2	77.9°, 119.6°	21.2 ± 1.0 km	N1662199058_1	234
NWT-24-3	72.7°, 134.3°	15.6 ± 0.6 km	N1662199639_1	235
NWT-24-4	75.8°, 162.1°	10.4 ± 0.4 km	N1662199639_1	235
NWT-24-5	80.4°, 191.8°	11.7 ± 1.2 km	N1662199058_1	234
NWT-24-6	71.7°, 153.2°	18.9 ± 1.5 km	N1662199639_1	235
NWT-24-7	75.3°, 139.0°	16.2 ± 0.4 km	N1662199639_1	235
NWT-24-8	74.8°, 129.3°	12.7 ± 1.2 km	N1662199058_1	234
NWT-24-9	72.8°, 164.7°	26.5 ± 3.6 km	N1662199639_1	235
NWT-24-10	69.3°, 150.2°	12.1 ± 1.2 km	N1662199639_1	235

Table III-E2. Continued.

Crater ID	Coordinates (Latitude, Longitude)	Crater Diameter	Image Used (ID Number)	Image Resolution (m/px)
Non-Wispy Terrain Study Location 25 (NWT-25) Coordinates: -135.3º, 29.9º				
NWT-25-1	27.3°, 218.2°	21.8 ± 1.3 km	N1507741300_2	256
NWT-25-2	23.6°, 222.0°	15.7 ± 1.0 km	N1507741300_2	256
NWT-25-3	36.6°, 220.2°	19.7 ± 1.2 km	N1643287088_1	271
NWT-25-4	29.6°, 230.8°	14.6 ± 0.4 km	N1665974517_1	225
NWT-25-5	33.0°, 230.8°	6.2 ± 0.2 km	N1665974517_1	225
NWT-25-6	31.8°, 223.0°	10.4 ± 0.8 km	N1643287088_1	271
NWT-25-7	22.5°, 229.5°	38.1 ± 2.1 km	N1507741300_2	256
NWT-25-8	25.4°, 225.8°	11.3 ± 1.3 km	N1507741300_2	256
NWT-25-9	37.9°, 228.5°	10.4 ± 0.7 km	N1665974517_1	225
NWT-25-10	25.8°, 221.2°	7.9 ± 0.4 km	N1507741300_2	256
Non-Wispy Terrain Study Location 26 (NWT-26) Coordinates: 137.5º, -26.1º				
NWT-26-1	-21.3°, 131.7°	29.3 ± 2.7 km	N1662200504_1	244
NWT-26-2	-26.6°, 145.5°	1.6 ± 0.1 km	N1507745708_2	32
NWT-26-3	-27.8°, 144.7°	1.0 ± 0.1 km	N1507745708_2	32
NWT-26-4	-24.9°, 134.7°	2.0 ± 0.1 km	N1507745681_2	36
NWT-26-5	-24.6°, 133.6°	1.9 ± 0.2 km	N1507745681_2	36
NWT-26-6	-25.4°, 144.5°	46.2 ± 1.9 km	N1662200504_1	244
NWT-26-7	-18.5°, 126.2°	8.3 ±0.5 km	N1662200504_1	244
NWT-26-8	-25.3°, 140.2°	8.7 ± 0.6 km	N1662200504_1	244
NWT-26-9	-22.8°, 134.1°	9.6 ± 0.3 km	N1662200504_1	244
NWT-26-10	-24.7°, 135.9°	14.2 ± 0.6 km	N1662200504_1	244
Non-Wispy Terrain Study Location 27 (NWT-27) Coordinates: 105.4º, 62.8º				
NWT-27-1	63.4°, 100.7°	10.0 ± 0.9 km	N1662199058_1	234
NWT-27-2	61.2°, 97.3°	9.6 ± 0.6 km	N1662198888_1	235
NWT-27-3	61.5°, 120.5°	27.2 ± 1.1 km	N1662199639_1	235
NWT-27-4	65.2°, 119.2°	11.0 ± 1.1 km	N1662199639_1	235
NWT-27-5	68.3°, 113.2°	19.0 ± 1.2 km	N1662199058_1	234
NWT-27-6	66.2°, 110.3°	10.8 ± 0.6 km	N1662199058_1	234
NWT-27-7	56.6°, 97.1°	20.3 ± 1.1 km	N1662198888_1	235
NWT-27-8	63.1°, 106.8°	10.8 ± 1.0 km	N1662199058_1	234
NWT-27-9	68.2°, 123.1°	18.3 ± 2.3 km	N1662199639_1	235
NWT-27-10	53.9°, 104.7°	55.7 ± 3.8 km	N1662199809_1	235

Table III-E2. Continued.

Crater ID	Coordinates (Latitude, Longitude)	Crater Diameter	Image Used (ID Number)	Image Resolution (m/px)
Non-Wispy Terrain Study Location 28 (NWT-28) Coordinates: 96.3º, -4.4º				
NWT-28-1	0.6°, 91.9°	39.6 ± 2.0 km	N1662198548_1	238
NWT-28-2	2.7°, 94.7°	18.0 ± 1.0 km	N1662198548_1	238
NWT-28-3	1.1°, 102.1°	14.3 ± 1.4 km	N1662200149_1	239
NWT-28-4	-9.7°, 103.0°	32.2 ± 4.1 km	N1662200319_1	241
NWT-28-5	-12.9°, 100.1°	16.4 ± 0.3 km	N1662200319_1	241
NWT-28-6	-10.2°, 96.6°	15.6 ± 1.8 km	N1662200319_1	241
NWT-28-7	-8.7°, 95.5°	10.8 ± 0.3 km	N1662200319_1	241
NWT-28-8	-12.9°, 91.2°	70.3 ± 2.3 km	N1569815285_1	402
NWT-28-9	-10.3°, 107.2°	20.1 ± 4.2 km	N1662200319_1	241
NWT-28-10	-7.9°, 107.6°	18.0 ± 0.9 km	N1662200149_1	239
Non-Wispy Terrain Study Location 29 (NWT-29) Coordinates: 17.0º, -1.9º				
NWT-29-1	4.1°, 11.7°	16.8 ± 0.5 km	N1649315242_1	198
NWT-29-2	-0.7°, 15.4°	52.8 ± 1.9 km	N1569827571_1	280
NWT-29-3	0.2°, 20.9°	19.8 ± 1.8 km	N1649315242_1	198
NWT-29-4	-5.6°, 17.0°	22.9 ± 1.2 km	N1569827571_1	280
NWT-29-5	-6.7°, 19.4°	17.9 ± 1.7 km	N1569827571_1	280
NWT-29-6	-5.2°, 11.3°	14.3 ± 0.7 km	N1569827571_1	280
NWT-29-7	2.2°, 21.3°	13.8 ± 0.9 km	N1649315242_1	198
NWT-29-8	-9.3°, 7.6°	20.5 ± 1.2 km	N1569827571_1	280
NWT-29-9	-11.4°, 15.0°	15.5 ± 0.7 km	N1569827571_1	280
NWT-29-10	-8.9°, 11.2°	16.3 ± 1.1 km	N1569827571_1	280
Non-Wispy Terrain Study Location 30 (NWT-30) Coordinates: -166.0º, 72.3º				
NWT-30-1	73.8°, 193.0°	8.7 ± 0.4 km	N1662199639_1	235
NWT-30-2	66.9°, 200.9°	11.2 ± 0.8 km	N1662201249_1	257
NWT-30-3	69.4°, 201.4°	10.3 ± 0.4 km	N1662201249_1	257
NWT-30-4	70.1°, 189.7°	13.6 ± 1.0 km	N1662199639_1	235
NWT-30-5	72.8°, 186.4°	11.9 ± 0.8 km	N1662199639_1	235
NWT-30-6	65.0°, 179.2°	45.9 ± 2.3 km	N1662199639_1	235
NWT-30-7	65.6°, 156.8°	11.4 ± 1.1 km	N1662199639_1	235
NWT-30-8	71.7°, 204.0°	8.4 ± 0.3 km	N1662201249_1	257
NWT-30-9	70.3°, 177.9°	21.4 ± 1.5 km	N1662199639_1	235
NWT-30-10	78.1°, 191.7°	12.0 ± 1.6 km	N1662199639_1	235

Appendix III-F: Details on Statistical Test Results

Details on statistical test results are given in this appendix. The results for all statistical tests applied to investigate impact crater geometries for craters within both the Wispy and Non-Wispy Terrain are given in Tables III-F1 through III-F6. Details on results for all Pearson's Chi-squared tests for a uniform crater rim azimuth distribution are given for craters analyzed within Wispy Terrain study locations (Table III-F1) and Non-Wispy Terrain study locations (Table III-F7). Details on results for the Kolmogorov-Smirnov tests for a statistical similarity between crater rim azimuths of nearby craters are given for analysis in Wispy Terrain study locations (Table III-F2), and Non-Wispy Terrain study locations (Table III-F8).

Details on the results of Dip tests for modality of crater rim azimuth distributions are given for craters analyzed in Wispy Terrain study locations (Table III-F3) and Non-Wispy Terrain study locations (Table III-F9). The common prominent crater rim azimuths, as well as consistent azimuths between craters and fractures are also given in these tables. Details on results of the Watson test for a circular normal distribution of Wispy Terrain crater rim and fracture azimuths are given in Table III-F4. The resulting two-sample circular statistical test to be employed for each set of data is also given in this table. Details on the results of these two-sample statistical tests utilized are given in table F5. The prominent crater rim azimuths for each identified PIC in each Wispy Terrain study location are given in Table III-F6. The prominent azimuths of the fractures closest to each identified PIC in these study locations are also given in this table.

Table III-F1. Results for Pearson's Chi-Square tests for Wispy Terrain crater rim azimuths.

Crater ID	Pearson's Chi-Square Test Results (p-values)	Uniform Distribution?
Wispy Terrain Study Location 1 (WT-1)		
WT-1-1	7.5×10^{-6}	No
WT-1-2	4.5×10^{-7}	No
WT-1-3	6.0×10^{-7}	No
WT-1-4	7.9×10^{-5}	No
WT-1-5	0.026	Yes
Wispy Terrain Study Location 2 (WT-2)		
WT-2-1	2.9×10^{-23}	No
WT-2-2	7.7×10^{-45}	No
WT-2-3	1.0×10^{-50}	No
WT-2-4	2.4×10^{-32}	No
WT-2-5	1.2×10^{-34}	No
Wispy Terrain Study Location 3 (WT-3)		
WT-3-1	2.3×10^{-54}	No
WT-3-2	1.3×10^{-20}	No
WT-3-3	2.0×10^{-52}	No
WT-3-4	6.9×10^{-47}	No
WT-3-5	1.0×10^{-24}	No
Wispy Terrain Study Location 4 (WT-4)		
WT-4-1	6.2×10^{-110}	No
WT-4-2	2.4×10^{-71}	No
WT-4-3	4.5×10^{-72}	No
WT-4-4	7.2×10^{-81}	No
WT-4-5	1.9×10^{-97}	No
Wispy Terrain Study Location 5 (WT-5)		
WT-5-1	3.4×10^{-23}	No
WT-5-2	1.4×10^{-42}	No
WT-5-3	5.1×10^{-61}	No
WT-5-4	9.5×10^{-40}	No
WT-5-5	1.2×10^{-20}	No

Table III-F2. Results for Kolmogorov-Smirnov tests for Wispy Terrain crater rim azimuths.

Crater ID	Closest Non-Uniform Crater		Kolmogorov-Smirnov Test Results (p-value)	Statistically Similar to Nearby Craters?
	Crater ID	Distance		
Wispy Terrain Study Location 1 (WT-1)				
WT-1-1	WT-1-4	102 km	0.146	Yes
WT-1-2	WT-1-3	21 km	0.097	Yes
WT-1-3	WT-1-2	21 km	0.097	Yes
WT-1-4	WT-1-1	102 km	0.146	Yes
Wispy Terrain Study Location 2 (WT-2)				
WT-2-1	WT-2-2	78 km	$<2.2 \times 10^{-16}$	No
WT-2-2	WT-2-3	41 km	0.139	Yes
WT-2-3	WT-2-2	41 km	0.139	Yes
WT-2-4	WT-2-2	99 km	1.3×10^{-5}	No
WT-2-5	WT-2-3	65 km	0.856	Yes
Wispy Terrain Study Location 3 (WT-3)				
WT-3-1	WT-3-2	19 km	0.578	Yes
WT-3-2	WT-3-1	19 km	0.578	Yes
WT-3-3	WT-3-2	64 km	1.9×10^{-8}	No
WT-3-4	WT-3-5	105 km	0.289	Yes
WT-3-5	WT-3-1	60 km	0.012	No
Wispy Terrain Study Location 4 (WT-4)				
WT-4-1	WT-4-3	129 km	3.3×10^{-13}	No
	WT-4-2	133 km	1.2×10^{-7}	
	WT-4-4	146 km	1.1×10^{-14}	
WT-4-2	WT-4-3	25 km	0.109	Yes
WT-4-3	WT-4-2	25 km	0.109	Yes
WT-4-4	WT-4-3	86 km	0.877	Yes
WT-4-5	WT-4-2	28 km	0.076	Yes
Wispy Terrain Study Location 5 (WT-5)				
WT-5-1	WT-5-2	8 km	1.2×10^{-10}	Yes
	WT-5-5	68 km	0.711	
WT-5-2	WT-5-1	8 km	1.2×10^{-10}	No
WT-5-3	WT-5-4	59 km	0.217	Yes
WT-5-4	WT-5-3	59 km	0.217	Yes
WT-5-5	WT-5-1	68 km	0.711	Yes

Table III-F3. Results for Dip tests for Wispy Terrain crater rim azimuths.

Crater ID	Dip Test p-value	Modality	Azimuth Mode(s)	Closest Fracture Azimuth Mode	Common PIC-PIC and PIC-Fracture Azimuths
Wispy Terrain Study Location 1 (WT-1)					
WT-1-1	4.8×10^{-5}	Multimodal	76°, 92°	81°	**Set 1:** 45° - 46°
WT-1-2	0.151	Unimodal	62°	46°	**Set 2:** 81° - 76°
WT-1-3	4.4×10^{-4}	Multimodal	90°, 76°	33°	
WT-1-4	6.0×10^{-5}	Multimodal	113°, 45°	45°	**Set 3:** 90° - 92°
Wispy Terrain Study Location 2 (WT-2)					
WT-2-2	0.413	Unimodal	10°	10°	**Set 1:** 10°
WT-2-3	0.544	Unimodal	10°	10°	
WT-2-5	0.841	Unimodal	10°	10°	
Wispy Terrain Study Location 3 (WT-3)					
WT-3-1	$< 2.2 \times 10^{-16}$	Multimodal	180°, 38°	180°	**Set 1:** 2° - 180°
WT-3-2	$< 2.2 \times 10^{-16}$	Multimodal	180°, 2°	180°	
WT-3-4	$< 2.2 \times 10^{-16}$	Multimodal	180°, 70°	180°	
Wispy Terrain Study Location 4 (WT-4)					
WT-4-2	$< 2.2 \times 10^{-16}$	Multimodal	160°, 167°	160°	**Set 1:** 160° - 164° - 167° **Set 2:** 175° - 177°
WT-4-3	$< 2.2 \times 10^{-16}$	Multimodal	160°, 164°	160°	
WT-4-4	$< 2.2 \times 10^{-16}$	Multimodal	160°, 177°	160°	
WT-4-5	$< 2.2 \times 10^{-16}$	Multimodal	160°, 175°	160°	
Wispy Terrain Study Location 5 (WT-5)					
WT-5-1	0.997	Unimodal	110°	110°	**Set 1:** 110°
WT-5-2	$< 2.2 \times 10^{-16}$	Multimodal	110°, 147°	110°	
WT-5-3	6.0×10^{-5}	Multimodal	110°, 164°	110°	
WT-5-4	0.299	Unimodal	110°	110°	
WT-5-5	0.680	Unimodal	110°	110°	

Table III-F4. Watson test results for Wispy Terrain crater rim azimuths and fracture azimuths.

Study Location ID	Watson Test				Both Datasets Normally Distributed?	Two-sample circular statistical test to use
	Impact Craters Test Statistic	Impact Craters Critical Value	Fractures Test Statistic	Fractures Critical Value		
WT-1	0.03	0.142	0.691	0.142	No	Watson Wheeler Test
WT-2	-	-	4.43	0.164	No	
WT-3	0.153	0.128	5.49	0.164	No	
WT-4	0.129	0.164	2.60	0.164	No	
WT-5	0.247	0.142	7.03	0.164	No	

Table III-F5. Results for two-sample tests for Wispy Terrain crater rim azimuths and fracture azimuths.

Study Location ID	Watson-Wheeler Two-sample Test p-value	Are Crater Rim Segments and Fracture Trends Statistically Similar?
WT-1	0.126	Yes
WT-2	0.053	Yes
WT-3	0.341	Yes
WT-4	0.500	Yes
WT-5	0.039	Yes

Table III-F6. Prominent Wispy Terrain PIC azimuths.

PIC Crater ID	PIC Azimuth Mode(s)	Closest Fracture Azimuth Mode
Wispy Terrain Study Location 1 (WT-1)		
WT-1-1	76°, 92°	81°
WT-1-2	62°	46°
WT-1-3	90°, 76°	33°
WT-1-4	113°, 45°	45°
Wispy Terrain Study Location 2 (WT-2)		
WT-2-2	10°	10°
WT-2-3	10°	10°
WT-2-5	10°	10°
Wispy Terrain Study Location 3 (WT-3)		
WT-3-1	180°, 38°	180°
WT-3-2	180°, 2°	180°
WT-3-4	180°, 70°	180°
Wispy Terrain Study Location 4 (WT-4)		
WT-4-2	160°, 167°	160°
WT-4-3	160°, 164°	160°
WT-4-4	160°, 177°	160°
WT-4-5	160°, 175°	160°
Wispy Terrain Study Location 5 (WT-5)		
WT-5-1	110°	110°
WT-5-2	110°, 147°	110°
WT-5-3	110°, 164°	110°
WT-5-4	110°	110°
WT-5-5	110°	110°

Table III-F7. Results for Pearson's Chi-Square tests for Non-Wispy Terrain crater rim azimuths.

Crater ID	Pearson's Chi-Square Test Results (p-values)	Uniform Distribution?
Non-Wispy Terrain Study Location 1 (NWT-1)		
NWT-1-1	0.340	Yes
NWT-1-2	0.040	Yes
NWT-1-3	5.3×10^{-9}	No
NWT-1-4	0.069	Yes
NWT-1-5	0.063	Yes
NWT-1-6	0.123	Yes
NWT-1-7	2.5×10^{-8}	No
NWT-1-8	0.002	No
NWT-1-9	5.3×10^{-4}	No
NWT-1-10	7.7×10^{-6}	No
Non-Wispy Terrain Study Location 2 (NWT-2)		
NWT-2-1	0.047	Yes
NWT-2-2	0.074	Yes
NWT-2-3	0.144	Yes
NWT-2-4	0.030	Yes
NWT-2-5	0.051	Yes
NWT-2-6	0.003	Yes
NWT-2-7	3.4×10^{-7}	No
NWT-2-8	0.469	Yes
NWT-2-9	0.075	Yes
NWT-2-10	0.189	Yes
Non-Wispy Terrain Study Location 3 (NWT-3)		
NWT-3-1	4.6×10^{-90}	No
NWT-3-2	2.4×10^{-155}	No
NWT-3-3	3.9×10^{-83}	No
NWT-3-4	2.9×10^{-44}	No
NWT-3-5	8.5×10^{-78}	No
NWT-3-6	4.4×10^{-236}	No
NWT-3-7	1.3×10^{-97}	No
NWT-3-8	1.7×10^{-146}	No
NWT-3-9	7.1×10^{-161}	No
NWT-3-10	1.5×10^{-320}	No
Non-Wispy Terrain Study Location 4 (NWT-4)		
NWT-4-1	3.4×10^{-167}	No
NWT-4-2	2.7×10^{-281}	No

Table III-F7. Continued.

Crater ID	Pearson's Chi-Square Test Results (p-values)	Uniform Distribution?
NWT-4-3	3.1×10^{-277}	No
NWT-4-4	5.2×10^{-136}	No
NWT-4-5	6.9×10^{-106}	No
NWT-4-6	3.4×10^{-152}	No
NWT-4-7	$3.2 \times 10^{-247-}$	No
NWT-4-8	4.8×10^{-160}	No
NWT-4-9	6.2×10^{-124}	No
NWT-4-10	1.7×10^{-202}	No
Non-Wispy Terrain Study Location 5 (NWT-5)		
NWT-5-1	1.1×10^{-31}	No
NWT-5-2	4.0×10^{-36}	No
NWT-5-3	4.5×10^{-20}	No
NWT-5-4	2.1×10^{-72}	No
NWT-5-5	1.0×10^{-49}	No
NWT-5-6	4.0×10^{-48}	No
NWT-5-7	8.3×10^{-50}	No
NWT-5-8	1.6×10^{-62}	No
NWT-5-9	3.9×10^{-16}	No
NWT-5-10	1.1×10^{-36}	No
Non-Wispy Terrain Study Location 6 (NWT-6)		
NWT-6-1	0.251	Yes
NWT-6-2	0.416	Yes
NWT-6-3	4.4×10^{-30}	No
NWT-6-4	4.1×10^{-4}	No
NWT-6-5	1.5×10^{-46}	No
NWT-6-6	0.142	Yes
NWT-6-7	0.001	No
NWT-6-8	1.6×10^{-14}	No
NWT-6-9	3.9×10^{-15}	No
NWT-6-10	0.004	No
Non-Wispy Terrain Study Location 7 (NWT-7)		
NWT-7-1	9.3×10^{-44}	No
NWT-7-2	1.7×10^{-9}	No
NWT-7-3	1.5×10^{-9}	No
NWT-7-4	1.5×10^{-17}	No
NWT-7-5	0.005	No
NWT-7-6	1.1×10^{-58}	No
NWT-7-7	2.5×10^{-7}	No

Table III-F7. Continued.

Crater ID	Pearson's Chi-Square Test Results (p-values)	Uniform Distribution?
NWT-7-8	3.3×10^{-5}	No
NWT-7-9	0.906	Yes
NWT-7-10	0.035	Yes
Non-Wispy Terrain Study Location 8 (NWT-8)		
NWT-8-1	0.223	Yes
NWT-8-2	7.7×10^{-8}	No
NWT-8-3	5.0×10^{-5}	No
NWT-8-4	9.4×10^{-12}	No
NWT-8-5	0.003	No
NWT-8-6	0.001	No
NWT-8-7	0.015	Yes
NWT-8-8	0.086	Yes
NWT-8-9	1.3×10^{-4}	No
NWT-8-10	2.7×10^{-4}	No
Non-Wispy Terrain Study Location 9 (NWT-9)		
NWT-9-1	7.4×10^{-46}	No
NWT-9-2	5.3×10^{-25}	No
NWT-9-3	4.3×10^{-43}	No
NWT-9-4	1.5×10^{-38}	No
NWT-9-5	5.1×10^{-33}	No
NWT-9-6	3.9×10^{-34}	No
NWT-9-7	1.5×10^{-53}	No
NWT-9-8	7.4×10^{-29}	No
NWT-9-9	1.6×10^{-19}	No
NWT-9-10	6.4×10^{-48}	No
Non-Wispy Terrain Study Location 10 (NWT-10)		
NWT-10-1	1.2×10^{-5}	No
NWT-10-2	3.4×10^{-4}	No
NWT-10-3	2.5×10^{-4}	No
NWT-10-4	2.5×10^{-11}	No
NWT-10-5	1.9×10^{-6}	No
NWT-10-6	1.2×10^{-7}	No
NWT-10-7	0.004	No
NWT-10-8	0.571	Yes
NWT-10-9	0.002	No
NWT-10-10	0.073	Yes
Non-Wispy Terrain Study Location 11 (NWT-11)		

Table III-F7. Continued.

Crater ID	Pearson's Chi-Square Test Results (p-values)	Uniform Distribution?
NWT-11-1	0.001	No
NWT-11-2	6.9×10^{-6}	No
NWT-11-3	1.6×10^{-82}	No
NWT-11-4	0.258	Yes
NWT-11-5	0.054	Yes
NWT-11-6	7.7×10^{-15}	No
NWT-11-7	4.6×10^{-14}	No
NWT-11-8	8.2×10^{-18}	No
NWT-11-9	2.4×10^{-8}	No
NWT-11-10	1.6×10^{-6}	No
Non-Wispy Terrain Study Location 12 (NWT-12)		
NWT-12-1	1.4×10^{-18}	No
NWT-12-2	1.2×10^{-15}	No
NWT-12-3	3.1×10^{-23}	No
NWT-12-4	2.3×10^{-25}	No
NWT-12-5	5.2×10^{-13}	No
NWT-12-6	1.0×10^{-5}	No
NWT-12-7	6.0×10^{-6}	No
NWT-12-8	8.6×10^{-10}	No
NWT-12-9	0.008	No
NWT-12-10	1.8×10^{-9}	No
Non-Wispy Terrain Study Location 13 (NWT-13)		
NWT-13-1	3.4×10^{-6}	No
NWT-13-2	1.7×10^{-47}	No
NWT-13-3	6.8×10^{-12}	No
NWT-13-4	0.057	Yes
NWT-13-5	7.2×10^{-15}	No
NWT-13-6	1.1×10^{-5}	No
NWT-13-7	5.7×10^{-6}	No
NWT-13-8	1.0×10^{-9}	No
NWT-13-9	7.8×10^{-4}	No
NWT-13-10	1.6×10^{-7}	No
Non-Wispy Terrain Study Location 14 (NWT-14)		
NWT-14-1	1.1×10^{-17}	No
NWT-14-2	3.3×10^{-46}	No
NWT-14-3	1.3×10^{-44}	No
NWT-14-4	2.0×10^{-12}	No
NWT-14-5	1.1×10^{-11}	No

Table III-F7. Continued.

Crater ID	Pearson's Chi-Square Test Results (p-values)	Uniform Distribution?
NWT-14-6	1.3×10^{-28}	No
NWT-14-7	3.9×10^{-57}	No
NWT-14-8	8.2×10^{-47}	No
NWT-14-9	0.299	Yes
NWT-14-10	1.2×10^{-4}	No
Non-Wispy Terrain Study Location 15 (NWT-15)		
NWT-15-1	0.002	No
NWT-15-2	1.7×10^{-49}	No
NWT-15-3	2.0×10^{-5}	No
NWT-15-4	6.8×10^{-27}	No
NWT-15-5	6.2×10^{-10}	No
NWT-15-6	7.4×10^{-5}	No
NWT-15-7	0.014	Yes
NWT-15-8	2.7×10^{-7}	No
NWT-15-9	1.4×10^{-7}	No
NWT-15-10	4.1×10^{-5}	No
Non-Wispy Terrain Study Location 16 (NWT-16)		
NWT-16-1	7.1×10^{-22}	No
NWT-16-2	3.8×10^{-9}	No
NWT-16-3	1.3×10^{-28}	No
NWT-16-4	6.8×10^{-11}	No
NWT-16-5	6.1×10^{-26}	No
NWT-16-6	1.2×10^{-7}	No
NWT-16-7	2.8×10^{-10}	No
NWT-16-8	4.7×10^{-13}	No
NWT-16-9	8.1×10^{-9}	No
NWT-16-10	9.0×10^{-22}	No
Non-Wispy Terrain Study Location 17 (NWT-17)		
NWT-17-1	1.1×10^{-86}	No
NWT-17-2	7.3×10^{-35}	No
NWT-17-3	1.3×10^{-26}	No
NWT-17-4	1.1×10^{-45}	No
NWT-17-5	1.4×10^{-52}	No
NWT-17-6	5.5×10^{-29}	No
NWT-17-7	1.8×10^{-23}	No
NWT-17-8	1.1×10^{-19}	No
NWT-17-9	9.9×10^{-32}	No
NWT-17-10	1.1×10^{-36}	No

Table III-F7. Continued.

Crater ID	Pearson's Chi-Square Test Results (p-values)	Uniform Distribution?
Non-Wispy Terrain Study Location 18 (NWT-18)		
NWT-18-1	5.2×10^{-16}	No
NWT-18-2	3.9×10^{-20}	No
NWT-18-3	0.522	Yes
NWT-18-4	7.9×10^{-8}	Yes
NWT-18-5	2.2×10^{-18}	No
NWT-18-6	4.1×10^{-18}	No
NWT-18-7	4.3×10^{-19}	No
NWT-18-8	2.8×10^{-7}	No
NWT-18-9	7.9×10^{-15}	No
NWT-18-10	3.5×10^{-8}	No
Non-Wispy Terrain Study Location 19 (NWT-19)		
NWT-19-1	0.652	Yes
NWT-19-2	0.156	Yes
NWT-19-3	0.029	Yes
NWT-19-4	0.628	Yes
NWT-19-5	0.506	Yes
NWT-19-6	$2.8 \text{ X } 10^{-4}$	No
NWT-19-7	2.3×10^{-7}	No
NWT-19-8	0.016	Yes
NWT-19-9	0.874	Yes
NWT-19-10	0.004	No
Non-Wispy Terrain Study Location 20 (NWT-20)		
NWT-20-1	4.7×10^{-11}	No
NWT-20-2	0.065	No
NWT-20-3	8.6×10^{-10}	No
NWT-20-4	0.008	No
NWT-20-5	0.504	Yes
NWT-20-6	0.871	Yes
NWT-20-7	1.4×10^{-23}	No
NWT-20-8	0.010	Yes
NWT-20-9	2.5×10^{-5}	No
NWT-20-10	0.192	Yes
Non-Wispy Terrain Study Location 21 (NWT-21)		
NWT-21-1	4.1×10^{-12}	No
NWT-21-2	3.5×10^{-20}	No
NWT-21-3	0.176	Yes
NWT-21-4	3.4×10^{-9}	No

Table III-F7. Continued.

Crater ID	Pearson's Chi-Square Test Results (p-values)	Uniform Distribution?
NWT-21-5	0.040	Yes
NWT-21-6	3.2×10^{-7}	No
NWT-21-7	0.002	No
NWT-21-8	2.2×10^{-18}	No
NWT-21-9	3.1×10^{-41}	No
NWT-21-10	1.2×10^{-6}	No
Non-Wispy Terrain Study Location 22 (NWT-22)		
NWT-22-1	2.9×10^{-18}	No
NWT-22-2	8.4×10^{-14}	No
NWT-22-3	6.3×10^{-9}	No
NWT-22-4	9.2×10^{-6}	No
NWT-22-5	1.1×10^{-6}	No
NWT-22-6	7.5×10^{-4}	No
NWT-22-7	2.9×10^{-16}	No
NWT-22-8	2.4×10^{-12}	No
NWT-22-9	1.8×10^{-18}	No
NWT-22-10	3.4×10^{-14}	No
Non-Wispy Terrain Study Location 23 (NWT-23)		
NWT-23-1	5.3×10^{-5}	No
NWT-23-2	0.294	Yes
NWT-23-3	0.372	Yes
NWT-23-4	0.988	Yes
NWT-23-5	0.693	Yes
NWT-23-6	0.282	Yes
NWT-23-7	0.059	Yes
NWT-23-8	0.002	Yes
NWT-23-9	4.6×10^{-7}	No
NWT-23-10	1.1×10^{-6}	Yes
Non-Wispy Terrain Study Location 24 (NWT-24)		
NWT-24-1	0.593	Yes
NWT-24-2	1.4×10^{-4}	No
NWT-24-3	0.137	Yes
NWT-24-4	0.819	Yes
NWT-24-5	1.0×10^{-4}	No
NWT-24-6	0.002	No
NWT-24-7	0.695	Yes
NWT-24-8	9.1×10^{-6}	No
NWT-24-9	0.001	No

Table III-F7. Continued.

Crater ID	Pearson's Chi-Square Test Results (p-values)	Uniform Distribution?
NWT-24-10	0.002	No
Non-Wispy Terrain Study Location 25 (NWT-25)		
NWT-25-1	6.5×10^{-68}	No
NWT-25-2	4.9×10^{-55}	No
NWT-25-3	1.0×10^{-106}	No
NWT-25-4	4.4×10^{-76}	No
NWT-25-5	9.4×10^{-25}	No
NWT-25-6	2.2×10^{-37}	No
NWT-25-7	3.3×10^{-101}	No
NWT-25-8	5.5×10^{-27}	No
NWT-25-9	2.4×10^{-96}	No
NWT-25-10	5.8×10^{-21}	No
Non-Wispy Terrain Study Location 26 (NWT-26)		
NWT-26-1	1.8×10^{-15}	No
NWT-26-2	1.7×10^{-7}	No
NWT-26-3	3.5×10^{-7}	No
NWT-26-4	5.0×10^{-16}	No
NWT-26-5	3.7×10^{-12}	No
NWT-26-6	1.2×10^{-78}	No
NWT-26-7	0.008	No
NWT-26-8	6.3×10^{-21}	No
NWT-26-9	6.4×10^{-9}	No
NWT-26-10	3.6×10^{-9}	No
Non-Wispy Terrain Study Location 27 (NWT-27)		
NWT-27-1	3.0×10^{-18}	No
NWT-27-2	3.3×10^{-7}	No
NWT-27-3	9.3×10^{-50}	No
NWT-27-4	1.5×10^{-30}	No
NWT-27-5	3.3×10^{-31}	No
NWT-27-6	1.6×10^{-14}	No
NWT-27-7	2.0×10^{-15}	No
NWT-27-8	5.2×10^{-10}	No
NWT-27-9	6.4×10^{-22}	No
NWT-27-10	6.2×10^{-31}	No
Non-Wispy Terrain Study Location 28 (NWT-28)		
NWT-28-1	0.185	Yes
NWT-28-2	0.034	Yes
NWT-28-3	6.1×10^{-26}	No

Table III-F7. Continued.

Crater ID	Pearson's Chi-Square Test Results (p-values)	Uniform Distribution?
NWT-28-4	9.2×10^{-13}	No
NWT-28-5	2.6×10^{-4}	No
NWT-28-6	2.6×10^{-4}	No
NWT-28-7	0.534	Yes
NWT-28-8	0.341	Yes
NWT-28-9	5.9×10^{-6}	No
NWT-28-10	6.8×10^{-5}	No
Non-Wispy Terrain Study Location 29 (NWT-29)		
NWT-29-1	0.444	Yes
NWT-29-2	0.067	Yes
NWT-29-3	0.002	No
NWT-29-4	0.113	Yes
NWT-29-5	1.9×10^{-4}	No
NWT-29-6	0.357	Yes
NWT-29-7	0.003	No
NWT-29-8	0.003	No
NWT-29-9	4.5×10^{-4}	No
NWT-29-10	2.4×10^{-5}	No
Non-Wispy Terrain Study Location 30 (NWT-30)		
NWT-30-1	0.216	Yes
NWT-30-2	0.007	No
NWT-30-3	0.058	Yes
NWT-30-4	3.7×10^{-10}	No
NWT-30-5	0.822	Yes
NWT-30-6	0.024	Yes
NWT-30-7	0.002	No
NWT-30-8	0.083	Yes
NWT-30-9	2.6×10^{-5}	No
NWT-30-10	0.056	Yes

Table III-F8. Results for Kolmogorov-Smirnov tests for Non-Wispy Terrain crater rim azimuths.

Crater ID	Closest Non-Uniform Crater ID	Closest Non-Uniform Crater Distance	Kolmogorov-Smirnov Test Results (p-value)	Similar to Nearby Craters?
Non-Wispy Terrain Study Location 1 (NWT-1)				
NWT-1-3	NWT-1-7	70 km	0.139	Yes
NWT-1-7	NWT-1-8	38 km	0.138	Yes
NWT-1-8	NWT-1-9	34 km	0.377	Yes
NWT-1-9	NWT-1-8	34 km	0.377	Yes
NWT-1-10	NWT-1-9	120 km	0.035	No
Non-Wispy Terrain Study Location 2 (NWT-2)				
Only one non-uniform impact crater detected				
Non-Wispy Terrain Study Location 3 (NWT3)				
NWT-3-1	NWT-3-2	25 km	0.068	Yes
NWT-3-2	NWT-3-1	25 km	0.068	Yes
NWT-3-3	NWT-3-5	20 km	0.201	Yes
NWT-3-4	NWT-3-8	49 km	0.329	Yes
NWT-3-5	NWT-3-3	20 km	0.201	Yes
NWT-3-6	NWT-3-9	72 km	2.5×10^{-9}	No
NWT-3-7	NWT-3-9	33 km	0.069	Yes
NWT-3-8	NWT-3-4	49 km	0.329	Yes
NWT-3-9	NWT-3-7	33 km	0.069	Yes
NWT-3-10	NWT-3-7	42 km	1.3×10^{-5}	No
Non-Wispy Terrain Study Location 4 (NWT4)				

Table III-F8. Continued.

Crater ID	Closest Non-Uniform Crater ID	Closest Non-Uniform Crater Distance	Kolmogorov-Smirnov Test Results (p-value)	Similar to Nearby Craters?
NWT-4-1	NWT-4-6	22 km	0.060	Yes
NWT-4-2	NWT-4-6	53 km	0.012	No
NWT-4-3	NWT-4-10	38 km	0.006	No
	NWT-4-8	44 km	0.015	
	NWT-4-5	90 km	0.004	
NWT-4-4	NWT-4-5	37 km	0.259	Yes
NWT-4-5	NWT-4-4	37 km	0.259	Yes
NWT-4-6	NWT-4-1	22 km	0.060	Yes
NWT-4-7	NWT-4-1	63 km	6.7×10^{-6}	No
NWT-4-8	NWT-4-5	49 km	0.005	No
NWT-4-9	NWT-4-5	51 km	0.123	Yes
NWT-4-10	NWT-4-5	127 km	9.4×10^{-4}	No
Non-Wispy Terrain Study Location 5 (NWT5)				
NWT-5-1	NWT-5-7	94 km	1.7×10^{-4}	No
NWT-5-2	NWT-5-3	54 km	0.023	No
	NWT-5-10	66 km	6.5×10^{-6}	
NWT-5-3	NWT-5-8	40 km	0.002	No
NWT-5-4	NWT-5-6	69 km	0.123	Yes
NWT-5-5	NWT-5-6	77 km	0.245	Yes
NWT-5-6	NWT-5-4	69 km	0.123	Yes
NWT-5-7	NWT-5-9	30 km	0.342	Yes
NWT-5-8	NWT-5-9	45 km	0.062	Yes

Table III-F8. Continued.

Crater ID	Closest Non-Uniform Crater ID	Closest Non-Uniform Crater Distance	Kolmogorov-Smirnov Test Results (p-value)	Similar to Nearby Craters?
NWT-5-9	**NWT-5-7**	**30 km**	**0.342**	**Yes**
NWT-5-10	NWT-5-3	57 km	0.223	Yes
Non-Wispy Terrain Study Location 6 (NWT6)				
NWT-6-3	NWT-6-5	274 km	0.284	Yes
NWT-6-4	NWT-6-7	212 km	0.524	Yes
NWT-6-5	NWT-6-3	274 km	0.284	Yes
NWT-6-7	NWT-6-4	212 km	0.524	Yes
NWT-6-8	NWT-6-10	737 km	1.5×10^{-6}	No
NWT-6-9	NWT-6-7	398 km	0.026	No
NWT-6-10	NWT-6-4	365 km	0.092	Yes
Non-Wispy Terrain Study Location 7 (NWT-7)				
NWT-7-1	NWT-7-5	201 km	0.222	Yes
NWT-7-2	NWT-7-3	56 km	0.326	Yes
NWT-7-3	NWT-7-2	56 km	0.326	Yes
NWT-7-4	NWT-7-7	186 km	1.7×10^{-11}	Yes
	NWT-7-3	139 km	0.280	
NWT-7-5	NWT-7-1	201 km	0.222	Yes
NWT-7-6	NWT-7-1	601 km	3.1×10^{-9}	No
NWT-7-7	NWT-7-4	186 km	1.7×10^{-11}	No
NWT-7-8	NWT-7-2	377 km	0.004	No
Non-Wispy Terrain Study Location 8 (NWT-8)				

Table III-F8. Continued.

Crater ID	Closest Non-Uniform Crater ID	Closest Non-Uniform Crater Distance	Kolmogorov-Smirnov Test Results (p-value)	Similar to Nearby Craters?
NWT-8-2	NWT-8-9	32 km	0.459	Yes
NWT-8-3	NWT-8-2	34 km	0.776	Yes
NWT-8-4	NWT-8-8	47 km	0.892	Yes
NWT-8-5	NWT-8-6	32 km	0.659	Yes
NWT-8-6	NWT-8-10	19 km	0.138	Yes
NWT-8-9	NWT-8-2	32 km	0.659	Yes
NWT-8-10	NWT-8-6	19 km	0.138	Yes
Non-Wispy Terrain Study Location 9 (NWT-9)				
NWT-9-1	NWT-9-2	45 km	0.058	Yes
NWT-9-2	NWT-9-1	45 km	0.058	Yes
NWT-9-3	NWT-9-1	49 km	0.009	No
NWT-9-4	NWT-9-7	38 km	0.235	Yes
NWT-9-5	NWT-9-9	40 km	0.125	Yes
NWT-9-6	NWT-9-9	105 km	0.006	No
NWT-9-7	NWT-9-4	38 km	0.235	Yes
NWT-9-8	NWT-9-1	83 km	0.004	No
NWT-9-9	NWT-9-5	40 km	0.125	Yes
NWT-9-10	NWT-9-7	80 km	0.004	No
Non-Wispy Terrain Study Location 10 (NWT-10)				
NWT-10-1	NWT-10-10	25 km	0.219	Yes

Table III-F8. Continued.

Crater ID	Closest Non-Uniform Crater ID	Closest Non-Uniform Crater Distance	Kolmogorov-Smirnov Test Results (p-value)	Similar to Nearby Craters?
NWT-10-2	**NWT-10-7**	**55 km**	**0.035**	**Yes**
	NWT-10-3	55 km	0.190	
NWT-10-3	NWT-10-6	33 km	0.429	Yes
NWT-10-4	NWT-10-6	40 km	0.004	No
NWT-10-5	NWT-10-9	46 km	0.048	No
NWT-10-6	NWT-10-3	33 km	0.429	Yes
NWT-10-7	NWT-10-1	37 km	0.027	No
NWT-10-9	NWT-10-6	112 km	0.323	Yes
NWT-10-10	NWT-10-1	25 km	0.219	Yes
Non-Wispy Terrain Study Location 11 (NWT-11)				
NWT-11-1	NWT-11-9	62 km	0.033	Yes
	NWT-11-6	136 km	0.080	
NWT-11-2	NWT-11-9	178 km	0.027	No
	NWT-11-3	197 km	0.011	
NWT-11-3	NWT-11-9	146 km	0.002	Yes
	NWT-11-7	149 km	0.140	
NWT-11-6	NWT-11-10	42 km	0.728	Yes
NWT-11-7	NWT-11-8	62 km	0.188	Yes
NWT-11-8	NWT-11-7	62 km	0.188	Yes
NWT-11-9	NWT-11-1	62 km	0.033	No
NWT-11-10	NWT-11-6	42 km	0.728	Yes
Non-Wispy Terrain Study Location 12 (NWT-12)				
NWT-12-1	NWT-12-10	140 km	0.317	Yes

Table III-F8. Continued.

Crater ID	Closest Non-Uniform Crater ID	Closest Non-Uniform Crater Distance	Kolmogorov-Smirnov Test Results (p-value)	Similar to Nearby Craters?
NWT-12-2	NWT-12-8	36 km	0.625	Yes
NWT-12-3	NWT-12-10	44 km	0.291	Yes
NWT-12-4	NWT-12-5	155 km	0.434	Yes
NWT-12-5	NWT-12-7	61 km	0.328	Yes
NWT-12-6	NWT-12-9	91 km	0.104	Yes
NWT-12-7	NWT-12-9	60 km	0.196	Yes
NWT-12-8	NWT-12-2	36 km	0.625	Yes
NWT-12-9	NWT-12-7	60 km	0.196	Yes
NWT-12-10	NWT-12-3	44 km	0.291	Yes
Non-Wispy Terrain Study Location 13 (NWT-13)				
NWT-13-1	NWT-13-9	43 km	9.7×10^{-4}	No
	NWT-13-8	60 km	0.003	
	NWT-13-10	70 km	0.017	
	NWT-13-2	74 km	7.7×10^{-11}	
	NWT-13-6	74 km	0.009	
	NWT-13-5	75 km	4.9×10^{-6}	
	NWT-13-3	105 km	6.3×10^{-6}	
	NWT-13-7	109 km	0.024	
NWT-13-2	NWT-13-3	50 km	0.001	Yes
	NWT-13-10	52 km	6.1×10^{-6}	
	NWT-13-8	67 km	0.003	
	NWT-13-6	87 km	0.052	
NWT-13-3	NWT-13-10	43 km	3.9×10^{-4}	No
	NWT-13-2	50 km	0.001	
NWT-13-5	NWT-13-6	40 km	9.0×10^{-4}	No
	NWT-13-8	40 km	7.7×10^{-6}	
	NWT-13-9	89 km	6.0×10^{-6}	
	NWT-13-2	106 km	1.7×10^{-5}	

Table III-F8. Continued.

Crater ID	Closest Non-Uniform Crater ID	Closest Non-Uniform Crater Distance	Kolmogorov-Smirnov Test Results (p-value)	Similar to Nearby Craters?
NWT-13-6	NWT-13-8	21 km	0.007	Yes
	NWT-13-2	87 km	0.052	
NWT-13-7	NWT-13-10	47 km	0.021	No
	NWT-13-2	96 km	2.6×10^{-7}	
NWT-13-8	NWT-13-6	21 km	0.007	No
NWT-13-9	NWT-13-6	99 km	0.002	No
NWT-13-10	NWT-13-2	52 km	6.1×10^{-6}	No
Non-Wispy Terrain Study Location 14 (NWT-14)				
NWT-14-1	NWT-14-4	47 km	0.122	Yes
NWT-14-2	NWT-14-5	80 km	0.447	Yes
NWT-14-3	NWT-14-6	33 km	0.009	No
	NWT-14-5	35 km	0.043	
	NWT-14-2	84 km	3.1×10^{-6}	
NWT-14-4	NWT-14-1	47 km	0.122	Yes
NWT-14-5	NWT-14-6	59 km	0.029	Yes
	NWT-14-2	80 km	0.447	
NWT-14-6	NWT-14-5	59 km	0.029	No
NWT-14-7	NWT-14-8	89 km	0.047	No
	NWT-14-4	109 km	0.014	
NWT-14-8	NWT-14-2	96 km	0.036	No
NWT-14-10	NWT-14-2	119 km	1.9×10^{-4}	No
Non-Wispy Terrain Study Location 15 (NWT-15)				
NWT-15-1	NWT-15-6	51 km	0.594	Yes
NWT-15-2	NWT-15-4	50 km	0.170	Yes
NWT-15-3	NWT-15-10	81 km	0.046	Yes
	NWT-15-6	150 km	0.092	

Table III-F8. Continued.

Crater ID	Closest Non-Uniform Crater ID	Closest Non-Uniform Crater Distance	Kolmogorov-Smirnov Test Results (p-value)	Similar to Nearby Craters?
NWT-15-4	NWT-15-2	50 km	0.170	Yes
NWT-15-5	NWT-15-2	99 km	4.2×10^{-4}	No
NWT-15-6	NWT-15-1	51 km	0.594	Yes
NWT-15-9	NWT-15-6	84 km	4.8×10^{-11}	No
NWT-15-10	NWT-15-2	130 km	4.3×10^{-4}	No
Non-Wispy Terrain Study Location 16 (NWT-16)				
NWT-16-1	NWT-16-5	27 km	5.8×10^{-5}	Yes
	NWT-16-3	41 km	0.002	
	NWT-16-2	49 km	0.068	
NWT-16-2	NWT-16-1	49 km	0.068	Yes
NWT-16-3	NWT-16-5	39 km	0.034	No
	NWT-16-2	86 km	0.007	
NWT-16-4	NWT-16-10	71 km	0.297	Yes
NWT-16-5	NWT-16-2	72 km	0.003	No
NWT-16-6	NWT-16-8	48 km	0.167	Yes
NWT-16-7	NWT-16-8	36 km	0.076	Yes
NWT-16-8	NWT-16-7	36 km	0.076	Yes
NWT-16-9	NWT-16-2	72 km	0.322	Yes
NWT-16-10	NWT-16-4	71 km	0.297	Yes
Non-Wispy Terrain Study Location 17 (NWT-17)				
NWT-17-1	NWT-17-9	86 km	0.019	No
	NWT-17-2	96 km	3.6×10^{-6}	
	NWT-17-6	98 km	0.031	

Table III-F8. Continued.

Crater ID	Closest Non-Uniform Crater ID	Closest Non-Uniform Crater Distance	Kolmogorov-Smirnov Test Results (p-value)	Similar to Nearby Craters?
NWT-17-2	NWT-17-3	91 km	3.5×10^{-4}	No
NWT-17-3	NWT-17-10	107 km	0.235	Yes
NWT-17-4	NWT-17-7	47 km	1.0×10^{-5}	No
NWT-17-5	NWT-17-8	31 km	0.002	No
NWT-17-6	NWT-17-9	68 km	1.9×10^{-4}	Yes
	NWT-17-8	76 km	0.310	
NWT-17-7	NWT-17-8	42 km	0.099	Yes
NWT-17-8	NWT-17-7	42 km	0.099	Yes
NWT-17-9	NWT-17-6	68 km	1.9×10^{-4}	No
NWT-17-10	NWT-17-3	107 km	0.235	Yes
Non-Wispy Terrain Study Location 18 (NWT-18)				
NWT-18-1	NWT-18-7	102 km	2.2×10^{-16}	No
	NWT-18-2	108 km	2.2×10^{-16}	
	NWT-18-5	114 km	1.6×10^{-5}	
NWT-18-2	NWT-18-5	194 km	2.2×10^{-16}	No
NWT-18-5	NWT-18-10	21 km	0.032	Yes
	NWT-18-7	45 km	2.2×10^{-16}	
	NWT-18-6	60 km	0.111	
NWT-18-6	NWT-18-10	39 km	0.184	Yes
NWT-18-7	NWT-18-8	40 km	5.6×10^{-4}	No
	NWT-18-5	45 km	2.2×10^{-16}	
NWT-18-8	NWT-18-5	74 km	2.2×10^{-16}	No
NWT-18-9	NWT-18-6	55 km	0.067	Yes
NWT-18-10	NWT-18-5	21 km	0.032	No

Table III-F8. Continued.

Crater ID	Closest Non-Uniform Crater ID	Closest Non-Uniform Crater Distance	Kolmogorov-Smirnov Test Results (p-value)	Similar to Nearby Craters?
Non-Wispy Terrain Study Location 19 (NWT-19)				
NWT-19-6	NWT-19-7	106 km	0.053	Yes
NWT-19-7	NWT-19-6	106 km	0.053	Yes
NWT-19-10	NWT-19-6	274 km	0.004	No
Non-Wispy Terrain Study Location 20 (NWT-20)				
NWT-20-1	NWT-20-3	82 km	0.007	Yes
	NWT-20-4	94 km	0.017	
	NWT-20-2	107 km	3.1×10^{-4}	
	NWT-20-7	115 km	6.2×10^{-9}	
	NWT-20-9	178 km	0.061	
NWT-20-2	NWT-20-7	19 km	2.7×10^{-4}	No
	NWT-20-4	48 km	5.7×10^{-6}	
	NWT-20-1	107 km	3.1×10^{-4}	
NWT-20-3	NWT-20-1	82 km	0.007	No
NWT-20-4	NWT-20-7	38 km	0.003	No
	NWT-20-1	94 km	0.017	
NWT-20-7	NWT-20-1	115 km	6.2×10^{-9}	No
NWT-20-9	NWT-20-1	178 km	0.061	Yes
Non-Wispy Terrain Study Location 21 (NWT-21)				
NWT-21-1	NWT-21-9	73 km	2.5×10^{-4}	No
NWT-21-2	NWT-21-9	159 km	1.9×10^{-6}	No
NWT-21-4	NWT-21-6	26 km	0.464	Yes
NWT-21-6	NWT-21-4	26 km	0.464	Yes
NWT-21-7	NWT-21-10	31 km	0.562	Yes
NWT-21-8	NWT-21-10	68 km	1.7×10^{-5}	No

Table III-F8. Continued.

Crater ID	Closest Non-Uniform Crater ID	Closest Non-Uniform Crater Distance	Kolmogorov-Smirnov Test Results (p-value)	Similar to Nearby Craters?
NWT-21-9	NWT-21-6	56 km	0.218	Yes
NWT-21-10	NWT-21-7	31 km	0.562	Yes
Non-Wispy Terrain Study Location 22 (NWT-22)				
NWT-22-1	NWT-22-3	48 km	0.047	No
NWT-22-2	NWT-22-5	77 km	1.4×10^{-14}	No
	NWT-22-6	82 km	1.8×10^{-6}	
	NWT-22-4	84 km	0.010	
	NWT-22-7	122 km	0.048	
	NWT-22-8	135 km	0.023	
NWT-22-3	NWT-22-8	18 km	0.130	Yes
NWT-22-4	NWT-22-6	21 km	3.6×10^{-4}	No
	NWT-22-8	128 km	0.004	
NWT-22-5	NWT-22-8	34 km	2.3×10^{-5}	No
NWT-22-6	NWT-22-8	147 km	1.8×10^{-4}	No
NWT-22-7	NWT-22-8	19 km	0.021	No
NWT-22-8	NWT-22-3	18 km	0.130	Yes
NWT-22-9	NWT-22-8	110 km	5.9×10^{-8}	No
NWT-22-10	NWT-22-8	73 km	7.0×10^{-4}	No
Non-Wispy Terrain Study Location 23 (NWT-23)				
NWT-23-1	NWT-23-9	54 km	3.4×10^{-4}	No
NWT-23-9	NWT-23-10	130 km	0.056	Yes
NWT-23-10	NWT-23-9	130 km	0.056	Yes
Non-Wispy Terrain Study Location 24 (NWT-24)				

Table III-F8. Continued.

Crater ID	Closest Non-Uniform Crater ID	Closest Non-Uniform Crater Distance	Kolmogorov-Smirnov Test Results (p-value)	Similar to Nearby Craters?
NWT-24-2	NWT-24-8	40 km	0.136	Yes
NWT-24-5	NWT-24-9	94 km	0.121	Yes
NWT-24-6	NWT-24-10	25 km	0.040	Yes
	NWT-24-9	37 km	0.109	
NWT-24-8	NWT-24-2	40 km	0.136	Yes
NWT-24-9	NWT-24-6	37 km	0.109	Yes
NWT-24-10	NWT-24-6	25 km	0.040	No
Non-Wispy Terrain Study Location 25 (NWT-25)				
NWT-25-1	NWT-25-10	29 km	0.785	Yes
NWT-25-2	NWT-25-10	22 km	0.276	Yes
NWT-25-3	NWT-25-6	51 km	0.011	Yes
	NWT-25-5	91 km	0.093	
NWT-25-4	NWT-25-5	33 km	0.299	Yes
NWT-25-5	4WT-25-10	33 km	0.107	Yes
NWT-25-6	NWT-25-3	51 km	0.011	No
NWT-25-7	NWT-25-8	43 km	0.018	No
NWT-25-8	NWT-25-2	38 km	0.059	Yes
NWT-25-9	NWT-25-5	51 km	0.017	No
NWT-25-10	NWT-25-2	22 km	0.276	Yes
Non-Wispy Terrain Study Location 26 (NWT-26)				

Table III-F8. Continued.

Crater ID	Closest Non-Uniform Crater ID	Closest Non-Uniform Crater Distance	Kolmogorov-Smirnov Test Results (p-value)	Similar to Nearby Craters?
NWT-26-1	NWT-26-9	41 km	6.2×10^{-5}	No
	NWT-26-5	54 km	2.1×10^{-9}	
	NWT-26-4	64 km	2.5×10^{-9}	
	NWT-26-10	75 km	1.5×10^{-6}	
	NWT-26-7	85 km	5.8×10^{-4}	
	NWT-26-8	123 km	1.9×10^{-7}	
	NWT-26-6	168 km	2.2×10^{-16}	
	NWT-26-3	187 km	1.5×10^{-5}	
	NWT-26-2	191 km	1.5×10^{-7}	
NWT-26-2	NWT-26-3	18 km	0.002	No
	NWT-26-6	37 km	6.6×10^{-8}	
	NWT-26-8	68 km	4.9×10^{-7}	
	NWT-26-10	120 km	0.007	
	NWT-26-4	135 km	5.5×10^{-5}	
	NWT-26-5	148 km	0.018	
	NWT-26-9	150 km	4.7×10^{-5}	
	NWT-26-7	276 km	2.8×10^{-4}	
NWT-26-3	NWT-26-6	37 km	5.5×10^{-6}	No
	NWT-26-8	65 km	2.3×10^{-4}	
	NWT-26-10	114 km	2.7×10^{-4}	
	NWT-26-4	128 km	3.8×10^{-6}	
	NWT-26-5	141 km	2.6×10^{-4}	
	NWT-26-9	146 km	3.9×10^{-4}	
	NWT-26-7	271 km	0.002	
NWT-26-4	NWT-26-5	13 km	8.5×10^{-8}	No
	NWT-26-10	16 km	7.0×10^{-5}	
	NWT-26-9	28 km	1.8×10^{-5}	
	NWT-26-8	68 km	0.007	
	NWT-26-6	116 km	8.0×10^{-12}	
	NWT-26-7	145 km	6.0×10^{-5}	
NWT-26-5	NWT-26-9	25 km	3.2×10^{-6}	No
	NWT-26-10	29 km	9.5×10^{-7}	
	NWT-26-8	81 km	2.4×10^{-7}	
	NWT-26-6	129 km	9.7×10^{-11}	
	NWT-26-7	132 km	2.8×10^{-5}	
NWT-26-6	NWT-26-8	49 km	2.2×10^{-16}	No
	NWT-26-10	101 km	9.9×10^{-6}	

Table III-F8. Continued.

Crater ID	Closest Non-Uniform Crater ID	Closest Non-Uniform Crater Distance	Kolmogorov-Smirnov Test Results (p-value)	Similar to Nearby Craters?
	NWT-26-9	128 km	1.1×10^{-13}	
	NWT-26-7	254 km	2.5×10^{-8}	
NWT-26-7	NWT-26-9	126 km	0.006	No
	NWT-26-10	158 km	0.019	
	NWT-26-8	208 km	0.018	
NWT-26-8	NWT-26-10	52 km	1.2×10^{-7}	No
	NWT-26-9	82 km	3.0×10^{-6}	
NWT-26-9	NWT-26-10	35 km	2.3×10^{-4}	No
NWT-26-10	NWT-26-9	35 km	2.3×10^{-4}	No
Non-Wispy Terrain Study Location 27 (NWT-27)				
NWT-27-1	NWT-27-2	28 km	0.003	Yes
	NWT-27-8	28 km	0.112	
NWT-27-2	NWT-27-1	28 km	0.003	No
NWT-27-3	NWT-27-8	63 km	0.068	Yes
NWT-27-4	NWT-27-9	32 km	0.116	Yes
NWT-27-5	NWT-27-6	26 km	0.473	Yes
NWT-27-6	NWT-27-5	26 km	0.473	Yes
NWT-27-7	NWT-27-10	43 km	0.558	Yes
NWT-27-8	NWT-27-1	28 km	0.112	Yes
NWT-27-9	NWT-27-4	32 km	0.116	Yes
NWT-27-10	NWT-27-7	43 km	0.558	Yes
Non-Wispy Terrain Study Location 28 (NWT-28)				
NWT-28-3	NWT-28-10	103 km	7.8×10^{-6}	No
	NWT-28-4	106 km	2.8×10^{-8}	
	NWT-28-9	120 km	4.8×10^{-7}	
	NWT-28-6	124 km	1.2×10^{-7}	

Table III-F8. Continued.

Crater ID	Closest Non-Uniform Crater ID	Closest Non-Uniform Crater Distance	Kolmogorov-Smirnov Test Results (p-value)	Similar to Nearby Craters?
	NWT-28-5	139 km	5.6×10^{-4}	
NWT-28-4	NWT-28-9	38 km	5.0×10^{-5}	Yes
	NWT-28-5	44 km	0.375	
NWT-28-5	NWT-28-4	44 km	0.375	Yes
NWT-28-6	NWT-28-5	42 km	0.169	Yes
NWT-28-9	NWT-28-10	24 km	0.002	No
	NWT-28-4	38 km	5.0×10^{-5}	
NWT-28-10	NWT-28-4	47 km	0.026	No
Non-Wispy Terrain Study Location 29 (NWT-29)				
NWT-29-3	NWT-29-7	21 km	0.265	Yes
NWT-29-5	NWT-29-9	60 km	0.013	No
	NWT-29-3	70 km	2.7×10^{-4}	
NWT-29-7	NWT-29-3	21 km	0.265	Yes
NWT-29-8	NWT-29-10	37 km	0.082	Yes
NWT-29-9	NWT-29-10	45 km	7.6×10^{-5}	No
NWT-29-10	NWT-29-8	37 km	0.082	Yes
Non-Wispy Terrain Study Location 30 (NWT-30)				
NWT-30-2	NWT-30-4	51 km	0.097	Yes
NWT-30-4	NWT-30-9	39 km	0.034	No
NWT-30-7	NWT-30-9	93 km	0.132	Yes
NWT-30-9	NWT-30-2	88 km	0.109	Yes

Table III-F9. Results for Dip tests for Non-Wispy Terrain crater rim azimuths.

Crater ID	Dip Test p-value	Modality ($\alpha = 0.05$)	Azimuth Mode(s)	Common Azimuth Mode(s) between PICs
Non-Wispy Terrain Study Location 1 (NWT-1)				
NWT-1-3	$< 2.2 \times 10^{-16}$	Multimodal	146º, 90º	Set 1: 90º
NWT-1-7	9.1×10^{-6}	Multimodal	90º, 166º	
NWT-1-8	3.6×10^{-5}	Multimodal	90º, 153º	Set 2: 162° - 166°
NWT-1-9	0.007	Multimodal	90º, 162º	
Non-Wispy Terrain Study Location 2 (NWT-2)				
No PICs identified				
Non-Wispy Terrain Study Location 3 (NWT-3)				
NWT-3-1	5.3×10^{-5}	Multimodal	111º, 115º	Set 1: 110° - 111° - 112° - 114° - 115° - 116° - 117° - 120°
NWT-3-2	1.5×10^{-5}	Multimodal	116º, 112º	
NWT-3-3	0.234	Unimodal	117º	
NWT-3-4	0.164	Unimodal	116º	
NWT-3-5	0.135	Unimodal	114º	
NWT-3-7	0.147	Unimodal	116º	
NWT-3-8	$< 2.2 \times 10^{-16}$	Multimodal	120º, 112º	
NWT-3-9	1.0×10^{-4}	Multimodal	117º, 110º	
Non-Wispy Terrain Study Location 4 (NWT-4)				
NWT-4-1	0.013	Multimodal	111º, 113º	Set 1: 104º - 107º - 110º - 111º - 112º - 113º - 114º
NWT-4-4	0.009	Multimodal	111º, 104º	
NWT-4-5	0.035	Multimodal	110º, 114º	
NWT-4-6	4.0×10^{-6}	Multimodal	107º, 112º	
NWT-4-9	0.056	Unimodal	121º	
Non-Wispy Terrain Study Location 5 (NWT-5)				
NWT-5-4	0.003	Multimodal	70º, 62º	Set 1: 50º - 52º - 56º - 57º - 59º - 60º 62º - 66º Set 2: 70º - 72º
NWT-5-5	0.143	Unimodal	66º	
NWT-5-6	4.8×10^{-4}	Multimodal	72º, 56º	
NWT-5-7	8.3×10^{-4}	Multimodal	59º, 44º	
NWT-5-8	0.001	Multimodal	57º, 50º	
NWT-5-9	0.306	Unimodal	52º	
NWT-5-10	0.014	Multimodal	52º, 60º	
Non-Wispy Terrain Study Location 6 (NWT-6)				
NWT-6-3	0.149	Unimodal	122º	Set 1: 118º - 120º - 121º - 122º - 128º
NWT-6-4	0.283	Unimodal	120º	
NWT-6-5	0.215	Unimodal	121º	
NWT-6-7	0.710	Unimodal	118º	
NWT-6-10	0.610	Unimodal	128º	

Table III-F9. Continued.

Crater ID	Dip Test p-value	Modality (α = 0.05)	Azimuth Mode(s)	Common Azimuth Mode(s) between PICs
Non-Wispy Terrain Study Location 7 (NWT-7)				
NWT-7-1	0.008	Multimodal	122º, 127º	Set 1: 118º - 120º - 122º - 127º - 130º - 132º
NWT-7-2	0.018	Multimodal	118º, 138º	
NWT-7-3	0.284	Unimodal	120º	
NWT-7-4	0.338	Unimodal	130º	
NWT-7-5	0.956	Unimodal	132º	
Non-Wispy Terrain Study Location 8 (NWT-8)				
NWT-8-2	0.196	Unimodal	42º	Set 1: 38º - 42º Set 2: 67º - 69º Set 3: 90º
NWT-8-3	0.495	Unimodal	38º	
NWT-8-4	0.065	Unimodal	90º	
NWT-8-5	0.158	Unimodal	67º	
NWT-8-6	0.486	Unimodal	22º	
NWT-8-9	0.956	Unimodal	90º	
NWT-8-10	0.006	Multimodal	69º, 58º	
Non-Wispy Terrain Study Location 9 (NWT-9)				
NWT-9-1	2.8×10^{-4}	Multimodal	116º, 125º	Set 1: 116º - 118º - 119º - 120º - 122º - 123º - 125º - 127º - 130º
NWT-9-2	0.003	Multimodal	118º, 127º	
NWT-9-4	0.008	Multimodal	123º, 120º	
NWT-9-5	0.008	Multimodal	130º, 125º	
NWT-9-7	0.006	Multimodal	122º, 119º	
NWT-9-9	0.043	Multimodal	116º, 101º	
Non-Wispy Terrain Study Location 10 (NWT-10)				
NWT-10-1	5.4×10^{-4}	Multimodal	115º, 107º	Set 1: 28º - 32º
NWT-10-2	0.099	Unimodal	32º	
NWT-10-3	0.211	Unimodal	50º	
NWT-10-6	0.654	Unimodal	43º	
NWT-10-9	0.214	Unimodal	92º	
NWT-10-10	0.205	Unimodal	28º	
Non-Wispy Terrain Study Location 11 (NWT-11)				
NWT-11-1	0.402	Unimodal	57º	Set 1: 54º - 57º - 58º - 61º - 64º
NWT-11-3	7.0×10^{-4}	Unimodal	64º	
NWT-11-6	0.145	Unimodal	48º	
NWT-11-7	0.656	Unimodal	58º	
NWT-11-8	0.772	Unimodal	54º	
NWT-11-10	0.976	Unimodal	61º	
Non-Wispy Terrain Study Location 12 (NWT-12)				

Table III-F9. Continued.

Crater ID	Dip Test p-value	Modality (α = 0.05)	Azimuth Mode(s)	Common Azimuth Mode(s) between PICs
NWT-12-1	0.331	Unimodal	61º	Set 1: 52º - 57º - 60º - 61º - 66º - 70º - 75º - 77º - 80º
NWT-12-2	0.017	Multimodal	52º, 70º	
NWT-12-3	3.1×10^{-4}	Multimodal	75º, 61º	
NWT-12-4	0.081	Unimodal	57º	
NWT-12-5	0.138	Unimodal	80º	
NWT-12-6	0.089	Unimodal	36º	
NWT-12-7	0.259	Unimodal	60º	
NWT-12-8	0.228	Unimodal	45º	
NWT-12-9	0.644	Unimodal	77º	
NWT-12-10	0.784	Unimodal	66º	
Non-Wispy Terrain Study Location 13 (NWT-13)				
NWT-13-2	$<2.2 \times 10^{-16}$	Multimodal	35º, 52º	-
NWT-13-6	0.032	Multimodal	90º, 28º	
Non-Wispy Terrain Study Location 14 (NWT-14)				
NWT-14-1	3.2×10^{-4}	Multimodal	90º, 134º	Set 1: 90º Set 2: 134º - 136º
NWT-14-2	1.4×10^{-4}	Multimodal	90º, 136º	
NWT-14-4	0.177	Unimodal	121º	
NWT-14-5	0.315	Unimodal	134º	
Non-Wispy Terrain Study Location 15 (NWT-15)				
NWT-15-1	0.005	Multimodal	93º, 2º	Set 1: 2º - 8º Set 2: 90º-93º
NWT-15-2	3.6×10^{-5}	Multimodal	84º, 90º	
NWT-15-3	0.005	Multimodal	90º, 8º	
NWT-15-4	0.016	Multimodal	90º, 50º	
NWT-15-6	2.0×10^{-6}	Multimodal	90º, 22º	
Non-Wispy Terrain Study Location 16 (NWT-16)				
NWT-16-1	0.035	Multimodal	90º, 129º	Set 1: 90º Set 2: 125º - 129º
NWT-16-2	0.066	Unimodal	90º	
NWT-16-4	0.016	Multimodal	90º, 118º	
NWT-16-6	0.020	Multimodal	90º, 125º	
NWT-16-7	0.213	Unimodal	150º	
NWT-16-8	0.285	Unimodal	108º	
NWT-16-9	0.337	Unimodal	90º	
NWT-16-10	0.179	Unimodal	110º	
Non-Wispy Terrain Study Location 17 (NWT-17)				
NWT-17-3	0.077	Unimodal	48º	Set 1: 48º - 49º - 52º - 54º
NWT-17-6	1.1×10^{-4}	Multimodal	90º, 41º	

Table III-F9. Continued.

Crater ID	Dip Test p-value	Modality (α = 0.05)	Azimuth Mode(s)	Common Azimuth Mode(s) between PICs
NWT-17-7	0.058	Unimodal	49º	
NWT-17-8	0.098	Unimodal	61º	
NWT-17-10	0.007	Multimodal	52º, 54º	
Non-Wispy Terrain Study Location 18 (NWT-18)				
NWT-18-5	8.0×10^{-4}	Multimodal	60º, 33º	
NWT-18-6	0.194	Unimodal	32º	Set 1: 32º - 33º
NWT-18-9	0.009	Multimodal	39º, 67º	
Non-Wispy Terrain Study Location 19 (NWT-19)				
NWT-19-6	0.014	Multimodal	137º, 27º	-
NWT-19-7	0.060	Unimodal	119º	
Non-Wispy Terrain Study Location 20 (NWT-20)				
NWT-20-1	$<2.2 \times 10^{-16}$	Multimodal	13º, 103º	-
NWT-20-9	$<2.2 \times 10^{-16}$	Multimodal	2º, 42º	
Non-Wispy Terrain Study Location 21 (NWT-21)				
NWT-21-4	9.4×10^{-4}	Multimodal	41º, 44º	
NWT-21-6	0.153	Unimodal	34º	Set 1: 41º - 42º - 44º
NWT-21-7	$<2.2 \times 10^{-16}$	Multimodal	90º, 15º	
NWT-21-9	5.1×10^{-4}	Multimodal	90º, 42º	Set 2: 90º
NWT-21-10	$<2.2 \times 10^{-16}$	Multimodal	90º, 51º	
Non-Wispy Terrain Study Location 22 (NWT-22)				
NWT-22-3	0.042	Multimodal	23º, 121º	-
NWT-22-8	2.2×10^{-7}	Multimodal	90º, 131º	
Non-Wispy Terrain Study Location 23 (NWT-23)				
NWT-23-9	7.9×10^{-7}	Multimodal	130º, 143º	-
NWT-23-10	$<2.2 \times 10^{-16}$	Multimodal	8º, 23º	
Non-Wispy Terrain Study Location 24 (NWT-24)				
NWT-24-2	6.3×10^{-6}	Multimodal	41º, 51º	
NWT-24-5	0.084	Unimodal	36º	Set 1: 33º - 35º - 36º - 41º
NWT-24-6	1.9×10^{-4}	Multimodal	25º, 63º	
NWT-24-8	2.5×10^{-5}	Multimodal	35º, 33º	Set 2: 51º
NWT-24-9	7.7×10^{-6}	Multimodal	6º, 51º	
Non-Wispy Terrain Study Location 25 (NWT-25)				

Table III-F9. Continued.

Crater ID	Dip Test p-value	Modality (α = 0.05)	Azimuth Mode(s)	Common Azimuth Mode(s) between PICs
NWT-25-1	0.050	Multimodal	122º, 115º	Set 1: 108º - 111º - 114º - 115º - 116º Set 2: 122º - 124º
NWT-25-2	0.068	Unimodal	115º	
NWT-25-3	0.004	Multimodal	102º, 111º	
NWT-25-4	0.014	Multimodal	122º, 114º	
NWT-25-5	0.050	Multimodal	124º, 108º	
NWT-25-8	0.095	Unimodal	116º	
NWT-25-10	0.020	Multimodal	114º, 124º	
Non-Wispy Terrain Study Location 26 (NWT-26)				
No PICs identified				
Non-Wispy Terrain Study Location 27 (NWT-27)				
NWT-27-1	0.095	Unimodal	123º	Set 1: 90º - 93º Set 2: 116º - 120º - 121º - 123º - 125º Set 3: 144º - 145º
NWT-27-3	0.002	Multimodal	145º, 125º	
NWT-27-4	0.006	Multimodal	144º, 138º	
NWT-27-5	0.064	Unimodal	116º	
NWT-27-6	0.180	Unimodal	121º	
NWT-27-7	0.062	Unimodal	90º	
NWT-27-8	0.504	Unimodal	104º	
NWT-27-9	0.069	Unimodal	120º	
NWT-27-10	0.131	Unimodal	93º	
Non-Wispy Terrain Study Location 28 (NWT-28)				
NWT-28-4	$<2.2 \times 10^{-16}$	Multimodal	117º, 30º	-
NWT-28-5	0.041	Multimodal	51º, 136º	
NWT-28-6	0.346	Unimodal	18º	
Non-Wispy Terrain Study Location 29 (NWT-29)				
NWT-29-3	4.2×10^{-4}	Multimodal	180º, 167º	Set 1: 90º Set 2: 111º - 113º
NWT-29-7	0.029	Multimodal	113º, 111º	
NWT-29-8	0.001	Multimodal	90º, 124º	
NWT-29-10	9.8×10^{-6}	Multimodal	90º, 77º	
Non-Wispy Terrain Study Location 30 (NWT-30)				
NWT-30-2	0.075	Unimodal	1º	-
NWT-30-7	8.5×10^{-5}	Multimodal	119º, 164º	
NWT-30-9	1.8×10^{-6}	Multimodal	7º, 33º	

CONCLUSION

In this dissertation, I have shown the utility of tectonic analyses on icy satellites as an important and effective tool for inferring geologic and geophysical processes of these bodies. Knowledge of these processes enables a better understanding of the histories of these bodies and the satellite systems in which they reside. In Chapter I, I find sufficient evidence to interpret the Arden Corona boundary as a listric normal fault system. I do not find sufficient evidence to interpret the 340˚ Chasma as a listric normal fault system, and it may instead be planar in geometry. A listric fault geometry implies the presence of a subsurface detachment, which likely marked Miranda's brittle-ductile transition (BDT) at the time of faulting. I estimate that the BDT depth in the region of the Arden Corona boundary during faulting was between 6.7 km and 9.0 km with an associated thermal gradient between 6 K km^{-1} and 25 K km^{-1}, and a heat flux between 31 mW m^{-2} and 112 mW m^{-2}. These estimates are consistent with a previously hypothesized heating event associated with an ancient tidal resonance of Miranda with Umbriel and/or Ariel. I conclude that Miranda's brittle-ductile transition was shallower at the time Arden Corona formed than at the time the global rift system formed.

In Chapter II, I find that many natural normal fault slopes on Tethys, Rhea, and Dione are much shallower than fault dips derived from laboratory deformation experiments in cryogenic H_2O ice. In the regions of Ithaca Chasma on Tethys, and Avaiki Chasmata on Rhea, none of the analyzed normal faults exhibit fault slopes that fall within the laboratory derived dip range. Within Dione's Wispy Terrain, the analyzed faults of Palatine Chasmata exhibit fault slopes that fall within this range, while only one fault in Padua Chasmata, has a fault slope that falls below this range. However, the steepest analyzed faults in the Wispy Terrain do fall within the hypothesized dip range. Our results provide evidence that either regolith deposition and/or viscous relaxation are the most viable explanations for the shallow fault slopes in all three study areas.

In Chapter III, I find evidence that polygonal impact craters (PICs) are widespread throughout Dione's Non-Wispy Terrain, reflecting abundant subtle and/or nonvisible fractures in this region. These results support interpretations by others of lineaments as subtle fractures. These inferred large scale fracture systems likely formed during a global stress event which may have been induced by spin-up and despinning. Our work shows that the identification of PICs and their azimuths is a useful tool in inferring the presence and azimuths of controlling subtle fractures on icy satellites. The rigorous technique developed in this work to accomplish this inference provides an approach for investigating subtle fractures and inferring the tectonic histories of other icy bodies.

VITA

Chloe Beddingfield was born April 26th, 1987, and is the daughter of Craig and Christina Beddingfield, and the sister of John Beddingfield. She grew up in Austin, Texas, and attended college to at Texas Tech University where she received a B.S. in Geosciences and a minor in Chemistry. Under the guidance of her undergraduate advisor, Dr. Aaron Yoshinobu, she developed a deep passion for planetary science. She then pursued a Ph.D. in Geology at the University of Tennessee under the guidance of her advisor, Dr. Devon Burr, and committee members Dr. William Dunne, Dr. Joshua Emery, and Dr. Liem Tran. After completion of her doctorate she will continue her career in planetary science as a postdoctoral research associate. She will work with Dr. Jeffrey Moersch and Dr. Harry McSween at the University of Tennessee.